REACTIVITY OF FULLERENES, ENDOHEDRAL METALLOFULLERENES, AND NANOTUBES, AND THEIR POSSIBLE APPLICATION IN SOLAR ENERGY CONVERSION

Juan Pablo Martínez López

Doctoral Thesis:

Reactivity of Fullerenes, Endohedral Metallofullerenes, and Nanotubes, and their Possible Application in Solar Energy Conversion

Juan Pablo Martínez López

October 2016, Doctoral Programme in Chemistry

Supervised by:

Dr. Albert Poater Teixidor
Dr. Sílvia Osuna Oliveras
Prof. Dr. F. Matthias Bickelhaupt
Prof. Dr. Miquel Solà Puig

Tutor:

Prof. Dr. Miquel Solà Puig

This manuscript has been presented to jointly opt for the doctoral degree from the University of Girona and the Free University of Amsterdam

Dr. Albert Poater Teixidor, Dr. Sílvia Osuna Oliveras, and Prof. Dr. Miquel Solà Puig from the University of Girona; and Prof. Dr. F. Matthias Bickelhaupt from the Free University of Amsterdam,

WE DECLARE:

That the thesis entitled "Reactivity of Fullerenes, Endohedral Metallofullerenes, and Nanotubes; and their Possible Application in Solar Energy Conversion", presented by Juan Pablo Martínez López to obtain a doctoral degree, has been completed under our supervision and meets the requirements to opt for an International Doctorate.

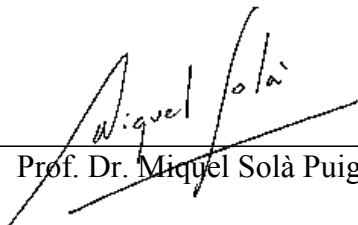For all intents and purposes, we hereby sign this document.

Signature

_____
Dr. Albert Poater Teixidor

_____
Dr. Sílvia Osuna Oliveras

_____
Prof. Dr. Miquel Solà Puig

_____
Prof. Dr. F. Matthias Bickelhaupt

Girona, October 2016

Amsterdam, October 2016

VRIJE UNIVERSITEIT

UNIVERSITAT DE GIRONA

Reactivity of Fullerenes, Endohedral Metallofullerenes, and Nanotubes, and
their Possible Application in Solar Energy Conversion

promotoren:	prof.dr. F.M. Bickelhaupt
	prof.dr. Miquel Solà Puig
copromotoren:	dr. Albert Poater Teixidor
	dr. Sílvia Osuna Oliveras

ACADEMISCH PROEFSCHRIFT
ter verkrijging van de graad
Doctor aan de Vrije Universiteit Amsterdam
op gezag van de Rector Magnificus
prof.dr. Vinod Subramaniam
en
Doctor in de Exacte Wetenschappen aan de Universitat de Girona
op gezag van de Rector
prof.dr. Sergi Bonet i Marull

in het openbaar te verdedigen
ten overstaan van de promotiecommissie
van de Facultiet der Exacte Wetenschappen van de Vrije Universiteit Amsterdam
en de Faculty of Sciences van de Universitat de Girona

op oktober 2016
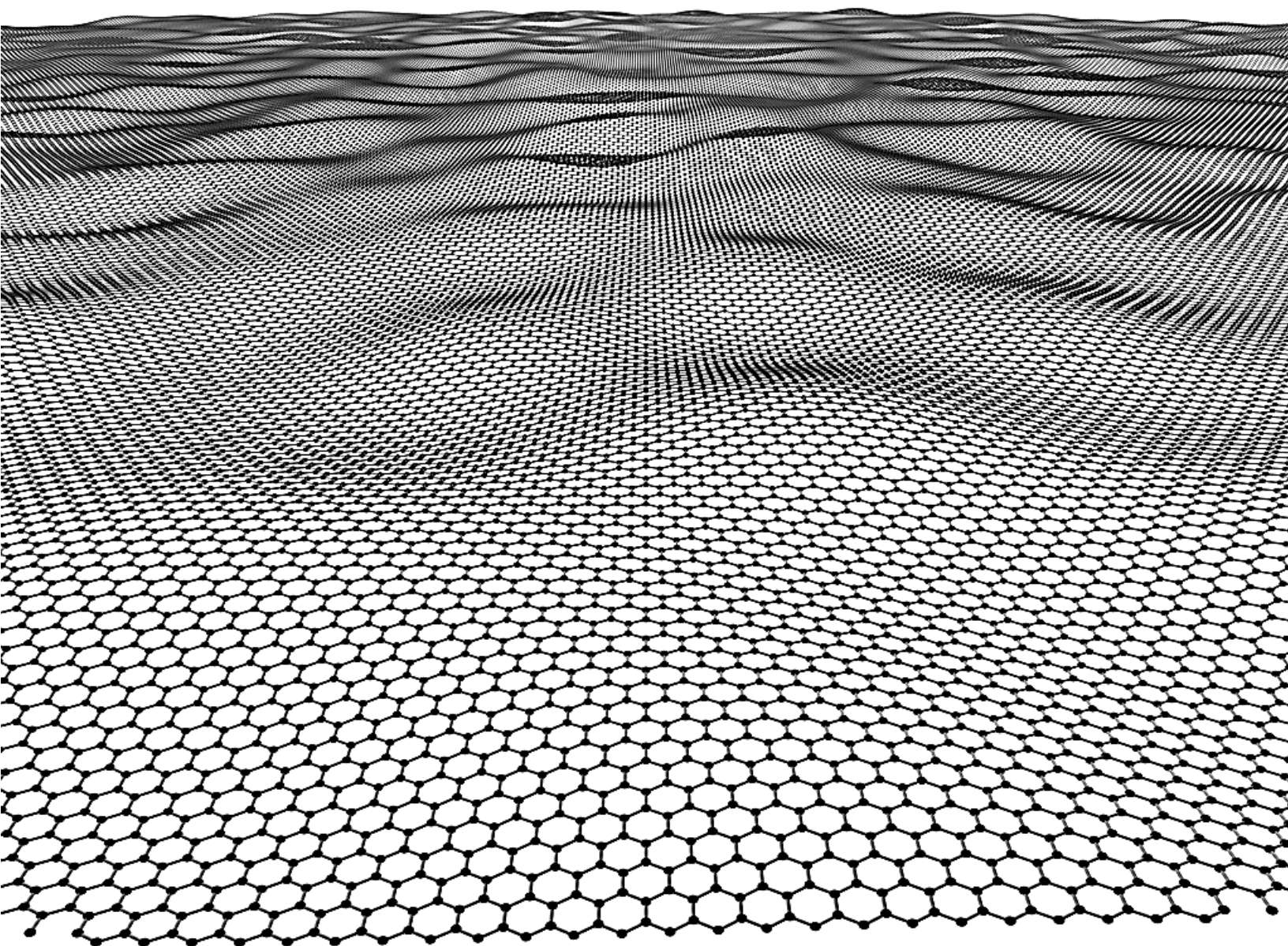in de aula van de universiteit,
De Boelelaan 1105

door

Juan Pablo Martínez López

geboren te Matehuala, Mexico

"There's plenty room at the bottom"

Richard Feynman, December 29th, 1959

Pasadena, California, U.S.A.

Acknowledgements

Finally, in a personal way, family, significant other, and friends cannot be excluded since they always provide emotional support through the different professional challenges that one faces through the entire life. To my close friend Dr. Uriel Sierra who arranged our assistance to the *Premios Príncipe de Asturias*, wherein I personally shacked the hand of Peter Higgs (the famous boson); and also we were interviewed for the national newspaper *La Nueva España* as foreign researchers assisting such an event. To my good friend Dr. René Loredo who invited me to a very interesting guided visit at the *Elettra Sincrotrone Trieste* in Italy. All of these extracurricular activities were rewarding experiences. To my parents and *EZ*, who are always supporting me in every aspect of life. Now it is time to go after new professional goals; certainly, it is an advantage counting with the strengths, knowledge, and experience that I have acquired from the doctoral studies developed at the University of Girona and the Free University of Amsterdam.

Juan Pablo Mtz., October 2016

List of Publications

This Thesis is presented as a compendium of publications.

Published articles included in this thesis:

1. Martínez, J.P.; Osuna, S.; Solà, M.; Voityuk, A., "Extent of Charge Separation and Exciton Delocalization for Electronically Excited States in a Triphenylamine-C_{60} Donor-Acceptor Conjugate: a Combined Molecular Dynamics and TD-DFT Study", *Theor. Chem. Acc.* **2015**, 134, 12. (Impact Factor 1.806, 3rd quartile)

2. Martínez, J.P.; Solà, M.; Poater, A., "On the Reaction Mechanism of the Rhodium-Catalyzed Arylation of Fullerene (C_{60}) with Organoboron Compounds in the Presence of Water", *ChemistryOpen* **2015**, 4, 774-778. (Impact Factor 3.585, classified as *Very Important Paper* by the editors, 2nd quartile)

3. Martínez, J.P.; Langa, F.; Bickelhaupt, F.M.; Osuna, S.; Solà, M., "(4+2) and (2+2) Cycloadditions of Benzyne to C_{60} and Zig-Zag Single-Walled Carbon Nanotubes: The Effect of the Curvature", *J. Phys. Chem. C* **2016**, 120, 1716-1726. (Impact Factor 4.509, 1st quartile)

4. Martínez, J.P.; Garcia-Borràs, M.; Osuna, S.; Poater, J.; Bickelhaupt, F.M.; Solà, M., "Reaction Mechanism and Regioselectivity of the Bingel-Hirsch Addition of Dimethyl Bromomalonate to La@C_{2v}-C_{82}", *Chem. Eur. J.* **2016**, 22, 5953-5962. (Impact Factor 5.771, 1st quartile)

5. Martínez, J.P.; Solà, M.; Voityuk, A.A., "Theoretical Estimation of the Rate of Photoinduced Charge Transfer Reactions in Triphenylamine C_{60} Donor-Acceptor Conjugate", *J. Comput. Chem.* **2016**, 37, 1396-1405. (Impact Factor 3.648, 1st quartile)

6. Martínez, J.P.; Vummaleti, S.V.C.; Falivene, L.; Nolan, S.P.; Cavallo, L.; Solà, M.; Poater, A., "In Silico Olefin Metathesis with Ru-based Catalysts Containing N-Heterocyclic Carbenes Bearing C_{60} Fullerenes", *Chem. Eur. J.* **2016**, 22, 6617-6623. (Impact Factor 5.771, 1st quartile)

List of Abbreviations

Abbreviation	Description
ASM	Activation Strain Model
BC	Benzyne Cycloaddition
BH	Bingel-Hirsch
cod	1,5-cyclooctadiene
COSMO	COnductor-like Screening MOdel
CR	Charge Recombination
CS	Charge Separation
CT	Charge Transfer
CTS	Charge Transfer State
DFT	Density Functional Theory
dmbm$^-$	DiMethyl BromoMalonate anion
ΔG_{cr}	Gibbs energy of a charge recombination reaction
ΔG_{cs}	Gibbs energy of a charge separation reaction
ΔG_{ct}	Gibbs energy of a photoinduced charge transfer reaction
DSSC	Dye-Sensitized Solar Cell
EMF	Endohedral MetalloFullerene
ET	Electron Transfer
HF	Hartree-Fock
HOMO	Highest Occupied Molecular Orbital
HS	Hybrid State
IPR	Isolated Pentagon Rule
IR	InfraRed
k_{cr}	Rate constant of a charge recombination reaction
k_{cs}	Rate constant of a charge separation reaction
k_{ct}	Rate constant of a photoinduced charge transfer reaction
λ	Total reorganization energy
λ_{ext}	Outer-sphere or external reorganization energy
λ_{int}	Inner-sphere or internal reorganization energy
LES	Localized Excited State
LR	Linear Response
LUMO	Lowest Unoccupied Molecular Orbital
μ	Molecular dipole moment
MD	Molecular Dynamics
MO	Molecular Orbital
MR	Membered Ring; it is indeed denoted as x-MR ($x = 3$, 4, 5, or 6)
NHC	N-Heterocyclic Carbene
NMR	Nuclear Magnetic Resonance
ω	Frequency, time

PES	Potential Energy Surface
SIMes	1,3-bis[2,4,6-(trimethyl)phenyl]imidazolidin-2-ylidene
SWCNT	Single-Walled Carbon NanoTube
TD	Time Dependent
TD-DFT	Time-Dependent Density Functional Theory
TNT	Trimetallic Nitride Template
TPA	TriPhenylAmine
TS	Transition State
UV-vis	UltraViolet-visible
$v_{ext}(\mathbf{r})$	External potential
V_{ij}	Electronic coupling

List of Figures

List of Tables

Contents

XVIII

Summary of the Thesis

Carbon is able to form several allotropes with interesting medical, scientific, and industrial applications, among others. Particularly, fullerenes and carbon nanotubes have attracted the attention of many scientific research groups through the entire world since they were discovered by Kroto, Smalley, and Curl in 1985, and by Sumio Iijima in 1991, respectively. The understanding of chemical and physical properties of these carbon nanostructures is crucial for the development of applications such as the synthesis of biomarkers, construction of efficient organic photovoltaic devices, and design of materials with increased resistance to thermal deformation, chemical corrosion, and mechanical stress; among others. Accordingly, this thesis is aimed at the comprehensive, quantum-computational description of the chemical functionalization and charge transfer events susceptible to take place at (endohedral)fullerenes and carbon nanotubes; thus providing a systematic understanding of experimentally reported phenomena.

The current manuscript contains a series of seven chapters distributed according to a compendium of publications. In Chapter 1, molecular structures and chemical functionalization of (endohedral)fullerenes and nanotubes are reviewed. In chapter 2, a revision of quantum-based theories, as well as methodologies used in the thesis, and the electron transfer problem is also introduced. In Chapter 3 the goals to reach in each one of the research projects included in this thesis are established; these latter ones are reported as a sequence of publications in chapters 4, 5, and 6.

Chapter 4 develops the study of cycloaddition reactions to carbon nanostructures. The main subject of study is the chemo- and regioselectivity of the Bingel-Hirsch addition of dimethyl bromomalonate to the endohedral metallofullerene La@C_{2v}-C_{82}; a special case study because of the paramagnetic nature and the many nonequivalent carbon atoms in the cage. Then, the (2+2) and (4+2) cycloadditions of benzyne to fullerene C_{60} and a series of zig-zag single-walled carbon nanotubes differing in diameter is analyzed in detail so as to account for the experimentally observed changes in reactivity; that is to say, (2+2) and (4+2) cycloadditions shall depend on the diameter and chirality of the carbon nanostructure.

The potential applications of fullerene C_{60} in chemical reactions catalyzed by transition metal complexes are discussed in Chapter 5. The first study consists in the quantum-based development of a Suzuki-Miyaura-like reaction mechanism for the arylation of C_{60} with organoboron compounds catalyzed by a rhodium complex in the presence of water, which leads to an arylated hydrofullerene. After that, the catalytic capability of a ruthenium complex, which is linked to N-heterocyclic carbenes containing C_{60}, is analyzed for olefin metathesis (ethylene in this study), wherein it is demonstrated that the inclusion of C_{60} in ruthenium-based catalysts improves the catalytic power.

In Chapter 6, charge transfer events are studied for a fullerene dye-sensitized solar cell, the triphenylamine-C_{60} donor-acceptor conjugate is taken as the reference system. Excitons with neutral, strong charge transfer, and even with partial charge transfer character are carefully described so as to determine nonadiabatic rates of photoinduced charge transfer reactions in such materials. The proper estimation of electron transfer parameters from a quantum-theoretical framework strongly influences the design of higher-efficient light-harvesting photovoltaic devices.

In Chapter 7, the most relevant results of the former chapters are summarized following the sequence of chapters 4-6. Finally, in Chapter 8, the main goals achieved in the current research work are highlighted for the chemical functionalization of carbon nanostructures and their potential application in solar energy conversion.

Resum de la Tesi

L'element de carboni és capaç de formar diversos al·lòtrops amb interessants aplicacions mèdiques, científiques i industrials, entre altres. En concret, els ful·lerens i nanotubs de carboni han atret l'atenció de molts grups d'investigació científica de tot el món des que van ser descoberts per Kroto, Smalley i Curl el 1985, i per Sumio Iijima el 1991, respectivament. La comprensió de les propietats químiques i físiques d'aquestes nanoestructures de carboni és crucial per desenvolupar aplicacions com la síntesi de biomarcadors, la construcció d'eficients dispositius fotovoltaics orgànics, i el disseny de materials amb alta resistència a la deformació tèrmica, la corrosió química, i a l'estrès mecànic; entre altres. D'acord amb això, mitjançant modelatge quàntic computacional, aquesta tesi està enfocada a la descripció detallada de la funcionalització química i esdeveniments de transferència de càrrega susceptibles d'ocórrer en els ful·lerens (endoèdrics) i nanotubs de carboni; proporcionant així un enteniment sistemàtic dels fenòmens observats experimentalment.

El present manuscrit conté una sèrie de set capítols distribuïts segons un compendi de publicacions. En el Capítol 1, es presenten les estructures moleculars i la funcionalització química dels ful·lerens (endoèdrics) i nanotubs de carboni. En el Capítol 2, es revisen les teories basades en mecànica quàntica, així com les metodologies utilitzades en aquesta tesi, i el problema de la transferència d'electrons. En el Capítol 3 s'estableixen els objectius a assolir en cada un dels projectes de recerca inclosos en aquesta tesi; aquests últims es presenten com una seqüència de publicacions dins dels capítols 4, 5 i 6.

En el Capítol 4 es desenvolupa un estudi sobre reaccions de cicloaddició a nanoestructures de carboni. L'objectiu principal d'estudi és la quimio i regioselectivitat de l'addició Bingel-Hirsch del dimetil bromomalonat al metal·loful·lerene endoèdric La@C_{2v}-C$_{82}$; un cas especial a causa de la seva naturalesa paramagnètica i dels molts àtoms de carboni no equivalents en l'estructura. Subseqüentment, les cicloadicions (2+2) i (4+2) del benzí al ful·lerè C_{60} i diversos nanotubs de carboni de paret simple tipus zig-zag de diferent diàmetre s'analitzen en detall per tal d'explicar els canvis en la reactivitat observats experimentalment; és a dir, les cicloadicions (2+2) i (4+2) dependran del diàmetre i de la quiralitat de la nanoestructura de carboni.

Les aplicacions potencials del ful·lerè C_{60} en reaccions químiques catalitzades per complexos de metalls de transició es discuteixen en el Capítol 5. El primer estudi consisteix en el desenvolupament, fonamentat en metodologia quàntica, d'un mecanisme de reacció tipus Suzuki-Miyaura per a l'arilació de C_{60} amb organoborats, la qual és catalitzada per un complex de rodi en presència d' aigua, que condueix a un hidroful·lerè arilat. Després d'això, la capacitat catalítica d'un complex de ruteni, el qual té com a lligands carbens N-heterocíclics contenint C_{60}, s'analitza per a la metàtesi d'olefines (etilè en aquest estudi), del qual es demostra que la inclusió de C_{60} en catalitzadors basats en ruteni millora el seu poder catalític.

En el Capítol 6 s'estudien els processos de transferència de càrrega per a una cèl·lula solar sensibilitzada per colorant a base de ful·lerè, sent la trifenilamina-C_{60} el conjugat donant-acceptor de referència. Els excitons amb caràcter neutre, amb forta transferència de càrrega, i amb caràcter parcial de transferència de càrrega es descriuen acuradament per tal de determinar les velocitats no adiabàtiques de reaccions de transferència de càrrega fotoinduïdes en aquests materials. L'estimació correcta dels paràmetres de transferència d'electrons a partir d'un marc teòric quàntic influeix significativament en el disseny de dispositius fotovoltaics de captació de llum amb una major eficiència.

En el Capítol 7, es resumeixen els resultats més rellevants seguint la seqüència dels capítols 4-6. Finalment, en el Capítol 8, es destaquen les principals fites assolides en el present treball de recerca per a la funcionalització química de nanoestructures de carboni i llurs potencials aplicacions en la conversió d'energia solar.

Samenvatting Proefschrift

Koolstof komt voor in verscheidene allotropen die elk interessante medische, wetenschappelijke en industriële toepassingen hebben. Met name de door Kroto, Smalley en Curl (1985) respectievelijk Sumio Iijima (1991) ontdekte fullerenen en koolstof nanobuisjes hebben wereldwijd de aandacht van veel onderzoeksgroepen getrokken. Het begrijpen van de chemische en fysische eigenschappen van deze koolstof nanostructuren is cruciaal voor de ontwikkeling van toepassingen zoals de synthese van biomarkers, de constructie van efficiënte organische zonnecellen en de ontwikkeling van materiaal met verhoogde weerstand tegen thermische vervorming, chemische corrosie en mechanische belasting. Hiervan uitgaande richt dit proefschrift zich op de uitgebreide, quantumcomputationele beschrijving van de chemische functionalisering van (endohedrale) fullerenen en koolstof nanobuisjes en ladingsoverdrachtsprocessen die in deze verbindingen kunnen plaatsvinden. Door het hier beschreven systematische onderzoek wordt een beter inzicht verkregen van de betekenis van eerder behaalde maar voorheen onvolledig begrepen experimentele gegevens.

Het onderhavige manuscript omvat zeven hoofdstukken. In hoofdstuk 1 worden moleculaire structuren en de chemische functionalisering van (endohedrale) fullerenen en nanobuisjes besproken. In hoofdstuk 2 wordt een overzicht gepresenteerd van op de quantummechanica gebaseerde theorieën evenals van rekenmethoden die worden gebruikt in het proefschrift. Tevens wordt het elektronen-overdrachtsprobleem geïntroduceerd. Hoofdstuk 3 geeft een overzicht van de doelstellingen van de verschillende deelprojecten die vervolgens in de hoofdstukken 4, 5 en 6 besproken worden. Deze resultaten zijn eveneens in de vorm van publicaties in wetenschappelijke tijdschriften verschenen.

Hoofdstuk 4 behandelt de studie van de cycloadditie reacties op koolstof nanostructuren. Het belangrijkste onderwerp van deze studie is de chemo- en regio-selectiviteit van de Bingel-Hirsch-additie van dimethylbroommalonaat aan endohedrale metallofullerenen La@C_{2v}-C$_{82}$. Dit is een speciale casestudie, vanwege de para-magnetische natuur en het grote aantal niet-equivalente koolstofatomen in de kooi. Vervolgens worden de (2+2) en (4+2) cycloaddities onderzocht van benzyn aan het fulleree C_{60} alsmede aan een reeks zig-zag single-walled koolstof nanobuisjes die in diameter verschillen. Deze gedetailleerde analyses dienen een beter begrip van de experimenteel waargenomen veranderingen in de reactiviteit van de (2+2) en (4+2) cycloaddities als functie van de diameter en de chiraliteit van de koolstof nanostructuur.

Hoofdstuk 5 behandelt de mogelijke toepassingen van het fulleree C_{60} bij door overgangsmetaalcomplexen gekatalyseerde chemische reacties. De eerste studie omvat de quantum-gebaseerde ontwikkeling van een Suzuki-Miyaura-achtig reactie-mechanisme voor de arylering van C_{60} met behulp van organoboorverbindingen. Deze reactie wordt in de aanwezigheid van water gekatalyseerd door een rhodium complex en leidt tot een gearyleerd

hydrofullereen. Vervolgens wordt het katalytische vermogen geanalyseerd van een ruthenium complex bij de metathese van alkenen, in dit geval etheen. Het betreffende ruthenium complex is gekoppeld aan N-heterocyclische carbenen met een C_{60}-groep. Hierbij wordt aangetoond dat de C_{60}-groepen een verbetering van het katalytisch vermogen teweegbrengen.

In Hoofdstuk 6 worden ladingsoverdrachtsprocessen voor een fullereen kleurstof-gesensibiliseerde zonnecel bestudeerd, waarbij het trifenylamine-C_{60} donor–acceptor conjugaat als referentiesysteem dient. Niet-adiabatische snelheden van foto-geïnduceerde ladingsoverdrachtsreacties worden bepaald door middel van een nauwkeurige beschrijving van excitonen met uiteenlopend ladingsoverdrachtskarakter (dat wil zeggen: geen, partieel, sterk). De juiste inschatting van elektronenoverdrachtsparameters op basis van quantumchemische berekeningen leidt tot een doelgerichter ontwerp van efficiëntere zonnecellen.

Hoofdstuk 7 geeft een samenvatting van de resultaten uit de drie voorgaande hoofdstukken. Tenslotte richt zich hoofdstuk 8 op de hoofddoelen die in dit onderzoek bereikt zijn en werkt de hoogtepunten uit met betrekking tot de chemische functionalisering van koolstof nanostructuren en hun toepassingsmogelijkheden in de winning en omzetting van energie uit zonlicht.

Resumen de la Tesis

El elemento de carbono es capaz de formar varios alótropos con interesantes aplicaciones médicas, científicas e industriales, entre otras. En particular, los fullerenos y nanotubos de carbono han atraído la atención de muchos grupos de investigación científica a través de todo el mundo desde que fueron descubiertos por Kroto, Smalley y Curl en 1985, y por Sumio Iijima en 1991, respectivamente. La comprensión de las propiedades químicas y físicas de estas nanoestructuras de carbono es crucial para desarrollar aplicaciones como la síntesis de biomarcadores, la construcción de eficientes dispositivos fotovoltaicos orgánicos, y el diseño de materiales con alta resistencia a la deformación térmica, la corrosión química, y al estrés mecánico; entre otras. De acuerdo con ello, mediante modelado cuántico computacional, esta tesis está enfocada a la descripción detallada de la funcionalización química y eventos de transferencia de carga susceptibles de ocurrir en los fullerenos (endoédricos) y nanotubos de carbono; proporcionando así un entendimiento sistemático de los fenómenos observados experimentalmente.

El presente manuscrito contiene una serie de siete capítulos distribuidos según un compendio de publicaciones. En el Capítulo 1, se revisan las estructuras moleculares y la funcionalización química de fullerenos (endoédricos) y nanotubos de carbono. En el Capítulo 2, se introduce una revisión de las teorías basadas en mecánica cuántica, así como las metodologías utilizadas en esta tesis, y el problema de la transferencia de electrones. En el Capítulo 3 se establecen los objetivos a alcanzar en cada uno de los proyectos de investigación incluidos en esta tesis; éstos últimos se presentan como una secuencia de publicaciones dentro de los capítulos 4, 5 y 6.

En el Capítulo 4 se desarrolla un estudio sobre reacciones de cicloadición en nanoestructuras de carbono. El objetivo principal de estudio es la quimio y regio-selectividad de la adición Bingel-Hirsch de dimetil bromomalonato en el metalofullereno endoédrico La@C_{2v}-C_{82}; un caso especial debido a la naturaleza paramagnética y a los muchos átomos de carbono no equivalentes en la estructura. Subsecuentemente, las cicloadiciones (2+2) y (4+2) de bencino en el fullereno C_{60} y en varios nanotubos de carbono de pared simple tipo zig-zag de diferente diámetro son analizadas en detalle con el fin de explicar los cambios en la reactividad observados experimentalmente; es decir, las cicloadiciones (2+2) y (4+2) dependerán del diámetro y de la quiralidad de la nanoestructura de carbono.

Las aplicaciones potenciales del fullereno C_{60} en las reacciones químicas catalizadas por complejos de metales de transición se discuten en el Capítulo 5. El primer estudio consiste en el desarrollo, fundamentado en metodología cuántica, de un mecanismo de reacción tipo Suzuki-Miyaura para la arilación de C_{60} con organoboratos catalizada por un complejo de rodio en presencia de agua, lo que conduce a un hidrofullereno arilado. Después de eso, la capacidad catalítica de un complejo de rutenio, que tiene como ligandos a carbenos N-heterocíclicos conteniendo C_{60}, se analiza para la metátesis de olefinas (etileno en este

estudio), del cual se demuestra que la inclusión de C_{60} en catalizadores a base de rutenio mejora el poder catalítico.

En el Capítulo 6 se estudian los eventos de transferencia de carga para una célula solar sensibilizada por colorante a base de fullereno, siendo la trifenilamina-C_{60} el conjugado donante-aceptor de referencia. Excitones con carácter neutro, con fuerte transferencia de carga, e incluso con carácter parcial de transferencia de carga se describen cuidadosamente con el fin de determinar las velocidades no adiabáticas de reacciones de transferencia de carga fotoinducidas en dichos materiales. La estimación correcta de los parámetros de transferencia de electrones a partir de un marco teórico cuántico influye significativamente en el diseño de dispositivos fotovoltaicos de captación de luz con una mayor eficiencia.

En el Capítulo 7, los resultados más relevantes son resumidos siguiendo la secuencia de los capítulos 4-6. Por último, en el Capítulo 8, se destacan las principales metas alcanzadas en el presente trabajo de investigación para la funcionalización química de nanoestructuras de carbono y su potencial aplicación en la conversión de energía solar.

Chapter 1

Carbon Nanostructures
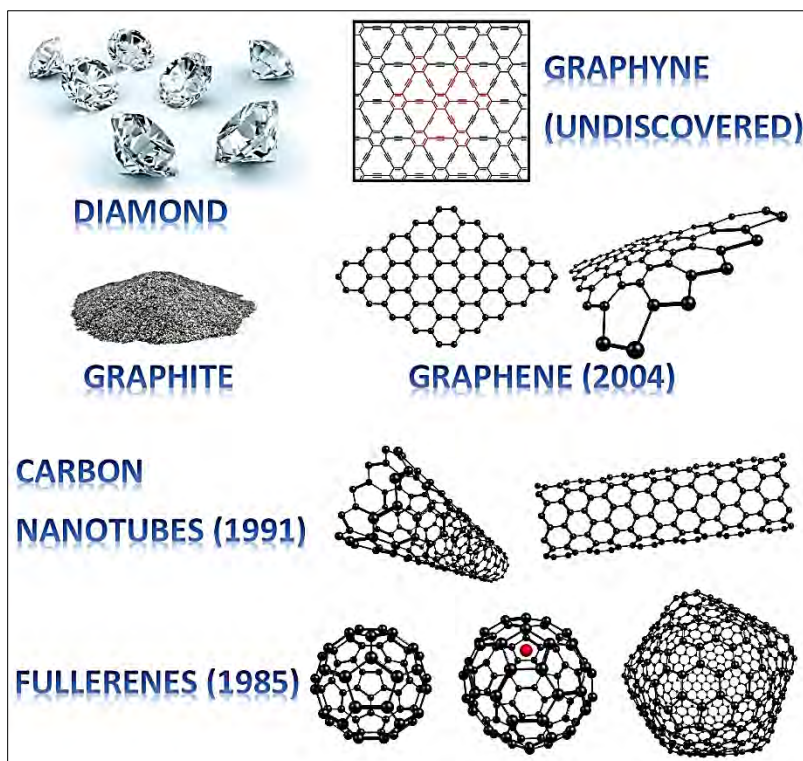
Figure 1.1 Some allotropes of carbon.

Among the different allotropes of carbon (see Figure 1.1), (endohedral)fullerenes and carbon nanotubes are interesting materials from which many technological applications and scientific progress can be done. This section is focused on such carbon nanostructures so that several concepts about their structure and chemical reactivity are reviewed.

1.1 Buckminsterfullerene

In 1985, H. Kroto, R. Curl, and R. Smalley first described the third allotrope of carbon which was called Buckminsterfullerene.[1] Because of this finding, a decade later, these authors were awarded with the Nobel Prize. Since then numerous research groups have extensively studied fullerenes with the aim of determining their reactivity; as well as their photophysical and electrochemical properties and the use of their derivatives, either in materials science or medical applications.[2–4] In 1990, Donald Huffman and Wolfgang Krätschmer designed a method in order to obtain large scale quantities of fullerenes (grams),[5] thus leading to the functionalization of these carbon spheres and the development of new and sophisticated structures.[2]

1.1.1 Structure

Fullerenes are closed-cage molecules of high symmetry exclusively constituted by carbon atoms. Unlike other allotropic forms, that is diamond and graphite in which the hybridizations in the carbon atoms are respectively sp^3 and sp^2, fullerenes are discrete molecules where the hybridization is mainly $sp^{2,3}$. This property is the main reason of the solubility of fullerenes in organic solvents.[6–8]

The most stable and abundant fullerene is C_{60}, which is of icosahedral symmetry with 12 pentagonal and 20 hexagonal rings. Pentagons, 5-membered rings (5-MR; general abbreviation: x-MR, x = 3, 4, 5, or 6), in the fullerene structure bring about the formation of the curvature of the structure since hexagonal networks, 6-MRs, tend to form bidimensional structures. There are two types of bonds, [6,6] bonds with 1.37 Å in length located at the junction of two 6-MRs, and [5,6] bonds located in the fusion of one 6-MR and one 5-MR; being this latter 1.45 Å in length (see Figure 1.2). Moreover, the curvature in the C_{60} structure causes a higher reactivity in the [6,6] bonds because of the release of energy produced by saturating a double bond.[3,7]

1.1.2 The isolated pentagon rule

The stability of fullerenes can be predicted by the isolated pentagon rule (IPR), proposed by H. Kroto in 1987.[9] This rule states that fullerene structures constituted by 5-MRs surrounded by 6-MRs are favored over those structures that present fused 5-MRs, since the junction of two 5-MRs brings about an increased tension in the bond angle with the consequent decrease of orbital overlap and destabilization of the π-system (pentalene type structures with 8 electrons π do not satisfy the Hückel rule).[10] However, it is also possible to find stable structures that do not follow this rule, leading to non-IPR fullerenes like $C_{72}Cl_4$.[11] Indeed, non-IPR structures are also produced by the encapsulation of metals inside the fullerene cage such as scandium and lanthanum.[12,13]
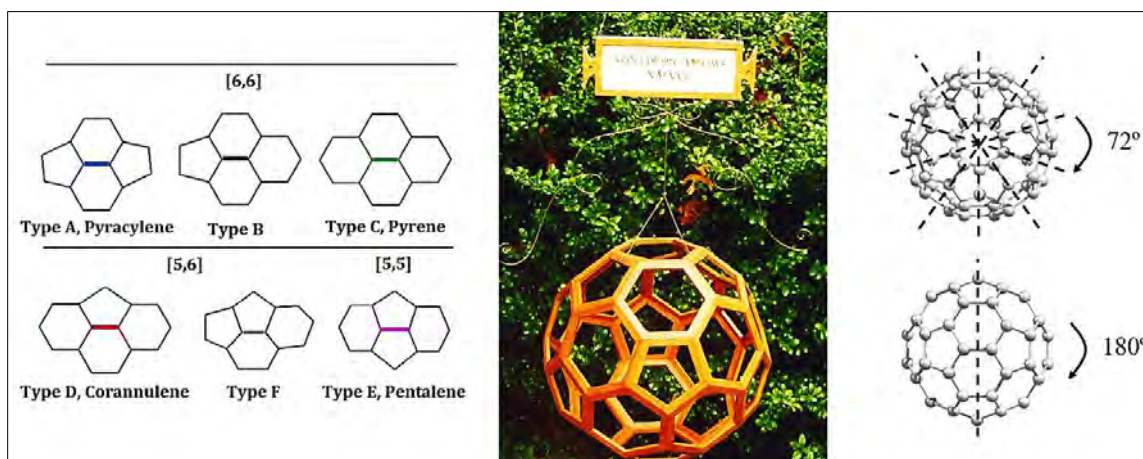
Figure 1.2 To the left, different bond types in fullerene structures. To the middle, Leonardo da Vinci's truncated icosahedron.[14] To the right, the fivefold and twofold symmetry operations of rotation in C_{60}.

1.1.3 Molecular symmetry

Centuries ago, in 1500 Leonardo da Vinci published several geometric sketches wherein the truncated icosahedron was introduced, an Archimedean solid constructed from 12 pentagonal faces, 20 hexagonal faces, 60 vertices, and 90 edges (see Figure 1.2). It is interesting to notice that the molecular structure of C_{60} certainly resembles the truncated icosahedron; where the 60 carbon atoms are localized at each one of the 60 vertices, and the 90 carbon-carbon bonds correspond to the 90 edges of the polyhedron. Therefore, in C_{60} it is possible to identify 120 symmetry operations, all of them included into the icosahedral point group (I_h) grouped into 10 classes.

Table 1.1 Symmetry operations for the icosahedral point group (I_h).

R	E	$12C_5$	$12C_5{}^*$	$20C_3$	$30C_2$	I	$12S_{10}{}^*$	$12S_{10}$	$20S_3$	$15\sigma_v$
A_g	1	+1	+1	+1	+1	+1	+1	+1	+1	+1
F_{1g}	3	$+\tau$	$1-\tau$	0	-1	+3	$+\tau$	$1-\tau$	0	-1
F_{2g}	3	$1-\tau$	$+\tau$	0	-1	+3	$1-\tau$	τ	0	-1
G_g	4	-1	-1	+1	0	+4	-1	-1	+1	0
H_g	5	0	0	-1	+1	+5	0	0	-1	+1
A_u	1	+1	+1	+1	+1	-1	-1	-1	-1	-1
F_{1u}	3	$+\tau$	$1-\tau$	0	-1	-3	$-\tau$	$1-\tau$	0	+1
F_{2u}	3	$1-\tau$	$+\tau$	0	-1	-3	$\tau-1$	$-\tau$	0	+1
G_u	4	-1	-1	+1	0	-4	+1	+1	-1	0
H_u	5	0	0	-1	+1	-5	0	0	+1	-1

*Rotation over a 5-MR ring (see schematization in Figure 1.2 to the right).

From Table 1.1, it is possible to distinguish the different classes of the I_h point group. The first one involves the identity operator E, which is in a class itself. Then, the 12 5-MRs in C_{60} define 12 fivefold rotations around the pentagonal centers. Similarly, the 20 6-MRs in C_{60} give rise to 12 threefold rotations around the hexagonal centers. Moreover, a twofold rotation can take place at the junction of two 6-MRs (i.e. a [6,6] bond of C_{60} as represented in Figure

1.2); since there are 30 edges related to these junctions, then 30 twofold rotations can be differentiated. There are therefore 60 junctions of a 5-MR with one 6-MR; that is 60 [5,6] bonds. Each of these operations is compounded with the inversion operation. In Table 1.1, it is also reported several symmetry operations involving the reflection operation σ. For all the ten classes the irreducible representations of the I_h point group are also provided. Finally, the molecular structure of C_{60} is a truncated icosahedron in view of the differences in bond lengths; unlike the regular truncated icosahedron wherein all the bond lengths are equal and therefore this latter is not consistent with the aromaticity of fullerenes.[15]

1.1.4 Physical properties

Fullerenes exhibit a wide range of solubility in organic solvents such as toluene and benzene; in fact, they are the only carbon allotropes soluble in common solvents at room temperature.[16] In water, it forms aggregates easily.[17] It has been observed that films of C_{60} and C_{70} doped with alkali metals conduct electricity at room temperature[18] and they are superconductors at 18 K.[19,20]

Electrochemical analyses of C_{60} by cyclic voltammetry and differential pulse polarography reveal the existence of at least seven oxidation states (C_{60}^n; $n = 0$, -1, -2,[21] -3,[22,23] -4, -5,[24,25] -6[26]). These six reductions are reversible and occur at intervals equally spaced by 200 mV. It has been observed that the electrochemical properties of C_{60} are also retained in their derivatives, especially in fulleroids.[27,28]

In the case of optical properties, experiments have detected two collective excitations in C_{60}: the first one, about 20 eV, corresponds to the collective motion of electrons in σ bonds; and the second one occurring around 6 eV indicates the movement of electrons in π-bonds. Applications of C_{60} in non-linear optics are based on the π-conjugated system in the structure.[29] In the ground state, C_{60} exhibits strong absorption bands in the UV region and weak absorptions in the visible region (up to 650 nm). Additionally, it exhibits an absorption band at 750 nm characterized by a triplet-triplet transition with a relatively large absorption coefficient, which is a limitation of the optical behavior of C_{60} and C_{70} solutions.[30] This unique property of C_{60} allows the application of fullerenes in transparent matrices as protectors against radiation of high-energy lasers. The combination of these properties leads to the use of C_{60} and derivatives in the design of new electronic materials and photovoltaic devices; particularly in the development of organic solar cells.[31–33]

1.1.5 Synthesis

Traditionally fullerenes are produced by electric arc discharge, combustion processes or vapor deposition methods in which graphite or other source of carbon is vaporized. However, in the search for synthetic routes with better yields and purer products, many methods have been developed for synthesizing fullerenes and a plethora of models have been introduced to explain the mechanisms that lead to the formation of fullerenes.[34–36]

Figure 1.3 Krätschmer-Huffman arc reactor for the synthesis of fullerenes.
Photography published[37] by the Echegoyen's research group.

Five years after the discovery of fullerenes, Krätschmer and coworkers[5] developed a method for the synthesis of C_{60}. This method consisted in the vaporization of graphite by heating in helium atmosphere. The access to larger amounts of C_{60} changed the way in which these compounds were studied and allowed the development of the so-called fullerene chemistry. However, this method, with yields lower than 1%, is not very efficient due to the severe reaction conditions (temperatures above 1300 C and pressures of 100 torr).[38] Other methods based on the vaporization of a carbon source such as pyrolysis, plasma formed by radiofrequency, or electric arc discharge have the same disadvantages as the method proposed by Krätschmer. Consequently, a variety of methods for synthesizing fullerenes have been proposed like the combustion method, from which industrial production is possible.[2,7,15]

1.1.6 Chemical functionalization

Fullerene C_{60} behaves as a polyolefin poor in electrons (with strong electron-withdrawing character); as a result, it undergoes a variety of chemical reactions (see Figure 1.4). Because of its electron deficient nature, the main reactions that fullerenes undergo are nucleophilic additions. Fullerenes are excellent dienophiles in Diels-Alder reactions; indeed, these reactions are widely used for their chemical functionalization. They can react with oxygenated species and aryl groups to form epoxides and analogues (fulleroids). Fullerenes are also reactive with electrophiles.[39]

Many reactions with fullerene C_{60} take place at [6,6] bonds in view of their better frontier orbital interactions;[40] they can form cyclic structures such as 3-MRs which may lead to the inclusion of carbon or nitrogen atoms; 4-, 5-, and 6-MRs cyclic structures are also possible.[41] The formation of 3-MRs usually involves (2+1) cycloaddition reactions.[42–44] Fullerenes undergo (2+2) cycloadditions[45] to generate 4-MRs such as cyclobutene;[46] while for the synthesis of 5-MRs, (3+2) cycloadditions can take place resulting in cyclic[47,48] and heteroatom-cyclic derivatives.[49,50] 6-MRs are obtained by (4+2) cycloadditions on [6,6] bonds.[51,52] In addition, holes in the surface of fullerenes can be formed by selective addition of azides,[53] heat treatment or photoinduced oxidation.[29]
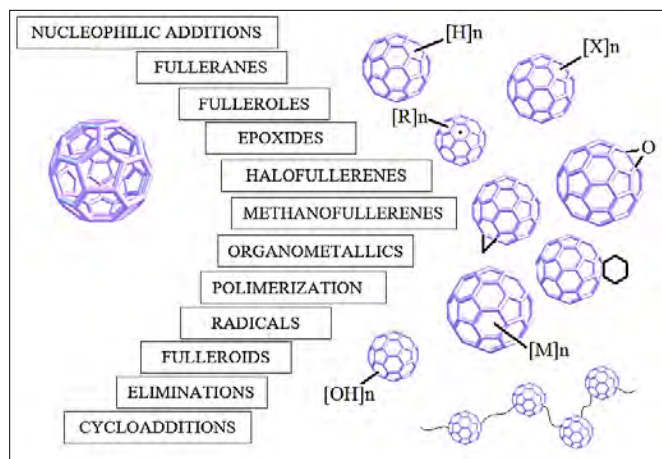
Figure 1.4 Chemical reactions and derivatives of C_{60}.

1.1.6.1 Nucleophilic additions

Fullerenes undergo a wide variety of nucleophilic addition reactions through the attack of species involving both carbon nucleophiles and heteroatoms as nitrogen, oxygen, and phosphorus.[54]

In the first step of the nucleophilic attack on C_{60}, an intermediate is formed as $Nu_nC_{60}^{n-}$. This intermediate can be captured as follows:

(i)   Addition of electrophiles E^+, such as H^+ or carbocations, to yield compounds with the chemical formula $C_{60}E_nNu_n$.
(ii)   Addition of neutral electrophiles EX like alkyl halides to obtain $C_{60}E_nNu_n$.
(iii)   Oxidation to produce $C_{60}Nu_2$.
(iv)   Intramolecular addition to form methanofullerenes or cyclohexanofullerenes.

Given the large number of reactive double bonds in C_{60}, polyadditions are also common in fullerene chemistry. The bis-adducts are obtained as side products along with a mixture of isomers, and the product distribution depends upon both electronic and structural factors.[3,7,54]

1.1.6.2 Cycloadditions

Cycloadditions have been probably the most studied reactions in chemistry of fullerenes due to their great versatility since various functional groups can be attached to fullerenes; as a result, a variety of new products can be synthesized. Different cycloadditions to C_{60} are schematized in Figure 1.5.
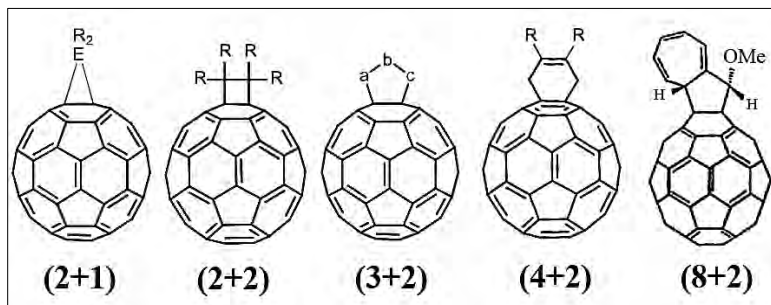
Figure 1.5 Cycloaddition reactions on C_{60}.

The (2+1) cycloaddition leads to the synthesis of compounds such as methanofullerenes wherein the fullerene sphere is fused to cyclic or heterocyclic fragments of three bonds, which may be obtained by a cyclopropanation reaction with α-halogenated carbanions [the Bingel-Hirsch (BH) reaction][55] or carbenes.[56–58] The double [6,6] bonds located at the surface of the fullerene are the reactive sites for such reactions and the energy comes from the release of spatial strain and interaction between reactants.

The (2+2) cycloaddition leads to cyclobutanefullerenes when cyclic[59] or acyclic[60] enones, dienones,[61] acetylenes,[62] etc., are used as reactants. This reaction proceeds photochemically in most cases. Moreover, the obtained products are the simplest adducts wherein diastereoisomers are produced.

The procedure for the functionalization of fullerenes most used in recent years has been the 1,3-dipolar cycloaddition of azomethine ylides, a special case of the (3+2) cycloaddition to fullerenes. Prato et al.[63] were the first authors in employing the 1,3-dipolar cycloaddition (usually known as the Prato reaction) of an azomethine ylide on a C_{60} double bond, thus obtaining the corresponding fulleropyrrolidine. Although azomethine ylides can be prepared according to different synthetic routes,[64] the most common procedure is decarboxylation of immonium salts obtained by condensation of α-amino acids with aldehydes or ketones. This process has numerous advantages such as synthetic simplicity, availability of reactants which may be commercial or easily prepared, and wide variety of products. Moreover, the addition of two substituents on the pyrrolidine ring can be done simultaneously; as well as subsequent modifications can be performed on them. The 1,3-dipolar cycloaddition of azomethine ylides with fullerenes generally produces a mixture of mono-, bis-, tris-, and tetra-adducts.

The Diels-Alder reaction is undoubtedly one of the most versatile reactions of organic chemistry, being the most elegant method for the creation of 6-MRs because of its remarkable diastereo-, chemo-, and regioselectivity. The application of the (4+2) cycloaddition in the chemistry of fullerenes has led to a wide variety of derivatives.[65] However, the main problem

encountered in the reaction of C_{60} with dienes is that the resulting cycloadduct easily undergoes cycloreversion toward the starting materials due to their thermal instability. On the other hand, o-quinodimethane can react with C_{60} so that the (4+2) reaction is not reversible (see Figure 1.6).[66]
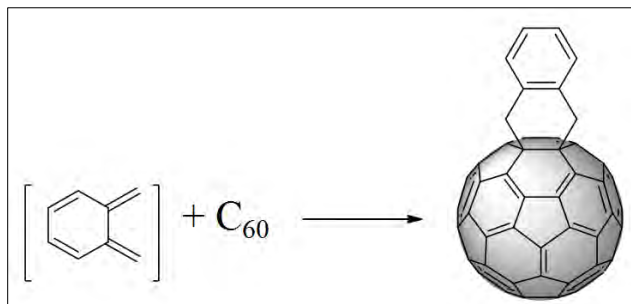
Figure 1.6 A nonreversible (4+2) cycloaddition to C_{60}.

There are a few examples in the literature of (8+2) cycloadditions to fullerenes due to the lack of dipoles to carry them out. An example of such transformation is the reaction of 7-(methoxymethylene)cyclohepta-1,3,5-triene with C_{60}.[67]

1.1.6.3 Reactions with metal complexes

Although it might be thought that the chemistry of fullerenes is fully established, there are still a variety of reactions to explore, especially those involving the use of metals. The singular three-dimensional geometry of these systems represents a unique scenery to carry out novel reactions and to elucidate possible reaction mechanisms. Usually, the organometallic chemistry of fullerenes has been focused on the following aspects (see also Figure 1.7):

(i)   Formation of fullerides (metallic salts of fullerenes M_nC_{60} (n = 1, 2, 3) with different stoichiometries), particularly with alkali metals.[19,68]

(ii)   Addition of metals to one or more double bonds of the fullerene to form coordination complexes. Several examples have been described with many metals: platinum,[69–71] palladium,[72–74] rhodium,[75,76] iridium,[77–80] molybdenum,[81] osmium,[82] ruthenium,[83,84] iron,[85] and tungsten.[86]

(iii)   Co-crystallization of fullerenes and metal complexes. In the crystal structure, the molecules are bonded by van der Waals forces and π-π couplings.[87–89]

(iv)   Formation of covalent bonds between fullerenes and various organic ligands such as derivatives of either pyrrolidine or phthalocyanine with a metal.[90–92]

(v)   Construction of fullerene polymers with metals by reaction with organometallic complexes. An example of such compounds are the polymers of C_{60} with Pd(0) and Pt(0).[72,93]

(vi)   Additions of organolithium or Grignard reagents.[94]
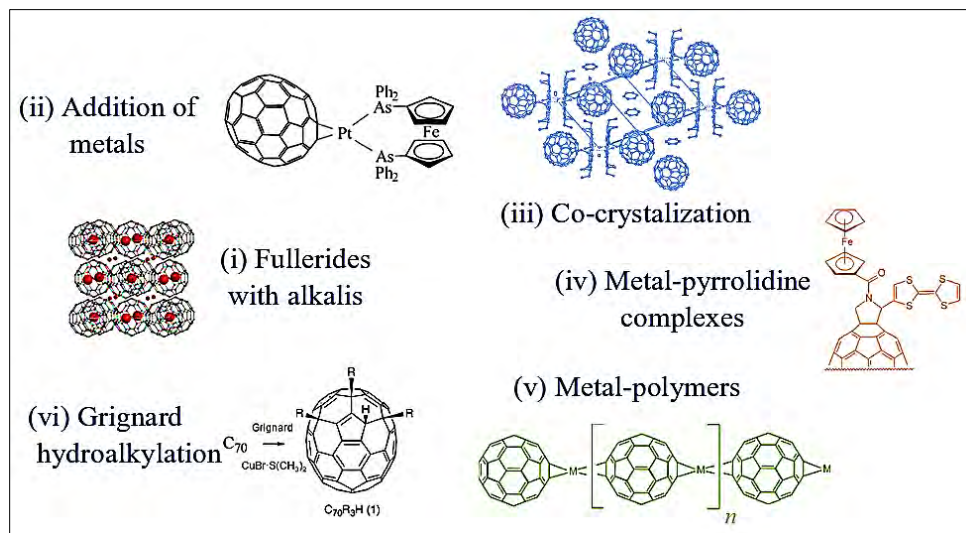
Figure 1.7 Examples of metal complexes formed with fullerenes.

In recent years, a new chemistry in fullerenes has been developed by using metals as catalysts or mediators of various reactions. The Pauson-Khand reaction, which involves the (2+2+1) cycloaddition between an alkene, an alkyne, and carbon monoxide catalyzed by transition metals was carried out for the first time in 2004 by Martín et al. using C_{60} as the alkene unit, which leads to an efficient and regioselective synthesis of fused cyclopentenones on the surface of the fullerene as depicted in Figure 1.8.[95,96] This process, which is not favored with olefins poor in electrons, occurs in C_{60} because of the curvature of the double bonds, which makes them more reactive.
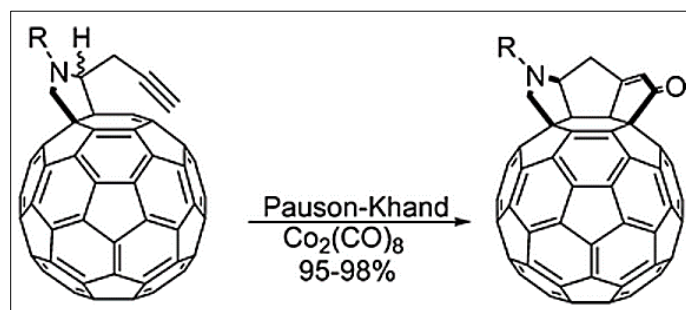
Figure 1.8 The Pauson-Khand reaction in fullerene C_{60}.

More recently, it has been described an interesting cycloaddition of alkyl and aryl diazo compounds catalyzed by Pd(II) which occurs on [5,6] bonds.[97] The functionalization of C_{60} by 1,3-dipolar cycloaddition of carbonyl ylides using catalysts of Rh(II) to form heterocycles fused to the fullerene is also important.[98] On the other hand, the 1,3-dipolar retro-cycloaddition on fulleropyrrolidines mediated by metals has been reported, too.[99,100] It is known[101] that pyrrolidines may undergo reactions of retro-cycloaddition leading to the formation of the alkene and the azomethine ylide; however, this process was considered unlikely in view of the lower basicity of the amino group in fulleropyrrolidines as a result of the electronegative character of the fullerene unit. Nonetheless, fulleropyrrolidines undergo

retro-cycloaddition releasing free fullerene upon heating to reflux in 1,2-dichlorobenzene in the presence of a dipolarophile like maleic anhydride able to effectively trap the ylide that is formed.[102] The conversion strongly depends on the substituents of the fulleropyrrolidine which exert a great influence on the stability of the 1,3-dipole generated by heat. The catalytic version of the retro-cycloaddition, using $Cu(OTf)_2$ or the Wilkinson's catalyst, leads to quantitative retro-cycloadditions regardless the substituents of the starting adduct. These conditions also allow the reversion of isoxazolinofullerenes towards pristine fullerenes and isoxazoline.[103] Finally, among the many reactions of metals with C_{60}, Table 1.2 accounts for some selected cases of metal-C_{60} complexes.

Table 1.2 Some examples of metal-C_{60} complexes.

Precursor	Reactants	Product	Reference
$[Ir(H)_2(o\text{-}HCB_{10}H_9CCH_2PPh_2\text{-}B,P)(PPh_3)(L)](L = CO$ or $PPh_3)$	C_{60}, reflux in toluene and t-BuNC	$[(\eta^2\text{-}C_{60})Ir(o\text{-}HCB_{10}H_9CCH_2PPh_2\text{-}B,P)(t\text{-}BuCN)_2]$	78
$Ir_2(CO)_2Cl_2(\mu\text{-}Ph_2P(CH_2)_7PPh_2)_2$	C_{60}	$(\eta^2\text{-}C_{60})_2Ir_2(CO)_2Cl_2(\mu\text{-}Ph_2P(CH_2)_7PPh_2)_2$	104
$(\eta^5\text{-}C_5H_5)_2ZrHCl$	C_{60} in benzene	$\{(\eta^5\text{-}C_5H_5)_2ZrHCl\}_nC_{60}H_n$ $(n = 1\text{-}3)$	105
$(\eta^5\text{-}C_5H_5)_2TaH_3$	C_{60} in benzene	$(\eta^5\text{-}C_5H_5)_2TaH((\eta^2\text{-}C_{60})$	106
$Rh_6(CO)_9(dppm)_2(\mu_3\text{-}\eta^2,\eta^2,\eta^2\text{-}C_{60})$	C_{60}, reflux in ClC_6H_5, then room temperature with CNR^a	$Rh_6(CO)_5(dppm)_2(CNR^a)(\mu_3\text{-}\eta^2,\eta^2,\eta^2\text{-}C_{60})_2$	107
$Rh_2Cl_2(CO)_4$	$C_{60}Me_5K$	$Rh(\eta^5\text{-}C_{60}Me_5)(CO)_2$	108
$Os_3(CO)_{11}(NCMe)$	C_{60}	$Os_3(CO)_{11}(\eta^2\text{-}C_{60})$	109,110
$Os_3(CO)_8(CNR^a)(\mu_3\text{-}\eta^2:\eta^2:\eta^2\text{-}C_{60})$	CNR in ClC_6H_5	$Os_3(CO)_8(CNR^a)(\mu_3\text{-}CNR)(\mu_3\text{-}\eta^1:\eta^2:\eta^1\text{-}C_{60})$	111,112
$Ru_3(CO)_{12}$	C_{60}	$Ru_3(CO)_9(\mu_3\text{-}\eta^2:\eta^2:\eta^2\text{-}C_{60})$ and Ru_3C_{60}	113,114
$Ru_5C(CO)_{15}$	C_{60} in ClC_6H_5 and PPh_3 or dppm	$Ru_5C(CO)_{11}(PPh_3)(\mu_3\text{-}\eta^2:\eta^2:\eta^2\text{-}C_{60})$ and $Ru_6C(CO)_{12}(dppm)(\mu_3\text{-}\eta^2:\eta^2:\eta^2\text{-}C_{60})$	83
$Fe(CO)_5$	C_{60} in arc discharge	FeC_{60}	115
$Na[Co(CO)_4]$	C_{60}	$NaCoC_{60}\cdot3THF$	116
Ni^+ in the gas phase	C_{60} in the gas phase	$Ni(C_{60})_2^+$	117
$M(PR_3)_4$ $(M = Pt, Pd, Ni; R = Et, Ph)$	C_{60}	$(\eta^2\text{-}C_{60})M(PR_3)_2$	105
$[(C_6H_5)_3P, AuCl$	C_{60} in toluene	$C_{60}\cdot2[(C_6H_5)_3P]AuCl\cdot0.1C_6H_5CH_3$	118
$LiClO_4, NaCF_3SO_3,$ or KCF_3SO_3	C_{60}	M_xC_{60} $(M = Li, Na, K)$	119

^{a} $R = CH_2C_6H_5$

1.2 Endohedral fullerenes

Conventional endohedral fullerenes are structures with species such as metal ions encapsulated inside the fullerene cage, for instance $La@C_{82}$. In these structures, electron transfer from the encaged metal ions to the carbon cage is demonstrated to occur. That is, in the mentioned example, formal charges are predicted to be $La^{3+}@C_{82}^{3-}$ and it results in the formation of non-dissociating salts. Not only can monometallofullerenes be synthesized, which were the first isolated endohedral fullerenes, but noble gasses like He and Kr and nonmetal atoms like N and P can be also encapsulated inside the carbon cage. These atoms are preferably incarcerated into C_{60}. Nonmetals endohedral fullerenes are prepared under high pressure or by ion bombardment of the preformed cage. However, these structures are neutral species, unlike the endohedral metallofullerenes (EMFs) which have formal charges. In this regard, it is important to know how the introduction of more than one metal ion changes the charge of the fullerene cage since strong doping reactions depend upon the electronic structure and oxidation state of the EMF under attack. In view of that, many di- and trimetallofullerenes have been isolated, which led to a new field of materials with interesting properties and applications.[120–123]

1.2.1 Structural aspects

1.2.1.1 Deviations from the isolated pentagon rule

Shinohara's group demonstrated[12] for the first time that the encapsulation of two atoms of Sc inside the cage of C_{66}, $Sc_2@C_{66}$ (depicted in Figure 1.9) is sufficient to break the isolated pentagon rule (non-IPR); that is, there are fused 5-MRs in the C_{66} cage of C_{2v} symmetry. Moreover, the authors also showed that some fullerenes with an even number of carbon atoms able to form IPR cages are stabilized in a non-IPR structure by a two-metal cluster; for instance, $La_2@C_{72}$.[13] On the other hand, Shinohara et al. reported[124] the incarceration of the Sc_2C_2 carbide structure into a non-IPR C_{2v}-C_{68} cage; thus giving rise to the family of M_2C_2 carbide clusters. These trends were different for the family of nitride clusters. In this regard, the stability of non-IPR cages can be explained by the maximum pentagon separation rule[125] and the maximum aromaticity criterion (MARC).[126] This latter is based on the additive local aromaticity (*ALA*) index defined as the sum of the local aromaticities, A_i, of all the n rings i contained in the fullerene cage, $ALA = \sum_{i=1}^{n} A_i$. Deviations to the IPR can be conveniently explained by making use of MARC; in fact, it can be verified that the most stable anionic fullerene isomer is the one whose total aromaticity is maximized. In this order of ideas, IPR and non-IPR anionic isomers can be compared regardless the number of adjacent pentagon pairs included in the structure under consideration. MARC turns out to be very useful since it correlates the experimental trends with the *ALA* index: the most aromatic anionic isomer leads to the most stable EMF.[126]
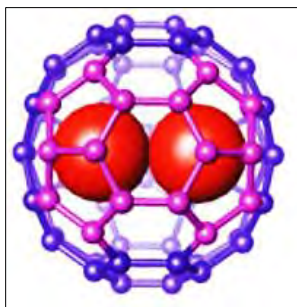
Figure 1.9 $Sc_2@C_{66}$, the first structure that violated the isolated pentagon rule. Figure adapted from original reference.[12]

1.2.1.2 Isomers: the case of La@C_{82}

Smalley and coworkers[127] were able to produce macroscopic quantities of higher fullerenes with La inside the cage, including La@C_{82}. There are nine distinct isomers of C_{82} satisfying the IPR (see Figure 1.10).[9,128,129] Out of these nine cages, La as a single metal has been incarcerated into the C_{2v}-C_{82} and C_s-C_{82} IPR cages.[130] None of these isomers is the most stable for empty C_{82} fullerene. The La@C_{2v}-C_{82} EMF, which in the case of Ce@C_{2v}-C_{82} is about four times more abundant than its analogous C_s-C_{82},[131] has been the subject of many studies.[132–134] For example, the first EMF functionalization was achieved for La@C_{2v}-C_{82} through a photochemical reaction with disilirane.[135] In this regard, La@C_{2v}-C_{82} has the capability to easily donate and, in turn, accept electrons due to its radical nature and redox properties; unlike the pristine counterpart C_{2v}-C_{82}. Consequently, the high electron affinity and low ionization potential of amphoteric species such as La@C_{2v}-C_{82} are useful to control the chemical reactivity towards nucleophiles and electrophiles.[136]
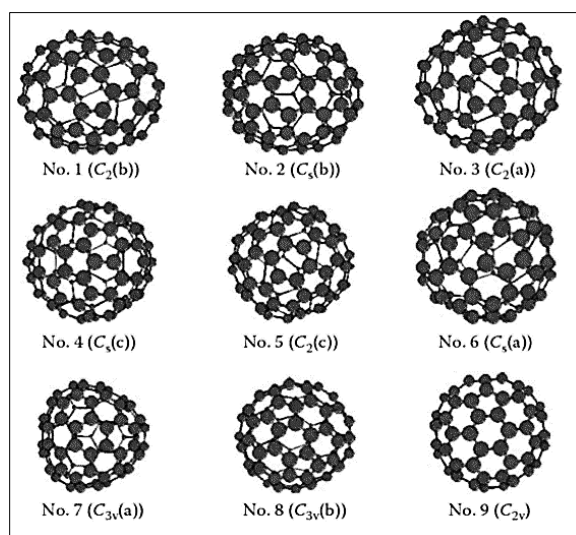
Figure 1.10 Nine isomers of C_{82} satisfying the isolated pentagon rule.

Additionally, the permanent magnetic moment of La@C_{2v}-C_{82} obstructs the direct application of nuclear magnetic resonance (NMR) analysis; therefore the corresponding spectrum is obtained from La@C_{2v}-C_{82}^- taking advantage of its uncommon stability.[137] The ^{13}C NMR spectrum of La@C_{2v}-C_{82}^- shows 24 different lines corresponding to 24 nonequivalent carbon atoms. In line with these results, by using synchrotron powder diffraction, the maximum entropy method (MEM)/Rietveld analysis revealed that the La atom is not localized at the center of the C_2 axis but adjacent to a 6-MR of the La@C_{2v}-C_{82} cage; the shortest La-C distance was determined to be 2.55 Å.[138] Based on all these structural and electronic properties of La@C_{2v}-C_{82}, the chemical functionalization of this EMF can be considered as an interesting subject of study. Then in the current thesis the chemistry of La@C_{2v}-C_{82} is examined.

1.2.1.3 Large-sized cages

Yang and Dunsch demonstrated that multimetallofullerenes can result in the stabilization of a large series of higher fullerene cages. They synthesized and isolated with a high yield for the first time one of the largest fullerene cage to date, a stable dimetallofullerene Dy$_2$@C_{100}; as well as the largest trimetallofullerene Dy$_3$@C_{98}.[139] Certainly, the encapsulation of metallic clusters in large-sized cages has opened a new field of research in fullerene chemistry. There are important consequences as the size of the cage increases: the number of IPR-isomers increases (for C_{100}, there are 450 isomers) and, as a consequence, there are a larger number of structures of metallofullerenes; that is to say, for Dy$_2$@C_{100} at least six cage isomers must be considered (see Figure 1.11). It is worth mentioning that the influence of the size of the electrically charged cage in physical and chemical properties is of high interest.
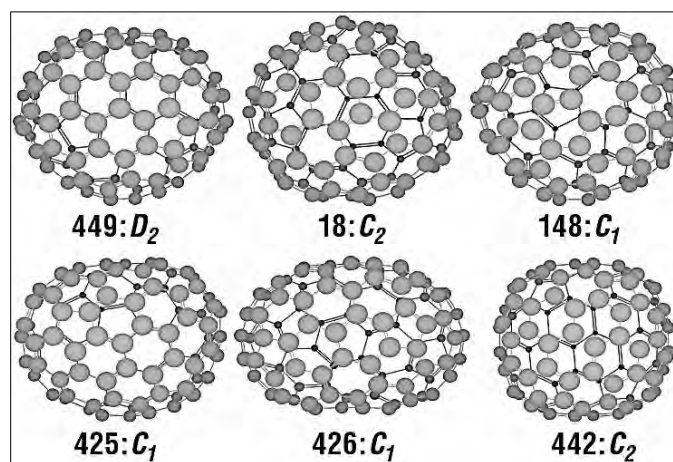
Figure 1.11 Six probable IPR cage isomers of Dy$_2$@C_{100} (Dy atoms omitted for clarity). Figure adapted from original reference.[139]

1.2.2 Nitride cluster fullerenes

A new class of endohedral fullerenes with a cluster containing nitrogen, an element that was initially avoided as a cooling gas in the fullerene community, was introduced via the synthesis of $Sc_3N@C_{80}$, which is the first most abundant member and the third most abundant fullerene structure. This structure was firstly produced in 1999 by using a Krätschmer-Huffman generator, wherein graphite rods containing metal oxides in the presence of a small portion of nitrogen gas were vaporized. The authors named this method as the trimetallic nitride template (TNT) process.[140] In this class of EMFs, the cage has to adopt a trimetal-nitride-cluster structure, which is not stable as a single molecule; indeed, this isomeric I_h-C_{80} form has not been isolated as an empty cage so far. The electron transfer from the nitride cluster stabilizes the icosahedral cage of C_{80}; as a result, both structures, the cage and the cluster, are stabilized each other (see Figure 1.12). Furthermore, following the TNT process, other clusters can be encapsulated in order to produce $Er_xSc_{3-x}N@C_{80}$ (x = 0-3)[140,141] and $A_xSc_{3-x}N@C_{68}$ (x = 0-2; A = Tm, Er, Gd, Ho, La).[142] In the latter case, the trimetallic nitride cluster is trapped in a non-IPR cage. Another example of a non-IPR endohedral fullerene is given by the encapsulation of Sc_3N into the D_3-C_{68} cage, which was confirmed by X-ray crystallography and NMR spectroscopy.[142,143] The TNT method can be also used for the synthesis of other EMFs, although with a relative low yield; these are: $Sc_3N@C_{78}$,[144] $Lu_3N@C_{80}$,[145,146] $Lu_{3-x}A_xN@C_{80}$ (x = 0-2; A = Gd, Ho),[146] and $Sc_3N@C_{80}$.[147]

Generally, the production of EMFs through standard arc discharge has a yield of 2% or less.[148] The production of $Sc_3N@C_{80}$ by means of the TNT process is higher ranging from 3 to 5%.[140] On the other hand, Dunsch and Yang introduced the development of the reactive gas atmosphere method. The dominant product resulting from the use of NH_3 as the reactive gas is the nitride cluster fullerene, while the yield of empty fullerene and other metallofullerenes was less than 5%. This allows an easy purification of the product since it can be performed by a simple chromatographic technique. Based on NMR, this led to the isolation of large families of $M_3N@C_{2n}$ structures (where M = Ho, Tb, Gd, Dy, Tm; $38 \leq n \leq 44$).[149–153]

$Sc_3N^{6+}@C_k^{6-}$
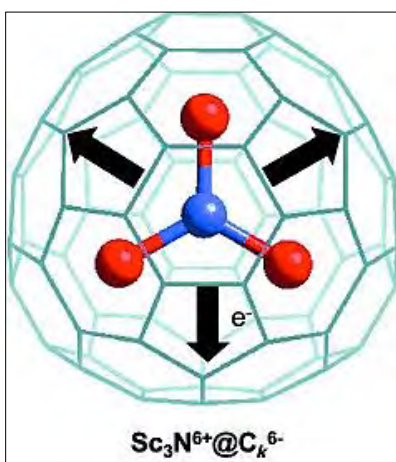
Figure 1.12 Schematic representation of the stabilization of trimetallic nitride template endohedral metallofullerenes according to the ionic model.

1.2.2.1 Properties of nitride cluster fullerenes

The Sc_3N cluster has a planar structure inside the cage, then $Sc_3N@C_{80}$ has an icosahedral symmetry (isomers I and I_h) as confirmed by X-ray crystallography and ^{13}C NMR spectroscopy.[140] On the other hand, despite of the same symmetry of the C_{80} cage and $Sc_3N@C_{80}$, the Gd_3N cluster is found to be pyramidal.[154] The structure and stability of this latter, together with the electron transfer to the cage, are rarely studied due to the difficulties to obtain consistent information from X-ray crystallography and NMR spectroscopy.[150,154–156] In this regard, vibrational spectroscopy is used for the structural analysis of a series of nitride cluster fullerenes, $M_3N@C_{80}$ (I, II) (M = Sc,[147] Gd,[150] Dy,[152] Tm[153]).

For a series of trimetallic nitride cluster regarding the C_{80} cage, a study was carried out so as to determine the visible/near-infrared (IR) absorption bands; those results were compared to the near-IR absorptions and small bandgap of $Sc_3N@C_{80}$.[140] No near-IR absorption bands were found and optical bandgaps above 1 eV were observed. It was concluded therefore that nitride cluster fullerenes are stable compounds in comparison to C_{60}.[147,155]

Nitride cluster fullerenes present similar reactivity to conventional EMFs. As a result, the C=C bonds are thought to be the reactive bonds wherein functionalization can take place. Accordingly, it can be found in the literature the synthesis of derivatives of $M_3N@C_{80}$ (M = Sc,[156–158] Y,[159] Gd,[160] Lu[161]).

The structure of $Sc_3N@C_{80}$ is formally a positively charged cluster inside a negatively charged icosahedral carbon cage, $[Sc_3N]^{6+}@C_{80}^{6-}$, as determined by high-energy spectroscopy.[162] Based on this type of studies, a series of $M_3N@C_{80}$ (I) (M = Sc,[162] Tm,[163,164] Dy[165]) reveal significant differences in the formal charges; that is, 2.4, 2.9, and 2.8 for Sc, Tm, and Dy, respectively, which lead to dissimilarities in the electron transfer to the C_{80} cage. The isomeric structure of the cages can be correlated to the vibrational structure of the EMFs; therefore, a structural characterization can be determined from those spectra. Both, IR and Raman spectroscopies can be used in the characterization of the structure of the caged cluster by analyzing the vibrational pattern. However, quantum-chemistry-based theoretical studies can be also used in the description of $M_3N@C_{80}$ (M = Sc, Lu, Gd) structures and their chemical functionalization.[147,155,163,166]

1.3 Carbon nanotubes

In 1991, Sumio Iijima characterized by means of high-resolution electron microscopy a new allotropic form of carbon which was named carbon nanotube.[167] Two years later, Iijima,[168] and also independently Donald Bethune,[169] discovered the so-called single-walled carbon nanotubes (SWCNTs). In this new material, the morphology is derived from a single graphene sheet, which is rolled into a cylinder that may be closed at the ends.

1.3.1 Types according to number of layers

Carbon nanotubes can be classified into two different types according to the number of layers as depicted in Figure 1.13: multi-walled carbon nanotubes (MWCNTs) which are those formed by concentric layers approximately separated by the analogous interplanar distance of graphite (0.36 nm); and SWCNTs, which can be described as a bidimensional graphite layer rolled into a cylinder of nanometric diameter. In addition to the high-resolution electron microscopy, the Raman spectroscopy is a very useful technique to distinguish between MWCNTs and SWCNTs. In this technique, all SWCNTs have characteristic bands of small intensity between 100 and 300 nm, which do not appear in MWCNTs. These bands of small wave number are associated to radial radiation around the nanotube and are known as *breathing* of SWCNTs, as a result they are related to the diameter of the nanotube.[170]
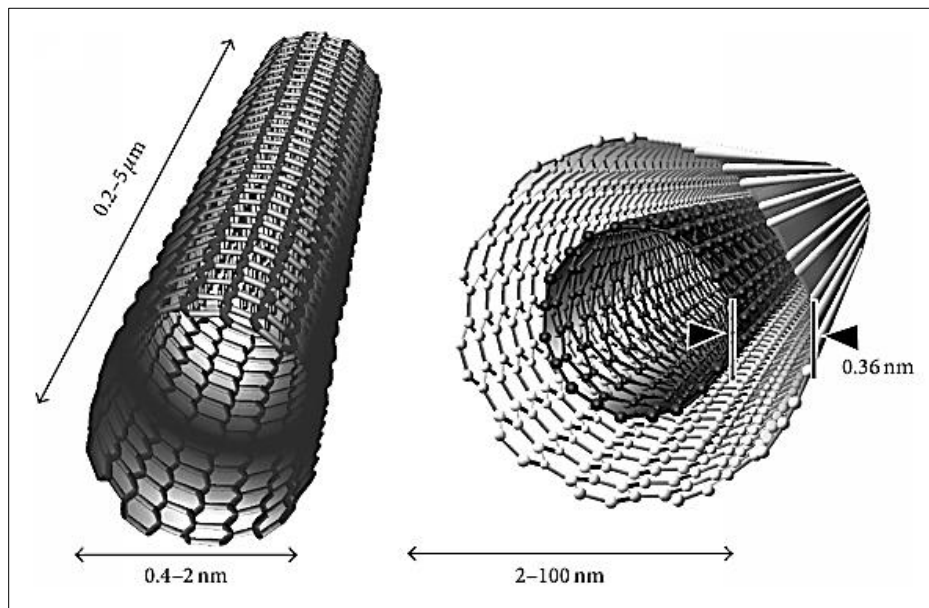
Figure 1.13 Single-walled (left) and multi-walled (right) carbon nanotubes.

1.3.2 Classification according to chirality

The chiral vector characterizes the orientation of 6-MRs in a graphene sheet, and the atoms in the corresponding sheet represent the same atom in the SWCNT structure. There are three classes of SWCNTs characterized by the chiral vector numbers (n,m). The first class is the case $n = m$, in which SWCNTs show a metallic-like band structure; armchair SWCNTs are classified in this category. The next case is when $n - m$ is a multiple of 3, and SWCNTs present semimetallic-like band structures. Other combinations of n and m give rise to SWCNTs that show semiconductor-like band structures (see Figure 1.14).[171]
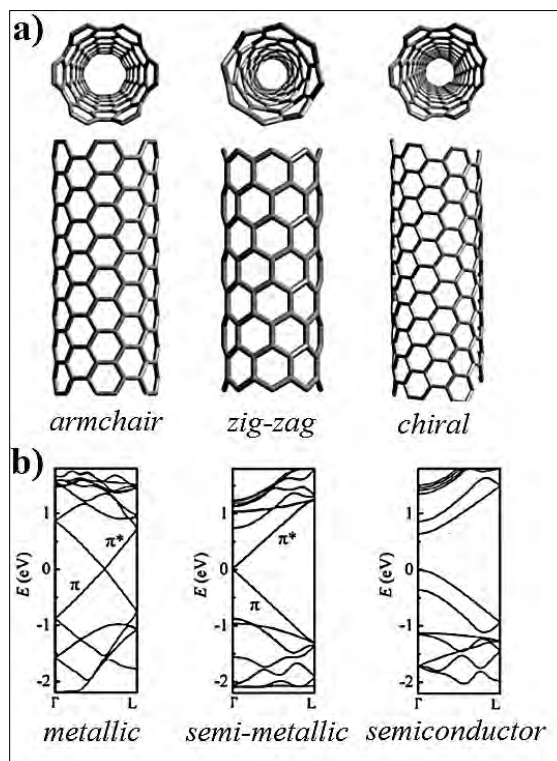
Figure 1.14 a) Classification of SWCNTs according to chirality and b) band structures.[172]

In a conventional model of graphene sheet (see Figure 1.15), in which it is assumed that all bond lengths are equal and all bond angles remain 120°, the length of the chiral vector $|\mathbf{C}|$ defines the circumference of the cylinder (where $\mathbf{C} = n\mathbf{a} + m\mathbf{b}$, and $\mathbf{a}$ and $\mathbf{b}$ form a non-orthogonal basis for the sheet). The direction of $\mathbf{C}$ relative to the basis vector $\mathbf{a}$ defines the chiral angle φ; consequently, $\varphi = 0$ for zig-zag SWCNTs. Besides, the unit cell length is given by the length of the translation vector $\mathbf{T}$, which is perpendicular to $\mathbf{C}$.[173] The diameter r_0 of the structure is calculated by the equation $r_0 = \sigma\sqrt{3(n^2 + mn + m^2)}/2\pi$; where σ stands for the 1.42 Å carbon-carbon bond length and r_0 is the nanotube radius. The length of these nanostructures can be also characterized by the number of unit cells in the network.[171]
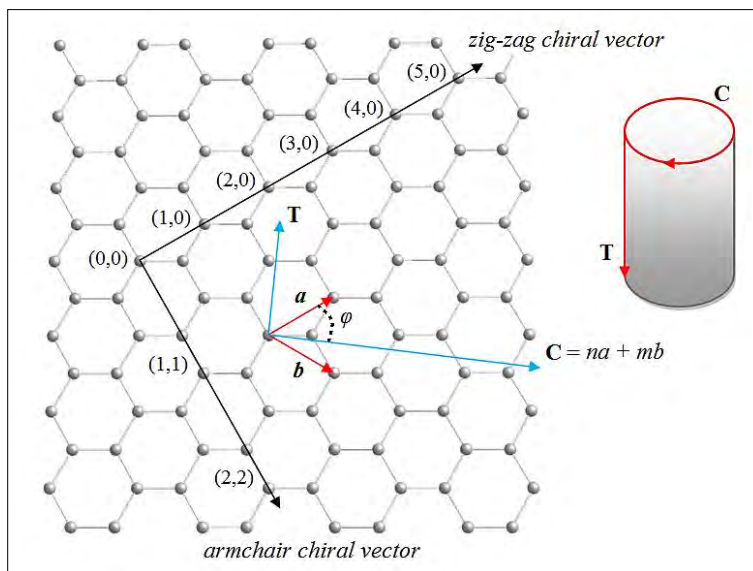
Figure 1.15 Conventional model to construct a SWCNT from a graphene sheet. The structure is designed via the basis vectors *a* and *b*, chiral angle *φ*, and chiral **C** and translational **T** vectors. Zig-zag and armchair SWCNTs are also represented.

1.3.3 Clar structures

A Clar structure follows the Clar's π-sextet rule,[174] which states that the Kekulé resonance structure with the largest number of disjoint aromatic π-sextets, i.e. benzene-like moieties, is the most likely structure of polycyclic aromatic hydrocarbons to be observed.[175] Aromatic π-sextets can be understood as six π-electrons localized in a single benzene-like ring separated from adjacent rings by carbon-carbon single bonds. SWCNTs can be also constructed under the Clar's π-sextet rule.[176–179] In this regard, Clar unit vectors $rp + sq$ can be obtained by simple algebraic relationships with the chiral unit vectors introduced above (*n,m*), where:

$$r = \frac{n - m}{3} \tag{1.1}$$

and

$$s = \frac{n + 2m}{3} \tag{1.2}$$

King and Ormsby pointed out that, using non-canonical representations of the Clar structure, the parameter R [defined as $R = mod(n - m, 3)$] is useful to describe the sidewall topology in terms of Clar networks (see Figure 1.16).[180] R takes three different values; therefore it leads to three different situations that determine the electronic properties of nanotubes. If $R = 0$, the Clar network is fully benzenoid and the infinite nanotube is metallic. On the other hand, $R = 1$ and $R = 2$ give rise to 6-MRs and one double bond; or even two double bonds for zig-zag SWCNTs with $R = 1$, wherein the resulting nanostructure is a semiconductor.
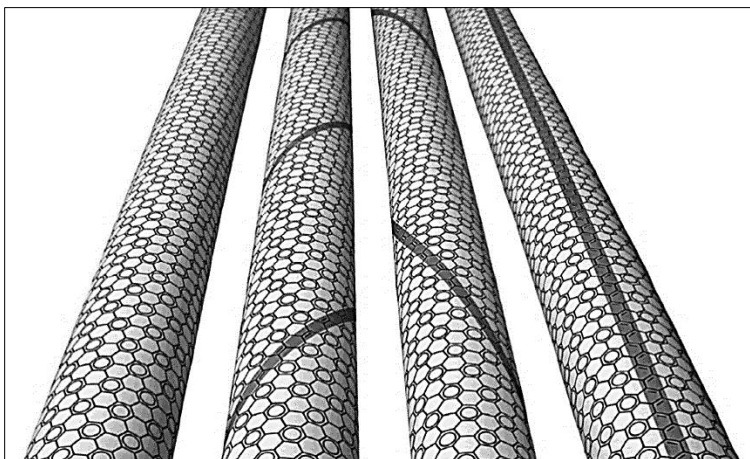
Figure 1.16 Valence bond representations of Clar structures for carbon nanotubes with chiral vector numbers, from left to right, (12, 9), (12, 8), (12, 7), and (19, 0); $R=mod(n - m, 3)$ is respectively 0, 1, 2, and 1. Black strips indicate the positions of the double bonds. Figure adapted from original reference.[180]

1.3.4 Properties and applications

One of the most noteworthy properties of carbon nanotubes is the high Young's modulus (1-2 TPa). In view of that, these materials are up to six times more elastic than steel and ten times more resistance than fibers like Kevlar.[181–185]

The electrical conductivity of carbon nanotubes is also remarkable, which is estimated to be 10^9 A/cm^2. In the case of conductive carbon nanotubes, it has been purposed that an electron inside the nanostructure experiences a *ballistic* conduction with no impediment and a uniformly accelerated movement as a function of the electric field.[186]

The morphology of SWCNTs is characterized by a cylinder of variable length that can reach up to several millimeters. The high ratio length/diameter, sometimes greater than 10^6, coupled with the high electric conductivity,[187,188] make these materials to be considered as molecular wires in the case of conductors. On the other hand, semiconductor SWCNTs are very interesting materials in the development of molecular transistors.[189–193]

SWCNTs have a high tendency to form agglomerations that strongly interact via van der Waals forces.[194] The agglomeration of SWCNTs represents many issues for the study of properties of a specific structure; besides it makes difficult their solvation in conventional solvents. This problem has been treated by various methods such as the addition of surfactants or covalent functionalizations.[195–198]

1.3.5 Synthesis

Carbon nanotubes may be prepared by various methods (vaporization of graphite by laser pulses, arc discharge in graphite electrode, pyrolysis, and high pressure of CO), being pyrolysis one of the most common processes, which takes place at temperatures above 700 °C with a suitable organic compound in the presence of a catalyst commonly constituted by nanoparticles of metal alloys such as Fe/Co, Co/Ni, or Fe/Mo.[199–203] In this case, the nanotube grows from the metallic nanoparticle that acts as a catalyst in the direction of the flowing gas resembling the shape of a comet, where the nucleus is equivalent to the metal catalyst and the *tail* corresponds to the nanotube growth (see Figure 1.17).[204] The size and composition of the metallic nanoparticle together with the nature of the organic precursor and the temperature are the main parameters that determine the formation, the yield, and the diameter of SWCNTs. On the other hand, it seems that big metallic particles (>20 nm) lead to the formation of MWCNTs and other multiple different carbonaceous materials (amorphous or structured).[205]
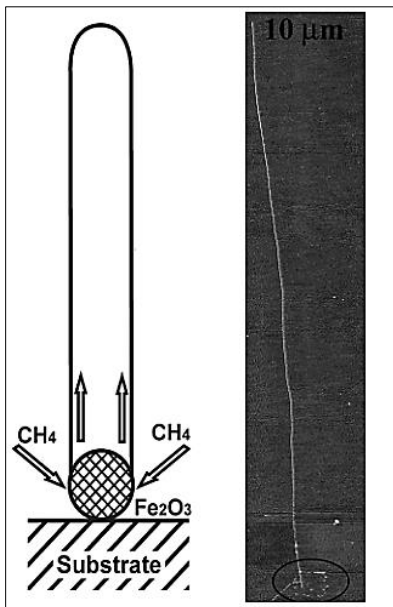
Figure 1.17 Schematization of the nanotube growth (left) and an image obtained with atomic force microscopy of a 50 μm long SWCNT grown from nanoparticles patterned into the circled region (right). Figure adapted from original reference.[206]

Commercial samples of carbon nanotubes are prepared by the high-pressure carbon monoxide method, HiPCO, wherein the carbon precursor is CO together with a catalyst of $Fe(CO)_5$ in the gas phase that react to form SWCNTs of high purity.[200] The source and the method for the synthesis of SWCNTs determine the proportion of metal nanoparticles that the final product may contain.

1.3.6. Purification

Purification is necessary due to the presence of metallic impurities in the raw material of the SWCNT. The procedure most widely used in the purification of carbon nanotubes consists in the treatment of raw materials at room or high temperatures with a strong acid which typically is an aqueous solution of nitric acid (about 3 M) or even mixtures of HNO_3/H_2SO_4. Under these conditions, the metallic residue is solvated producing impurities together with the partial oxidation of the SWCNT and other carbonaceous residues. Depending on the size of the metallic and carbonaceous residues, temperature, time and concentration of the acid, it can be produced a complete dissolution of the amorphous carbon together with a shortening of the length of the nanotubes by oxidative degradation of carbon-carbon bonds; thus forming shorter and purer SWCNTs with a higher degree of functionalization with oxygenated groups. The oxidative treatment produces ruptures at the nanotube edges, being the carboxyl group the predominant functional group at the ends of the SWCNTs.[207,208]

1.3.7 Functionalization of carbon nanotubes

One of the active areas of research in chemistry in recent years is aimed at the functionalization of SWCNTs. The main purpose is the implementation of SWCNTs properties such as electrical conductivity and mechanical resistance. The functionalization may be performed essentially following two complementary strategies (see Figure 1.18), both based on the formation of charge transfer complexes of high stability.[209,210] In the case of using molecules such as pyrene derivatives, porphyrins, and aromatic macrocycles, it has been established that these moieties interact with the walls of the nanotubes through either donor-acceptor or π-π interactions.[211] In the case of using polymers, they can be aligned around the axis of the nanotube coating to it helically, forming a supramolecular aggregate.[212] The modification of nanotubes can be also done by means of covalent junctions. Covalent bonds can be formed by reacting either oxygenated groups or the walls of the SWCNT.[212] The functionalization at the ends of SWCNTs via carboxyl groups has the advantages that the integrity of the aromatic nature of the nanotube is not damaged and reactions can be completed under relatively well-established mild conditions. Besides, the functionalization of carboxyl groups preferably takes place at the ends of the SWCNTs. This method involves, however, low density of such groups so that the percentage of functionalization is low.[213] This generally causes difficulties in the determination of the presence of these subunits by standard spectroscopic techniques; particularly by UV-vis, IR, Raman, and NMR spectroscopy.
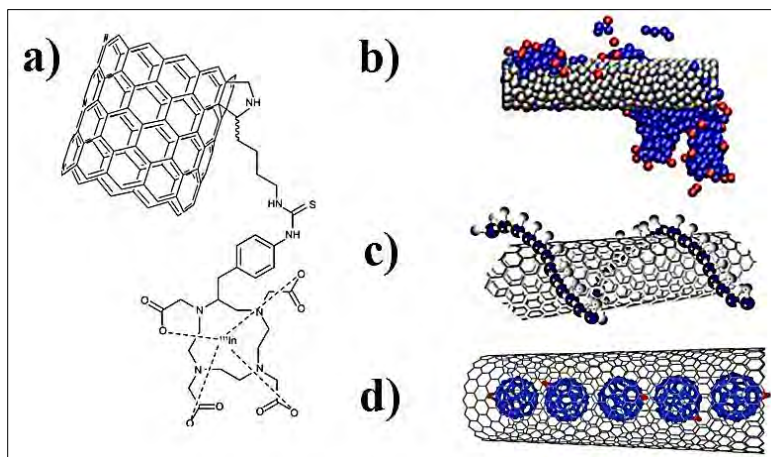
Figure 1.18 Examples of chemical functionalization of SWCNTs: a) covalent on the walls, b) exohedral noncovalent with surfactants, c) exohedral noncovalent with polymers, and d) endohedral noncovalent with fullerenes.

Among the main reactions that carbon nanotubes undergo are the addition of radicals centered in carbon atoms, the addition of carbenes and (3+2) cycloadditions; in this latter the nanotube wall acts as a dipolarophile.[212] The main advantage of the functionalization carried out in the walls of the nanotube is the high degree of functionalization, which is even greater than that one obtained from reactions with carboxyl groups. When the amount of organic component is sufficiently high, its presence is evidently easier to establish by spectroscopic techniques. However, an excessive degree of functionalization may eventually lead to a decrease or loss of the conductive properties of the SWCNT by interrupting the overlap of the π-orbitals. Figure 1.19 illustrates the differences of these types of functionalization.
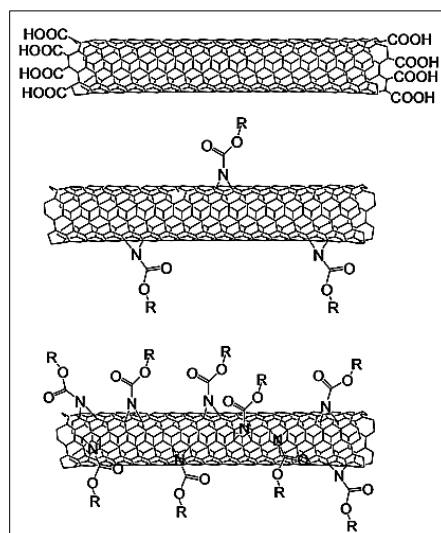
Figure 1.19 Covalent functionalization of SWCNTs at the edges, walls, and massively.

Qualitative estimations of the degree of functionalization in SWCNTs is performed via Raman spectroscopy, which is one of the most useful methods for characterizing and distinguishing them from MWCNTs. The strategy is based on changes that occur in the spectrum of the original SWCNT; then they are compared after derivatization.[214–216] On the other hand, the functionalization with carboxyl groups typically shows no appreciable changes in the Raman spectrum as compared to the original nanotube. This can be understood by considering the small degree of functionalization in this latter case. In contrast, the functionalization of the walls, especially when the degree of the functionalization is high, produces significant changes which are manifested as a decrease in the intensity of the band corresponding to the tangential stress around 1600 cm^{-1}, and an increase in the relative intensity of the band at 1400 cm^{-1}. These facts indicate the presence of defects.[217,218]

The derivatization of SWCNTs through carboxyl groups can be simply carried out by esterification or by the formation of peptide bonds. This second option has the advantage that covalent bonds result more resistant to undergo hydrolysis under acidic or basic conditions. However, the functionalization through ester bonds may be desirable in those cases where the resulting material is required to be used in organic solvents in neutral media. Furthermore, other strategies have also arisen; that is for instance, the inclusion of Si atoms in SWCNTs promote the binding of other molecules to them.[219] On the other hand, fluorination of these materials, which improves their solubility in organic solvents, leads to side-wall polyderivatization.[220] Increasing the solubility in organic solvents of SWCNTs or derivatives turns out in better processability of these materials and the application of spectroscopic techniques in solution that are not possible with pure SWCNTs.[212] The attachment of other molecules to a SWCNT modifies its physical properties so that it may be conveniently tuned. That is to say, in the case of (2+2) cycloaddition of fluorinated olefins to SWCNT, the final adduct exhibits high-mobility semiconducting behavior free from metallic interference.[172] SWCNTs can be also functionalized through the (2+2) cycloaddition of benzyne (see Figure 1.20).[221–223] Finally, functionalized SWCNTs have been shown to be useful assemblies in fields of materials,[224] medical,[225] and biological[226] sciences.
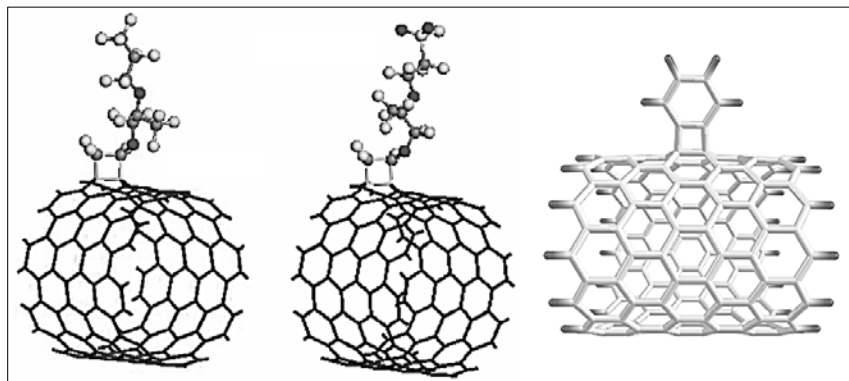
Figure 1.20 From left to right, (2+2) cycloadditions of perfluoro-(5-methyl-3,6-dioxanon-1-ene), perfluoro-2(2-fluorosulfonylethoxy) propyl vinyl ether, and benzyne to SWCNTs.

Chapter 2

Theoretical Framework

Computational Quantum Chemistry

According to classical mechanics, the motion of a particle of constant mass can be described by the following equation:

$$F = ma = m\frac{d^2x}{dt^2} \tag{2.1}$$

where F is the force acting on a particle with mass m, and the acceleration a is given in terms of position x and time t. However, since late nineteenth and early twentieth centuries, it was discovered that classical mechanics does not describe correctly the behavior of small particles such as atomic nuclei or electrons due to the implications of the mass of such particles (see Figure 2.1). The behavior of these particles began to be described by a set of laws now known as quantum mechanics. This set of laws came from the study of phenomena such as the photoelectric effect, the black body radiation, the wave-particle duality, among others; which could not be explained by classical physics. As a consequence of the wave-particle duality described by De Broglie in 1927,[227] Werner Heisenberg proposed the uncertainty principle.[228] This principle states that the measurement itself of a molecular property in a system introduces an uncontrollable disturbance in the system. In general, the description of atomic and subatomic particles through this set of postulates is the cornerstone of quantum mechanics and, in turn, these have been used in the determination of the molecular behavior.[229]
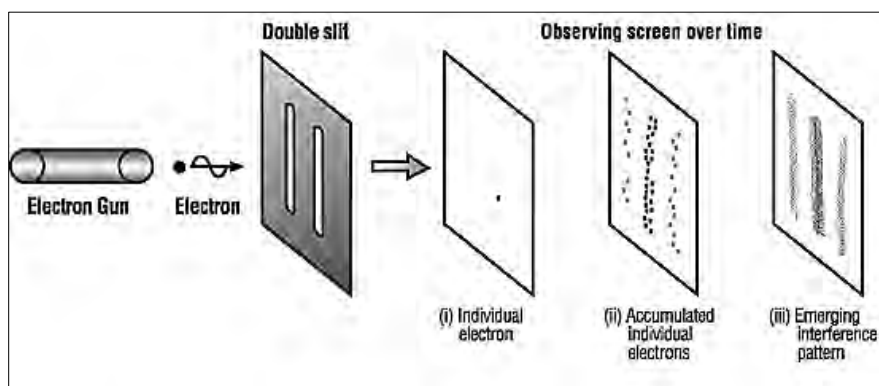
Figure 2.1 The double-slit experiment.

2.1 The Schrödinger equation

The Schrödinger equation[230] is a mathematical expression that represents the energy E of a particle which depends on the wavefunction of such an entity.

$$\hat{H}\Psi(r_1, r_2, \ldots, r_N) = E\Psi(r_1, r_2, \ldots, r_N) \tag{2.2}$$

wherein Ψ is the wavefunction and $\hat{H}$ is the Hamiltonian of the system. This latter is expressed as follows:

$$\hat{H} = -\frac{\hbar^2}{2}\sum_A \frac{1}{m_A}\nabla_A^2 - \frac{\hbar^2}{2}\sum_i \frac{1}{m_i}\nabla_i^2 + \sum_B \sum_{A<B} \frac{Z_A Z_B e^2}{4\pi\varepsilon_0 r_{AB}} - \sum_i \sum_A \frac{Z_A e^2}{4\pi\varepsilon_0 r_{iA}}$$
$$+ \sum_j \sum_{i<j} \frac{e^2}{4\pi\varepsilon_0 r_{ij}} \tag{2.3}$$

or well,

$$\hat{H} = \hat{T}_N + \hat{T}_e + \hat{V}_{NN} + \hat{V}_{eN} + \hat{V}_{ee} \tag{2.4}$$

The first two terms of the Hamiltonian correspond to the kinetic energy of nuclei A and electrons i; then the following terms describe the interactions between nuclei A and B, nuclei A and electrons i, and electrons i and j; respectively. Many calculations of molecular wavefunctions are based on the separation of the electronic Hamiltonian first formulated by Born and Oppenheimer.[231] The nuclear kinetic energy terms are omitted and the remaining quantum operator is a Hamiltonian of electrons only. The stationary nuclei enter to the problem only as generators of an electric potential in which the electrons move in a quantum mechanical way. Within this framework, the molecular Hamiltonian has been simplified to the so-called electronic Hamiltonian including internuclear repulsion that operates only on functions of the electronic coordinates:[229]

$$\hat{H}_{elect} = \hat{T}_e + \hat{V}_{NN} + \hat{V}_{eN} + \hat{V}_{ee} \tag{2.5}$$

2.2 Molecular orbitals

According to the molecular orbital (MO) theory, MOs are formed by the interaction of atomic orbitals. This approach is useful to generate simple MOs, which can be constructed through a linear combination of atomic orbitals (LCAO). Some assumptions have to be taken into consideration:

(i)   MOs are formed by the overlap of atomic orbitals.
(ii)   Atomic orbitals significantly interact each other if they are energetically similar.
(iii) When two atomic orbitals overlap, they interact with each other to form two MOs; those are the bonding and antibonding orbitals.

Like a pair of electromagnetic waves, atomic orbitals can interact either in or out of phase as schematized in Figure 2.2. When the atomic orbitals are in phase, an accumulation of electron density occurs, which is equivalent to an increase in negative charge in the region of overlap between the cores. This generates an increase in the intensity of the attraction between the electronic charge and atomic nuclei involved in the bond. Since electrons in a MO have lower potential energy than they have in isolated atoms, the increase in the intensity of attraction is accompanied by a reduction in the kinetic energy of the electrons in the system. This is known as a bonding MO. On the other hand, when two atomic orbitals interact out of phase, the resulting interaction leads to a decrease in negative charge; as a consequence, it creates a decrease in the attraction between the electronic charge and the atomic nuclei. This leads to a greater potential energy which destabilizes the bond between atoms and forms a nodal plane. In this case, electrons are more stable in the atomic orbitals of isolated atoms. This is known as an antibonding MO.[232]
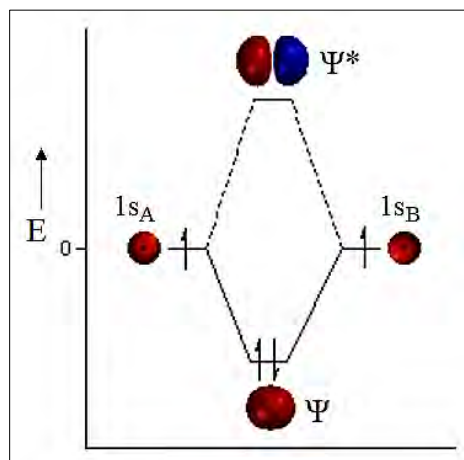
Figure 2.2 Linear combination of atomic orbitals leading to antibonding Ψ^* and bonding Ψ molecular orbitals.

The MO theory differs from the valence bond theory; this latter is based on the Lewis model of valence electrons. However, in several cases, the MO theory predicts the electron density to be located between two nuclei, which represents a chemical bond; thus resembling the main element of the valence bond theory.[229]

2.3 The Hartree-Fock approximation

The calculation of the Schrödinger equation for atoms with many electrons is complicated through analytical solutions; therefore, different approaches have been developed to solve such a predicament. In this regard, in the Hartree-Fock (HF) approximation wavefunctions are constructed as a LCAO and arranged in a mathematical determinant also known as the Slater determinant:[233]

$$\Psi_{HF}(r_1, r_2, \dots, r_N) = (N!)^{-1/2} \begin{vmatrix} \phi_1(r_1) & \phi_2(r_1) & \dots & \phi_N(r_1) \\ \phi_1(r_2) & \phi_2(r_2) & \dots & \phi_N(r_2) \\ \vdots & \vdots & & \vdots \\ \phi_1(r_N) & \phi_2(r_N) & \dots & \phi_N(r_N) \end{vmatrix} \tag{2.6}$$

wherein $\phi(r)$ is an atomic orbital and N is the total number of electrons. The energy of the system is obtained by variationally minimizing the HF energy through:

$$E_{HF} = MIN \langle \Psi | \hat{H} | \Psi \rangle \tag{2.7}$$

Nonetheless, the variational theorem, equation (2.8), states that for a time-independent Hamiltonian operator any trial wavefunction will have an energy expectation value that is greater than or equal to the true ground state wavefunction corresponding to the given Hamiltonian. Because of this, the HF energy is an upper bound to the true ground state energy of a given molecule. In the context of the HF method, the best possible solution is found at the HF limit; i.e. the limit of the HF energy as the basis set approaches completeness.

$$E_\Psi = \frac{\langle \Psi | \hat{H} | \Psi \rangle}{\langle \Psi | \Psi \rangle} \geq E_{\Psi \, exact} \tag{2.8}$$

The HF method can favorably predict the ground state of small non-ionized molecules such as benzene. For large molecules, the accuracy shall depend indirectly on computational resources and the precision of defining atomic orbitals. This method is also a self-consistent field approximation, because wavefunctions are recursively minimized.[229,234]

2.4 Basis sets

A basis set describes the behavior of a wavefunction of a single electron in an atom. That is, it is the solution of the HF equations for an atomic orbital. The first functions of this type were the Slater type functions due to its similarity to the atomic orbitals of the hydrogen atom as depicted in Figure 2.3a:

$$\phi_i(\zeta, n, l, m; r, \theta, \phi) = Nr^{n-1}e^{-\zeta r}Y_{lm}(\theta, \phi) \tag{2.9}$$

here N is a normalizing constant; ζ is a characteristic exponent; r, θ, and ϕ are spherical coordinates; Y_{lm} is a spherical harmonic; n, l, and m are respectively the principal, secondary, and magnetic quantum numbers. The geometric form of a Slater type orbital (STO) can be approximated by a sum of Gaussian functions with different exponents and coefficients (Figure 2.3b). Gaussian functions significantly reduce the computational time because the integration of a Gaussian function is faster (in view of the Gaussian product theorem).[235,236] Gaussian functions are described as follows:

$$g(\alpha, a, b, c; x, y, z) = Ne^{-\alpha r^2}x^a y^b z^c \tag{2.10}$$

where N is a normalizing constant; α is a characteristic exponent; x, y, and z are Cartesian coordinates; and a, b, and c are exponents. The sum of these exponents, $L=a+b+c$, is related to an s-type orbital if $L = 0$; analogously $L = 1$ for p-type orbitals, and $L = 2$ for d-type orbitals.[237]
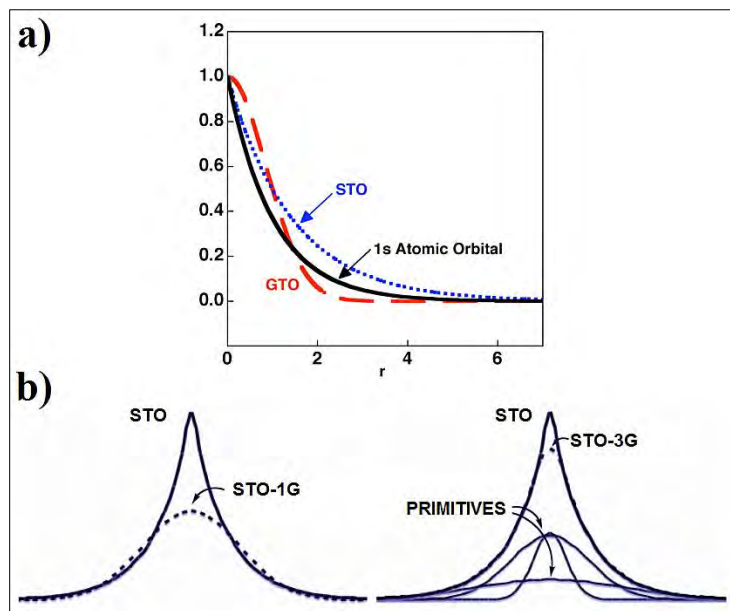
Figure 2.3 a) Comparison of Gaussian and Slater type orbitals for the 1s hydrogen orbital.
b) Contractions of Gaussian functions to a Slater type orbital.

Primitive Gaussian functions are obtained by electronic optimizations of atoms through calculations such as HF or configuration interaction (CI; a post-Hartree-Fock linear variational method). Exponents and coefficients are varied until the lowest total energy of the atoms is reached. Gaussian functions are grouped into levels (they are not the energy levels of an atom). A level is a collection of Gaussian functions that have the same value of L. Primitive Gaussian functions are usually contracted as linear combinations for the calculation of atomic or molecular properties. Better results are attained if the coefficients of the Gaussian functions were left free to vary. However, this represents a large computational effort in both hard disk and storage of integrals; as well as the internal memory of the computer. Contraction of Gaussian functions is performed by a curve-fitting. The number of contractions used to represent a STO is called *zeta* and it corresponds to the number of basis sets per orbital (e.g. double zeta, DZ; triple zeta, TZ; and so on). One of the smallest basis sets is STO-3G, which is used by popular semiempirical methods.[238] The STO-3G basis set is the result of the contraction of three Gaussian functions and it has been adjusted by the method of least-squares to a STO (see Figure 2.3b).[229,239]

2.4.1 Pople functions

For valence orbitals, sometimes more basis sets are assigned to the rest of the orbitals; these are known as split valence (SV) basis sets. In the Pople convention, the nature of SV basis set is emphasized following the syntax: *n-ij*G or *n-ijk*G, where *n* is the number of primitive functions for internal levels, *ij* or *ijk* are the number of primitive functions for contractions of the valence level. The notations *ij* and *ijk* describe basis sets of double and triple zeta quality, respectively. Generally, *s*- or *p*-type contractions are converted into *sp*-type levels. For example, a 4-31G basis set corresponds to 4 primitive functions which represent the internal level; and contractions of 3 and 1 primitive functions represent the valence level. Pople functions can be extended with polarization functions *d* in heavy atoms; here an asterisk is added to the basis sets. For instance, the 4-31G* basis set in the case of methane contains 8 functions *s*-type, 4 *p*-type, and one *d*/4*s* type; where the latter is precisely the polarization function.[240,241]

2.4.2 Polarization and diffuse functions

Polarization functions are functions with a value of L higher than those ones representing the orbitals of the corresponding atom. Polarization functions are important for reaching better precision in reproducing a chemical bond since they improve correlation effects. With the addition of *d*-type functions to the basis set, each atom adds up to 5 or 6 functions, while with the addition of *f*-type functions there is an increment of 7 or 10 basis functions, which increases the computational time. The exponents of the functions of polarization cannot be obtained from HF calculations because the electrons do not occupy virtual orbitals within this approximation. On the other hand, they are estimated from calculations including correlation. For example, the function of Pople 6-31G(d), or 6-31G*, adds 6 *d*-type functions as the polarization functions. Similarly, 6-31G(d,p), or 6-31G**, includes additional *p*-type polarization functions to the hydrogen atoms. Diffuse functions are very important to describe anions and weak bonds. These functions have small exponents and slowly vanish as a function of the distance to the nucleus. Within the Pople's notation, they are represented by the sign +.[229,239,240]

2.5 Pseudopotentials

First introduced by Hans Hellman[242] in 1934, pseudopotentials are approximations that simplify the complex description of the effects of the motion of core electrons; that is, a modified effective potential is introduced in the Schrödinger equation instead of the Coulomb potential term in order to describe non-valence electrons of an atom together with its nucleus.

2.5.1 Effective core potentials

In most cases, the internal atomic levels are not significantly affected by changes in the chemical bond. This has motivated the development of effective core potentials (ECPs) which enable the treatment of internal electron levels as an average potential instead of actual particles. ECPs are not orbitals, but modifications to the Hamiltonian operator made with the aim to improve the computational performance. Relativistic effects are also added, which are important in transition metals and heavy atoms. For the rest of the electrons, as well as the valence electrons, basis sets optimized for each type of ECP are included. ECPs are generally published as parameters of the following expression:

$$ECP = \sum_{i=1}^{M} d_i r^{n_i} e^{-\zeta_i r^2} \tag{2.11}$$

here M is the number of terms in the expression, d_i is a coefficient for each term, r is the distance to the nucleus, and n_i and ζ_i are exponents at the i-th term. To specify an ECP, it is necessary to include the number of internal electrons that are going to be replaced by the ECP, the angular-momentum quantum number (l), and the number of terms in the Gaussian polynomial expansion.[243,244] This strategy is implemented in the Gaussian09 computational package used in this thesis.[245]

2.5.2 The frozen core approximation

The frozen core approximation (FCA) is an alternative method that uses a *frozen* core to optimize the computational resources by reducing the size of the basis set. In view of the fact that core atomic orbitals are practically unaltered during the formation of a bond, the quality of the calculations remains unchanged by using the FCA;[246,247] which represents savings in the computational time. Unlike ECP, a FCA calculation is indeed an all-electron calculation. FCA also allows the calculation of total charge density and potential in the valence and in the core region.

In the FCA, the valence basis set used in the self-consistent field equations is explicitly orthogonalized to the frozen core. Thus, a series of auxiliary core functions, χ_μ^{core}, are added to the valence basis set. One χ_μ^{core} per frozen core orbital is therefore included. A valence function is replaced by a linear combination as follows:

$$\chi_v^{valence} \rightarrow \chi_v^{valence} + \sum_{\mu} c_{\mu v} \chi_v^{core} \tag{2.12}$$

Coefficients $c_{\mu v}$ are obtained from the condition that each such modified valence function is orthogonal to each frozen core orbital. The frozen core orbitals are taken from very accurate single-atom calculations with large STO basis sets. This approach can be executed in the Amsterdam Density Functional computational package used in the current thesis.[248,249]

2.6 Density functional theory

The density functional theory (DFT) represents an alternative to conventional *ab initio* methods to solve the Schrödinger equation. According to DFT, the energy of a many-electron system can be expressed from the electron density $n(\mathbf{r})$. The function of $n(\mathbf{r})$ depends on three spatial variables x, y, z; while polyelectronic wavefunctions require three variables for each one of the N electrons in the molecular system. This reduction in the number of variables results in a reduction of computing time for a procedure based on DFT as compared to post-HF methods.[250]

2.6.1 The Hohenberg-Kohn theorems

DFT is formally based on the theorems formulated by Hohenberg and Kohn in 1964.[251,252] The first theorem states that there is a one-to-one relationship between the external potential $v_{ext}(\mathbf{r})$ and the ground state density, and hence the total energy is a unique functional of $n(\mathbf{r})$. The energy functional $E[n(\mathbf{r})]$ referred in the first Hohenberg-Kohn theorem can be written in terms of $v_{ext}(\mathbf{r})$ in the following way:

$$E[n(\mathbf{r})] = \int n(\mathbf{r})v_{ext}(\mathbf{r})d\mathbf{r} + F[n(\mathbf{r})] \tag{2.13}$$

where $F[n(\mathbf{r})]$ is unknown; although it is a universal functional of $n(\mathbf{r})$. Accordingly, assuming a nondegenerate ground state, the Hamiltonian for the system can be written in the following way: the electron wavefunction Ψ that minimizes the energy expectation value gives the ground-state energy.

$$E[n(\mathbf{r})] = \langle \Psi | \widehat{H} | \Psi \rangle \tag{2.14}$$

then, the Hamiltonian can be written as:

$$\widehat{H} = \widehat{F} + \widehat{V}_{ext} \tag{2.15}$$

$$\widehat{F} = \widehat{T}_e + \widehat{V}_{ee} \tag{2.16}$$

The electron operator $\widehat{F}$ is the same for all N-electron systems; as a result, $\widehat{H}$ is completely defined by N and $v_{ext}(\mathbf{r})$. The proof of the first theorem is remarkably simple and proceeds by *reductio ad absurdum*. Let us consider two external potentials, $v_{ext,1}(\mathbf{r})$ and $v_{ext,2}(\mathbf{r})$ which differ by more than a constant, that give rise to the same density $n_0(\mathbf{r})$. The corresponding Hamiltonians, $\widehat{H}_1$ and $\widehat{H}_2$, will therefore have different ground-state wavefunctions, Ψ_1 and Ψ_2, which give $n_0(\mathbf{r})$. The variational principle then leads to:

$$E_1^0 < \langle \Psi_2 | \widehat{H}_1 | \Psi_2 \rangle = \langle \Psi_2 | \widehat{H}_2 | \Psi_2 \rangle + \langle \Psi_2 | \widehat{H}_1 - \widehat{H}_2 | \Psi_2 \rangle$$

$$= E_2^0 + \int n_0(\mathbf{r})[v_{ext,1}(\mathbf{r}) - v_{ext,2}(\mathbf{r})]d\mathbf{r} \tag{2.17}$$

here E_1^0 and E_2^0 are the ground-state energies of the corresponding Hamiltonians. An equivalent expression of equation 2.17 is obtained by interchanging the subscripts; which leads to the inequality:

$$E_1^0 + E_2^0 < E_2^0 + E_1^0 \tag{2.18}$$

which is a contradiction and, as a result, the ground-state density uniquely determines $v_{ext}(\mathbf{r})$ within an additive constant. To sum up, the electrons determine the positions of the nuclei in a system and all ground-state electronic properties because $v_{ext}(\mathbf{r})$ and N completely define the Hamiltonian of the system.

The second theorem states that the ground state energy can be obtained variationally: the density that minimizes the total energy is the exact ground-state density. The proof of this theorem is given as follows:

$$n(\mathbf{r}) \rightarrow v_{ext}(\mathbf{r}) \tag{2.19}$$

and given that $v_{ext}(\mathbf{r})$ and N determine $\hat{H}$ and Ψ, the expectation value of $\hat{F}$ is also a functional of $n(\mathbf{r})$:

$$F[n(\mathbf{r})] = \langle \Psi | \hat{F} | \Psi \rangle \tag{2.20}$$

then

$$E_v[n'(\mathbf{r})] = \int n'(\mathbf{r}) v_{ext}(\mathbf{r}) d\mathbf{r} + F[n'(\mathbf{r})] \tag{2.21}$$

where $E_v[n'(\mathbf{r})]$ is a v-representable[253,254] energy functional for which $v_{ext}(\mathbf{r})$ is unrelated to another density $n'(\mathbf{r})$. The variational principle leads to:

$$\langle \Psi' | \hat{F} | \Psi' \rangle + \langle \Psi' | \hat{V}_{ext} | \Psi' \rangle > \langle \Psi | \hat{F} | \Psi \rangle + \langle \Psi | \hat{V}_{ext} | \Psi \rangle \tag{2.22}$$

$$\int n'(\mathbf{r}) v_{ext}(\mathbf{r}) d\mathbf{r} + F[n'(\mathbf{r})] > \int n(\mathbf{r}) v_{ext}(\mathbf{r}) d\mathbf{r} + F[n(\mathbf{r})] \tag{2.23}$$

and therefore the variational principle of the second Hohenberg-Kohn theorem is obtained:

$$E_v[n'(\mathbf{r})] > E_v[n(\mathbf{r})] \tag{2.24}$$

2.6.2 The fundamental equation

Minimizing the functional of the energy with respect to $n(\mathbf{r})$, $\delta E_v[n(\mathbf{r})] = 0$, should be performed ensuring conservation of the N-representability[254] during the optimization process. This is done by introducing the restriction:

$$\int n(\mathbf{r}) d\mathbf{r} - N = 0 \tag{2.25}$$

through the Lagrange's method of undetermined multipliers. In order to do so, an electron density function is constructed so that:

$$\delta \left[F[n(\boldsymbol{r})] + \int n(\boldsymbol{r}) v_{ext}(\boldsymbol{r}) d\boldsymbol{r} - \theta \left(\int n(\boldsymbol{r}) d\boldsymbol{r} - N \right) \right] = 0 \tag{2.26}$$

$$\delta \left[E_v[n(\boldsymbol{r})] - \theta \left(\int n(\boldsymbol{r}) d\boldsymbol{r} - N \right) \right] = 0 \tag{2.27}$$

here θ is a Lagrange multiplier. By using the definition of the derivative of a functional it is obtained:

$$\int \frac{\delta E_v[n(\boldsymbol{r})]}{\delta n(\boldsymbol{r})} \delta n(\boldsymbol{r}) d\boldsymbol{r} - \theta \int \delta n(\boldsymbol{r}) d\boldsymbol{r} = 0 \tag{2.28}$$

$$\int \left\{ \frac{\delta E_v[n(\boldsymbol{r})]}{\delta n(\boldsymbol{r})} - \theta \right\} \delta n(\boldsymbol{r}) d\boldsymbol{r} = 0 \tag{2.29}$$

thus providing the condition of a restricted minimization and giving the value of θ at the minimum. Then, the fundamental equation of DFT is expressed as:[250]

$$\frac{\delta E_v[n(\boldsymbol{r})]}{\delta n(\boldsymbol{r})} = \frac{\delta F[n(\boldsymbol{r})]}{\delta n(\boldsymbol{r})} + v_{ext}(\boldsymbol{r}) = \theta \tag{2.30}$$

2.6.3 The Kohn-Sham equations

The fundamental equation in DFT provides a formula for minimizing energy and thereby determines $n(\mathbf{r})$ of the ground state. A problem arises when the expression that relates the electronic Hamiltonian with $n(\mathbf{r})$ is not exactly known; particularly the exact functional form of the kinetic energy. In contrast, the kinetic energy is easily calculated if the wavefunction is known. To solve this predicament, Kohn and Sham[252] considered a system of N non-interacting electrons as a reference system moving under the influence of $v_{ext}(\mathbf{r})$. In this system, the fundamental equation of DFT, considering the exact kinetic energy of non-interacting electrons T_e^{KS}, is:

$$\frac{\delta E_v[n(\boldsymbol{r})]}{\delta n(\boldsymbol{r})} = \frac{\delta T_e^{KS}[n(\boldsymbol{r})]}{\delta n(\boldsymbol{r})} + v_{ext}(\boldsymbol{r}) = \mu \tag{2.31}$$

given that

$$E_v[n(\boldsymbol{r})] = T_e^{KS}[n(\boldsymbol{r})] + \int n(\boldsymbol{r}) v_{ext}(\boldsymbol{r}) d\boldsymbol{r} \tag{2.32}$$

On the other hand, in a real system electrons interact each other so that the energy is:

$$E_v[n(\boldsymbol{r})] = T_e[n(\boldsymbol{r})] + \int n(\boldsymbol{r}) v_{ext}(\boldsymbol{r}) d\boldsymbol{r} + V_{ee}[n(\boldsymbol{r})] \tag{2.33}$$

Here the integral term corresponds to $V_{eN}[n(\mathbf{r})]$ and it refers to the functional of the classical potential energy between nuclei and electrons, and $V_{ee}[n(\mathbf{r})]$ is the interaction between electrons. The value of T_e is not the same as T_e^{KS}.

The greatest contribution of Kohn and Sham was the demonstration for the first time that the electronic Hamiltonian can be separated in terms of kinetic, Coulomb-repulsion and exchange-correlation energies; that is:

$$E_v[n(\mathbf{r})] = T_e^{KS}[n(\mathbf{r})] + V_{eN}[n(\mathbf{r})] + J_{ee}[n(\mathbf{r})] + (T_e[n(\mathbf{r})] - T_e^{KS}[n(\mathbf{r})])$$
$$+ (V_{ee}[n(\mathbf{r})] - J_{ee}[n(\mathbf{r})]) \tag{2.34}$$

with the Coulomb term given by:

$$J_{ee}[n(\mathbf{r})] = \frac{1}{2} \int \frac{n(\mathbf{r})n(\mathbf{r}')}{|\mathbf{r} - \mathbf{r}'|} d\mathbf{r} d\mathbf{r}' \tag{2.35}$$

In the equation 2.34, $(T_e[n(\mathbf{r})] - T_e^{KS}[n(\mathbf{r})])$ is the difference between the kinetic energy of the real and the reference systems. On the other hand, the exchange-correlation contribution is given by $(V_{ee}[n(\mathbf{r})] - J_{ee}[n(\mathbf{r})])$. These two contributions are usually grouped into a single term as $E_{xc}[n(\mathbf{r})]$:

$$E_{xc}[n(\mathbf{r})] = (T_e[n(\mathbf{r})] - T_e^{KS}[n(\mathbf{r})]) + (V_{ee}[n(\mathbf{r})] - J_{ee}[n(\mathbf{r})]) \tag{2.36}$$

$E_{xc}[n(\mathbf{r})]$ contains all contributions to the total energy for which there is no simple expression as a function of $n(\mathbf{r})$. Then, the energy of the system is:

$$E_v[n(\mathbf{r})] = T_e^{KS}[n(\mathbf{r})] + V_{eN}[n(\mathbf{r})] + \frac{1}{2} \int \frac{n(\mathbf{r})n(\mathbf{r}')}{|\mathbf{r} - \mathbf{r}'|} d\mathbf{r} d\mathbf{r}' + E_{xc}[n(\mathbf{r})] \tag{2.37}$$

which naturally leads to:

$$\frac{\delta E_v[n(\mathbf{r})]}{\delta n(\mathbf{r})} = \frac{\delta T_e^{KS}[n(\mathbf{r})]}{\delta n(\mathbf{r})} + v_{ext}(\mathbf{r}) + \frac{1}{2} \int \frac{n(\mathbf{r}')}{|\mathbf{r} - \mathbf{r}'|} d\mathbf{r}' + \frac{\delta E_{xc}[n(\mathbf{r})]}{\delta n(\mathbf{r})} = \mu \tag{2.38}$$

taking the exchange-correlation potential as:

$$V_{xc}(\mathbf{r}) = \frac{\delta E_{xc}[n(\mathbf{r})]}{\delta n(\mathbf{r})} \tag{2.39}$$

and the Coulomb potential as:

$$V_{Coul}(\mathbf{r}) = v_{ext}(\mathbf{r}) + \frac{1}{2} \int \frac{n(\mathbf{r}')}{|\mathbf{r} - \mathbf{r}'|} d\mathbf{r}' \tag{2.40}$$

the following expression is obtained:

$$\frac{\delta T_e^{KS}[n(\mathbf{r})]}{\delta n(\mathbf{r})} + V_{Coul}(\mathbf{r}) + V_{xc}(\mathbf{r}) = \mu \tag{2.41}$$

$$\frac{\delta T_e^{KS}[n(\boldsymbol{r})]}{\delta n(\boldsymbol{r})} + V_{KS}(\boldsymbol{r}) = \mu \tag{2.42}$$

wherein $V_{KS}(\mathbf{r})$ is called the Kohn-Sham potential. When comparing equation 2.31 with equation 2.42, wherein $v_{ext}(\mathbf{r})$ is turned into $V_{KS}(\mathbf{r})$, it is concluded that the equation to solve a system of interacting electrons is the same as the equation to solve a system of non-interacting electrons.

The equations to be solved in order to find the density of the ground state, $n_0(\mathbf{r})$, shall be simply the Schrödinger's equation for the system of one electron rewritten as (in atomic units):

$$\left[-\frac{1}{2}\nabla_i^2 + V_{KS}(\boldsymbol{r}) \right] \phi_i = \varepsilon_i \phi_i \tag{2.43}$$

$$V_{KS}(\boldsymbol{r}) = V_{eN}(\boldsymbol{r}) + \frac{1}{2}\int \frac{n(\boldsymbol{r}')}{|\boldsymbol{r}-\boldsymbol{r}'|}d\boldsymbol{r}' + V_{xc}(\boldsymbol{r}) \tag{2.44}$$

Equations (2.43) and (2.44) are very similar to the HF equations. Orbitals ϕ_i are called Kohn-Sham orbitals; from which $n(\mathbf{r})$ is calculated as follows:

$$n(\boldsymbol{r}) = 2\sum_{i=1}^{N/2}|\phi_i(\boldsymbol{r})|^2 \tag{2.45}$$

where the factor 2 is due to the degeneracy of the spin generated by the assumption that the orbitals are doubly occupied. Like in the HF approximation, the procedure to find solutions starts with trials of MOs from which $n(\mathbf{r})$ is determined. This trial density, in turn, is used to get the value for $V_{KS}(\mathbf{r})$; then the equations of eigenvalues and eigenfunctions are solved. The process is iteratively repeated until convergence is reached, which indicates that the ground state energy has been determined.[250]

2.6.4 The local density approximation

In the local density approximation (LDA), $E_{xc}[n(\mathbf{r})]$ is a functional that exclusively depends on $n(\mathbf{r})$ and the correlation-exchange term is usually treated separately. The treatment of the exchange term is based on the assumption that the density hardly varies with position; that is, its derivative with respect to position is approximately zero so that the resulting $n(\mathbf{r})$ resembles a homogenous electron gas within the Thomas-Fermi theory. On the other hand, the correlation term is not exactly known; therefore, numerical estimations are usually necessary.[255] One of the methods used to determine correlation effects is the quantum Monte-Carlo method implemented in a homogeneous gas of non-interacting electrons.[256]

In general, for a spin-unpolarized system, a LDA for the exchange-correlation energy is written as:

$$E_{xc}^{LDA}[n] = \int n(\boldsymbol{r})\varepsilon_{xc}(n)d\boldsymbol{r} \tag{2.46}$$

where ε_{xc} is the exchange-correlation energy per particle of a homogeneous electron gas of charge density n. The exchange-correlation energy is decomposed into exchange and correlation terms linearly,

$$E_{xc} = E_x + E_c \tag{2.47}$$

and, consequently, separate expressions for E_x and E_c may be sought. Moreover, α-spin and β-spin electron densities can be included within the LDA method in order to apply the unrestricted formalism of the Kohn-Sham equations, thus providing a treatment of open-shell systems. This approximation is known as the local spin density approximation, LSDA:

$$E_{xc}^{LSDA}[n^\alpha, n^\beta] = \int n(\boldsymbol{r})\varepsilon_{xc}(n^\alpha, n^\beta)d\boldsymbol{r} \tag{2.48}$$

2.6.5 The generalized gradient approximation

In view of the fact that the model of the homogenous electron gas is ineffective to accurately predict properties of chemical bonds, it was developed a method that introduces density gradients in the description of the exchange-correlation effects. In the latter method, the value of $n(\mathbf{r})$ at each point is taken into account as well as the variation of $n(\mathbf{r})$ around each point. This method is called the generalized gradient approximation (GGA). Under this approach the exchange-correlation energy is redefined including local values of the derivatives of $n(\mathbf{r})$:

$$\varepsilon_{XC}^{GGA}[n(\boldsymbol{r})] = \varepsilon_{XC}^{LDA}[n(\boldsymbol{r})] + \Delta\varepsilon_{XC}\left[\frac{|\nabla n(\boldsymbol{r})|}{n^{4/3}(\boldsymbol{r})}\right] \tag{2.49}$$

Subsequently, quantitative improvements of exchange-correlation functionals have been introduced,[257,258] thus establishing that the exact exchange-correlation energy satisfies the relation:

$$E_{xc}[n(\boldsymbol{r})] \geq -1.68 \int n(\boldsymbol{r})r^{4/3}d\boldsymbol{r} \tag{2.50}$$

Several density functionals have been developed within the GGA such as the Perdew-Wang (PW91)[259–262] and Becke (B)[263] functionals for the calculation of the exchange contribution, and the Lee-Yang-Par (LYP)[264,265] and Perdew (P86)[266] for the treatment of the correlation term. Several density functionals were used for the different studies presented in the current thesis; for instance, cycloadditions to carbon nanostructures were quantum-chemically explored via BP86.

2.6.6 Hybrid density functionals

Hybrid density functionals result from the combination of several exchange-correlation functionals, experimental parameters and/or the HF energy. These functionals are based on the adiabatic connection method, wherein Ψ and $v_{ext}(\mathbf{r})$ is a function of a parameter, λ, defining the interaction of the particles in a given system. The value of λ varies from 0 (the non-interacting system) to 1 (the real system). In non-interacting systems there is no exchange-correlation potential. However, $\lambda = 1$ completely recovers the exchange-correlation potential defined in equation 2.39 as follows:

$$V_{xc}[n(\mathbf{r})] = \int_0^1 \langle \Psi(\lambda)|v_{xc}(\lambda)|\Psi(\lambda)\rangle d\lambda = \int_0^1 V_{xc}(\lambda)d\lambda \tag{2.51}$$

even though the functional dependence related to λ is rather unknown. Nevertheless, the introduction of adjustable parameters led to the hybrid functionals family:

$$V_{xc} = V_x^{HF} + z(V_{xc}^{DFT} - V_x^{HF}) \tag{2.52}$$

for which fails are corrected by the adjustment of a set of parameters z. For example, the popular B3LYP[267] functional is defined by:

$$E_{xc}^{B3LYP} = (1 - a_0)E_x^{LSDA} + a_0 E_x^{exact} + a_x E_x^{B88} + (1 - a_c)E_c^{VWN} + a_c E_c^{LYP} \tag{2.53}$$

here E_x^{exact} is the functional calculated from a HF-like expression; and a_0, a_x, and a_c are parameters which are calculated from experimental energies of atomization. Subsequently, other hybrid functionals have been proposed with the aim of reaching improvements in chemical accuracy; although greater accuracy may require the use of higher order density derivatives.

2.6.7 Long-range corrected density functionals

The introduction of the HF exchange in hybrid functionals not only improves outcomes as compared with LSDA and GGA values but also partially corrects wrong asymptotic behavior of the exchange potential of such functionals, which do not follow a $-r^{-1}$ decay for remote regions of the nucleus as it should occur at the exact exchange.[268] The improvement produced via hybrid functionals is not, however, completely satisfactory and, for example, the B3LYP functional has a behavior of $-0.2r^{-1}$,[269] which explains its failure in cases involving a more dispersed electron density.[270] This deficiency is corrected by the division of the interelectronic repulsion term of the exchange potential into two regions, one short-range (SR) and the other long-range (LR), following the partitioning scheme developed by Ewald:[271]

$$\frac{1}{r_{12}} = \frac{1 - erf(\mu r_{12})}{r_{12}} + \frac{erf(\mu r_{12})}{r_{12}} \tag{2.54}$$

wherein *erf* is the error function (which is a normalized form of a Gaussian function) and μ is a parameter controlling such a function. The first term defines the SR decay followed by the LR decay in the second term; those are described by the functionals V_x^{SR} and V_x^{LR}, respectively. The first case is a GGA exchange functional modified to account for an interelectronic term and, in the second case, the long-range exchange is simply calculated with the HF exchange potential.

According to equation 2.54, the exchange when $r_{12} \rightarrow 0$ does not include any HF exchange while at infinite distances, $r_{12} \rightarrow \infty$, all the exchange is exact. Successively, Yanai et al. introduced more flexibility in the scheme of division of the interelectronic repulsion term by adding two parameters that allow the HF contribution to be variable at $r_{12} \rightarrow 0$ and $r_{12} \rightarrow \infty$. This extension is called the Coulomb attenuating method (CAM), and it is expressed as follows:

$$\frac{1}{r_{12}} = \frac{1 - [\alpha + \beta erf(\mu r_{12})]}{r_{12}} + \frac{\alpha + \beta erf(\mu r_{12})}{r_{12}} \tag{2.55}$$

wherein α and β control the contribution of the exact exchange as a function of r_{12}. Besides, the authors specifically optimized parameters using BLYP for V_x^{SR} based on the B3LYP functional, which was used for gradient corrections. Meanwhile, choosing the values $\alpha = 0.2$ and $\beta = 0.6$, the exact exchange contribution varies from 0.2 to 0.6 for r_{12} leading to the CAM-B3LYP functional. In some cases, CAM-B3LYP and B3LYP produce similar results; although improvements with the former can be observed, for instance, in the description of states characterized by strong charge transfer character.[269]

2.7 Time-dependent density functional theory

According to the first theorem by Hohenberg-Kohn, it is clear that DFT is a ground-state quantum theory. Nonetheless, it is possible to extend the DFT ideas to the study of excited states by the introduction of a time-dependent (TD) potential. In fact, in 1984 Runge and Gross[272] formulated a theorem that assumes the extension of the first DFT theorem to time-dependent systems, in which it is demonstrated that there exists a correlation between a wavefunction, a TD external potential, and the corresponding TD electron density. That is, the TD wavefunction is defined by the density $\Psi n(\mathbf{r},t)$ so that any TD molecular property such as excitation energies is also a functional of the density, like in DFT.[273] This theorem is the foundation of all the TD-DFT methodology.[274]

The TD density $\Psi n(\mathbf{r},t)$ is determined by the minimization of the action-integral functional instead of the energy; this integral is:

$$A[n(\boldsymbol{r},t)] = \int_{t_0}^{t_1} \left\langle \Psi n(\boldsymbol{r},t) \middle| i\frac{\partial}{\partial t} - \widehat{H}(\boldsymbol{r},t) \middle| \Psi n(\boldsymbol{r},t) \right\rangle dt \tag{2.56}$$

which can be divided into a universal functional and a term that depends on the total external potential and includes the interaction with the nuclei of the system and the TD potential:

$$A[n(\mathbf{r},t)] = B[n(\mathbf{r},t)] - \int_{t_0}^{t_1} dt \int n(\mathbf{r},t)[V_{eN}(\mathbf{r}) + V_t(\mathbf{r},t)]d\mathbf{r} \tag{2.57}$$

here $V_t(\mathbf{r},t)$ is the TD external potential. The universal functional $B[n(\mathbf{r},t)]$ is given by:

$$B[n(\mathbf{r},t)] = \int_{t_0}^{t_1} \left\langle \Psi n(\mathbf{r},t) \left| i\frac{\partial}{\partial t} - \hat{T}_e(\mathbf{r}) - \hat{V}_{ee}(\mathbf{r}) \right| \Psi n(\mathbf{r},t) \right\rangle dt \tag{2.58}$$

2.7.1 Kohn-Sham time-dependent density functional theory

In the case of TD-DFT, $n(\mathbf{r},t)$ can be calculated through a TD Kohn-Sham formulation, where it is defined a reference system of non-interacting electrons under a TD external potential that gives rise to $n(\mathbf{r},t)$; that is $v^{TD\text{-}KS}$. Therefore, the resulting wavefunction is a Slater determinant from which every orbital is calculated by solving the corresponding mono-electron equation:

$$i\frac{\partial}{\partial t}\Psi(\mathbf{r},t) = \left[-\frac{1}{2}\nabla^2 + V_{eN}(\mathbf{r}) + v^{TD-KS}(\mathbf{r},t)\right]\Psi(\mathbf{r},t) \tag{2.59}$$

thus providing the orbitals of the real system:

$$n(\mathbf{r},t) = 2\sum_{i=1}^{N/2}|\phi_i(\mathbf{r},t)|^2 \tag{2.60}$$

Proceeding exactly as in the original Kohn-Sham formulation, the TD universal functional, analogous to $F[n(\mathbf{r})]$, is given as follows:

$$B_{KS}[n(\mathbf{r},t)] = \int_{t_0}^{t_1} \left\langle \Psi(\mathbf{r},t) \left| i\frac{\partial}{\partial t} - \hat{T}_e(\mathbf{r}) \right| \Psi(\mathbf{r},t) \right\rangle dt \tag{2.61}$$

thus defining the action-integral functional:

$$A[n(\mathbf{r},t)] = B_{KS}[n(\mathbf{r},t)] - J_{ee}^{TD}[n(\mathbf{r},t)] - V_{eN}^{TD}[n(\mathbf{r},t)]$$
$$-V_t^{TD}[n(\mathbf{r},t)] - V_{xc}[n(\mathbf{r},t)] \tag{2.62}$$

here $J_{ee}^{TD}[n(\mathbf{r},t)]$ and $V_{eN}^{TD}[n(\mathbf{r},t)]$ has a similar form as their time-independent counterpart. $V_t^{TD}[n(\mathbf{r},t)]$ is calculated in the same way as $V_{eN}^{TD}[n(\mathbf{r},t)]$ by using the TD potential. The last term accounts for the exchange-correlation contribution and is defined as:

$$V_{xc}[n(\mathbf{r},t)] = B_{KS}[n(\mathbf{r},t)] - J_{ee}^{TD}[n(\mathbf{r},t)] - B[n(\mathbf{r},t)] \tag{2.63}$$

The minimization of the wavefunction using the Euler-Lagrange method leads to the calculation of the spatial orbitals of the reference system by specifying the form of the potential $v^{TD\text{-}KS}$. Then:

$$i\frac{\partial}{\partial t}\Psi(\boldsymbol{r},t) = \left[-\frac{1}{2}\nabla^2 + V_{eN}(\boldsymbol{r}) + V_t(\boldsymbol{r},t) + \int \frac{n(\boldsymbol{r}',t)}{|\boldsymbol{r}-\boldsymbol{r}'|} + \frac{\delta V_{xc}[n(\boldsymbol{r},t)]}{\delta n(\boldsymbol{r},t)}\right]\Psi(\boldsymbol{r},t) \quad (2.64)$$

here, from equation 2.59, $v^{TD\text{-}KS}$ is:

$$v^{TD-KS}(\boldsymbol{r},t) = V_t(\boldsymbol{r},t) + \int \frac{n(\boldsymbol{r}',t)}{|\boldsymbol{r}-\boldsymbol{r}'|} + \frac{\delta V_{xc}[n(\boldsymbol{r},t)]}{\delta n(\boldsymbol{r},t)} \quad (2.65)$$

Comparing the potential in equation 2.65 with the static analogous one, $v_{ext}(\boldsymbol{r})$, it is observed that this TD version is different because of the addition of $V_t(\boldsymbol{r},t)$ and, moreover, it changes the definition of the exchange-correlation term that has to be included. The latter is also expected to be time-dependent.[274]

2.7.2 The linear response approximation

Instead of developing new exchange-correlation functionals for the solution of equation 2.59, the adiabatic local density approximation (ALDA) is usually used in which $n(\boldsymbol{r},t)$ is supposed to be invariant with the time. As a result, the functionals developed within the static Kohn-Sham formulation can be also used in the ALDA. Consequently, the TD external potential must be defined in order to solve the former equation and obtain $n(\boldsymbol{r},t)$. An absorption spectrum can be therefore calculated by considering a TD external potential defined as a result of an oscillating electric field of the electromagnetic radiation. Unfortunately, the solution of the TD Kohn-Sham equations turns out to be very complicated. However, in the case of interactions of low intensity, first-order perturbative treatments can be resourced like the use of linear response (LR) functions.[275] In electron-density systems, the linear response $\delta n(\boldsymbol{r},t)$ is a consequence of the interaction with a TD external potential and is given as follows:

$$\delta n(\boldsymbol{r},\omega) = \int \chi(\boldsymbol{r},\boldsymbol{r}',\omega)\delta V_{ext}(\boldsymbol{r}',\omega)d\boldsymbol{r}' \quad (2.66)$$

where the time dependence t has been substituted by the frequency dependence ω associated to an external potential, and $\chi(\boldsymbol{r},\boldsymbol{r}',\omega)$ is the LR function for the density. Taking advantage of the Kohn-Sham formulation, the response of the density can be expressed through the LR function $\chi_{KS}(\boldsymbol{r},\boldsymbol{r}',\omega)$ of the reference system; thus using the already well-stablished methods to determine wavefunctions. The response of the density is calculated as follows:

$$\delta n(\boldsymbol{r},\omega) = \int \chi_{KS}(\boldsymbol{r},\boldsymbol{r}',\omega)\delta V_{eff}(\boldsymbol{r}',\omega)d\boldsymbol{r}' \quad (2.67)$$

here, an effective potential is considered to contain all the components of potential energy:

$$\delta V_{eff}(\boldsymbol{r}',\omega) = \delta V_{eff}(\boldsymbol{r}',\omega) + \int \frac{\delta n(\boldsymbol{r}'',\omega)}{|\boldsymbol{r}'-\boldsymbol{r}''|}d\boldsymbol{r}'' + \delta v_{xc}(\boldsymbol{r}',\omega) \quad (2.68)$$

and the solution of these equations can be achieved by density matrix formulations as developed within the HF theory[276,277] which involves an iterative process. The LR function for a non-interacting system is expressed as follows:

$$\chi_{KS}(\boldsymbol{r},\boldsymbol{r}',\omega) = \sum_{a}^{n(occ)} \sum_{i>n}^{virt} n_a \phi_a(\boldsymbol{r})\phi_i(\boldsymbol{r})\phi_i(\boldsymbol{r}')\phi_a(\boldsymbol{r}') \left(\frac{1}{(\varepsilon_a - \varepsilon_i) + \omega} + \frac{1}{(\varepsilon_a - \varepsilon_i) - \omega} \right) \quad (2.69)$$

where ϕ_i is the i-th Kohn-Sham orbital of energy ε_i. The introduction of virtual orbitals leads to the inclusion of terms related to monoexcitations.[274]

2.7.3 Excitation energies

The perturbation of interest is an oscillating electric field with frequency ω, $|\mathbf{E}| = E_0 \cos(\omega t)$, since it reasonably describes the effect of the electromagnetic radiation of such a frequency. The first-order response of the molecular dipole moment to that perturbation is:

$$\boldsymbol{\mu} = \boldsymbol{\mu}_0 + \boldsymbol{\alpha}(\omega)\mathbf{E} \quad (2.70)$$

where $\boldsymbol{\mu}_0$ is the permanent molecular dipole moment and $\boldsymbol{\alpha}(\omega)$ is the frequency-dependent polarizability, which describes the response of the dipole moment to the electric field. Once obtained, the first-order response $\delta n(\mathbf{r},t)$ can be used to calculate the polarizability:

$$\alpha_{ij}(\omega) = -2 \int r_j \delta n(\boldsymbol{r},\omega)d\boldsymbol{r} \quad (2.71)$$

or well,

$$\alpha(\omega) = \sum_m \frac{f_m}{\omega_m^2 - \omega^2} \quad (2.72)$$

following divergences (poles) for the values of frequencies corresponding to the exact excitation energies (ω_m); therefore, the calculation of excitation energies can be done by means of the polarizability. The probability of transition is provided by the oscillator strength, f_m, which is calculated as:

$$f_m = \frac{2}{3}(\omega_m)[|\langle \Psi_0|x|\Psi_m\rangle|^2 + |\langle \Psi_0|y|\Psi_m\rangle|^2 + |\langle \Psi_0|z|\Psi_m\rangle|^2] \quad (2.73)$$

where x, y, and z are positional operators.[274,278]

2.8 Molecular dynamics

There are methods that provide a correct description of macroscopic systems, for which it is necessary to use a sufficiently large number of representative configurations of a potential energy surface. The two most common methods are the Monte-Carlo method and molecular dynamics (MD).[279–281] The Monte-Carlo method has two main advantages: it is computationally efficient, and it gives comparable results to the MD method for the calculation of thermodynamic properties in equilibrium. In fact, the Monte-Carlo method is also suitable to calculate properties of polymers in solution.[282] However, this method does not provide information of the velocities of the particles; therefore, dynamic properties cannot be obtained from it. In view of that, MD is the most widely used method in the study of a variety of systems.[283]

2.8.1 Equations of motion

Classical MD is based on the solution of the Newton's equations of motion for the trajectory of nuclei under an effective potential, $V_{eff}(R)$, caused by the electron cloud along with the interaction between nuclei. This potential is not necessarily described within a quantum-mechanical approach; in fact, it is usually calculated using low-cost computational techniques such as molecular mechanics (MM). However, for systems of large size, $V_{eff}(R)$ can be calculated by either *ab initio* or semiempirical methods; as a result, two approaches are distinguished: Born-Oppenheimer molecular dynamics (BOMD) and semiempirical Born-Oppenheimer molecular dynamics (SEBOMD). Quantum dynamics simulations are also possible; i.e. the TD Schrödinger equation is solved for the propagation of nuclear coordinates. Nevertheless, this latter is computationally too expensive even in systems of a few atoms. On the other hand, in some systems it is possible to use hybrid quantum-classical dynamics such as Ehrenfest dynamics.[283,284]

The Newton's second law of motion for an atom A is expressed as follows:

$$m_A \frac{d^2 r_A}{dt^2} = F_A \tag{2.74}$$

being m_A the mass of the particle and F_A the force resulting from all the interactions in which the atom A is involved; it can be also calculated as:

$$\frac{\partial E_{MM}}{\partial r_A} = F_A \tag{2.75}$$

wherein E_{MM} is the energy calculated by MM:

$$E_{MM} = E_{covalent} + E_{noncovalent} \tag{2.76}$$

$$E_{covalent} = E_{bond} + E_{angle} + E_{dihedral} \tag{2.77}$$

$$E_{noncovalent} = E_{electrostatic} + E_{Van\,der\,Waals} \tag{2.78}$$

2.8.2 Algorithms

Due to the couplings of the movements of all particles in the system, the equation 2.74 cannot be solved analytically. In view of that, numerical methods are used, which consist in the propagation of movements in accordance with this equation. The algorithm used must meet certain requirements; that is, it must be reversible in time and also the energy ought to be conserved. Algorithms are usually based on the so-called finite difference methods, which perform Taylor series expansions of the position as a function of the time as follows:

$$r_A(t + \Delta t) = r_A(t) + v_A(t)(\Delta t) + \frac{1}{2!}a_A(t)(\Delta t)^2 + \frac{1}{3!}\frac{d^3r(t)}{dt^3}\bigg|_t (\Delta t)^3 + \cdots \qquad (2.79)$$

The most common methods use developments of up to cubic order like the Verlet algorithm[285] and its derivatives such as the algorithms velocity-Verlet[286] and leap-frog.[287] They are mathematically equivalent, but they differ in accuracy and computational efficiency.

The leap-frog algorithm provides better accuracy than the original Verlet algorithm and is equivalent to the velocity-Verlet algorithm if a coupling of pressure or temperature is not included. With the leap-frog algorithm, the positions are calculated at each $t + \Delta t$ and velocities are computed in the middle of these intervals, $t + 0.5\Delta t$. The kinetic and potential energies are obtained at intervals differing in $0.5\Delta t$ ensuring small errors and better efficiency as compared to the velocity-Verlet algorithm (although this latter does provide direct positions and velocities at every step). The integration step (Δt) should be at least one order of magnitude less than the period of the most rapid movements occurring in the system, which are often molecular vibrations involving hydrogen atoms (t ~ 10 *fs*); therefore, $\Delta t = 1$ *fs* should be used in this example. In fact, 1-2 *fs* are usually used.[283,288]

2.8.3 Thermodynamic properties

The direct integration of the equations of motion generates paths where energy is conserved, thus resulting in a microcanonical ensemble, the *NVE* ensemble. Let us recall that an ensemble is a large collective of systems that, while differing in their microscopic description, is constructed to the bulk as a replica of the real thermodynamic system under study. Then, a system is defined by the number of particles (N), volume (V), and energy (E); magnitudes required to specify the thermodynamic state. The system therefore shall consist of a large number of systems, all of them with the same values *NVE*, and it must be compatible with the thermodynamic system under consideration. By making use of the averages measured in all the systems, a thermodynamic property $\langle A \rangle$ can be calculated such as the internal energy, entropy, among others. Particularly, the average value of a thermodynamic property is given by:

$$\langle A \rangle = \int \int A(\boldsymbol{r}, \boldsymbol{p}) \frac{e^{-E(r,p)/k_BT}}{\int \int e^{-E(r',p')/k_BT} dr' d\boldsymbol{p}'} d\boldsymbol{r} d\boldsymbol{p} = \lim_{t \to \infty} \frac{1}{t} \int_{t_0}^{t_0+t} A(\tau) d\tau \qquad (2.80)$$

$$P = \frac{e^{-E(r,p)/k_BT}}{\int \int e^{-E(r',p')/k_BT} dr' d\boldsymbol{p}'} \qquad (2.81)$$

here $\mathbf{r}$ and $\mathbf{p}$ respectively correspond to the position coordinates and velocities in the phase space; and P represents the probability of reaching a configuration. The last equality in equation 2.80 implies that all accessible microstates are equally probable over a long period of time; this last statement is known as the Ergodic hypothesis firstly formulated by Boltzmann.[289]

Although conceptually the microcanonical ensemble is accessible and simple, it is extremely difficult to experimentally achieve the necessary conditions to obtain the description of a system under this framework since the energy cannot be directly measured; as a result, to keep the energy as a constant turns out to be problematic. In view of that, experimental data are normally obtained by keeping constant the temperature; thus giving rise to the canonical ensemble or the *NVT* ensemble. In some cases, pressure is kept constant instead of volume, which results in the isothermal-isobaric ensemble or the *NPT* ensemble. Furthermore, during the simulation, it must be incorporated algorithms able to keep constant the temperature of the experiment and, if necessary, the pressure. With those algorithms, it should be possible to generate either a *NVT* or a *NPT* thermodynamic ensembles.[283,289]

2.9 Chemical reactivity with computational quantum methods

During a chemical reaction a rearrangement of molecular bonds occurs. The transition state theory encompasses the understanding of the reorganization of bonds leading to the prediction of the rate of chemical reactions. This theory assumes that the Born-Oppenheimer approximation is valid and the separation of nuclear and electronic movements is possible because they occur at very different time scales. In the conventional form, this theory is linked to the concept of transition state (TS) structure of a hypersurface of potential energy.[290]

McIver and Komornicki[291] define the structure of a TS as the point on a potential energy surface (PES), depicted in Figure 2.4, that meets the following conditions: (i) it is a stationary point; that is, the energy gradient at this point is zero; (ii) the matrix of force constants (the Hessian matrix) at such a point should have a single negative eigenvalue; and (iii) it should be the point of highest potential energy in a continuous line connecting reactants and products. The location of a TS is completely defined in the PES by the first and second derivatives of the energy with respect to coordinates.[235]
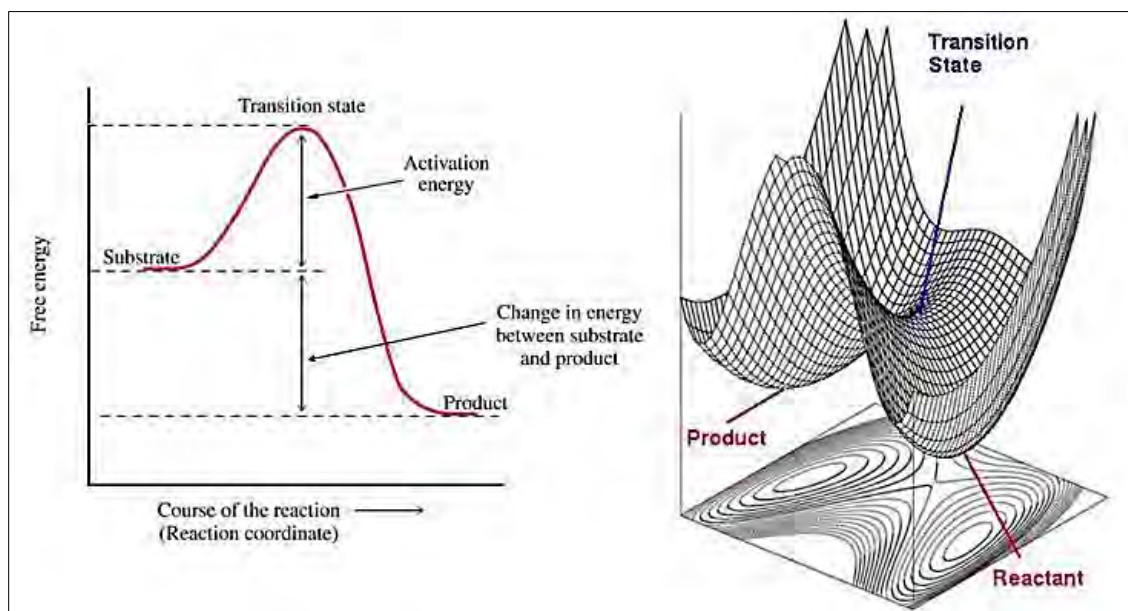
Figure 2.4 Schematic representation of a transition state in a one- (to the left), two- (to the right, at the bottom contour lines), and three-dimensional (to the right) potential energy surface.

In the case of a first-order saddle point, in the Hessian matrix one of the eigenvalues is negative and all the others are positive. Frequencies of harmonic molecular vibrations are related to the force constant matrix according to equation 2.82. The force acting on a harmonic spring depends on the mass m and the force constant k and it can be written as:

$$\vec{F} = m\vec{a} = m\frac{\overrightarrow{\partial^2 x}}{\partial t^2} = -k\vec{x} \tag{2.82}$$

This differential equation has only one periodic solution $x(\omega)$ with frequency ω:

$$\omega = \frac{1}{2\pi}\left(\frac{k}{m}\right)^{1/2} \tag{2.83}$$

Frequencies are related to the Hessian matrix because they are calculated with the mass-weighted eigenvalues f_{mw}^i to obtain frequency values ω_i and wave numbers $\widetilde{\omega_i}$:

$$\omega_i = \frac{\sqrt{f_{mw}^i}}{2\pi} \quad ; \quad \widetilde{\omega_i} = \frac{\sqrt{f_{mw}^i}}{2\pi c} \tag{2.84}$$

At a minimum, all force constants are strictly positive. In a TS, however, one constant force is negative, producing a complex number. Then the PES is defined in terms of minima such as reactants or reactant complexes, intermediates, products or product complexes, and maxima corresponding to saddle points; being the TS structure a first-order saddle point.[235,292]

2.9.1 Population analysis

The population analysis can be used to calculate partial charges of atoms by partitioning the electron density or otherwise the wavefunction in localized charges in nuclei, bond orders, among others. By making use of charge distributions, it can be estimated the fraction of charge in an atom as a function of the probability density. Particularly, the Mulliken population analysis[293] is based on orbital overlaps. In contrast, in the Hirshfeld and Voronoi deformation density (VDD) charge analysis, basis functions are not explicitly used, but the flow of electron density from or to an atom due to bond deformation is determined by spatial integration of the deformation density over the atomic Voronoi cell.[294] Besides, the natural population analysis (NPA) is useful to obtain occupation numbers and charges. Although MOs are not directly used, NPA uses natural orbitals, which are those eigenfunctions of the first-order reduced density matrix. These natural orbitals are localized and orthogonalized.[295–299]

Aspects in geometry such as hybridizations, coordinates, and bond orders have implications in the interactions of electrons with electrophilic species. For example, in the framework of molecular orbital theory, the estimation of the number of bonds between pairs of atoms in a molecule is done by the determination of the bond order, which is directly related to the bond length and energy. In general, a higher bond order corresponds to an increased energy and reduced length. It is also possible to observe a direct relationship with hybridization since the electron density is more approached to the nucleus as the *s*-orbital character in the hybrid orbital increases, therefore the electrons will be more strongly attracted.[239,240] Accordingly, the population analysis is a convenient tool in the prediction and description of chemical reactions.

2.9.2 Solvent effects

The most direct strategy to include the solvent at the quantum mechanical approach is to explicitly include a reduced set of solvent molecules in the system. This method has two main problems:

(i)   The size of the system is always too small to represent a real solvated medium.
(ii)   The computational cost can be enormous as the size of the system increases.

Some alternatives have been developed to properly include solvent effects; that is, classical particles can be used so that they can be sampled by MD or Monte-Carlo calculations.[281,283] Furthermore, macroscopic representations of solvents (continuum solvation models) can be also used.[300] These methods can reduce the degrees of freedom associated with the molecules of a solvent.

A continuum solvation model is, for instance, the conductor-like screening model (COSMO)[301] in which a cavity around the solute molecule is created and it interacts with the solvent represented by a dielectric (see Figure 2.5). The charge distribution of the solute polarizes the dielectric medium. The response of the dielectric medium is given by the

generation of point charges (polarization) on the surface of the cavity. In contrast to other implementations of continuum medium, in this model the generation of these point charges requires the solution of boundary conditions of the dielectric. For the generation of point charges, it is used the simpler boundary condition for the conductor, which depends on the dielectric constant ε_s of the solvent that is used. Accordingly, the polarizability of the continuum material is governed by ε_s.
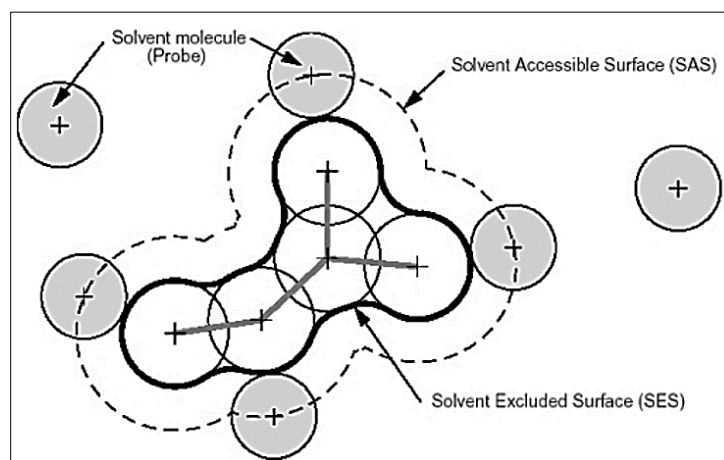
Figure 2.5 Schematic representation of a dielectric continuum solvation model. Figure adapted from original reference.[300]

In COSMO, if the solvent is an ideal conductor of the electrostatic potential, then it may be imposed the restriction that the electrostatic potential must be zero at the surface. As a result, it is less sensitive to the size and shape chosen for the cavity. If the charge distribution q on the solute molecule is known, it is possible to calculate the charge q^* on the surface. By using real solvents, it can be assumed that the charge q is a function of q^*:

$$q = f(\varepsilon_s)\, q^*$$
(2.85)

In turn, the factor $f(\varepsilon_s)$ is a function of the dielectric:

$$f(\varepsilon_s) = \frac{\varepsilon_s - 1}{\varepsilon_s - x}$$
(2.86)

wherein x can be either 0.0[302] or 0.5.[303] COSMO is more accurate for solvents having a high dielectric constant since a solvent with high values of ε_s behaves as an ideal conductor. However, in the current thesis not only COSMO was used but also the Polarizable Continuum Model[300] was another method to treat solvent effects.

2.9.3 The activation strain model

The understanding of chemical reactions and their associated barriers can be attained by the analysis of the reactive fragments participating in the formation or rupture of bonds. In the activation strain model (ASM), also known as distortion/interaction model,[304–306] the activation energy $\Delta E^{\ddagger}$ of the TS is given by two main contributions: the strain energy $\Delta E^{\ddagger}_{strain}$ and the interaction energy $\Delta E^{\ddagger}_{int}$:

$$\Delta E^{\ddagger} = \Delta E^{\ddagger}_{strain} + \Delta E^{\ddagger}_{int} \tag{2.87}$$

The energy required to deform reactants from their equilibrium geometry into the geometry they acquire in the activated complex is defined as the activation strain $\Delta E^{\ddagger}_{strain}$. If many reactants, $\Delta E^{\ddagger}_{strain}$ is given by the contribution of each deformed structure. The transition state interaction, $\Delta E^{\ddagger}_{int}$, is the interaction between the deformed reactants in the TS. The ASM is usually extended along the reaction coordinated ζ as $\Delta E^{\ddagger}$ by itself is meaningless. However, if the whole intrinsic reaction coordinate cannot be obtained, the application of the ASM analysis can be conveniently done only at local stationary points.[305,307–310]
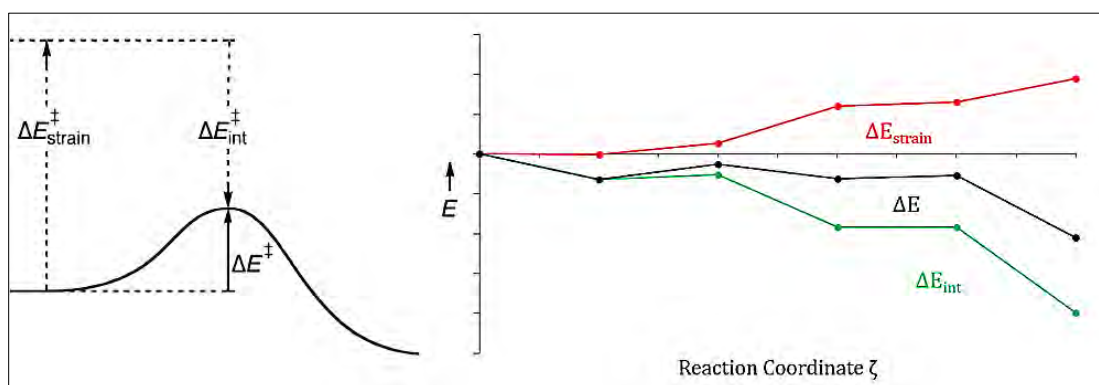
Figure 2.6 Illustration of the activation energy, $\Delta E^{\ddagger}$ to the left,
and the activation strain model along a reaction coordinate ζ, to the right.

The Electron Transfer Problem

One of the most important phenomena in chemistry, physics, and biology is known as the electron transfer problem.[311–316] That is, a number of processes involving isolated molecules and supermolecules, ions and excess of electrons in solution, surfaces and interfaces, condensed phase, and solar cells are related to non-radiative and radiative electron transfer (ET). In view of that, theoretical models describing ET have been developed; for instance, Franck and Libby established that the Franck-Condon principle is applicable not only to the vertical radiative processes but also to non-radiative horizontal ET.[317] Later, Marcus[318–322] and Hush and coworkers[323] expressed the need of a readjustment to the electron transfer problem by taking into consideration the coordination shells of reactants in self-exchange reactions and the dielectric medium. These authors demonstrated that a decrease in the energy barrier of a ET process is brought about by the interaction of reactants, which gives rise to the splitting at the intersection of potential surfaces.
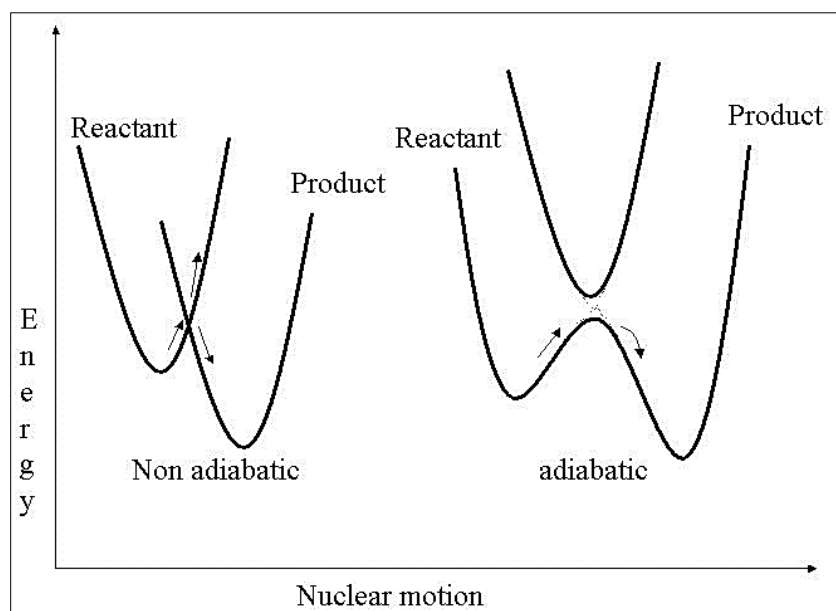
Figure 2.7 Potential energy diagrams of nonadiabatic
and adiabatic intersecting curves during electron transfer.

2.10 The Landau-Zener model

The nonadiabatic ET (see Figure 2.7) between the donor and acceptor centers is treated by the Fermi's golden rule:[324,325]

$$k_{et} = \frac{2\pi V_{ij}^2 FC}{\hbar} \tag{2.88}$$

where FC is the Franck-Condon factor which is the nuclear contribution to the transition probability. Given the overlap of the vibrational wavefunction in the ground and excited state, that is the overlap integral $S_{\sigma',\sigma}$, where σ' and σ respectively refer to the quantum numbers of the ground and excited states, the FC factor can be calculated as the square of nuclear overlap terms:

$$FC = \sum_{\sigma'}^{\infty} \sum_{\sigma}^{\infty} S_{\sigma',\sigma}^2 \tag{2.89}$$

On the other hand, V_{ij} represents the electronic contribution to the transition probability; it is an electronic coupling term (resonance integral) that depends upon the overlap of electronic wavefunctions in the initial and final states of the process. Furthermore, in the crossing area, the rate constant of the transition k_{tr} can be written in an Arrhenius-like expression which shall depend on the height of the energy barrier (activation energy, E_a), the frequency to reach the crossing area (ω), and the transition coefficient (A):

$$k_{tr} = A\omega e^{-E_a/RT} \tag{2.90}$$

The probability (P) that a transition in the crossing area will occur is determined by the Landau-Zener formula:[326,327]

$$P_{nonadiabatic} = exp\left[-\frac{2\pi V_{ij}^2}{\hbar v \frac{\partial}{\partial q}(E_i - E_j)} \right] \quad ; \quad P_{adiabatic} = 1 - P_{nonadiabatic} \tag{2.91}$$

here $\hbar$ is the reduced Planck constant; v is the Landau-Zener velocity associated to the nuclear motion given in terms of the perturbation variable q, dq/dt; and the force related to the movement of nuclei is given by the variation of the nonadiabatic crossing states E_i and E_j with respect to q at a certain value of the coordinate Q_{tr}. Equation (2.91) establishes that the ET can be governed by the overlap of electronic wavefunctions in the initial and final states so that V_{ij} determines the probability of transition. This equation highlights the important role of V_{ij} in the theory; that is to say, if this value is sufficiently high, then the terms are split with a decrease of the activation barrier and the process occurs adiabatically, $P_{adiabatic} \rightarrow 1$, since $P_{nonadiabatic} \rightarrow 0$. In the nonadiabatic case, $P_{nonadiabatic} > 0$, the interaction between the donor and acceptor in the region of the coordinate Q_{tr} is nearly negligible. Consequently, the terms practically do not split and $P_{adiabatic} \rightarrow 0$.

2.11 The Marcus model

In the Marcus model,[318,321,322,328] the deformation of the equilibrium geometry of reactants, products, and solvent is described by identical parabolas defined by the driving force of the process; that is, the standard Gibbs energy ΔG_0 (see Figure 2.8). Within the nonadiabatic regime, in the frame of the Eyring theory of the transition state, the electron transfer rate constant k_{et} is expressed as:

$$k_{et} = \frac{2\pi}{\hbar} V_{ij}^2 \frac{1}{\sqrt{4\pi\lambda k_B T}} exp\left[-\frac{(\lambda + \Delta G_0)^2}{4\lambda k_B T}\right] \tag{2.92}$$

where k_B is the Boltzmann constant, T the temperature, and λ is the reorganization energy defined as the energy required to conform bonding and solvent conditions from reactants to products. However, the Marcus equation has to meet some conditions:

    i)   All reactive nuclear modes such as local nuclear modes, solvent inertial polarization modes, and some other types of collective modes are purely classical. The electronic transition in the ET process is via the minimum energy at the crossing of the initial and final state potential surfaces.

    ii)   The potential surfaces are essentially parabolic surfaces with insignificant splitting at the crossing area.

    iii)   Vibrational frequencies and normal modes are the same in the initial and final states (quantum nuclear effects are not included, see Figure 2.9).
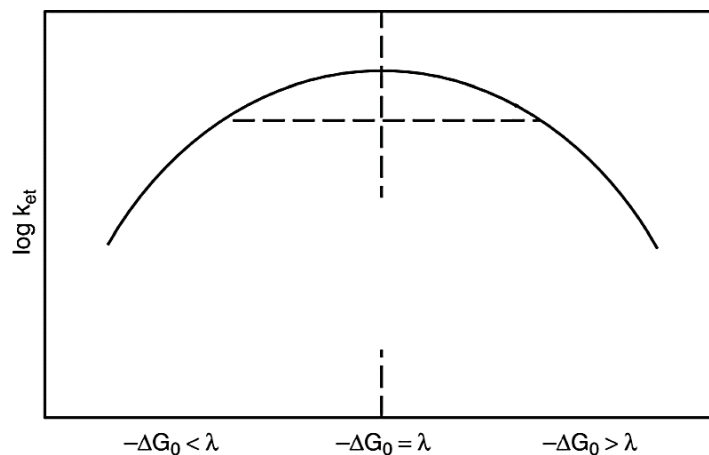
Figure 2.8 Marcus parabola: the driving force as a function
of the logarithm of the rate constant of electron transfer.

Experimental and theoretical approaches can be used to measure ΔG_0. For instance, given a fast solvation of photoinduced ET processes, ΔG_0 can be approximated as follows:

$$\Delta G_0 = E_{D/D^+} - \left(E_{A/A^-} + E_{D^*}\right) - \frac{e^2}{\varepsilon_s}(r_{D^+} + r_{A^-}) \tag{2.93}$$

where E_{D/D^+} and E_{A/A^-} are the standard redox potential of the donor and acceptor, respectively, E_{D^*} is the energy of the donor excited state, r_{D^+} and r_{A^-} are the radii of the donor and acceptor defined in a two-sphere model, and ε_s is the medium dielectric constant. In the following subsections, the inclusion of nuclear contributions and the assessment of V_{ij} and λ is reviewed.

2.12 Electronic and nuclear quantum mechanical effects

Levich et al.[329], utilizing the Landau-Zener theory for the intersection crossing area suggesting harmonic one-dimensional potential surface, proposed a formula that includes high-frequency modes (see Figure 2.9) in the low-temperature limit thus describing parabolic nonadiabatic ET:

$$k_{et} = \frac{2\pi}{\hbar} V_{ij}^2 \frac{1}{\sqrt{4\pi\lambda_{ext}k_BT}} \sum_j e^{-S} \frac{S^j}{j!} exp\left[-\frac{\left(j\hbar\omega_j + \lambda_{ext} + \Delta G_0\right)^2}{4\lambda_{ext}k_BT} \right] \tag{2.94}$$

where j is the number of high-frequency modes ω_j, λ_{ext} denote the external reorganization energy, and S is the Huang-Rhys factor which is a function of the nuclei coordinates.[330–334]
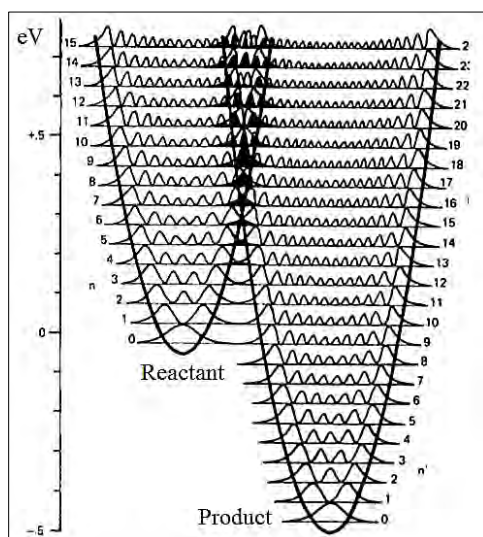
Figure 2.9 Schematic one-dimensional representation of the intersection between reactant and product vibrational levels. In this example, the optimal overlap of the initial vibrational level of the reactant is given at the 9th level of the product. Figure adapted from original references.[335,336]

In the case of thermal excitations of the local molecular medium, the inclusion of nuclear degrees of freedom resembles the normal region described by the classical Marcus model. On the other hand, significant deviations are expected in the inverted region. The inverted region cannot be experimentally observed if the stabilization of the ET product occurs faster than the equilibration of the solvent polarization. Moreover, when the ET reaction is very fast in the region of maximum rate (i.e. where $-\Delta G_0 = \lambda$), the process can be controlled by diffusion and, therefore, is no longer dependent on λ, V_{ij}, and ΔG_0.[336]

2.13 The electronic coupling

The estimation of V_{ij} can be done via several theoretical frameworks.[337–339] In some studies, the implications of using a particular level of theory,[340,341] basis set,[342] or methods are discussed in detail.[343] In this section the two-state model for the evaluation of V_{ij} is reviewed.

2.13.1 The Hamiltonian in two-state systems

Let us consider a physical system in which the state space is two-dimensional and assume that, if the system is not externally perturbed, then the Hamiltonian is $\widehat{H}_0$. The eigenstates of this Hamiltonian are $|\phi_1\rangle$ and $|\phi_2\rangle$, and the corresponding eigenvalues are E_1 and E_2; therefore:

$$\widehat{H}_0|\phi_1\rangle = E_1|\phi_1\rangle \ ; \ \ \widehat{H}_0|\phi_2\rangle = E_2|\phi_2\rangle \ ; \ \ \langle\phi_i|\phi_j\rangle = \delta_{ij} \tag{2.95}$$

An external TD perturbation shall disturb the system so that $\widehat{H} = \widehat{H}_0 + \widehat{W}$. In the $\{|\phi_1\rangle, |\phi_2\rangle\}$ basis $\widehat{W}$ is represented by the Hermitian matrix:

$$\mathbf{W} = \begin{pmatrix} W_{11} & W_{12} \\ W_{21} & W_{22} \end{pmatrix} \tag{2.96}$$

where W_{11} and W_{22} are real and $W_{12} = W_{21}{}^*$. Besides, in the same $\{|\phi_1\rangle, |\phi_2\rangle\}$ basis $\widehat{H}$ is represented by the matrix:

$$\mathbf{H} = \begin{pmatrix} E_1 + W_{11} & W_{12} \\ W_{21} & E_2 + W_{22} \end{pmatrix} \tag{2.97}$$

leading to the eigenvalues (denoted as $E_{\pm}$):

$$E_{\pm} = \frac{1}{2}(E_1 + W_{11} + E_2 + W_{22}) \pm \frac{1}{2}\sqrt{(E_1 + W_{11} - E_2 - W_{22})^2 + 4|W_{12}|^2} \tag{2.98}$$

and the eigenvectors:

$$|\Psi_+\rangle = \cos\left(\frac{\theta}{2}\right)\exp\left(-\frac{i\varphi}{2}\right)|\phi_1\rangle + \sin\left(\frac{\theta}{2}\right)\exp\left(\frac{i\varphi}{2}\right)|\phi_2\rangle \tag{2.99}$$

$$|\Psi_-\rangle = -\sin\left(\frac{\theta}{2}\right)\exp\left(-\frac{i\varphi}{2}\right)|\phi_1\rangle + \cos\left(\frac{\theta}{2}\right)\exp\left(\frac{i\varphi}{2}\right)|\phi_2\rangle \tag{2.100}$$

having $\tan(\theta) = 2|W_{12}|/(E_1 + W_{11} - E_2 - W_{22})$ and $W_{21} = |W_{12}|e^{i\varphi}$.

2.13.2 Two-state electronic couplings

The assessment of V_{ij} is usually performed by means of the two-state model described in the previous subsection; wherein the Hamiltonian can be written in two different representations:

$$H = \begin{pmatrix} E_i & V_{ij} \\ V_{ji} & E_j \end{pmatrix} \leftrightarrow \begin{pmatrix} E_1 & 0 \\ 0 & E_2 \end{pmatrix} \tag{2.101}$$

here the first matrix represents the charge-localized nonadiabatic states i and j, and the matrix to the right accounts for adiabatic eigenstates (recall that the Hamiltonian matrix is diagonal in the adiabatic representation). Following the definitions given in equations 2.97 and 2.98, the eigenstates E_1 and E_2 are:

$$E_{1,2} = \frac{1}{2}\left(E_i + E_j\right) \pm \frac{1}{2}\sqrt{\left(E_i - E_j\right)^2 + 4\left|V_{ij}\right|^2} \tag{2.102}$$

which explicitly displays the manner in which nonadiabatic quantities are related to adiabatic state information. The transition state in the ET problem must satisfy the resonant situation $E_i = E_j$; then, from equation 2.102, $|E_1 - E_2| = 2V_{ij}$.[340] In view of that, quantum chemistry codes or experimental data can provide the necessary information for the estimation of ET parameters in the nonadiabatic regime; in this case V_{ij}. As a matter of fact, in Table 2.1 the adiabatic representations of two-state quantum operators to evaluate V_{ij} in terms of the dipole moment and charge difference are provided. As a final point, the expected performance of a two-state model for the estimation of V_{ij} can be assessed, and even improved, by comparison with a three-state model as shown by Voityuk; then the two state model becomes less accurate with the increasing energy difference of the corresponding states.[344,345]

Table 2.1 Representation of two-state models for the evaluation of the electronic coupling.

Approach	Charge-localized states	Eigenstates	Electronic coupling
Generalized Mulliken-Hush[337,346]	$\begin{pmatrix} \mu_i & 0 \\ 0 & \mu_j \end{pmatrix}$	$\begin{pmatrix} \mu_1 & \mu_{12} \\ \mu_{12} & \mu_2 \end{pmatrix}$	$V_{ij} = \dfrac{\mu_{12}\Delta E_{12}}{\sqrt{(\mu_1 - \mu_2)^2 + 4\mu_{12}^2}}$
Fragment charge difference[347]	$\begin{pmatrix} \Delta q_i & 0 \\ 0 & \Delta q_j \end{pmatrix}$	$\begin{pmatrix} \Delta q_1 & \Delta q_{12} \\ \Delta q_{12} & \Delta q_2 \end{pmatrix}$	$V_{ij} = \dfrac{\Delta q_{12}\Delta E_{12}}{\sqrt{(\Delta q_1 - \Delta q_2)^2 + 4\Delta q_{12}^2}}$

2.14 The reorganization energy

The total reorganization energy λ is usually decomposed into two terms, the internal reorganization energy λ_{int} and the external reorganization energy λ_{ext}, so that $\lambda = \lambda_{int} + \lambda_{ext}$.[336] In Figure 2.10, the schematization of the ET parameters involved in the evaluation of k_{et} is depicted in detail.
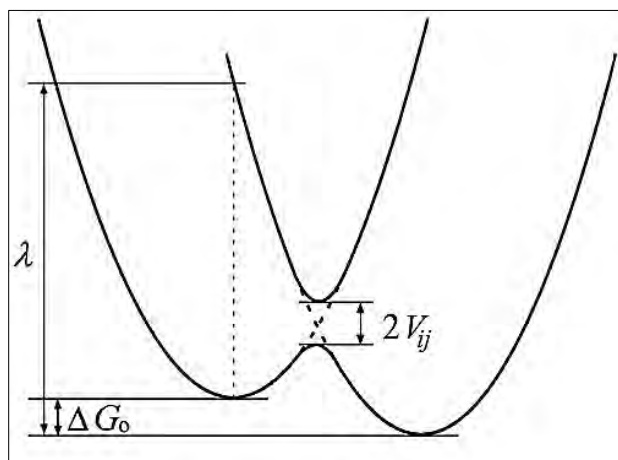
Figure 2.10 Energy diagram for electron transfer including electronic coupling, reorganization, and Gibbs energies.

Internal reorganization energy, λ_{int}. The energy required to rearrange all the nuclei of the system due to a charge transfer (CT) reaction leading from a neutral state to a charge transfer state (CTS, an electric-charged exciton state characterized by the physical separation of charges between two moieties often identified as the donor and acceptor fragments) is computed as follows:

$$\lambda_{int} = \frac{1}{2}(E'_n - E_n + E'_{CTS} - E_{CTS}) \tag{2.103}$$

where $E_{n(CTS)}$ is the energy of the neutral (CTS) state computed in the equilibrium geometry of the neutral (CTS) state and $E'_{n(CTs)}$ is the energy of the neutral (CTS) state computed in the equilibrium geometry of the CTS (neutral state). Nevertheless, λ_{int} can be also calculated by considering isolated donor and acceptor fragments as a separated contribution to the internal organization of each fragment:

$$\lambda_{int} = \lambda_D + \lambda_A \tag{2.104}$$

$$\lambda_{D(A)} = \frac{1}{2}(E'_n - E_n + E'_{ion} - E_{ion}) \tag{2.105}$$

where $\lambda_{D(A)}$ is the reorganization energy of either the donor or the acceptor. $E_{n(ion)}$ is the energy of the neutral (ionic) state computed in the equilibrium geometry of the neutral (ionic) state; and $E'_{n(ion)}$ is the energy of the neutral (ionic) state computed in the equilibrium geometry of the ionic (neutral) state.

External reorganization energy, λ_{ext}. Changes in solvent polarization is one of the parameters that introduces more uncertainty to the estimation of k_{ct}. Some authors set the value of λ_{ext} as an adjustable parameter.[348,349] On the other hand, the direct evaluation of λ_{ext} can be consistently performed via QM/MM[350] or a polarizable force field.[351] Furthermore, in some cases, neither implicit nor explicit solvent models are sufficient enough to reproduce experimental observations and, therefore, different results might be expected.[352] In the current manuscript, three different approaches were used for the estimation of λ_{ext}:

(i) Two-sphere Marcus model, λ_{ext} (M)[318,320,321]

$$\lambda_{ext}(M) = \frac{1}{4\pi\varepsilon_0} \Delta e^2 \left(\frac{1}{2a_1} + \frac{1}{2a_2} - \frac{1}{R} \right) \left(\frac{1}{\varepsilon_{OP}} - \frac{1}{\varepsilon_s} \right) \tag{2.106}$$

where ε_o and Δe are respectively the vacuum permittivity and the amount of transferred charge; a_1, a_2, and R are respectively the donor and acceptor sphere radii and the distance between the sphere centers; and ε_{OP} and ε_s are the optical and zero-frequency dielectric constants of the surrounding media.[245]

(ii) Non-equilibrium versus equilibrium solvation, $\lambda_{ext}(E_{noneq}\text{-}E_{eq})$

The difference between non-equilibrium and equilibrium solvation naturally arises from excited state calculations in solution. That is to say, a very fast process occurs when the solvent polarizes its electron distribution (electronic polarization); but the solvent may be reoriented (dipole polarization; e.g. rotation), which is a much slower process. If the solvent does not have enough time to fully respond, like in a vertical electronic excitation, then the situation is described by non-equilibrium solvation (E_{noneq}). In contrast, if the solvent does have enough time to fully respond to the solute in both ways (electronic and dipole polarizations) then the situation is described by equilibrium solvation (E_{eq}). Accordingly, λ_{ext} is simply the energy difference between E_{noneq} and E_{eq}.[245]

(iii) Dynamic polarization response, $\lambda_{ext}(E_{noneq}(\omega)\text{-}E_{eq})$

In this approach, E_{eq} is exactly the same as explained in (ii); that is, the time or frequency (ω) to reach E_{eq} is such that the electronic and dipole polarizations can be completed. In this regard, molecular movements depend upon ω of the change of direction of the electric field; in fact, as ω increases the dipole polarization effect tends to vanish and ε_s shall be only dependent on the electronic polarization, as a result the non-equilibrium effects shall appear subsequently in the different contributions to the polarization (i.e. orientational, atomic, and electronic polarization). In the case of photon absorption or emission involving electronic transitions, the solute electronic polarization changes so quickly that one can assume $\varepsilon_s = \varepsilon_{OP} = n^2$ (refractive index). Therefore, only solvent electrons are able to rearrange in order to stay in equilibrium with the solute, while solvent molecular motions are frozen during the process. This situation leads to a non-equilibrium solvation, $E_{noneq}(\omega)$. Then λ_{ext} is simply the energy difference between $E_{noneq}(\omega)$ and E_{eq}.[245,300,353]

2.15 Electron transfer in polyaromatic organic compounds via quantum chemistry methods

Quantum chemistry methods used for the description of phenomena related to the ET problem in polyaromatic organic compounds have been applied at different levels of theory and approaches. For instance, Friend et al.[354] examined the amount of charge delocalization upon IR absorption for a set of donor-acceptor organic semiconductors, including fullerene derivatives, as computed via the Austin model 1[355] (AM1) method coupled to a single configuration interaction (SCI) scheme. In a second step of their study they determined CTS with the intermediate neglect of differential overlap[356] (INDO) method coupled to SCI (active space of 100 occupied and 100 unoccupied molecular orbitals) in presence of a static electric field. Furthermore, Brédas et al.[357] developed a computational method to evaluate V_{ij} between intramolecular excited states and CTS in the phthalocyanine/perylene-tetracarboxylic-diimide donor-acceptor complex. They computed ground and excited states through the Zerner's INDO[358] Hamiltonian coupled to a configuration interaction scheme involving single and double electronic excitations (CISD); although they used the same HF orbital basis set to compute the electronic states of both neutral and charged configurations, thus resulting in a reduced computational cost. Moreover, in the phthalocyanine/perylene donor-acceptor complex, Cornil et al.[359] analyzed the different parameters affecting k_{et} at different levels of theory such as the AM1 method coupled to a full configuration interaction (FCI) scheme within an active space built from a few frontier electronic levels for the calculation of ΔG of reactions, AM1/CI for λ_{int}, and INDO/SCI for V_{ij}.

There are also investigations in the field of fullerenes based on Kohn-Sham DFT. For instance, Kanai and Grossman carried out DFT calculations with the aim of studying the electronic structure of the poly(3-hexylthiophene) (P3HT)/C_{60} interface; looking mostly at the extension of electronic excited states and the relative orbital energy alignment.[360] On the other hand, it has been proposed that excitation energies for CTS may be computed through the constrained density functional theory[361] (C-DFT), wherein charges $+1e^-$ and $-1e^-$ are respectively restricted to the donor and acceptor moieties so that a self-consistent field solution is searched. Within this framework, Difley and Voorhis determined CTS in two organic heterodimers.[362] Moreover, Troisi et al. studied the electronic structure and the different parameters affecting k_{et} for several structures of the P3HT/phenyl-C_{61}-butyric acid methyl ester (PCBM) interface as computed by unrestricted DFT combined with MD simulations.[363] TD-DFT has been also another useful tool in the research of the ET problem; for example, Nelson et al.[364] studied the influence of the chemical structure on excitation energies, oscillator strengths, and electronic structure for a series of oligomer-fullerene blends.

Chapter 3

Objectives

The main goals to be achieved in the current thesis by means of restricted, unrestricted, and/or time-dependent density functional methodology are highlighted as follows:

1. Exploration of the chemo- and regioselectivity of a series of cycloaddition reactions to carbon nanostructures. Particularly, the Bingel-Hirsch addition of dimethyl bromomalonate to the endohedral metallofullerene La@C_{2v}-C_{82} results in a relevant (2+1) cycloaddition reaction due to the paramagnetic nature and the many nonequivalent carbon atoms in this nanostructure. The target is to reach a complete study through the all 65 possible mechanistic pathways, which are originated from the combination of 24 nonequivalent carbon atoms and 35 different bonds present in the cage, so as to describe the thermodynamics and kinetics of the reactions under consideration. In view of that, the characterization of the experimentally observed but hitherto unidentified Bingel-Hirsch adducts is the main goal to achieve. After that, the (4+2) (1,4-addition) and (2+2) (1,2-addition) cycloadditions of benzyne to a series of carbon nanostructures are also investigated. The objective is the determination of the thermodynamics and kinetics of these cycloaddition reactions in order to characterize the cycloadducts formed in fullerene C_{60} and several zig-zag single-walled carbon nanotubes with chiral indices (8,0), (9,0), (12,0), (13,0), and (18,0). The study encompasses an analysis of the effect of the curvature, a compilation of other experimental and theoretical results accounting for the (4+2) and (2+2) cycloadditions of benzyne to endohedral metallofullerenes and a series of armchair single-walled carbon nanotubes, and also an examination of the structural deformation and interaction of reactants at stationary structures through the reaction coordinate with the aim of reporting a complete, consistent exploration of these reactions in carbon nanostructures.

2. Evaluation of chemical reactions catalyzed by transition metal complexes in which fullerene C_{60} is involved. In this regard, two studies were developed with the purpose of describing the thermodynamics and kinetics of chemical reactions with C_{60} as well as the role of the catalysts. In the first study, the main target is the formulation of a Suzuki-Miyaura-like reaction mechanism for the hydroarylation of C_{60} with organoboron compounds catalyzed by a rhodium complex in the presence of water. The study is focused on the determination of the fundamental role of water and the catalyst through the reaction with the intention of explaining experimental observations. In the second study, olefin metathesis catalyzed by ruthenium

complexes containing N-heterocyclic carbenes and C_{60} is reported. The goal is the elucidation of the influence of C_{60} in the catalyst synthetized *in silico* which is evaluated from several frameworks such as energetics, steric impediment, amphoteric behavior, and conceptual theory (electrophilicity). Therefore, this theoretical study is aimed at the promotion of a new family of ruthenium-based fullerene catalysts.

3. Investigation of charge transfer events that can occur in a donor-acceptor conjugate containing a fullerene moiety with the objective of identifying its potential applications in solar energy conversion. By making use of time-dependent density functional methodology combined with molecular dynamics, the main purpose is the description of stable bound exciton states susceptible to be accessed by either light absorption or dissociation of less-stable exciton states in the triphenylamine-C_{60} donor-acceptor conjugate. The picture generated by detailed information of exciton states with neutral, partial charge transfer, or strong charge transfer character is used to evaluate electron transfer parameters according to the photoinduced charge transfer reactions occurring in the donor-acceptor conjugate under study. All the information collected in this study is focused on the estimation of rate constants of photoinduced charge separation and charge recombination reactions, which provide the evidence required to assess the potential of fullerenes as promising materials in the construction of organic dye-sensitized solar cells.

The objectives exposed above are directed at the characterization and *in silico* synthesis of interesting adducts produced via (metal-catalyzed) chemical reactions involving carbon nanostructures, and their potential applications in the design of organic photovoltaic devices.

Chapter 4

Cycloaddition Reactions to

Carbon Nanostructures

4.1 Reaction Mechanism and Regioselectivity of the Bingel-Hirsch Addition of Dimethyl Bromomalonate to La@C_{2v}-C$_{82}$
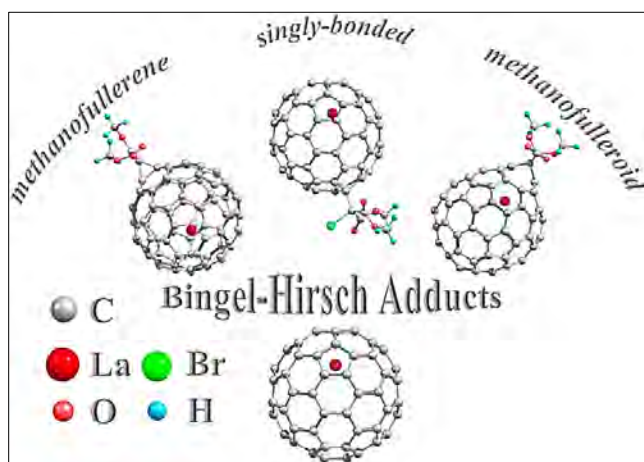
J.P.M. participated in the design of the project, performed all the calculations, analyzed the results, and co-wrote the manuscript.

Bingel–Hirsch Reactions

Reaction Mechanism and Regioselectivity of the Bingel–Hirsch Addition of Dimethyl Bromomalonate to La@C_{2v}-C_{82}

Juan Pablo Martínez,[a] Marc Garcia-Borràs,[a] Sílvia Osuna,[a] Jordi Poater,[b, c, d] F. Matthias Bickelhaupt,*[b, e] and Miquel Solà*[a]

Abstract: We quantum chemically explore the thermodynamics and kinetics of all 65 possible mechanistic pathways of the Bingel–Hirsch addition of dimethyl bromomalonate to the endohedral metallofullerene La@C_{2v}-C_{82} that result from the combination of 24 nonequivalent carbon atoms and 35 different bonds present in La@C_{2v}-C_{82} by using dispersion-corrected DFT calculations. Experimentally, this reaction leads to four singly bonded derivatives and one fulleroid adduct. Of these five products, only the singly bonded deriv-ative on C23 could be experimentally identified unambiguously. Our calculations show that La@C_{2v}-C_{82} is not particularly regioselective under Bingel–Hirsch conditions. From the obtained results, however, it is possible to make a tentative assignment of the products observed experimentally. We propose that the observed fulleroid adduct results from the attack at bond 19 and that the singly bonded derivatives correspond to the C2, C19, C21, and C23 initial attacks. However, other possibilities cannot be ruled out completely.

1. Introduction

The encapsulation of metallic clusters into fullerene cages led to the discovery of endohedral metallofullerenes (EMFs),[1–7] materials with a large number of promising applications in the fields of biosciences as biocides,[8] medical sciences as photoactive nanoparticles with uses in radiotherapy,[9] molecular electronics as molecular switching devices,[10] and photovoltaics as charge carriers in dye-sensitized solar cells.[11]

Motivated by the first detection of La@C_{60}, Smalley and co-workers[12] were able to produce macroscopic quantities of higher fullerenes with La inside the cage, including La@C_{82}. There are nine distinct isomers of C_{82} satisfying the so-called isolated pentagon rule (IPR).[13–15] Of these nine cages, La as a single metal has been incarcerated into the C_{2v}-C_{82} and C_s-C_{82} IPR cages.[16] None of these isomers is the most stable for the empty C_{82} fullerene. The La@C_{2v}-C_{82} EMF, which in the case of Ce@C_{2v}-C_{82} is approximately four times more abundant than the analogous C_s-C_{82},[17] has been the subject of many studies.[18–20] For example, the first EMF functionalization was achieved for La@C_{2v}-C_{82} through a photochemical reaction with disilirane.[21]

The electronic and structural properties of the La@C_{2v}-C_{82} cage have been studied already. According to the ionic model,[22–25] charge transfer from the La atom to the fullerene cage occurs, and as a result, the formal electronic structure of La@C_{2v}-C_{82} is described as La^{3+}@C_{2v}-C_{82}^{3-}, with a number of unpaired electrons located on the fullerene cage. In this regard, La@C_{2v}-C_{82} has the capability to easily donate, and in turn, accept electrons owing to its radical nature and redox properties, unlike its pristine counterpart C_{2v}-C_{82}. Consequently, the high electron affinity and low ionization potential of amphoteric species such as La@C_{2v}-C_{82} are useful for controlling the chemical reactivity toward nucleophiles and electrophiles.[26] Additionally, the permanent magnetic moment of La@C_{2v}-C_{82} obstructs the direct application of nuclear magnetic resonance (NMR) analysis; therefore, the corresponding spectrum is obtained from La@C_{2v}-C_{82}^-, taking advantage of its uncommon stability.[27] The ^{13}C NMR spectrum of La@C_{2v}-C_{82}^- shows 24 different lines corresponding to 24 nonequivalent carbon atoms. In line with these results, by using synchrotron powder diffraction, the maximum entropy method (MEM)/Rietveld analysis revealed that the La atom is not localized at the center of the C_2 axis, but is adjacent to a six-membered ring (6-MR) of the La@C_{2v}-C_{82} cage, with the shortest La–C distance determined to be 2.55 Å.[28] Lastly, by considering the symmetry of La@C_{2v}-

[a] J. P. Martínez, Dr. M. Garcia-Borràs, Dr. S. Osuna, Prof. Dr. M. Solà
Institut de Química Computacional i Catàlisi and Departament de Química
Universitat de Girona, Campus de Montilivi
17071 Girona, Catalonia (Spain)
E-mail: Miquel.Sola@udg.edu

[b] Dr. J. Poater, Prof. Dr. F. M. Bickelhaupt
Department of Theoretical Chemistry and
Amsterdam Center for Multiscale Modeling, Vrije Universiteit Amsterdam
De Boelelaan 1083, 1081 HV Amsterdam (The Netherlands)
E-mail: F.M.Bickelhaupt@vu.nl

[c] Dr. J. Poater
Departament de Química Orgànica & IQTCUB, Universitat de Barcelona
Martí i Franquès 1-11, 08028 Barcelona, Catalonia (Spain)

[d] Dr. J. Poater
Institució Catalana de Recerca i Estudis Avançats (ICREA)
Pg. Lluís Companys 23, 08010 Barcelona, Catalonia (Spain)

[e] Prof. Dr. F. M. Bickelhaupt
Radboud University Nijmegen, Institute for Molecules and Materials
Heyendaalseweg 135, 6525 AJ Nijmegen (The Netherlands)

Supporting information and ORCID from the author for this article are available on the WWW under http://dx.doi.org/10.1002/chem.201504668.

C_{82}, it is possible to differentiate 19 [6,6] and 16 [5,6] different bonds (see Scheme 1a).

Chemical functionalization of EMFs[5,6] is commonly achieved through cycloaddition reactions, the most important being: Diels–Alder,[18,29] 1,3-dipolar (or Prato),[30] and nucleophilic [2+1] Bingel–Hirsch (BH) additions.[31–33] The BH addition is a cyclopropanation reaction in which a fullerene and diethyl bromomalonate react in the presence of a strong base such as 1,8-diazabicycloundec-7-ene (DBU) or sodium hydride to produce a methanofullerene or a fulleroid.[34] In the first step of the mechanism, the base abstracts the acidic proton of the malonate derivative to generate a carbanion or enolate. Then, this carbanion attacks the fullerene nucleophilically, thus generating a new carbanion with charge localized at the cage. In the final step, bromide is displaced in a nucleophilic substitution S_N2 reaction, causing an intramolecular three-membered ring closure. Scheme 1b illustrates the mechanism of the BH reaction in La@C_{2v}-C_{82}, in which we have introduced the nomenclature used throughout the manuscript. Accordingly, the

initial attack on bond γ formed between adjacent carbon atoms Cα and Cβ leads to the formation of a singly bonded derivative, which is labeled as the intermediate structure, either $I_{C\alpha,\gamma}$ or $I_{C\beta,\gamma}$, followed by the corresponding transition-state structure, either $TS_{C\alpha,\gamma}$ or $TS_{C\beta,\gamma}$, leading to the formation of a closed-cage Bingel product methanofullerene *$P_{C\alpha C\beta,\gamma}$ or an open-cage fulleroid $P_{C\alpha C\beta,\gamma}$. Moreover, as there are 19 [6,6] and 16 [5,6] different bonds in La@C_{2v}-C_{82}, γ can take 35 different values; on the other hand, there are 24 different values for either Cα or Cβ because of the 24 nonequivalent carbon atoms forming the cage.

The first successful functionalization of EMFs through the BH reaction was achieved by Alford and co-workers, wherein Gd@C_{60}[C(COOC$_2$H$_5$)]$_n$ ($n=1$–10) was the main product.[35] Application of the same procedure to ^{212}Pb@C_{60} led to the formation of ^{212}Pb@C_{60}[C(CO$_2$H)$_2$]$_x$.[36] In 2005, Echegoyen et al.[37] reported the selective BH formation of Y$_3$N@I_h-C_{80} and Er$_3$N@I_h-C_{80} [6,6] monoadducts under mild conditions.[38] In some cases, [6,6] products could be further converted to [5,6] adducts by heating. The same authors also noticed that the BH reaction did not occur in Sc$_3$N@I_h-C_{80} and Lu$_3$N@I_h-C_{80} under the same reaction conditions.[37] The X-ray structure of Y$_3$N@I_h-C_{80}[C(CO$_2$CH$_2$Ph)$_2$] confirmed that the BH monoadduct was the result of the attack on a [6,6] bond that led to the formation of a fulleroid structure with one of the Y atoms pointing directly to the attacked open bond.[39] DFT calculations indicated that the open [6,6] adduct is more stable than the closed one, and that the rotation of the metallic cluster inside the cage is partially hindered once the adduct is formed.[39] Later, in 2010, Echegoyen and co-workers reported that Sc$_3$N@I_h-C_{80} and Lu$_3$N@I_h-C_{80} can undergo BH additions to yield open [6,6] adducts by changing the common BH reaction conditions. NaH was used as the base and a 4:1 mixture of o-DCB and N,N-dimethylformamide as the solvent.[40] Interestingly, the BH reaction of TiSc$_2$N@I_h-C_{80} afforded two unconventional singly bonded monoadducts, revealing a change in the addition pattern and an improved reactivity of TiSc$_2$N@I_h-C_{80} compared with that of Sc$_3$N@I_h-C_{80}.[41] A study of the BH reactions of Gd$_3$N@C_{80}, Gd$_3$N@C_{84}, and Gd$_3$N@C_{88} performed by Echegoyen et al. led to the conclusion that the EMF reactivity is reduced as the size of the fullerene cage increases.[42] BH additions to non-IPR cages have been achieved experimentally for Sc$_3$N@D_3(6140)-C_{68},[43] Gd$_3$N@C_s(39663)-C_{82}, and Gd$_3$N@C_s(51365)-C_{84} EMFs.[42,44] For the former, according to theoretical studies[45] and experiments,[43] the addition takes place at a [6,6] bond close to a [5,5] bond and to the Sc atom. For the other systems,[42,44] the BH addition occurs on a [5,6] bond adjacent to the unique [5,5] bond. Unexpectedly, the addition never occurs on the a priori more reactive [5,5] bond. This result was attributed to the larger aromaticity of the adducts of the [6,6] and [5,6] additions to the Sc$_3$N@D_3(6140)-C_{68} and Gd$_3$N@C_s(51365)-C_{84} EMFs, respectively.[46] It is worth mentioning that theoretical studies of the reaction mechanism of BH additions to Sc$_3$N@I_h-C_{80} and Sc$_3$N@D_3(6140)-C_{68}[45] and to Y$_3$N@C_s(39663)-C_{82} and Y$_3$N@C_s(51365)-C_{84}[47] were performed by Poblet and co-workers. Their results show that the BH thermodynamic and kinetic products do not coincide, with the kineti-

Scheme 1. a) The 24 nonequivalent carbon atoms and the 35 different bonds of La@C_{2v}-C_{82}. For bonds, numbers denote [6,6] bonds and lower-case letters denote [5,6] bonds. Bond types are distinguished by color code (type A: blue; type B: black; type C: green; type D: red). Labels as assigned in a previous study.[18] b) General mechanism of the nucleophilic [2+1] Bingel–Hirsch reaction in La@C_{2v}-C_{82}. Nomenclature used in the current work is also provided. The attack on a bond γ formed between adjacent carbon atoms Cα and Cβ leads to the formation of an intermediate, either $I_{C\alpha,\gamma}$ or $I_{C\beta,\gamma}$, proceeding to the respective transition state, either $TS_{C\alpha,\gamma}$ or $TS_{C\beta,\gamma}$, which leads to the formation of a methanofullerene *$P_{C\alpha C\beta,\gamma}$ or fulleroid $P_{C\alpha C\beta,\gamma}$.

cally controlled product being the one observed under experimental conditions. Very recently, in collaboration with Echegoyen's group, some of us studied experimentally and theoretically the BH addition to Sc₃N@D_{5h}-C_{80}.[48] Our results showed that the addition takes place under kinetic control in a [6,6] bond, and confirmed that the most stable thermodynamic and kinetic products differ.

The BH addition to La@C_{2v}-C_{82} was explored experimentally by Nagase, Akasaka, and co-workers,[20,49,50] using diethyl bromomalonate as a reactant. The BH reaction was monitored by multistage high-performance liquid chromatography (HPLC), which allowed the isolation of different monoadducts. They were able to isolate four ESR-inactive adducts, which were assigned to singly bonded products, and one ESR-active species, which was considered to be a BH adduct. X-ray crystallographic analysis of one ESR-inactive product confirmed a singly bonded derivative of La@C_{2v}-C_{82}, corresponding to an oxidized BH intermediate formed at the C23 position (see Scheme 1a). Moreover, upon heating to 80 °C in anhydrous o-dichlorobenzene (o-DCB), all the synthesized singly bonded products decompose to give the parent La@C_{2v}-C_{82} as the major product. On the contrary, the BH product showed higher thermal stability. On the basis that a more positively charged carbon atom could be a more favored reaction site toward a nucleophilic attack, the authors proposed C18, C14, and C21 as the possible addition sites for the three unknown ESR-inactive products. The authors based their estimations on Mulliken charge distribution analysis as determined by DFT calculations.[49]

We consider that the theoretical study of the BH addition to La@C_{2v}-C_{82} is timely and relevant for three main reasons: 1) the relatively high abundance of La@C_{82} among endohedral monometallofullerenes makes the reactivity of this EMF one of the most studied (albeit not yet fully understood); 2) the radical character of the fullerenic cage in La@C_{2v}-C_{82} means an unconventional reaction mechanism for the BH addition to La@C_{2v}-C_{82} can be expected (this is confirmed by the presence of singly bonded derivatives in the observed products); and 3) experiments were unable to identify definitively all adducts generated in the BH addition to La@C_{2v}-C_{82}. In this contribution, we have performed an extensive quantum chemical (DFT) exploration of the various mechanistic pathways of the BH reaction between the anion dimethyl bromomalonate (dmbm⁻) and La@C_{2v}-C_{82} through different reaction sites with two main objectives: 1) to determine the reaction mechanisms of the different reaction pathways; and 2) to evaluate the regioselectivity of the BH reaction of dmbm⁻ to La@C_{2v}-C_{82} to provide a comprehensive description of the preference of different positions to react. For the particular case of the Diels–Alder reaction of (1,2,3,4,5-pentamethyl)cyclopentadiene to La@C_{2v}-C_{82},[51] some of us[18] demonstrated by means of DFT calculations that this cycloaddition occurs regioselectively at bond o (shown in Scheme 1a), which corresponds to both the thermodynamically and kinetically most favored attack, independently of the diene used for the reaction. We anticipate here that our results will show that the BH reaction of dmbm⁻ to La@C_{2v}-C_{82} is not as regioselective as the Diels–Alder reaction.

2. Computational Details

All DFT calculations were performed by using the Amsterdam Density Functional (ADF) program.[52] An uncontracted set of Slater-type orbitals (STOs) of double-ζ (DZP) and triple-ζ (TZP) quality containing diffuse functions and one set of polarization functions were used to expand the molecular orbitals (MOs). The frozen-core approximation (FCA)[52] was employed during the SCF procedure for the core orbitals of C, O, and La (1s for C and O and 1s2s2p3s3p4s3d4p for La). It was shown that the FCA has a negligible effect on the optimized geometries.[53,54] Scalar relativistic corrections were included self-consistently by using the Zeroth Order Regular Approximation (ZORA).[55] The local density approximation (Slater exchange) with nonlocal corrections for exchange (Becke88)[56] and correlation (Perdew86)[57] (i.e., the BP86 functional) were used to calculate energies and gradients self-consistently. Although it is well documented that standard DFT functionals such as BP86 underestimate energy barriers,[58] this underestimation should be similar for all the BH transition states we encounter here, and should not affect the main conclusions. Calculations were executed under the unrestricted formalism. Moreover, dispersion energy corrections as developed by Grimme et al.,[59,60] including the so-called Becke and Johnson damping (D3-BJ), were added in the calculation of DFT energies and gradients. It has been shown that dispersion corrections are essential for a correct description of the thermodynamics and kinetics of reactions with fullerenes, nanotubes, and other systems and reactions involving nonrepulsive steric contact.[61] Geometry optimizations were performed without symmetry constraints in the gas phase. All stationary points were characterized by analytical frequency calculations. Electronic energies were obtained in solution with the TZP basis set by single-point energy calculations at the geometries optimized with the DZP basis (i.e., BP86-D3(BJ)/TZP//BP86-D3(BJ)/DZP). Solvent effects were introduced using the COnductor-like Screening MOdel (COSMO)[62] as implemented in ADF, performing single-point energy calculations on the gas-phase optimized structures and using toluene as a solvent. In Tables S1 and S2 (Supporting Information) we show that the gas-phase geometry is practically identical to the geometry optimized under the implicit presence of toluene. In the search for minima and first-order saddle points, the QUILD code (QUantum regions Interconnected by Local Descriptors)[63] was used. QUILD works as a wrapper around the ADF program; it creates input files for ADF, then executes this program and collects energies and gradients. QUILD uses adapted delocalized coordinates and constructs model Hessians with the appropriate number of eigenvalues.[64] This latter feature is particularly useful in the search for transition-state structures. Gibbs energies in solution (G_{tol}) were calculated from electronic energies at the (COSMO:Toluene)BP86-D3(BJ)/TZP//BP86-D3(BJ)/DZP level of theory. Corrections by zero-point energies, thermal contributions to the internal energy, and the entropy term were determined in the gas phase at the BP86-D3(BJ)/DZP level of theory using the statistical thermodynamics expressions of an ideal gas under standard conditions at 298 K. Lastly, to account for the condition change from 1 atm to 1 M concentration related to the phase change from gas to solution, we added to the G_{tol} values a concentration correction of 1.89 kcal mol⁻¹.[65–67]

3. Results and Discussion

This section is divided as follows. First, the 65 possible reaction pathways are defined to introduce the reader to the many different stationary points. Then, on the basis of a complete ther-

modynamic study of the system, a classification of available energy profiles is performed so as to identify the thermodynamic products and, in turn, the potentially accessible kinetic products. Such a classification is designed with the purpose of predicting the experimentally observed products, either a singly bonded or a cyclopropanated derivative. The kinetic study is therefore conducted through all those reaction pathways that, in fact, lead to a cyclopropanated derivative prone to be observed experimentally.

3.1 General aspects of the 65 possible reaction pathways

In the initial step of the BH addition, a singly bonded derivative is formed when $dmbm^-$ is attached to a specific carbon atom of La@C_{2v}-C_{82}. In the resulting structure, bromine is oriented toward an adjacent 6-MR or five-membered ring (5-MR) so that the reactive carbon atom of $dmbm^-$ faces the carbon atom of the cage that will be attacked (see Figure 1). The rotation of the dihedral angle φ by $\pm 120°$ in the resulting intermediate structure (φ is a structural parameter indicating the alignment between the bromine atom and a bond of the EMF cage; φ is equal to $0°$ or $\pm 180°$ if bromine is exactly aligned with a [6,6] bond) generates three orientational isomers for each intermediate structure leading to different products. This is general, except if $dmbm^-$ is linked to carbon atoms C2, C3, C5, C8, C17, C20, and C24, for which only two orientational isomers can be distinguished because of the symmetry of the cage. Every single nonequivalent carbon atom represents one reaction site, and the formation of distinct orientational isomers of a singly bonded derivative gives rise to 65 different reaction pathways, some of them leading to the same product (e.g., cyclopropanation to bond 1 can be achieved from either C1 or C2; see Scheme 1a).

As mentioned in the introduction, it is well known that under typical conditions and in the case of EMFs, the BH reaction occurs under kinetic control.[47,68] Therefore, a complete

DFT-based study must be performed through the 65 different reaction pathways available in La@C_{2v}-C_{82}. However, it is important to keep in mind that there are two possible reaction pathways leading to $P_{C\alpha C\beta,\gamma}$ (or *$P_{C\alpha C\beta,\gamma}$ if this is the case). One of them follows the consecutive formation of $I_{C\alpha,\gamma}$ and $TS_{C\alpha,\gamma}$; analogously, the other goes through $I_{C\beta,\gamma}$ and $TS_{C\beta,\gamma}$. In this regard, on the basis of the energetic stability of $I_{C\alpha,\gamma}$, $I_{C\beta,\gamma}$, and $P_{C\alpha C\beta,\gamma}$ (or *$P_{C\alpha C\beta,\gamma}$), in Scheme 2 we represent the three situations susceptible to occur. Observe that profile type I is defined as the energy profile in which both reaction pathways lead to a Bingel product that is more stable than the two possible intermediate precursors ($I_{C\alpha,\gamma}$ and $I_{C\beta,\gamma}$). If one reaction pathway could be reverted, then profile type II is defined, in which the BH product is more stable than only one of the intermediate precursors. Finally, profile type III corresponds to the energy profile involving a destabilized Bingel product with respect to $I_{C\alpha,\gamma}$ and $I_{C\beta,\gamma}$. For profiles II and III we expect that the corresponding BH retro-reaction will occur and the BH product will not be accumulated. Accordingly, the following subsections are arranged according to the profile classification of the 65 reaction pathways, with the aim of describing all the most thermodynamically and kinetically favored BH reactions.

3.2. Classification of the 65 possible reaction pathways

Gibbs energies in toluene (ΔG_{tol}) relative to the separated reactants for the formation of the 65 different $I_{C\alpha,\gamma}$ structures are reported in Table 1, as well as ΔG_{tol} for the 35 most stable BH adducts (mostly $P_{C\alpha C\beta,\gamma}$ adducts). On the basis of Scheme 2 and the values of ΔG_{tol} for the structures related to a single pathway, it is possible to define the profile type in which that reaction pathway can be classified (e.g., for the attack on bond 1, $P_{C1C2,1}$ is more stabilized than $I_{C1,1}$ and $I_{C2,1}$; therefore, the situation is described by profile type I). After analyzing the profile type for all the 65 available reaction pathways, as reported in Table 1, we find that only 15 attacks out of 35 are of profile
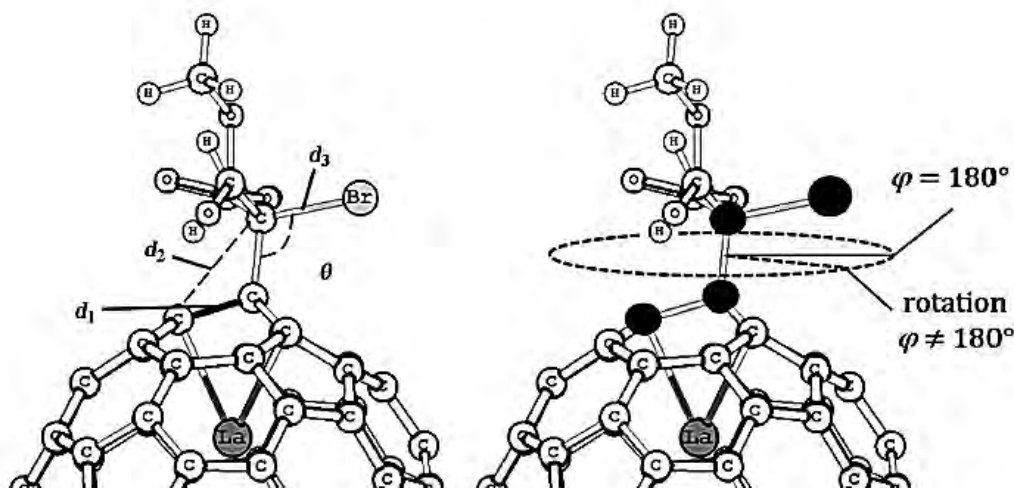
Figure 1. Structural parameters of a singly bonded derivative. The distances d_n are geometrical descriptors of the cyclopropanation reaction occurring at the bond highlighted in black (to the left). Angle θ and dihedral angle φ (this latter formed by the black-marked carbon atoms to the right) describe the position and orientation of the bromine atom (see text for details).
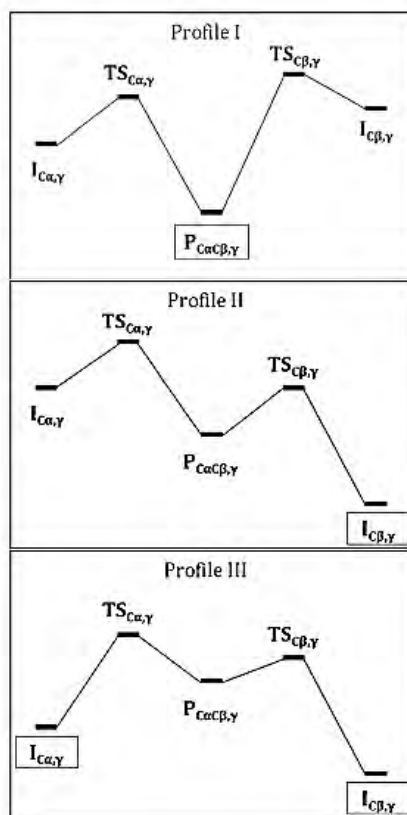
Scheme 2. Representation of the two reaction pathways leading to the formation of a Bingel–Hirsch adduct as a fulleroid or a methanofullerene through the attack on bond γ with adjacent reaction centers Cα and Cβ. The energy profile in which the retro-Bingel–Hirsch addition is hampered is classified as profile type I. On the contrary, if one or two reaction pathways can be regressed to a singly bonded derivative then the resulting profiles are classified as II or III, respectively. For each diagram, the most likely structure to be accumulated experimentally is enclosed in a rectangular box.

Table 1. Classification according to Scheme 2 based on energetic stability (in kcalmol^{-1}) of $I_{C\alpha,\gamma}$, $I_{C\beta,\gamma}$ and $P_{C\alpha C\beta,\gamma}$, of all possible Gibbs energy profiles for the Bingel-Hirsch addition to La@C_{2v}-C_{82} in toluene. The structural classification (see Scheme 1a) of bond γ is also given. The most stable intermediates are marked in italics (criterion: $\Delta G_{tot} < -10.0$ kcal mol^{-1}).

γ	Bond type	Cα	Cβ	$I_{C\alpha,\gamma}$	$I_{C\beta,\gamma}$	$P_{C\alpha C\beta,\gamma}$	Profile
					ΔG_{tot}		
1	B	1	2	−7.82	−13.49	−15.40	I
2	B	6	7	−8.15[a]	−10.38	−9.71	II
3	B	4	7	−8.78	−10.86	−12.37	I
4	B	7	10	−8.96	−8.03[a]	−7.96[b]	III
5	B	5	8	−3.58[a]	−7.81[a]	−2.89	III
6	B	9	12	−5.67[a]	−7.40	−0.48	III
7	B	12	13	−7.84	−10.59	−12.39	I
8	B	8	11	−7.81	−11.54	−6.03	III
9	C	15	15	0.69	0.69	−15.93	I
10	C	12	15	−7.91	2.18	−11.97	I
11	B	15	18	−0.15	−9.46	−15.40	I
12	A	16	19	−3.59[a]	−11.16	−9.93[b]	II
13	B	14	17	−8.05	−6.44	−10.66	I
14	C	17	20	−6.99	3.87	−16.56	I
15	B	20	21	5.09	−10.88	−9.56	II
16	A	22	22	−6.48	−6.48	−10.09[b]	I
17	B	23	24	−13.46	1.92	−7.86	II
18	C	24	24	2.42	2.42	−18.04	I
19	B	2	3	−14.92	−7.63	−18.52	I
a	D	1	1	−7.76	−7.76	−15.58	I
b	D	18	22	−11.28	−6.48[a]	−4.49	III
c	D	3	6	−8.09	−7.81	−7.27	III
d	D	1	4	−7.82[a]	−9.47	−8.79	II
e	D	4	5	−9.58	−3.58	−9.45	II
f	D	6	9	−8.15	−5.67	−12.42	I
g	D	9	9	−5.67[a]	−5.67[a]	2.10[b]	III
h	D	10	13	−7.23	−10.73	−10.77	I
i	D	10	11	−8.03	−10.40	−12.71	I
j	D	11	14	−11.55	−9.09	−9.26	II
k	D	14	16	−9.11	−3.59	−0.29	III
l	D	13	16	−11.30	−3.59[a]	−4.93	II
m	D	18	19	−10.28	−10.58	−7.23	III
n	D	19	21	−11.68	−10.49	−9.86	III
o	D	21	23	−11.14	−13.74	−10.30	III
p	D	22	23	−4.63	−12.37	−8.87	II

[a] ΔG_{tot} for these intermediates was estimated from the energy of the most stable orientational isomer for that specific reaction site. For instance, the energy of $I_{C9,6}$ is not calculated, but is taken as the energy of $I_{C9,f}$ as the orientational isomers are energetically very similar. Moreover, from the energy of $I_{C12,6}$ it is anticipated that bond 6 is not involved in a profile type I. [b] Only in these four cases, $^*P_{C7C10,4}$, $^*P_{C9C9,g}$, $^*P_{C16C19,12}$ and $^*P_{C2\times C22,16}$ the most stable Bingel-Hirsch adduct is a methanofullerene instead of a fulleroid structure.

type I. These 15 attacks can occur through 26 different pathways (Cα=Cβ for bonds 9, 16, 18, and a) and generate relatively stable BH products. To determine the kinetics of the entire BH addition to La@C_{2v}-C_{82}, we focus on reaction pathways with profile type I, because only in this situation is the BH adduct going to be observed experimentally. Furthermore, in principle, the 65 different intermediates $I_{C\alpha,\gamma}$ must be characterized completely. However, in a few cases exhibiting type II and III profiles, we did not optimize all possible orientational isomers of intermediate $I_{C\alpha,\gamma}$ as they exhibit similar energetics (see superscript [a] in Table 1). To sum up, by defining strategically three different profiles of the BH addition to La@C_{2v}-C_{82} based on ΔG_{tot} of all the possible intermediates, methanofullerenes, and fulleroids, we can avoid the study of a number of reaction pathways and still provide a full description of this reaction; therefore, in the following subsection the kinetic study is described for the 26 reaction pathways related to profile type I.

3.3. Analysis of structural parameters through the reaction coordinate

Relevant structural parameters (d_1, d_2, d_3, θ, and φ as defined in Figure 1) are summarized in Table 2 for the 26 reaction pathways under consideration. The distance d_1 describes the bond length of the attacked C–C bond γ of the cage, d_2 corresponds to the C_{C82}–C_{dmbm}– bond that is formed during the ring closure, and d_3 refers to the C_{dmbm}–C_{Br} bond length. The angles θ and φ are useful parameters for the examination of the exact localization of bromine through the reaction coordinate. In addition, from the reaction sites Cα involved in those 26 reaction pathways, there are seven 666 positions (carbon atoms surrounded

Table 2. Structural parameters (in Å, °) and Gibbs energies in toluene ΔG_{tol} (in kcal mol^{-1}) relative to separated reactants of key stationary points in the explored Bingel–Hirsch reaction pathways.[a]

Cα	γ	Intermediate ($I_{Cα,γ}$)						Transition State ($TS_{Cα,γ}$)						Product ($P_{CαCβ,γ}$)		
		d_1	d_2	d_3	$θ$	$φ$[b]	ΔG_{tol}	d_1	d_2	d_3	$θ$	$φ$[b]	$\Delta G_{tol}^{\ddagger}$	d_1	d_2	ΔG_{tol}
C1	1	1.520	2.552	2.004	108.8	−172.7	−7.82	1.538	1.799	2.844	89.5	179.0	13.71	2.134	1.484	−15.40
C1	a	1.544	2.597	1.998	107.9	53.7	−7.76	1.556	1.825	2.825	88.6	60.2	16.58	2.168	1.486	−15.58
C2	1	1.540	2.588	1.995	107.6	178.0	−13.49	1.562	1.825	2.745	92.5	−179.6	13.13	2.134	1.484	−15.40
C2	19	1.541	2.596	1.995	107.5	54.9	−14.92	1.561	1.888	2.764	89.4	63.2	15.75	2.154	1.481	−18.52
C3	19	1.532	2.562	2.003	108.8	−173.0	−7.63	1.539	1.855	2.796	90.0	176.7	6.29	2.154	1.481	−18.52
C4	3	1.520	2.559	2.003	108.5	−175.2	−8.78	1.542	1.806	2.847	88.6	178.2	14.25	2.157	1.481	−12.37
C6	f	1.552	2.593	2.006	108.0	53.5	−8.15	1.543	1.919	2.836	84.8	56.6	9.41	2.187	1.484	−12.42
C7	3	1.539	2.591	1.994	107.3	57.5	−10.86	1.628	1.842	2.708	93.1	75.7	16.20	2.157	1.481	−12.37
C9	f	1.545	2.583	2.000	108.2	−64.9	−5.67	1.543	1.877	2.748	89.4	−72.2	9.49	2.187	1.484	−12.42
C10	h	1.550	2.586	2.006	108.0	−63.2	−7.23	1.545	1.855	2.813	86.1	−69.2	9.13	2.187	1.488	−10.77
C10	i	1.551	2.593	1.998	107.7	54.5	−8.03	[c]	[c]	[c]	[c]	[c]	13.26[d]	2.233	1.488	−12.71
C11	i	1.549	2.617	1.985	108.7	−42.4	−10.40	1.544	1.847	2.799	89.1	−58.2	15.74	2.233	1.488	−12.71
C12	7	1.525	2.578	2.002	108.1	55.4	−7.84	1.546	1.905	2.755	88.0	71.3	11.90	2.208	1.475	−12.39
C12	10	1.580	2.601	2.001	107.2	−69.3	−7.91	1.597	1.859	2.861	86.4	−76.8	17.16	2.284	1.489	−11.97
C13	7	1.531	2.575	2.007	107.8	−175.8	−10.59	1.547	1.934	2.888	82.6	172.8	10.50	2.208	1.475	−12.39
C13	h	1.539	2.593	1.999	108.0	52.3	−10.73	1.538	1.928	2.834	84.7	49.1	15.96	2.187	1.488	−10.77
C14	13	1.542	2.600	1.993	109.8	−158.7	−8.05	1.544	1.882	2.852	85.6	−170.5	9.82	2.192	1.493	−10.66
C15	9	1.577	2.573	2.004	108.2	177.0	0.69	1.593	1.859	2.785	89.4	175.3	13.21	2.318	1.492	−15.93
C15	10	1.562	2.567	2.001	108.2	59.4	2.18	1.574	1.853	2.795	89.6	70.2	13.59	2.284	1.489	−11.97
C15	11	1.539	2.562	2.010	109.7	−68.6	−0.15	1.551	1.901	2.700	90.9	−76.7	5.72	2.231	1.497	−15.40
C17	13	1.527	2.576	2.001	108.3	−179.7	−6.44[d]	1.548	1.889	2.723	90.4	−176.3	17.89	2.192	1.493	−10.66
C17	14	1.586	2.593	2.001	107.3	−58.0	−6.99[d]	[c]	[c]	[c]	[c]	[c]	20.58[d]	2.305	1.495	−16.56
C18	11	1.551	2.575	2.012	108.0	178.6	−9.46	1.554	1.972	2.921	80.6	161.2	9.76	2.231	1.497	−15.40
C20	14	1.575	2.574	2.004	107.8	−175.8	3.87	1.618	1.912	2.839	85.3	−176.4	17.47	2.305	1.495	−16.56
C22	16	1.479	2.535	1.991	110.9	174.2	−6.48	1.481	1.908	2.755	92.9	−175.1	6.75	1.517	1.512	−10.09[e]
C24	18	1.577	2.602	1.990	108.4	−70.8	2.42	1.624	1.945	2.840	84.0	−82.9	18.13	2.311	1.493	−18.04

[a] Structural parameters defined in Figure 1. $\Delta G_{tol}^{\ddagger}$ (kcal mol^{-1}) is the Gibbs energy barrier in toluene for the ring-closure step; this is estimated as the energy difference between $TS_{Cα,γ}$ and $I_{Cα,γ}$ if the intermediate is more stable than the separated reactants; otherwise it is the energy difference between $TS_{Cα,γ}$ and the separated reactants. All reaction pathways are of profile type I as explained in Scheme 2. [b] For the dihedral angle $φ$, if Cα is a 566 center then bromine can be oriented $±180°$ with respect to a [6,6] bond $γ$, and the other [5,6] bonds result in $φ ≈ ±180° ±120° ≈ ±60°$. On the other hand, if Cα is a 666 center, we select the bond having the label with the smallest number as the reference point (e.g., for $I_{C15,9}$ $φ ≈ ±180°$ and the others, $I_{C15,11}$ and $I_{C15,10}$, have $φ ≈ ±60°$). [c] See Figure S1 in the Supporting Information for a discussion of the transition states for these reaction pathways. $\Delta G_{tol}^{\ddagger}$ values are estimated from linear transits. [d] See Figures S2 and S3 in the Supporting Information for a discussion of the movement of the La atom in these structures. [e] Only in the case of $^*P_{C22C22,16}$ the most stable Bingel–Hirsch adduct is a methanofullerene instead of a fulleroid structure.

by three hexagons) and eleven 566 (carbon atoms surrounded by one pentagon and two hexagons), which lead to eleven [6,6] and four [5,6] BH adducts (one bond is type A, six are type B, four type C, and four type D). Therefore, there are fifteen potential $P_{CαCβ,γ}$ (or $^*P_{CαCβ,γ}$ if more stable) structures to be observed.

The structural parameter d_1 remains constant through the different $I_{Cα,γ}$ and $TS_{Cα,γ}$ structures under study. However, for the cyclopropanated adduct $d_1 > 2.0$ Å, indicating the rupture of the attacked C–C bond $γ$ in the cage (except for $^*P_{C22C22,16}$, for which it was not even possible to optimize the analogous open-cage structure $P_{C22C22,16}$). On the other hand, the structural parameter d_2 starts in $I_{Cα,γ}$ at approximately 2.6 Å and is shortened to 1.8–1.9 Å at $TS_{Cα,γ}$; then d_2 acquires the characteristic value of a hybridized C(sp^3)–C(sp^2) bond length upon formation of $P_{CαCβ,γ}$ (i.e., $≈ 1.48$ Å), thus confirming the ring closure.

The other parameters, d_3, $θ$, and $φ$, account for the position of bromine through the reaction coordinate. The bond length d_3 between bromine and the reactive carbon atom of dmbm$^-$ is approximately 2.0 Å for the initial structure $I_{Cα,γ}$, and is elongated by 0.7–0.9 Å while d_2 is simultaneously shortened to

reach the transition-state structure in an S_N2-like process. In the final product, bromine is completely dissociated as bromide: $d_3 \rightarrow \infty$. Moreover, the reactive carbon atom of dmbm$^-$ has a tetrahedral arrangement in every $I_{Cα,γ}$ structure as $θ$ is nearly 109.5°. When $TS_{Cα,γ}$ is reached, $θ$ is decreased to 90° as the reaction evolves toward the ring closure. On the other hand, we observe that $I_{Cα,γ}$, $I_{Cα,δ}$, and $I_{Cα,ε}$ (the latter if available) formed at the center Cα are structurally very similar, and differ only in their dihedral angle $φ$. If Cα is a 566 center then bromine can be oriented $±180°$ with respect to a [6,6] bond $γ$, and the other [5,6] bonds $δ$ or $ε$ result in $φ ≈ ±180° ±120° ≈ ±60°$ (see, for instance, $φ$ for intermediates at C1 in Table 2). In the case of a 666 center, we selected the bond having the label with the smallest number as the reference point (e.g., in Table 2, for $I_{C15,9}$ $φ ≈ ±180°$ and the others, $I_{C15,10}$ and $I_{C15,11}$, have $φ ≈ ±60°$).

3.4. Fulleroids versus methanofullerenes

We also studied the relative stabilities of open-cage/closed-cage (fulleroid/methanofullerene) monoadducts. In all cases in which it was possible to optimize both the closed- and open-

cage adducts, the fulleroid structure was found to be more stable than the methanofullerene adduct, except for the case of *P$_{C9C9,q}$. In general, one may optimize both structures, but the fulleroid is usually the most stable (see Table S3 in the Supporting Information for a complete analysis of all optimized closed- and open-cage BH adducts).[68] In the cases of *P$_{C7C10,4}$, *P$_{C16C19,12}$, and *P$_{C22C22,16}$, we were unable to optimize an open-cage adduct, and only the methanofullerene BH adducts were located. The reaction barrier for the conversion of the cyclopropanated adduct to the fulleroid structure is found to be around 1 kcal mol^{-1}. To illustrate this point, Figure 2 depicts
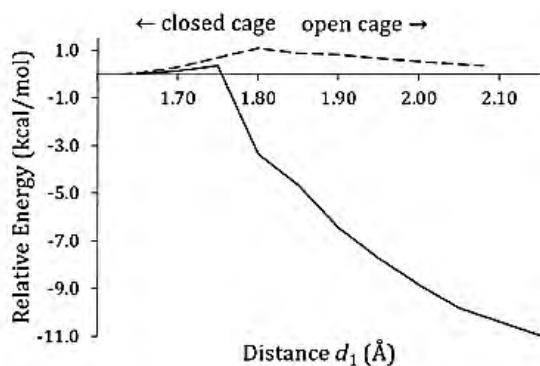
Figure 2. Gas-phase linear transit for rupture of bonds 1 in *P$_{C1C2,1}$ (solid line) and o in *P$_{C21C23,o}$ (dashed line). Initial (left) and final (right) points correspond to the closed and open cages, respectively, at their optimized geometries. Energies (kcal mol^{-1}) are relative to the gas-phase optimized closed-cage adduct at the BP86-D3(BJ)/DZP level of theory.

the gas-phase linear transit from methanofullerenes *P$_{C1C2,1}$ and *P$_{C21C23,o}$ to fulleroids P$_{C1C2,1}$ and P$_{C21C23,o}$, respectively. For the former, the fulleroid is the most stable, whereas in the latter, the cyclopropanated structure is marginally more stable than the analogous fulleroid in the gas phase but not in solution. Solvent effects stabilize open-cage adducts more than closed-cage ones (see Table S3).

To discuss the origin of the higher stability of the open-cage adducts, we performed an activation strain analysis (ASM)[69–71] of the reactivity (also known as the distortion/interaction model)[72–74] along the reaction pathways leading to the open-cage P$_{C1C2,19}$ (see Figure 3). In the ASM analysis, the relative energy with respect to separated reactants, ΔE, along the reaction coordinate is decomposed into the strain ΔE_{strain} associated with deforming the individual reactants and the actual interaction ΔE_{int} between the deformed reactants (see Equation below).

$$\Delta E = \Delta E_{strain} + \Delta E_{int}$$

The open-cage structure P$_{C1C2,19}$ is found to be 33.2 kcal mol^{-1} more distorted in terms of ΔE_{strain} than the *P$_{C1C2,19}$ closed one. This large structural deformation in the open-cage structure is compensated by the interaction term, ΔE_{int}, which is 43.6 kcal mol^{-1} more stabilizing than the interaction in its corresponding closed-cage adduct. The resulting binding
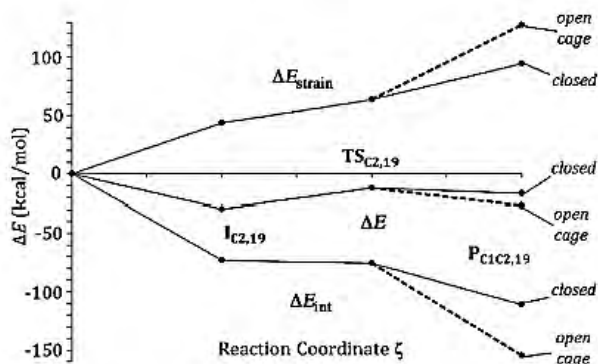
Figure 3. Activation strain diagram for the Bingel–Hirsch pathway at bond 19 between C1 and C2 (dashed line = path to open-cage P$_{C1C2,19}$; solid line = path to closed-cage *P$_{C1C2,19}$).

energy given as $\Delta E_{def} + \Delta E_{int}$ shows that the open-cage P$_{C1C2,19}$ is more stabilized by 10.4 kcal mol^{-1} as compared with the closed-cage one. The reason for the ΔE_{int} term being more stabilizing in the open cage is twofold. First, the breaking of the attacked C–C bond in the fullerene cage stabilizes the LUMO and destabilizes the HOMO of the carbon cage, making frontier orbital interactions more favorable.[75] Moreover, in open-cage adducts, all carbon atoms keep their sp^2 hybridization forming homoaromatic rings, maintaining their π-delocalization. This π-homoconjugation has been shown to be crucial for the final stabilization of open-cage EMF BH adducts.[19,46] In addition, we applied the ASM analysis to other reaction pathways, and in all cases, we arrived at the same conclusion that, regardless of the higher structural distortion, the open-cage adduct tends to be more stabilized than the closed-cage one because of the higher interaction between the reactants (see Table S4, Supporting Information).

3.5. The most favored reaction pathways

We were able to optimize 24 TS$_{C\alpha,\gamma}$ out of the 26 possible transition states of reaction pathways with profile type I. In Figure S1 (Supporting Information), linear transit calculations of the two missing TS$_{C\alpha,\gamma}$ structures show that they are very high in energy. From the experimental evidence provided by Nagase et al.,[20,49] five different structures were isolated, revealing the following product distribution (%): 55.4, 22.1, 5.5, 5.1, and 11.9. From the reaction energies ΔG_{tol} reported in Table 1, we have determined that the most stable intermediate is generated at the C2 position, with the orientational isomer I$_{C2,19}$ very close in energy to I$_{C23,o}$ (1.2 kcal mol^{-1} difference). The orientational isomers of I$_{C2}$ and I$_{C23}$ are connected to the corresponding addition products via relatively high-energy transition states. Indeed, TS$_{C2,1}$, TS$_{C2,19}$, TS$_{C23,17}$, TS$_{C23,o}$, and TS$_{C23,p}$ are associated with energy barriers of 13.1, 15.8, 13.5, 21.5, and 15.2 kcal mol^{-1}, respectively (the latter three barriers are not shown in Table 2 because they were not classified as profile type I; however, they are reported in Table S5 in the Supporting Information). Those activation energies are not in competition with the lowest ones, which are calculated for TS$_{C15,11}$ and

ChemPubSoc
Europe
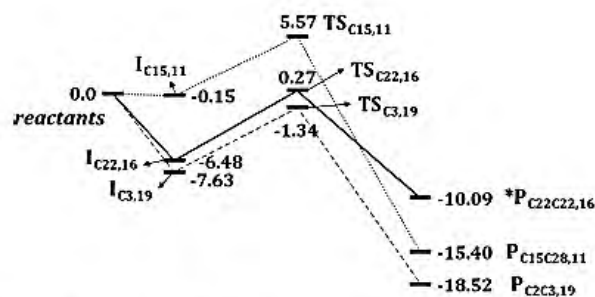
Figure 4. Comparison of the Gibbs energy profiles (in kcal mol^{-1}) for the lowest-barrier pathways to addition at C15 on bond 11 (dotted line), C3 on bond 19 (dashed line), and C22 on bond 16 (solid line).

TS$_{C3,19}$ to be 5.7 and 6.3 kcal mol^{-1} (see Figure 4), respectively. Nonetheless, I$_{C15,11}$ and I$_{C3,19}$ are destabilized relative to I$_{C2,19}$ by 14.8 and 7.3 kcal mol^{-1}, respectively. In fact, if formed, I$_{C15,11}$ would probably decompose into reactants, because the process leading to the formation of this intermediate is certainly not favored ($\Delta G_{tol} = -0.2$ kcal mol^{-1}). A similar statement was given by Zhao et al. in a very recent study of the BH addition to the non-IPR Sc$_2$@C$_{66}$, wherein reaction pathways with the lowest-energy barriers but destabilized intermediates were discarded to produce the experimentally observed BH adduct.[68] From these results, we conclude that the most favored reaction pathway leads to the formation of a fulleroid derivative on bond 19 rather than on bond 11 (although the possible formation of the latter cannot be totally discarded). These results are in agreement with the experimental evidence, as only one of the five characterized structures corresponds to a BH product (P). In fact, from the ^{13}C NMR spectrum of anion P, and on the basis of the similar NMR spectra of previously reported cycloadditions leading to open-cage adducts,[19, 49] the authors concluded that the observed signals correspond to sp^2 carbon atoms of an open-cage adduct attacked at a [6,6] position. For instance, in the case of the formation of the Y$_3$N@C$_{80}$ fulleroid, X-ray analysis confirmed the formation of an open-cage monoadduct on a [6,6] bond.[39] Moreover, on the basis of NMR and UV spectra and DFT calculations, a [6,6] bond was suggested to be the attacked site for the formation of the Sc$_3$N@C$_{80}$ BH derivative.[76] We conclude, therefore, that the isolated La@C$_{2v}$-C$_{82}$ monoadduct structure corresponds to P$_{C2C3,19}$, that is, a fulleroid formed on a [6,6] bond. There is also another competitive reaction pathway leading to *P$_{C2C22,16}$, a methanofullerene, for which the respective energy barrier is only 0.5 kcal mol^{-1} higher than that for the formation of P$_{C2C3,19}$ (see Figure 4). Nevertheless, the formation of a BH product on bond 16 is discarded because the obtained closed-cage monoadduct is not in agreement with the experimentally observed fulleroid structure. It is interesting to notice that additions with the lowest energy barriers produce well-stabilized fulleroids. Indeed, the most stable fulleroid is P$_{C2C3,19}$. The great stability of P$_{C2C3,19}$ is in line with the experimental higher stability of the fulleroid as compared to the singly-bonded derivatives when heating at 80 °C.[49]

Three [6,6] bonds are determined to be the most reactive for the formation of the final BH adduct: 11 (type B), 16

(type A), and 19 (type B). For 16 and 19, the initial intermediate formation occurs on a 566 carbon atom (C3 and C22), and for 11 at a 666 carbon atom (C15). The closure and final BH product formation always takes place on a [6,6] bond. Attacks at bonds of type C (or pyrene), which involve only 666 carbons, result in relatively high energy barriers. Additionally, all the reaction pathways on pyrene bonds are classified with profile type I. Type D (or corannulene) bonds can be considered relatively unreactive, because many reaction pathways occurring at corannulene positions exhibit type II and III energy profiles, and those additions with profile I involving type D bonds have energy barriers higher than 10 kcal mol^{-1}. In general, we observe that the ring closure between dmbm$^-$ and a [6,6] bond during the second step of the BH reaction is favored if a 5-MR is adjacent to the initially functionalized carbon atom, as shown for bond types A and B. Interestingly, bonds 11, 16, and 19 are among the ten most reactive bonds for the Diels–Alder cycloaddition to La@C$_{2v}$-C$_{82}$, but they are less reactive than bond o, which is the most reactive in this type of reaction.[18]

On the basis of the ESR, NMR, and X-ray analyses carried out by Nagase et al.,[49] four adducts were assigned to be singly bonded derivatives. Those structures should correspond to the thermodynamically most stable intermediates: 666 positions C2 and C7 and 566 carbons C11, C13, C18, C19, C21, and C23 (see Table 1). The reaction pathways involving the intermediates formed at C23 are classified into profiles II or III: intermediates I$_{C23,17}$, I$_{C23,o}$, and I$_{C23,p}$ are at least 3 kcal mol^{-1} more stable than the corresponding fulleroids P$_{C23C24,17}$, P$_{C21C23,o}$, and P$_{C22C23,p}$, respectively. In addition, their formation is associated with activation energies two or three times larger than the lowest ones (see Table S5, Supporting Information). Consequently, we can conclude that the formation of the three products involving the formation of a C23 intermediate are kinetically hampered, resulting in an accumulation of the intermediate I$_{C23}$ as the major product instead of the cyclopropanated derivative. This is in good agreement with the experimental observations, as I$_{C23}$ was the only structure confirmed by X-ray and had the highest yield (55.4%). The other structure with the second highest yield (22.1%) is also a singly bonded derivative. We assign this structure as I$_{C2}$ because it is actually the thermodynamically most stable singly bonded structure (1.2 kcal mol^{-1} below the energy of I$_{C23}$), and the reaction pathways through the bonds around C2 are associated with activation energies higher than 13 kcal mol^{-1}. In view of that, one might expect the same yield for I$_{C2}$ and I$_{C23}$. Nonetheless, unlike C23, reaction pathways around C2 do actually produce well-stabilized fulleroids and are classified as type I. In fact, the most stable structure is P$_{C2C3,19}$. Consequently, a portion of I$_{C2}$ may be consumed to produce P$_{C2C3,19}$ during the BH reaction, thus making it the second most abundant singly bonded adduct.

The remaining two experimentally characterized singly bonded derivatives with a product distribution of 5% should correspond to the other well-stabilized intermediates, which are formed at C7, C11, C13, C18, C19, and C21 positions. On the basis of our computations, we predict that the I$_{C19}$ and I$_{C21}$ structures are the ones detected experimentally because they

are thermodynamically stable (after C2 and C23, the lowest-energy intermediate is generated at C19) and all the BH products coming from C19 and C21 intermediates are nonstable fulleroids (i.e., their reaction pathways are classified into profiles II or III, just like C23). However, the formation of singly bonded derivatives on the C7, C11, C13, C18 positions cannot be fully discarded. Consequently, our results show that La@C_{2v}-C$_{82}$ is not particularly regioselective under Bingel–Hirsch conditions. As a final remark, let us mention that we did not find any correlation between the predicted adducts and the position of the La atom in the La@C_{2v}-C$_{82}$ cage in terms of Voronoi-deformation-density (VDD) charge distribution[77] and spin density, as reported in Table 3. These results actually highlight the fact that these quantities cannot be used to make predictions about possible BH reaction sites.

Table 3. VDD atomic charges and spin densities ρ (both in a.u.) for selected carbon atoms in the La@C_{2v}-C$_{82}$ cage.[a]

Cα	VDD	ρ
C2	−0.01	0.02
C3	−0.01	0.02
C11	−0.01	0.00
C13	−0.01	−0.01
C15	0.00	0.02
C18	−0.01	0.04
C19	−0.01	0.03
C21	0.00	−0.01
C22	−0.01	−0.01
C23	0.00	0.05

[a] Computed at BP86-D3(BJ)/DZP level of theory.

4. Conclusion

We have identified quantum chemically the five experimentally observed but hitherto uncharacterized products in the Bingel–Hirsch (BH) addition of dimethyl bromomalonate to La@C_{2v}-C$_{82}$. Only one of the experimentally observed products is a fulleroid. Our computations indicate that this is the fulleroid at bond 19, which emerges as the kinetically and thermodynamically most favorable Bingel–Hirsch adduct; however, our analysis, made through all possible cyclopropanated derivatives, suggests that the fulleroid on bond 11 cannot be totally disregarded.

On the basis of experimental results by Nagase et al.,[49] four adducts can be assigned as singly bonded derivatives. We assign two of the observed products with the highest yields to the thermodynamically most stable intermediates, I$_{C2}$ and I$_{C23}$. According to our computations, these intermediates are traps on the Bingel–Hirsch reaction pathways. Formation of the final Bingel–Hirsch adduct is kinetically hampered, leading to accumulation of these intermediates, especially in the case of I$_{C23}$. Likewise, the remaining two experimentally reported singly bonded derivatives with a reduced product distribution are probably I$_{C19}$ and I$_{C21}$. Note, however, that the other well-stabilized intermediates formed at C7, C11, C13, and C18 may be in direct competition.

Finally, our computational exploration also shows that the Bingel–Hirsch addition to La@C_{2v}-C$_{82}$ is not particularly regioselective. It differs in this respect from the Diels–Alder cycloaddition, which occurs exclusively at bond o. Thus, in the case of the Bingel–Hirsch reaction, one may anticipate the formation of at least ten products even under relatively mild reaction conditions.

[1] J. R. Heath, S. C. O'Brien, Q. Zhang, Y. Liu, R. F. Curl, F. K. Tittel, R. E. Smalley, *J. Am. Chem. Soc.* **1985**, *107*, 7779–7780.

[2] X. Lu, L. Feng, T. Akasaka, S. Nagase, *Chem. Soc. Rev.* **2012**, *41*, 7723–7760.

[3] M. N. Chaur, F. Melin, A. L. Ortiz, L. Echegoyen, *Angew. Chem. Int. Ed.* **2009**, *48*, 7514–7538; *Angew. Chem.* **2009**, *121*, 7650–7675.

[4] S. Yang, F. Liu, C. Chen, M. Jiao, T. Wei, *Chem. Commun.* **2011**, *47*, 11822–11839.

[5] A. A. Popov, S. Yang, L. Dunsch, *Chem. Rev.* **2013**, *113*, 5989–6113.

[6] X. Lu, L. Bao, T. Akasaka, S. Nagase, *Chem. Commun.* **2014**, *50*, 14701–14715.

[7] H. Cong, B. Yu, T. Akasaka, X. Lu, *Coord. Chem. Rev.* **2013**, *257*, 2880–2898.

[8] D. M. McCluskey, T. N. Smith, P. K. Madasu, C. E. Coumbe, M. A. Mackey, P. A. Fulmer, J. H. Wynne, S. Stevenson, J. P. Phillips, *ACS Appl. Mater. Interfaces* **2009**, *1*, 882–887.

[9] J. D. Wilson, W. C. Broaddus, H. C. Dorn, P. P. Fatouros, C. E. Chalfant, M. D. Shultz, *Bioconjugate Chem.* **2012**, *23*, 1873–1880.

[10] Y. Yasutake, Z. Shi, T. Okazaki, H. Shinohara, Y. Majima, *Nano Lett.* **2005**, *5*, 1057–1060.

[11] J. R. Pinzón, D. C. Gasca, S. G. Sankaranarayanan, G. Bottari, T. Torres, D. M. Guldi, L. Echegoyen, *J. Am. Chem. Soc.* **2009**, *131*, 7727–7734.

[12] Y. Chai, T. Guo, C. Jin, R. E. Haufler, L. P. F. Chibante, J. Fure, L. Wang, J. M. Alford, R. E. Smalley, *J. Phys. Chem.* **1991**, *95*, 7564–7568.

[13] X. Lu, K. Nakajima, Y. Iiduka, H. Nikawa, N. Mizorogi, Z. Slanina, T. Tsuchiya, S. Nagase, T. Akasaka, *J. Am. Chem. Soc.* **2011**, *133*, 19553–19558.

[14] D. E. Manolopoulos, P. W. Fowler, *An Atlas of Fullerenes*, Clarendon, Oxford, **1995**.

[15] H. W. Kroto, *Nature* **1987**, *329*, 529–531.

[16] T. Akasaka, T. Wakahara, S. Nagase, K. Kobayashi, M. Waelchli, K. Yamamoto, M. Kondo, S. Shirakura, Y. Maeda, T. Kato, Y. Nakadaira, X. Gao, E. v. Caemelbecke, K. M. Kadish, *J. Phys. Chem. B* **2001**, *105*, 2971–2974.

[17] K. Muthukumar, J. A. Larsson, *J. Phys. Chem. A* **2008**, *112*, 1071–1075.

[18] M. Garcia-Borràs, J. M. Luis, M. Swart, M. Solà, *Chem. Eur. J.* **2013**, *19*, 4468–4479.

[19] M. Garcia-Borràs, S. Osuna, J. M. Luis, M. Swart, M. Solà, *Chem. Soc. Rev.* **2014**, *43*, 5089–5105.

[20] L. Feng, T. Nakahodo, T. Wakahara, T. Tsuchiya, Y. Maeda, T. Akasaka, T. Kato, E. Horn, K. Yoza, N. Mizorogi, S. Nagase, *J. Am. Chem. Soc.* **2005**, *127*, 17136–17137.

[21] T. Akasaka, S. Nagase, K. Kobayashi, T. Suzuki, T. Kato, K. Yamamoto, H. Funasaka, T. Takahashi, *J. Chem. Soc. Chem. Commun.* **1995**, 1343–1344.

[22] R. Valencia, A. Rodríguez-Fortea, J. M. Poblet, *J. Phys. Chem. A* **2008**, *112*, 4550–4555.

[23] S. Nagase, K. Kobayashi, *Chem. Phys. Lett.* **1993**, *214*, 57–63.

[24] T. Akasaka, T. Kato, K. Kobayashi, S. Nagase, K. Yamamoto, H. Funasaka, T. Takahashi, *Nature* **1995**, *374*, 600–601.

[25] J. M. Campanera, C. Bo, J. M. Poblet, *Angew. Chem. Int. Ed.* **2005**, *44*, 7230–7233; *Angew. Chem.* **2005**, *117*, 7396–7399.

[26] Y. Maeda, J. Miyashita, T. Hasegawa, T. Wakahara, T. Tsuchiya, L. Feng, Y. Lian, T. Akasaka, K. Kobayashi, S. Nagase, M. Kako, K. Yamamoto, K. M. Kadish, *J. Am. Chem. Soc.* **2005**, *127*, 2143–2146.

[27] T. Akasaka, T. Wakahara, S. Nagase, K. Kobayashi, M. Waelchli, K. Yamamoto, M. Kondo, S. Shirakura, S. Okubo, Y. Maeda, T. Kato, M. Kako, Y. Nakadaira, R. Nagahata, X. Gao, E. v. Caemelbecke, K. M. Kadish, *J. Am. Chem. Soc.* **2000**, *122*, 9316–9317.

[28] E. Nishibori, M. Takata, M. Sakata, H. Tanaka, M. Hasegawa, H. Shinohara, *Chem. Phys. Lett.* **2000**, *330*, 497–502.

[29] Y. Maeda, J. Miyashita, T. Hasegawa, T. Wakahara, T. Tsuchiya, T. Nakahodo, T. Akasaka, N. Mizorogi, K. Kobayashi, S. Nagase, T. Kato, N. Ban, H. Nakajima, Y. Watanabe, *J. Am. Chem. Soc.* **2005**, *127*, 12190–12191.

[30] C. M. Cardona, A. Kitaygorodskiy, A. Ortiz, M. A. Herranz, L. Echegoyen, *J. Org. Chem.* **2005**, *70*, 5092–5097.

[31] C. Bingel, *Chem. Ber.* **1993**, *126*, 1957–1959.

[32] A. Hirsch, I. Lamparth, T. Groesser, H. R. Karfunkel, *J. Am. Chem. Soc.* **1994**, *116*, 9385–9386.

[33] D. M. Rivera-Nazario, J. R. Pinzón, S. Stevenson, L. A. Echegoyen, *J. Phys. Org. Chem.* **2013**, *26*, 194–205.

[34] A. F. Kiely, R. C. Haddon, M. S. Meier, J. P. Selegue, C. P. Brock, B. O. Patrick, G.-W. Wang, Y. Chen, *J. Am. Chem. Soc.* **1999**, *121*, 7971–7972.

[35] R. D. Bolskar, A. F. Benedetto, L. O. Husebo, R. E. Price, E. F. Jackson, S. Wallace, L. J. Wilson, J. M. Alford, *J. Am. Chem. Soc.* **2003**, *125*, 5471–5478.

[36] M. D. Diener, J. M. Alford, S. J. Kennel, S. Mirzadeh, *J. Am. Chem. Soc.* **2007**, *129*, 5131–5138.

[37] C. M. Cardona, A. Kitaygorodskiy, L. Echegoyen, *J. Am. Chem. Soc.* **2005**, *127*, 10448–10453.

[38] T. Cai, C. Slebodnick, L. Xu, K. Harich, T. E. Glass, C. Chancellor, J. C. Fettinger, M. M. Olmstead, A. L. Balch, H. W. Gibson, H. C. Dorn, *J. Am. Chem. Soc.* **2006**, *128*, 6486–6492.

[39] O. Lukoyanova, C. M. Cardona, J. Rivera, L. Z. Lugo-Morales, C. J. Chancellor, M. M. Olmstead, A. Rodríguez-Fortea, J. M. Poblet, A. L. Balch, L. Echegoyen, *J. Am. Chem. Soc.* **2007**, *129*, 10423–10430.

[40] J. R. Pinzón, T. Zuo, L. Echegoyen, *Chem. Eur. J.* **2010**, *16*, 4864–4869.

[41] S. Yang, C. Chen, X. Li, T. Wei, F. Liu, S. Wang, *Chem. Commun.* **2013**, *49*, 10844–10846.

[42] M. N. Chaur, F. Melin, A. J. Athans, B. Elliott, K. Walker, B. C. Holloway, L. Echegoyen, *Chem. Commun.* **2008**, 2665–2667.

[43] T. Cai, L. Xu, C. Shu, J. E. Reid, H. W. Gibson, H. C. Dorn, *J. Phys. Chem. C* **2008**, *112*, 19203–19208.

[44] N. Alegret, M. N. Chaur, E. Santos, A. Rodríguez-Fortea, L. Echegoyen, J. M. Poblet, *J. Org. Chem.* **2010**, *75*, 8299–8302.

[45] N. Alegret, A. Rodríguez-Fortea, J. M. Poblet, *Chem. Eur. J.* **2013**, *19*, 5061–5069.

[46] M. Garcia-Borràs, S. Osuna, M. Swart, J. M. Luis, L. Echegoyen, M. Solà, *Chem. Commun.* **2013**, *49*, 8767–8769.

[47] N. Alegret, P. Salvadó, A. Rodríguez-Fortea, J. M. Poblet, *J. Org. Chem.* **2013**, *78*, 9986–9990.

[48] M. Garcia-Borràs, M. R. Cerón, S. Osuna, M. Izquierdo, J. M. Luis, L. Echegoyen, M. Solà, *Angew. Chem. Int. Ed.* **2016**, *55*, 2374–2377.

[49] L. Feng, T. Wakahara, T. Nakahodo, T. Tsuchiya, Q. Piao, Y. Maeda, Y. Lian, T. Akasaka, E. Horn, K. Yoza, T. Kato, N. Mizorogi, S. Nagase, *Chem. Eur. J.* **2006**, *12*, 5578–5586.

[50] L. Feng, T. Tsuchiya, T. Wakahara, T. Nakahodo, Q. Piao, Y. Maeda, T. Akasaka, T. Kato, K. Yoza, E. Horn, N. Mizorogi, S. Nagase, *J. Am. Chem. Soc.* **2006**, *128*, 5990–5991.

[51] Y. Maeda, S. Sato, K. Inada, H. Nikawa, M. Yamada, N. Mizorogi, T. Hasegawa, T. Tsuchiya, T. Akasaka, T. Kato, Z. Slanina, S. Nagase, *Chem. Eur. J.* **2010**, *16*, 2193–2197.

[52] G. te Velde, F. M. Bickelhaupt, E. J. Baerends, C. Fonseca Guerra, S. J. A. van Gisbergen, J. G. Snijders, T. Ziegler, *J. Comput. Chem.* **2001**, *22*, 931–967.

[53] M. Swart, J. G. Snijders, *Theor. Chem. Acc.* **2004**, *111*, 56–56.

[54] J. G. Snijders, M. Swart, *Theor. Chem. Acc.* **2003**, *110*, 34–41.

[55] E. van Lenthe, E. J. Baerends, J. G. Snijders, *J. Chem. Phys.* **1993**, *99*, 4597–4610.

[56] A. D. Becke, *Phys. Rev. A* **1988**, *38*, 3098–3100.

[57] J. Perdew, *Phys. Rev. B* **1986**, *33*, 8822–8824.

[58] M. Swart, M. Solà, F. M. Bickelhaupt, *J. Comput. Chem.* **2007**, *28*, 1551–1560.

[59] S. Grimme, J. Antony, S. Ehrlich, H. Krieg, *J. Chem. Phys.* **2010**, *132*, 154104.

[60] S. Grimme, S. Ehrlich, L. Goerigk, *J. Comput. Chem.* **2011**, *32*, 1456–1465.

[61] S. Osuna, M. Swart, M. Solà, *J. Phys. Chem. A* **2011**, *115*, 3491–3496.

[62] A. Klamt, *J. Phys. Chem.* **1995**, *99*, 2224–2235.

[63] M. Swart, F. M. Bickelhaupt, *J. Comput. Chem.* **2008**, *29*, 724–734.

[64] M. Swart, F. M. Bickelhaupt, *Int. J. Quantum Chem.* **2006**, *106*, 2536–2544.

[65] C. P. Kelly, C. J. Cramer, D. G. Truhlar, *J. Chem. Theory Comput.* **2005**, *1*, 1133–1152.

[66] C. P. Kelly, C. J. Cramer, D. G. Truhlar, *J. Phys. Chem. B* **2006**, *110*, 16066–16081.

[67] V. S. Bryantsev, M. S. Diallo, W. A. Goddard, *J. Phys. Chem. B* **2008**, *112*, 9709–9719.

[68] Q.-Z. Li, J.-J. Zheng, X. Zhao, *J. Phys. Chem. C* **2015**, *119*, 26196–26201.

[69] L. P. Wolters, F. M. Bickelhaupt, *WIREs Comput. Mol. Sci.* **2015**, *5*, 324–343.

[70] F. M. Bickelhaupt, *J. Comput. Chem.* **1999**, *20*, 114–128.

[71] I. Fernández, F. M. Bickelhaupt, *Chem. Soc. Rev.* **2014**, *43*, 4953–4967.

[72] K. N. Houk, R. W. Gandour, R. W. Strozier, N. G. Rondan, L. A. Paquette, *J. Am. Chem. Soc.* **1979**, *101*, 6797–6802.

[73] D. H. Ess, K. N. Houk, *J. Am. Chem. Soc.* **2007**, *129*, 10646–10647.

[74] Y. Cao, Y. Liang, L. Zhang, S. Osuna, A.-L. M. Hoyt, A. L. Briseno, K. N. Houk, *J. Am. Chem. Soc.* **2014**, *136*, 10743–10751.

[75] M. Cases, M. Duran, J. Mestres, N. Martín, M. Solà, *Fullerenes for the New Millennium*, (Eds.: P. V. Kamat, K. M. Kadish, D. M. Guldi), The Electrochemical Society, Pennington, **2011**, pp. 244–269.

[76] C. Shu, T. Cai, L. Xu, T. Zuo, J. Reid, K. Harich, H. C. Dorn, H. W. Gibson, *J. Am. Chem. Soc.* **2007**, *129*, 15710–15717.

[77] C. Fonseca Guerra, J.-W. Handgraaf, E. J. Baerends, F. M. Bickelhaupt, *J. Comput. Chem.* **2004**, *25*, 189–210.
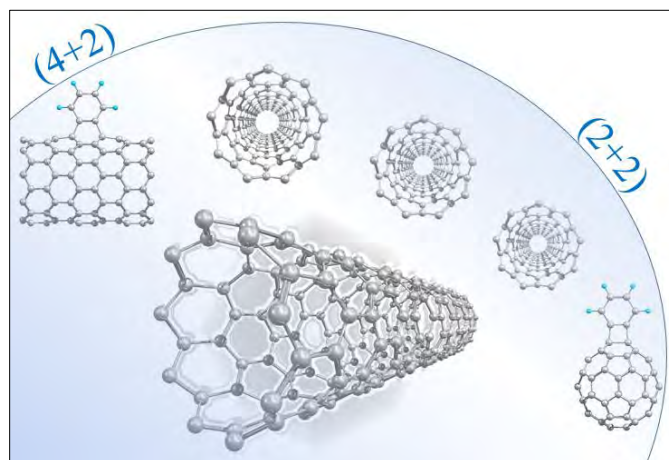
4.2 (4+2) and (2+2) Cycloadditions of Benzyne to C_{60} and Zig-Zag Single-Walled Carbon Nanotubes: The Effect of the Curvature

J.P.M. participated in the design of the project, performed all the calculations, analyzed the results, and co-wrote the manuscript.

(4 + 2) and (2 + 2) Cycloadditions of Benzyne to C$_{60}$ and Zig-Zag Single-Walled Carbon Nanotubes: The Effect of the Curvature

Juan Pablo Martínez,[†] Fernando Langa,[‡] F. Matthias Bickelhaupt,[§,⊥] Sílvia Osuna,*,[†] and Miquel Solà*,[†]

[†]Institut de Química Computacional i Catàlisi and Departament de Química, Universitat de Girona, Campus de Montilivi, 17071 Girona, Catalonia Spain

[‡]Universidad de Castilla-La Mancha, Instituto de Nanociencia, Nanotecnología y Materiales Moleculares (INAMOL), Campus de la Fábrica de Armas, 45071 Toledo, Spain

[§]Department of Theoretical Chemistry and Amsterdam Center for Multiscale Modeling (ACMM), Vrije Universiteit Amsterdam, De Boeleaan 1083, NL-1081 HV Amsterdam, The Netherlands

[⊥]Institute of Molecules and Materials (IMM), Radboud University Nijmegen, Heyendaalseweg 135, NL-6525 AJ Nijmegen, The Netherlands

S *Supporting Information*

ABSTRACT: Addition of benzyne to carbon nanostructures can proceed via (4 + 2) (1,4-addition) or (2 + 2) (1,2-addition) cycloadditions depending on the species under consideration. In this work, we analyze by means of density functional theory (DFT) calculations the reaction mechanisms for the (4 + 2) and (2 + 2) cycloadditions of benzyne to nanostructures of different curvature, namely, C$_{60}$ and a series of zigzag single-walled carbon nanotubes. Our DFT calculations reveal that, except for the concerted (4 + 2) cycloaddition of benzyne to zigzag single-walled carbon nanotubes, all cycloadditions studied are stepwise processes with the initial formation of a biradical singly bonded intermediate. From this intermediate, the rotation of the benzyne moiety determines the course of the reaction. The Gibbs energy profiles lead to the following conclusions: (i) except for the 1,4-addition of benzyne to a six-membered ring of C$_{60}$, all 1,2- and 1,4-additions studied are exothermic processes; (ii) for C$_{60}$ the (2 + 2) benzyne cycloaddition is the most favored reaction pathway; (iii) for zigzag single-walled carbon nanotubes, the (4 + 2) benzyne cycloaddition is preferred over the (2 + 2) reaction pathway; and (iv) there is a gradual decrease in the exothermicity of the reaction and an increase of energy barriers as the diameter of the nanostructure of carbon is increased. By making use of the activation strain model, it is found that the deformation of the initial reactants in the rate-determining transition state is the key factor determining the chemoselectivity of the cycloadditions with benzyne.
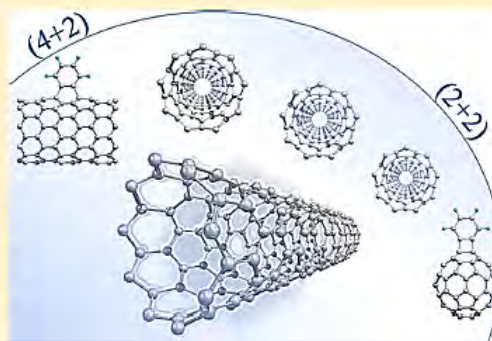
1. INTRODUCTION

Nanostructured allotropes of carbon such as fullerene C$_{60}$ and carbon nanotubes (CNTs) encompass an active area of research in many fields of nanoscience and nanotechnology.[1-4] Three decades after its discovery,[5] fullerene C$_{60}$ is still an attractive material due to its unique structure and specific properties.[6,7] Numerous derivatives can be synthesized from C$_{60}$ with the purpose of promoting applications in biology,[8] medicine,[9] and photovoltaics,[10] among others.[11,12] There is also a great interest in CNTs due to their large values of modulus of elasticity,[13,14] their high stability (they are stable up to 2800 °C in vacuum and 750 °C in air[15]), their thermal conductivity, which is even better than that of some good thermal conductors like copper,[15,16] and their particular electronic and optical properties, which depending on their sidewall curvature, chirality, and local environment can be similar to those of certain metals or semiconductors.[17-19] In

view of that, it is not difficult to imagine the synthesis of interesting materials developed from CNTs taking advantage of their outstanding thermal and electrical properties combined with high specific stiffness and strength.[20,21] In fact, functionalized CNTs have been shown to be useful assemblies in fields of materials, medical, and biological sciences.[22-24] However, the actual application of these nanomaterials is hampered because their selective purification is hard to achieve due to poor solubility of CNTs in conventional solvents or the formation of agglomerates because of their strong π-stacking tendencies.[25-27] These problems can be partially or totally solved with proper chemical modifications.[28-30] The most common chemical reactions used to functionalize carbon

Scheme 1. Generalized Representation of the Reaction Mechanisms Studied in the Current Manuscript[a]
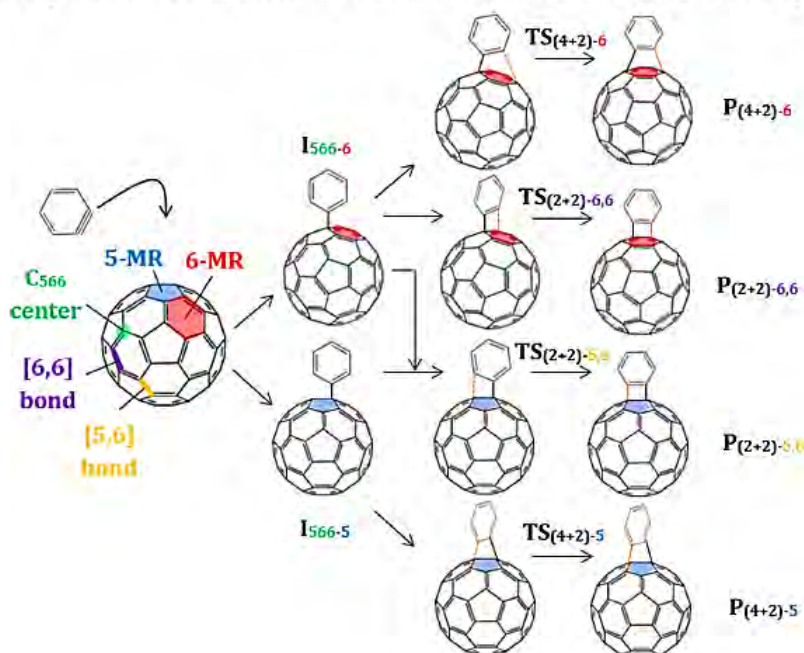
[a]Biradical singly-bonded intermediates are represented as I; transition states and final products are labeled as TS and P, respectively. Two subscripts separated by a dash are used to indicate how the species are formed; in fact, they refer to chemoselectivity−regioselectivity. The left subscript takes the values of "(4 + 2)" and "(2 + 2)" to denote whether the 1,4- or 1,2-addition takes place, respectively; but it also acquires the value of "566" indicating the formation of biradical singly-bonded structures related to the attack on a 566 carbon center (i.e., a C_{566} center, see green dot in the fullerene structure). The right subscript takes the values of "5" and "6" to indicate whether a five- or six-membered ring (see 5-MR in blue, and 6-MR in red) is under attack; but it can also have the values of "5,6" and "6,6" to denote whether a [5,6] or [6,6] bond is attacked (see, respectively, orange and purple labels). An analogous terminology is used for SWCNTs.

nanostructures are the Diels−Alder reaction, the 1,3-dipolar (Prato) cycloaddition, photochemical silylation, carbene and nitrene additions, Bingel−Hirsch reaction, and (2 + 2) cycloadditions.[31−36]

There is experimental evidence describing the chemical functionalization of fullerenes through (2 + 2) aryne cyclo-additions (1,2-additions). To our knowledge, the first study of the reaction of fullerenes and benzyne was reported by Cooks et al.[37] already in 1992. These authors found that the (2 + 2) benzyne cycloaddition (BC) to C_{60} occurs at the [6,6] bonds of C_{60} (although they did not exclude the possibility of a [5,6] addition) to form mono-, di-, tri-, and tetra-adducts. Three years later, the group of Nogami[38] characterized by X-ray the adduct of the (2 + 2) cycloaddition of 4,5-dimethoxybenzyne to C_{60}. This adduct was shown to exhibit a benzocyclobutene structure attached to a closed [6,6] bond of C_{60}. In 2001, Nishimura et al. were able to synthesize, isolate, and characterize eight regioisomers corresponding to all possible [6,6] bisadducts generated by the (2 + 2) bisaddition of 4,5-dimethoxybenzyne to C_{60}.[39] More recently, Yang et al.[40] claimed on the basis of NMR, UV−vis spectroscopy, and cyclic voltammetry, the formation of an unprecedented [5,6]-open adduct from the (2 + 2) cycloaddition of benzyne to C_{60}. In the case of C_{70}, the first studies were reported by the group of Taylor.[41,42] They found that C_{70} can accommodate up to 10 benzyne addends. From the ^{1}H NMR spectra, they concluded that benzyne addition to C_{70} gives four possible monoadducts; three of them corresponding to (2 + 2) additions to [6,6] bonds and one being the result of a (4 + 2) cycloaddition (1,4-

addition) in a six-membered ring (6-MR). In 1998, Meier et al.[43] found by X-ray crystallography that one of the four monoadducts generated by the BC to C_{70} is a closed-cage [6,6] adduct. Two of the remaining three monoadducts were assigned to [6,6] bonds additions, and the last one on the basis of ^{13}C NMR results was considered the result of a [5,6] attack to C_{70}. The first successful BC to endohedral metallofullerenes (EMFs) was carried out in Gd@C_{82} by Gu et al.[44] who reported the formation of two different (2 + 2) monoadducts. The addition of benzyne to La@C_{82} was shown to take place preferentially at the [5,6] bonds to yield close cyclobutene rings.[45] Echegoyen et al.[46] reported that the BC with $Sc_3N@I_h$-C_{80} produced two thermally stable cycloadducts corresponding to the addition of benzyne to both a [5,6] and a [6,6] bond as confirmed by the X-ray crystal structures. These bonds were found to be elongated but not broken in the resulting cycloadduct (i.e., the carbon−carbon distance is ∼1.65 Å in the final product).[47] The (2 + 2) cycloaddition of $Sc_3N@I_h$-C_{80} with 4,5-diisopropoxybenzyne also yields two adducts that were assigned to the [6,6]- and [5,6]-regioisomers.[48] As far as we know, there is not a single experimental work reporting the (4 + 2) BC to (metallo)-fullerenes. It has been claimed that small diameter carbon nanostructures like fullerenes promote better the (2 + 2) cycloaddition.[37,39]

Within the chemical functionalization of CNTs, some proposals to reach covalent junctions between functional groups and nanotubes have been already provided.[49−52] In the case of the BC to CNTs, more than one decade ago it was

suggested that the addition of arynes to single-walled CNTs (SWCNTs) could lead to the synthesis of paddle-wheel-like nanostructures.[53] Later Langa and co-workers[27,54] published the reaction between benzyne and SWCNTs under microwave irradiation with a high degree of functionalization. The authors found that the aryne addition increases the mass of SWCNTs by a factor ranging from 5% to 19%, confirming thus the functionalization of these materials. In view of that, Nagase and co-workers[55] recently described energy profiles of the $(4 + 2)$ and $(2 + 2)$ BC to armchair SWCNTs based on density functional theory (DFT) methodology. They determined that the $(4 + 2)$ cycloaddition of benzyne in a slanted position is the most favorable for large diameters of the nanotube. For small diameters (<10 Å), the $(2 + 2)$ addition in a slanted bond is preferred thermodynamically, yet kinetically the most favorable attack is the one in the perpendicular position.

In summary, benzyne reacts with fullerenes and EMFs through $(2 + 2)$ cycloadditions that occur preferentially at [6,6] bonds, although there are several examples of [5,6] attacks. For SWCNTs, cycloadditions of benzyne can produce both $(2 + 2)$ and $(4 + 2)$ adducts depending on the shape and curvature of the nanotube, as well as their intrinsic electronic nature. The mechanistic details of the BC to all these nanostructures of carbon have not been entirely elucidated yet, and the reasons for the chemoselectivity (preference of the $(2 + 2)$ over the $(4 + 2)$ BC) and regioselectivity (the [6,6] attack is more frequently found than the [5,6] addition in fullerenes) of the BCs have not been discussed to date. In this contribution, we aim to provide a comprehensive description and analysis of the chemo- and regioselectivity of the BC to different nanostructures of carbon. First, we present a study of both $(4 + 2)$ and $(2 + 2)$ additions to fullerene C_{60}. A generalization of the reaction mechanisms occurring in C_{60} is summarized in Scheme 1, wherein we have included terminology that is useful to identify every structure discussed through the whole manuscript. After defining the potential energy surface for the benzyne cycloaddition (PES-BC) to C_{60}, we discuss the PES-BC of the $(4 + 2)$ and $(2 + 2)$ BC to zigzag SWCNTs. An equivalent terminology as defined in Scheme 1 is also used in the description of the reaction mechanisms studied for zigzag SWCNTs. We do not consider armchair SWCNTs because their reaction pathways were already discussed in the work by Nagase and co-workers.[55] The effect of the sidewall curvature on the chemical reactivity of the nanostructures has been directly analyzed. To that aim, we have investigated both $(4 + 2)$ and $(2 + 2)$ additions to carbon nanostructures whose diameter ranges from 14.1 Å (large-diameter zigzag SWCNT) to 6.8 Å (i.e., fullerene C_{60}).

2. METHODOLOGY

All DFT calculations were performed using the Amsterdam Density Functional (ADF) program.[56] Molecular orbitals (MOs) were expanded in terms of an uncontracted set of Slater-type orbitals (STOs) of double-ζ (DZP) and triple-ζ (TZP) quality containing diffuse functions and one set of polarization functions. STOs correctly describe the asymptotic, long-range, and near-the-nucleus (cusp) behaviors. However, their evaluation for systems with many tens of atoms can be computationally very expensive; therefore the frozen-core approximation[56] was used, which freezes the core orbitals (i.e., the orbital 1s of the carbon atoms) during the self-consistent field procedure. It was shown that the frozen core approximation has a negligible effect on the optimized

equilibrium geometries.[57,58] Scalar relativistic corrections were also included self-consistently by using the zeroth order regular approximation (ZORA).[59,60]

Energies and gradients were calculated via the local density approximation (Slater exchange) with nonlocal corrections for exchange (Becke88)[61] and correlation (Perdew86)[62] (i.e., the BP86 functional). Moreover, energy dispersion corrections as developed by Grimme[63] (D_2) were added to the DFT energy. It has been shown that dispersion corrections are essential for a correct description of the thermodynamics and kinetics of reactions with fullerenes and nanotubes.[64] For open-shell systems, unrestricted calculations with broken symmetry were performed. This is particularly important in the case of biradical intermediates.

Geometry optimizations without symmetry constraints and analytical frequency calculations were performed in the gas phase at the BP86-D_2/DZP level of theory. Electronic energies were obtained in the gas phase with the TZP basis at the geometries optimized with the DZP basis (i.e., BP86-D_2/TZP//BP86-D_2/DZP). In the search for stationary points, the QUILD code (quantum regions interconnected by local descriptions)[65] was used. QUILD works as a wrapper around the ADF program; it creates input files for ADF, then executes the program and collects energies and gradients generated by ADF. In addition, the efficiency of QUILD is reflected in the use of techniques such as adapted delocalized coordinates and the fact that this code constructs model Hessians with the appropriate number of eigenvalues.[66] This latter feature is particularly useful for the search for transition state (TS) structures.

Relative Gibbs energies (ΔG) were determined from electronic energies at the BP86-D_2/TZP//BP86-D_2/DZP level of theory together with corrections of zero-point energies, thermal contributions to the internal energy, and entropy determined in the gas phase at 298 K with the BP86-D_2/DZP method considering an ideal gas in standard conditions. It is likely that the entropy term may be overestimated by our gas-phase calculations based on harmonic frequencies; although we expect a comparable error for the different reaction pathways and, therefore, comparisons should not be affected by this possible overestimation of the entropy correction.[67] Solvent effects were not included in the present calculations since the BC is usually carried out in rather nonpolar solvents. The absence of charge-separated species along the reaction coordinate suggests that solvent effects are unimportant in this reaction.

Finally, in the Supporting Information we provide a detailed description of the construction of the SWCNT models to be used in computational modeling (see Figure S1 and additional explanation; also see Table S1 and Figure S2 and discussion for a comparative study of the benzyne cycloaddition to SWCNT constructed with different approaches). Moreover, for all structures we make sure that the number of cells is suitable for the purpose of our study; that is, electronic properties such as electronic energies were conveniently converged with respect to the size of the implemented model (see Table S2 and associated discussion).

3. RESULTS AND DISCUSSION

This section is divided into two parts. Section 3.1 contains a detailed study of the BC to C_{60} with an exhaustive description of the different reaction pathways. Then, by making use of the information in section 3.1, in section 3.2, the reaction

Article
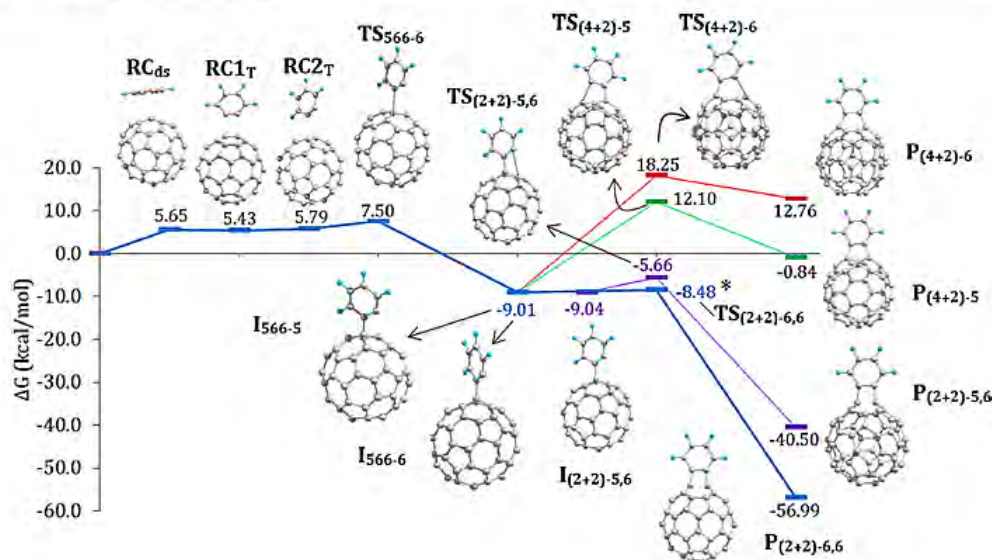
Figure 1. Gibbs energy profile (in kcal/mol) for the (2 + 2) (in blue and purple) and (4 + 2) (in red and green) benzyne cycloadditions to fullerene C_{60}. The energy for the transition state for the rotation toward a [6,6] bond marked with a star (*), $TS_{(2+2)-6,6}$, corresponds to a linear-transit maximum point (see Figure 2). Blue and purple colored ΔG values stand for open-shell singlet structures.

mechanisms for zigzag SWCNTs are reported. The introduction of nanotubes of different diameter enables us to discuss the curvature effect of sidewall BC to different nanostructures of carbon. The effect of the curvature is studied with activation strain analyses at the transition state of the (2 + 2) and (4 + 2) reactions.

3.1. Benzyne Cycloaddition to C_{60}. As far as we know, a detailed mechanistic study of the BC to C_{60} has not been consistently established yet. We, therefore, explore the PES-BC to C_{60} considering the four possible cycloadducts produced from the 1,2-addition to [5,6] and [6,6] bonds and the 1,4-addition to 5- and 6-MRs. The Gibbs energy profile in terms of changes in Gibbs energies for the formation of the four different adducts is depicted in Figure 1.

In the first stage of the reaction mechanism, a reactant complex (RC) is formed in which the main interactions between benzyne and C_{60} are noncovalent.[68] We distinguish two arrangements of benzyne with respect to the fullerene surface, RC_{ds} and RC_T; subscripts ds and T standing for displaced sandwiched and T-shaped configurations as schematized in Figure 1. Nevertheless, a detailed analysis of the structure and energy of those species is provided in Figures S3 and S4 in the Supporting Information. In the first TS structure, namely, TS_{566-6}, benzyne is attacking a C atom in the ring junction between one five-membered ring (5-MR) and two six-membered rings (6-MRs) of C_{60} to generate a biradical singly bonded intermediate, I_{566-6}. In both the TS and intermediate, the C≡C of benzyne is oriented toward a 6-MR of the cage as shown in Scheme 1. TS_{566-6} has a small imaginary frequency due to the flatness of the PES-BC, 23.2i cm^{-1}, with a normal mode that suggests a reaction progress toward an intermediate structure with biradical character in which only one carbon in benzyne is covalently attached to a C_{566} center. The ability of benzyne to rotate in a very flat surface also gives rise to the formation of an orientational isomer, I_{566-5}, isoenergetic to I_{566-6}. More importantly, the description of the (2 + 2) and (4 + 2) BC to C_{60} can be consistently done from the idea of a rotating benzyne, the formation of biradical singly bonded

intermediate structures being the rate-determining step of the (2 + 2) reaction (but not for the (4 + 2) addition, see Figure 1). For all singly bonded intermediates and transition states, we determine that triplet ($\langle S^2 \rangle \approx 2.0$) and open-shell singlet ($\langle S^2 \rangle \approx 1.0$) biradical structures present similar energies (absolute energy differences of ca. 0.5 kcal/mol) indicating a weak spin coupling between the unpaired electrons of the two fragments. However, these energy comparisons are done at the open-shell singlet optimized geometry; therefore we deduce that a geometry relaxation for the triplet state could slightly stabilize it, and consequently, the ground state for biradical singly bonded structures could be the triplet state. Additionally, it is worth mentioning that small deformations of spherical C_{60} can bring about an appearance of fine structure in the electronic energy spectrum compared with the spherical case.[69] Still, we assume that the system follows the singlet potential energy surface through the entire reaction pathway since the singlet-to-triplet spin-crossing is expected to be not allowed due to the small spin-coupling term of the dipole moment of the transition integral. In fact, the major change between the open-shell singlet and triplet spin densities is located in the two radical carbon atoms. Additional information in the electronic structure and spin–orbit interactions for carbon nanostructures can be found in the works by Ando[70] and Pincak et al.[71−73]

As mentioned earlier, the biradical singly bonded intermediate I_{566-5} and I_{566-6} structures are the key structures leading to the different cycloadducts: I_{566-5} presents the benzyne faced to a 5-MR, and thus it is the precursor of the 1,4-addition to a pentagonal ring, whereas I_{566-6} faced to 6-MR leads to the formation of 6-MR-based cycloadducts. At these points, the (4 + 2) addition of benzyne can take place via $TS_{(4+2)-5}$ or $TS_{(4+2)-6}$ to yield $P_{(4+2)-5}$ and $P_{(4+2)-6}$, respectively. The (4 + 2) BC to C_{60} is kinetically hampered in view of the larger energy barriers (more than 20 kcal/mol) compared with its (2 + 2) BC counterpart. Moreover, the formation of $P_{(4+2)-6}$ is an endergonic process.

The possible rotation of benzyne in the intermediate structures is now evaluated to formulate a mechanistic pathway

leading to the (2 + 2) cycloadducts as schematized in Figure 2a. Coincidently the rotating-benzyne mechanism has been formulated very recently for EMFs by Zhao et al.[74] There are two types of bonds to be attacked: [5,6] and [6,6] bonds. From I_{566-5}, only [5,6] bonds can be attacked to achieve the product resulting from the (2 + 2) BC, $P_{(2+2)-5,6}$. Nevertheless, from I_{566-6} both types of bonds are available to react giving rise to either $P_{(2+2)-5,6}$ or $P_{(2+2)-6,6}$. This situation shows that [5,6] adducts in C_{60} are statistically favored. We have performed linear transit (LT) calculations to assess the energetic cost for the rotation of benzyne in the biradical singly bonded intermediates (see Figure 2b–d). Our LT results indicate that the carbon–carbon bond between benzyne and C_{60} in both structures I_{566-6} and I_{566-5} can freely rotate since the rotation occurs in a practically barrierless process. In Figure 2, the dihedral angle φ is monitored in order to describe the benzyne rotation. Bonds [6,6] and [5,6] are defined at $\varphi = 0°$ and $\varphi = 124°$, respectively. In this context, φ in I_{566-6} must be decreased from 103° to 0° to reach a [6,6] bond. The maximum point of the linear transit toward a [6,6] bond is

given at $\varphi = 50°$, and it provides an upper bound limit representing an energy barrier of 0.53 kcal/mol (see Figure 2b). This energetic cost is reported in Figure 1 as $TS_{(2+2)-6,6}$. This small energy barrier for the (2 + 2) addition toward the [6,6] bond demonstrates that the rate-determining step for this process is given by the precursor TS_{566-6}. For the (2 + 2) BC to a [5,6] bond, we were able to locate another biradical singly bonded intermediate, $I_{(2+2)-5,6}$ resulting from the rotation of benzyne toward a [5,6] bond ($\varphi = 124°$) from either I_{566-6} ($\varphi = 103°$) or I_{566-5} ($\varphi = 174°$) (see Figure 2c,d, respectively). This rotation does not lead to a ring closure as observed for [6,6]. Unlike the barrierless ring closure on a [6,6] bond, the course of the (2 + 2) BC is slightly hampered by an energy barrier of 3.4 kcal/mol characterized by a true transition state associated with the four-membered ring closure, $TS_{(2+2)-5,6}$.

Our complete analysis of the (4 + 2) and (2 + 2) cycloaddition to C_{60} indicates that the (2 + 2) BC to the [6,6] bond of C_{60} is the most kinetically and thermodynamically favored reaction pathway. However, the difference in Gibbs energy barriers between [5,6] and [6,6] additions is small; as a result we do not entirely discard the possibility of observing the (2 + 2) BC on a [5,6] bond. These results are in line with the experimental observation that only (2 + 2) BC are observed in fullerenes and that both [6,6] and [5,6] additions have been reported in the literature, with the [6,6] addition being more frequently observed than the [5,6] one.[37,38,40–42]

We have also investigated the possible open-cage structure of $P_{(2+2)-5,6}$ and $P_{(2+2)-6,6}$. Our results suggest that an open-cage structure of $P_{(2+2)-6,6}$ is not possible since we were not able to locate any structure with a long (>2 Å) attacked C–C [6,6]-bond. Nevertheless, an open-cage $P_{(2+2)-5,6}$ was characterized to be a local-minimum structure; yet the Gibbs energy in this structure is 4.3 kcal/mol above the energy of its closed-cage counterpart. Besides, the maximum point of a linear transit going from closed to open cage is calculated at 5.6 kcal/mol (see Figure S5 in the Supporting Information). The structural deformation in the open-cage $P_{(2+2)-5,6}$ is significantly larger than that of the closed-cage cycloadduct (by 57.3 kcal/mol). This is partially but not fully compensated by the large interaction energy in open-cage $P_{(2+2)-5,6}$ due to better frontier orbital interactions among the deformed benzyne and C_{60} moieties.[75] We conclude that a closed-cage product is more likely to be observed. In this regard, our results resemble the work of Iyoda et al.,[38] wherein the closed-cage product on a [6,6] bond is the most stabilized cycloadduct and it can be produced with a low-energy barrier; even though it is also suggested that the BC on a [5,6] may be kinetically competitive. On the other hand, when the reactant is 4,5-dibutoxybenzyne, Yang et al.[40] suggested the formation of an open-cage [5,6] cycloadduct based on indirect evidence taken from ^1H and ^{13}C NMR, UV–vis spectra, and cyclic voltammetry results. From our calculations and taking into account similar experimental evidence,[38,47] we conclude that the BC to C_{60} can be conducted toward the formation of both cycloadducts $P_{(2+2)-6,6}$ and $P_{(2+2)-5,6}$, but we cannot support the hypothesis of open-cage structures.

3.2. Benzyne Cycloaddition to SWCNTs and the Curvature Effect.
Models designed to construct SWCNTs under the Clar theory have been named finite-length Clar cells (FLCC), and we refer the reader to the seminal papers dealing with this subject.[76–80] In this regard, we make use of complete Clar networks, which are fully benzenoid structures (see Scheme 2). These structures are more stable than their

Figure 2. Schematic representation of the rotation of benzyne through stationary structures before ring closure. (a) For I structures, a dihedral angle φ is defined by the two carbon atoms in a [6,6] bond and the two aryne ones (indicated in blue). (b) Linear transit (LT; relative energy with respect to I_{566}) for the rotation of benzyne from I_{566-6} toward a [6,6] bond. (c) LT for the rotation of benzyne from I_{566-6} toward a [5,6] bond. (d) LT for the rotation of benzyne from I_{566-5} toward a [5,6] bond.

Scheme 2. Graphical Representation of the Clar's Aromatic π-Sextet Rule in (a) Phenanthrene, and (b) a Two-Cell Armchair SWCNT[a]

aromatic π-sextet

The Clar structure has the largest number of aromatic π-sextet

The Clar structure for a 2-cells armchair SWCNT
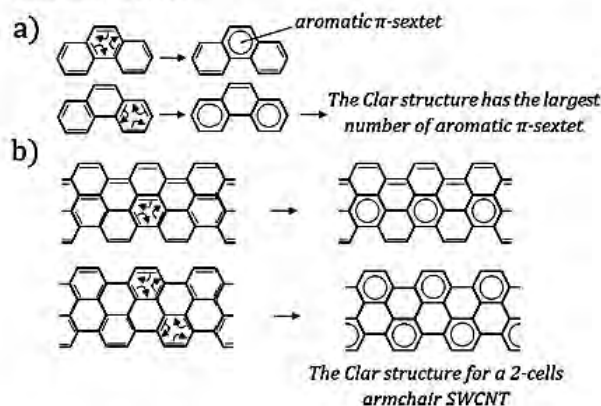
[a]The rule states that a Clar structure is the one with the largest number of aromatic π-sextets. For a given polycyclic aromatic hydrocarbon (PAH), the Clar structure is the structure that better agrees with the experimental behavior of the PAH.

Figure 3. Finite-length Clar 3-cell models and unit cells for (a) (9,0)-SWCNT, (b) (8,0)-SWCNT, and (c) (13,0)-SWCNT. Models for (12,0)- and (18,0)-SWCNT follow the same structural pattern as (9,0)-SWCNT. Benzenoid centers studied in this contribution are highlighted with a gray-filled hexagon. Dangling bonds are saturated with hydrogen atoms.

counterpart Kekulé structures because aromaticity provides stability to conjugated systems due to the nature of molecular orbitals.[51,81−84] However, by taking into consideration a molecular orbital model based on orbital-overlap arguments, the aromatic character of molecular systems involving π electrons has been purposed to be strongly influenced by the geometry of the ring structure; as a result a regular or distorted geometrical arrangement indeed affects the aromaticity or antiaromaticity in the system.[85,86] In addition, complete Clar network models for SWCNTs are fully benzenoid structures, have closed-shell singlet ground states (at variance with many non-FLCC), and reach faster convergence in their electronic properties with respect to the number of cells of the nanotube than conventional models for SWCNTs. In this FLCC classification, we select three different structures: (9,0)-, (12,0)-, and (18,0)-SWCNT. Additionally, we include some FLCC structures lacking completeness of the Clar network such as (8,0)- and (13,0)-SWCNT. All models are represented in Figure 3.

The BC to (9,0)-SWCNT is first described since the mechanistic details are exactly the same for all considered SWCNTs. As can be seen in Figure 4, the reaction starts with the formation of RC_{ds} (a true local-minimum point in the PES-BC) followed by TS structures for either the (4 + 2) or (2 + 2) BC. We were not able to optimize a RC_T structure. Like the BC to C_{60}, we confirmed $TS_{666\text{-}6}$ to be a transition structure with a frequency of 254.3i cm^{-1} associated with a normal mode connecting RC_{ds} and the intermediate structure $I_{666\text{-}6}$. To reach $TS_{666\text{-}6}$, benzyne has to be approximated to the nanotube surface with one of the aryne carbon atoms at a distance of 2.01 Å and a dihedral angle (as described in Figure 5a) of φ = 66°. The formation of the intermediate structure $I_{666\text{-}6}$ has a Gibbs energy barrier of 9.8 kcal/mol. Observe that both $TS_{666\text{-}6}$ and $I_{666\text{-}6}$ present one of the aryne carbon atoms oriented toward a C_{666} center of the nanotube, and the other one toward a 6-MR (following the definitions introduced in Scheme 1). Therefore, the benzyne rotation observed in the case of C_{60} to yield the different cycloadducts also occurs in SWCNTs.

Once the biradical singly bonded intermediate $I_{666\text{-}6}$ is formed, the final (2 + 2) cycloadduct formation can take place via two different pathways: the attack of benzyne following a parallel orientation "p" with respect to the nanotube axis (shown in blue in Figure 4) or in an oblique fashion "o" (in red, Figure 4). One could therefore postulate the formation of the two possible intermediates that arise from these two orientations, that is, $I_{(2+2)\text{-}p}$ or $I_{(2+2)\text{-}o}$. The former could not be, however, characterized since the (2 + 2) BC evolves toward ring closure before the rotation of benzyne in $I_{666\text{-}6}$ is completed (check LT calculations in Figure S6). As a matter of fact, the biradical singly bonded intermediate $I_{666\text{-}6}$ localizes benzyne with a distance of 1.54 Å and φ = 100°, and the rotation toward a parallel position means reducing φ to 0°. Analogously, the oblique position is found at φ = 120°. In the case of a (2 + 2) BC in parallel orientation, we in fact optimized a first-order saddle point at φ = 19°. The vibrational frequency calculation confirmed a small negative frequency of 75.3i cm^{-1} due to the flatness of the PES-BC; and the associated normal mode suggests that this is a transition state for the rotation of benzyne from $I_{666\text{-}6}$ toward the parallel position (i.e., $TS_{666\text{-}p}$). Nonetheless, the small energy barrier of 3.7 kcal/mol calculated with $TS_{666\text{-}p}$ indicates that the reaction evolves to the formation of $P_{(2+2)\text{-}p}$ practically in a barrierless process (see details in Figure S6); thus $I_{(2+2)\text{-}p}$ and $TS_{(2+2)\text{-}p}$ could not be characterized. In the case of the oblique position, we optimized another first-order saddle point at φ = 105° but with the unbounded carbon atom in benzyne closer to the unbounded carbon atom in (9,0)-SCWNT (2.44 Å; this distance is 2.86 Å in $I_{666\text{-}6}$). The vibrational frequency calculation confirmed a negative frequency of 279.5i cm^{-1} associated with a normal mode resembling a ring closure; therefore we distinguish this structure as a true transition state for the ring closure of the (2 + 2) BC in oblique position, $TS_{(2+2)\text{-}o}$. Since $TS_{(2+2)\text{-}o}$ is not exactly localized at the oblique position (φ = 120°), we deduce that the reaction can proceed without previous formation of $I_{(2+2)\text{-}o}$. The energy barrier calculated with $TS_{(2+2)\text{-}o}$ is also
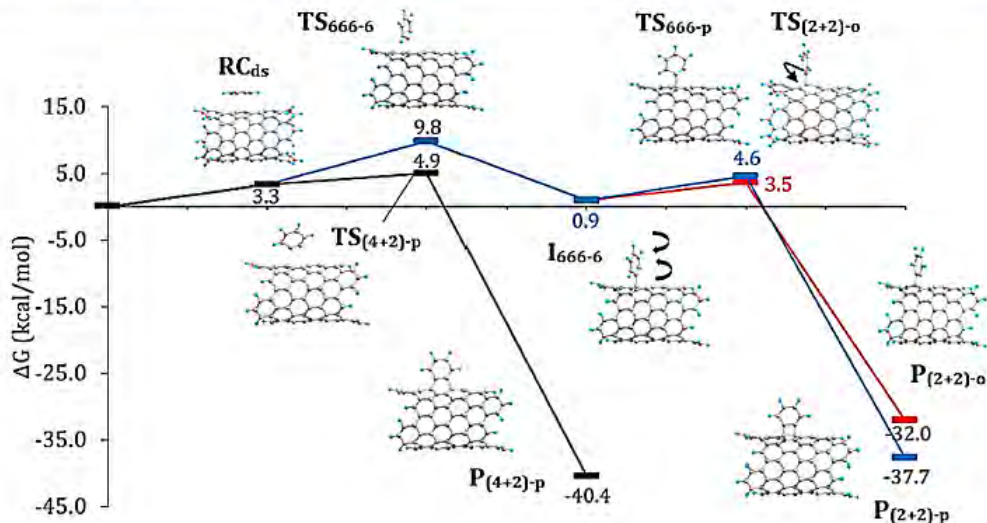
Figure 4. Gibbs energy profiles for the (2 + 2) (for blue and red lines, benzyne is, respectively, added in parallel and oblique position with respect to the nanotube axis) and (4 + 2) (black line) benzyne cycloadditions to (9,0)-SWCNT. Blue and red colored ΔG values stand for open-shell singlet structures.
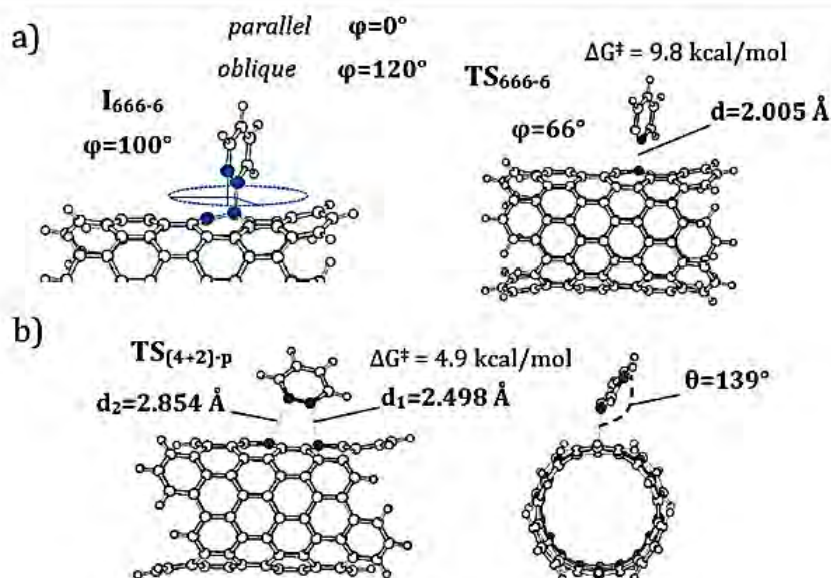
Figure 5. Schematic representation of the rotation and bent orientation of benzyne in the different stationary structures before ring closure occurs. (a) A dihedral angle φ is defined by the four blue-colored carbon atoms and used in the structural description of intermediate and transition state structures through the (2 + 2) BC. (b) A tilt angle θ is depicted and used in the structural description of the (4 + 2) BC. Gibbs energy barriers $\Delta G^{\ddagger}$ and some relevant distances between black-colored carbon atoms are given for TSs.

small, 2.6 kcal/mol, thus concluding that the (2 + 2) BC can equally proceed at parallel and oblique positions.

In the case of the (4 + 2) BC, $P_{(4+2)\text{-o}}$ is highly destabilized since its energy lies 9.2 kcal/mol above the energy of the reactants; consequently benzyne can only add to the parallel position with respect to the nanotube axis. In this regard, a TS structure was also obtained (with an imaginary frequency of 39.6i cm^{-1}, see linear transit in Figure S7 in the Supporting Information). In RC_{ds}, benzyne is completely tilted with θ = 89.9° (the tilt angle θ is defined in Figure 5b), and the aryne carbon atoms are localized at 3.27 Å from the nanotube surface. To reach $TS_{(4+2)\text{-p}}$ the tilt angle is reduced (θ = 139.1°) and

benzyne is approximated to the nanotube surface at a distance of 2.50 Å, which is longer than the distance in $TS_{666\text{-}6}$ (compare Figure 5, panels a and b). The structure $TS_{(4+2)\text{-p}}$ depicted in Figure 5b is a concerted transition state leading to $P_{(4+2)\text{-p}}$ with a Gibbs energy barrier of only 4.9 kcal/mol. We conclude therefore that the (4 + 2) BC to (9,0)-SWCNT in parallel position is both kinetically and thermodynamically favored. This notwithstanding, the binding energies of benzyne to (9,0)-SWCNT for the (4 + 2) and (2 + 2) differ only by a few kcal/mol as reported recently by Vasiliev et al. in a series of zigzag SWCNTs.[87]

The Journal of Physical Chemistry C

The mechanism as formulated in (9,0)-SWCNT can be also applied for the rest of the structures under consideration. In Table 1, we report reaction energies (ΔE) for the formation of benzyne cycloadducts as well as the initial activation energy E_a^I (i.e., the energy barrier from the reactant complex to the following TS). Results in Table 1 demonstrate that the (4 + 2) BC is always the preferred reaction pathway for finite-diameter zigzag SWCNTs because of the substantially lower E_a^I. It is also observed that the larger the curvature of the SWCNT, the lower the energy barriers and the larger the exothermicity[87] of the (2 + 2) and (4 + 2) additions. Moreover, P$_{(4+2)\text{-}p}$ is the most stabilized product in all the cases, and thus the kinetics and thermodynamics correspond to the same addition.

We also investigated the mechanistic details of the BC to nonbenzenoid centers like those reaction sites found at (8,0)- and (13,0)-SWCNTs and non-FLCC structures (the latter being zigzag SWCNTs uniformly cut at the tube ends with a high-spin ground state and electron localization at the edges). We reach the conclusion that the (4 + 2) BC in parallel position to non-benzenoid centers and non-FLCC models of (n,0)-SWCNTs is still favored (see Figures S2 and S8 and Tables S1 and S3 and discussion in the Supporting Information for complete details).

Nagase and co-workers[55] concluded that the activation energy for large-diameter (n,n)-SWCNTs is lower for the (4 + 2) BC but the (2 + 2) products are the most stable. Our results in Table 1 show that a gradual increase of the diameter of the SWCNT causes a steady increase in E_a^I and ΔE for both types of BC. This trend resembles the tendency observed by Nagase et al.[55] In zigzag SWCNTs, however, the (4 + 2) addition is for all diameters preferred kinetically and thermodynamically over the (2 + 2) one.

To explain changes in reactivity due to the curvature of the nanostructure, we make use of the activation strain model, ASM,[88−91] also known as distortion/interaction model.[92−94] ASM is a helpful tool to better understand the origin of energy barriers. These barriers are analyzed in terms of strain and interaction energies between fragments participating in the formation or rupture of chemical bonds. Figure 6 schematizes the ASM for the BC to (9,0)-SWCNT.

In the ASM, activation energies can be separated into strain and interaction energies, that is, $\Delta E^{\ddagger} = \Delta E_{\text{strain}}^{\ddagger} + \Delta E_{\text{int}}^{\ddagger}$. The strain energy, $\Delta E_{\text{strain}}^{\ddagger}$, is the energy required to deform reactants from their equilibrium geometry into the geometry they acquire in the activated complex, and the transition state interaction energy, $\Delta E_{\text{int}}^{\ddagger}$, is the interaction energy between the deformed reactants in the transition state. This model can be

Figure 6. Schematic representation of the activation strain model for the cycloadditions of benzyne to (9,0)-SWCNT: (a) parallel (4 + 2) BC; (b) parallel (2 + 2) BC. Red, green, and black lines correspond to strain, interaction, and total energies, respectively.

extended through all the structures along the reaction coordinate; but here we only focus on the localized stationary points. Figure 6a shows that the (4 + 2) BC to (9,0)-SWCNT evolves with practically no deformation of the reactants, while for the (2 + 2) BC involves the formation of intermediate structures in which the reactants are significantly deformed before the ring closure. Despite the fact that (4 + 2) BC generates a more deformed 6-MR structure (ΔE_{strain} = 80.5 kcal/mol for P$_{(4+2)\text{-}p}$), we confirm that the formation of the less-strained 4-MR structure produced through the (2 + 2) BC (ΔE_{strain} = 56.7 kcal/mol for P$_{(2+2)\text{-}p}$) is not favored due to the preceding formation of a biradical singly bonded TS (ΔE_{strain} = 7.9 kcal/mol for TS$_{666\text{-}6}$), which cannot compete with the unstrained concerted transition state in the (4 + 2) BC (ΔE_{strain} = 1.2 kcal/mol for TS$_{(4+2)\text{-}p}$). Since the interaction energy is practically the same at the first TS of both BCs (−14.6 and −15.5 kcal/mol for the (4 + 2) and (2 + 2) BC, respectively), we conclude that the strain energy determines the course of the reaction. Therefore, those cycloadducts produced via a "less strained" reaction pathway will be favored. The same conclusion was reached by Houk and Osuna in a study of a series of (4 + 2) cycloadditions to PAHs.[95]

It is more illustrative to carefully analyze the TS energy, $\Delta E^{\ddagger}$, at the first step of the BC to SWCNTs. Figure 7 shows the evolution of $\Delta E_{\text{strain}}^{\ddagger}$ and $\Delta E_{\text{int}}^{\ddagger}$ as a function of the diameter and shape of the nanostructures, and Table 2 reports some structural parameters for the species under consideration. Observe that benzyne is farther and more tilted for tube-shaped structures with smaller diameters. This result agrees with the Hammond postulate that follows naturally from the ASM and states that more exothermic reactions have TSs with more reactant-like character.[84,96] In order to examine $\Delta E^{\ddagger}$ for C$_{60}$, the second TSs (i.e., those TSs related to the ring closure, TS$_{(2+2)}$ and TS$_{(4+2)}$) must be taken into consideration since the first TS (TS$_{566\text{-}6}$) is common for both BCs. Accordingly, it is

Table 1. Initial Activation Energies (E_a^I) and Reaction Energies (ΔE) in Terms of Electronic Energy (kcal/mol) as a Function of the Diameter of the Structure (Å)^a

		E_a^I		ΔE	
(n,m)	diameter	(4 + 2)	(2 + 2)	(4 + 2)	(2 + 2)
(8,0)	6.26	1.25	4.74	−61.68	−59.49
(9,0)	7.05	1.32	5.67	−57.39	−53.92
(12,0)	9.39	2.36	7.94	−47.88	−45.17
(13,0)	10.18	2.42	7.81	−47.28	−42.61
(18,0)	14.09	5.22	8.90	−39.54	−37.81

$^a\Delta E$ is the energy difference between products and reactants. E_a^I is the energy difference between the first transition state and the reactant complex.
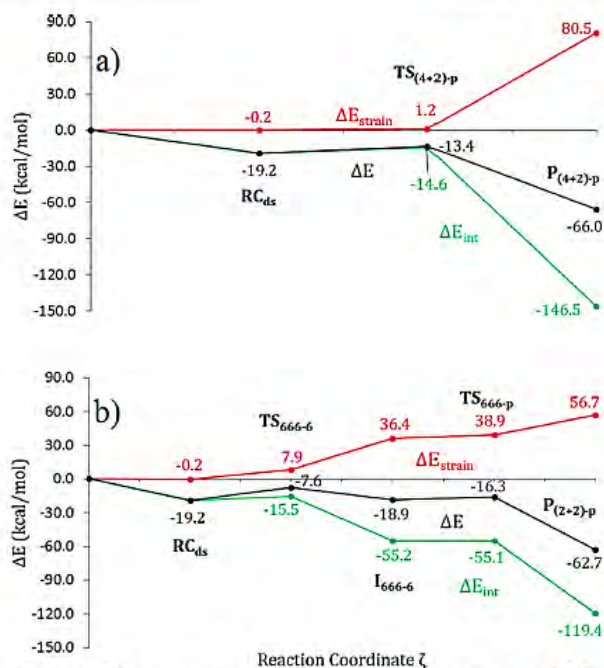
Figure 7. Strain energy, $\Delta E^{\ddagger}_{strain}$ (top), and transition state interaction, $\Delta E^{\ddagger}_{int}$ (bottom), as a function of the diameter and shape of the carbon nanostructure. Black and blue bars, respectively, correspond to the (2 + 2) and (4 + 2) BC. Green and red bars account for the TS energy ($\Delta E^{\ddagger} = \Delta E^{\ddagger}_{strain} + \Delta E^{\ddagger}_{int}$) for the (2 + 2) and (4 + 2) BC, respectively. In the case of C_{60}, the values correspond to $TS_{(2+2)\text{-}5,6}$ and $TS_{(4+2)\text{-}5}$. For SWCNTs, the first (2 + 2) TS is compared with the (4 + 2) TS.

Table 2. Some Structural Parameters of the Main Transition State Structures for the Cycloaddition of Benzyne to Different Carbon Nanostructures[a]

	(2 + 2)		(4 + 2)		
	d	φ	d_1	d_2	θ
C_{60}[b]	1.505	123.1	1.575	2.302	
(8,0)	2.065	74.7	2.498	2.698	134.2
(9,0)	2.005	66.2	2.498	2.854	139.1
(12,0)	1.949	62.1	2.258	2.811	149.5
(13,0)	1.936	61.8	2.258	2.791	149.8
(18,0)	1.925	60.9	2.165	2.750	150.4

[a]Distances in Å and angles in degrees. [b]Structures are $TS_{(2+2)\text{-}5,6}$ and $TS_{(4+2)\text{-}5}$.

expected that the reactants in both (4 + 2) and (2 + 2) BCs are significantly deformed at the TS structures $TS_{(2+2)}$ and $TS_{(4+2)}$ because one carbon atom of C_{60} is already covalently linked to one carbon atom of benzyne, thus bringing about relatively larger deformation (when compared with $\Delta E^{\ddagger}_{strain}$ in SWCNTs), which is only compensated by larger values of the interaction energy, as shown in Figure 7. In C_{60}, the (4 + 2) TS involves a larger deformation by 7.8 kcal/mol compared with the corresponding (2 + 2) TS due to the higher C_{60} distortion required for the formation of a 6-MR ring. Furthermore, the interaction energy for the (2 + 2) TS is more favored by 9.6 kcal/mol; as a result, the (4 + 2) BC to C_{60} is disfavored not only by the structural strain but also by the interaction energy. In the case of the tube-shaped nanostructures, the interaction between reactants at the (2 + 2) TS is slightly more favored than their counterpart (4 + 2) by 3.9 to 0.4 kcal/mol. This outcome certainly suggests that the structural strain is the main factor determining the reactivity of the carbon nanostructure. That is to say, for SWCNTs there is more deformation of the reactants in the (2 + 2) TSs, being from 6.8 to 4.4 kcal/mol more strained than the (4 + 2) TSs, which in fact hinders the course of the (2 + 2) BC. The origin of the increased distortion in the TS as the diameter of the SWCNT increases is due to the initially less and in the TS more pyramidalized carbon atoms in the nanotubes with larger diameters. In Table 2, the distances d_1 and d_2 previously defined in Figure 5b are shown. As the nanotube diameter increases, distances d_1 and d_2 decrease.

Consequently, the reacting carbon atoms in the nanotube have to adopt a closer situation to an sp^3-type geometrical configuration, which causes more deformation.

The nearly null variation in $\Delta E^{\ddagger}_{int}$ as a function of the diameter of the nanotube observed in Figure 7 can be partially explained in terms of frontier molecular orbital (FMO) theory. In Table S4 in the Supporting Information, HOMO and LUMO energies of each one of the fragments (i.e., benzyne and $(n,0)$-SWCNT) interacting in the corresponding TS for both (4 + 2) and (2 + 2) BCs are reported. We observe no significant variation of the HOMO and LUMO energies of the interacting fragments comparing the smallest against the largest diameter nanotube under study, a result that is attributed to the negligible variation in $\Delta E^{\ddagger}_{int}$ as the curvature of the structure is increased, thus reinforcing our conclusions that the structural deformation is indeed the main factor determining the chemoselectivity of the cycloadditions with benzyne.

4. CONCLUSIONS

In this work, we have studied the mechanisms for the sidewall cycloadditions of benzyne to different nanostructures of carbon to account for the chemoselectivity ((2 + 2) vs (4 + 2) additions) and regioselectivity ([5,6] vs [6,6] in fullerenes or parallel vs oblique addition in nanotubes) of the reaction. The (2 + 2) additions are preferred over the (4 + 2) for C_{60} and for the armchair SWCNTs of small diameter, whereas the zigzag SWCNTs and the armchair SWCNTs of large diameter favor the (4 + 2) attack.[54] From the results obtained in the present work and previous studies (the following conclusions 2 and 4 are extracted from refs 74 and 55, respectively), we reach the following picture for the benzyne cycloaddition to carbon nanostructures of different curvature:

1. In C_{60}, once the biradical singly bonded intermediate structure is formed, the rotation of benzyne in such an intermediate leads to the formation of closed-cage (2 + 2) cycloadducts in a practically barrierless process. The attack on a [6,6] bond of the cage produces the most kinetically and thermodynamically preferred reaction pathway, in good agreement with experimental evidence. Nonetheless, the attack on a [5,6] bond kinetically competes with the attack on a [6,6] bond; therefore the corresponding [5,6] product can be also observed as suggested in previous reports based on indirect experimental evidence.

2. For the $X_3N@C_{80}$ (X = Sc, Y) endohedral metallofullerenes,[74] the situation is similar. The (2 + 2) addition is preferred over the (4 + 2) one and the [5,6] and [6,6] attacks compete, although the former is favored in the case of $Sc_3N@C_{80}$.

3. For zigzag SWCNTs, the sidewall (4 + 2) cycloaddition of benzyne in the parallel position to the SWCNTs is the most kinetically and thermodynamically preferred reaction pathway. When the diameter of the zigzag SWCNTs increases, the energy barrier increases and the exothermicity of the reaction decreases.

4. In armchair SWCNTs,[55] the (4 + 2) cycloaddition of benzyne in an oblique position is the most favorable for large diameters of the nanotube. For small diameters, the oblique (2 + 2) addition is preferred thermodynamically, whereas kinetically the most favorable attack is the one in the perpendicular (or orthogonal) position. Like zigzag nanotubes, when the diameter of the armchair SWCNTs

The Journal of Physical Chemistry C

increases, the reaction becomes less exothermic and the energy barrier increases.

The changes in chemoselectivity and regioselectivity can be explained in terms of structural strain and interaction between reactants. Thus, the sidewall (4 + 2) cycloaddition to zigzag SWCNTs evolves with practically no structural deformation making it the most favorable reaction pathway.

ASSOCIATED CONTENT

Supporting Information

The Supporting Information is available free of charge on the ACS Publications website at DOI: 10.1021/acs.jpcc.5b11499.

Construction of conventional single-walled carbon nanostructures (i.e., non-Clar structures) and detailed explanation of how they are built, the four possible additions to conventional structure of (9,0)-SWCNT, comparison between reaction energies (considering reactants, reactant complex, transition states, and cyclo-adducts for both (4 + 2) and (2 + 2) additions) obtained with this model of (9,0)-SWCNT and the one constructed under the Clar theory with detailed discussion, performance of the size of the model implemented to construct (9,0)-SWCNT, potential energy surface for noncovalent interactions between benzyne and C_{60}, potential energy surface corresponding to the rupture of the attacked [5,6] bond of C_{60} in the (2 + 2) cycloadduct, linear transits around the transition state structures involving the ring closure of the (2 + 2) and (4 + 2) cycloadditions of benzyne to (9,0)-SWCNT, cycloadditions of benzyne to benzenoid and non-benzenoid reaction sites, comparison of the reaction energies calculated on a benzenoid reaction site with the analogous non-benzenoid ones, HOMO and LUMO absolute energies for interacting fragments in the first TS structure of the benzyne cycloadditions, orbital energies for fragments benzyne and (8,0)-SWCNT and benzyne and (18,0)-SWCNT, bibliography related to the construction of single-walled carbon nanotubes, Carte-sian coordinates and Gibbs and electronic energies for all optimized structures of reactants, reactant complexes, transition states (with their respective imaginary frequency), and cycloadducts, including structures derived from conventional nanotube models and non-benzenoid centers, as well as six-unit-cells structures (PDF)

AUTHOR INFORMATION

Corresponding Authors
*E-mail: silvia.osuna@udg.edu.
*E-mail: miquel.sola@udg.edu.

Notes
The authors declare no competing financial interest.

REFERENCES

(1) Yang, Z.; Ren, J.; Zhang, Z.; Chen, X.; Guan, G.; Qiu, L.; Zhang, Y.; Peng, H. *Chem. Rev.* 2015, *115*, 5159−5223.
(2) Su, D. S.; Perathoner, S.; Centi, G. *Chem. Rev.* 2013, *113*, 5782−5816.
(3) Delgado, J. L.; Herranz, M.; Martín, N. *J. Mater. Chem.* 2008, *18*, 1417−1426.
(4) Li, Z.; Liu, Z.; Sun, H.; Gao, C. *Chem. Rev.* 2015, *115*, 7046−7117.
(5) Kroto, H. W.; Heath, J. R.; O'Brien, S. C.; Curl, R. F.; Smalley, R. E. *Nature* 1985, *318*, 162−163.
(6) Kroto, H. W.; Allaf, A. W.; Balm, S. P. *Chem. Rev.* 1991, *91*, 1213−1235.
(7) Thilgen, C.; Diederich, F. *Chem. Rev.* 2006, *106*, 5049−5135.
(8) Jennepalli, S.; Pyne, S. G.; Keller, P. A. *RSC Adv.* 2014, *4*, 46383−46398.
(9) Tong, J.; Zimmerman, M. C.; Li, S.; Yi, X.; Luxenhofer, R.; Jordan, R.; Kabanov, A. V. *Biomaterials* 2011, *32*, 3654−3665.
(10) Li, C.-Z.; Yip, H.-L.; Jen, A. K.-Y. *J. Mater. Chem.* 2012, *22*, 4161−4177.
(11) Babu, S. S.; Praveen, V. K.; Ajayaghosh, A. *Chem. Rev.* 2014, *114*, 1973−2129.
(12) Martín, N.; Sánchez, L.; Illescas, B.; Pérez, I. *Chem. Rev.* 1998, *98*, 2527−2548.
(13) Yang, Y. H.; Li, W. Z. *Appl. Phys. Lett.* 2011, *98*, 041901.
(14) Treacy, M. M. J.; Ebbesen, T. W.; Gibson, J. M. *Nature* 1996, *381*, 678−680.
(15) Thostenson, E.; Li, C.; Chou, T. *Compos. Sci. Technol.* 2005, *65*, 491−516.
(16) Pop, E.; Mann, D.; Wang, Q.; Goodson, K.; Dai, H. *Nano Lett.* 2006, *6*, 96−100.
(17) Ouyang, M.; Huang, J.-L.; Lieber, C. M. *Acc. Chem. Res.* 2002, *35*, 1018−1025.
(18) Itkis, M. E.; Niyogi, S.; Meng, M. E.; Hamon, M. A.; Hu, H.; Haddon, R. C. *Nano Lett.* 2002, *2*, 155−159.
(19) Kataura, H.; Kumazawa, Y.; Maniwa, Y.; Umezu, I.; Suzuki, S.; Ohtsuka, Y.; Achiba, Y. *Synth. Met.* 1999, *103*, 2555−2558.
(20) Yan, Y.; Miao, J.; Yang, Z.; Xiao, F.-X.; Yang, H. B.; Liu, B.; Yang, Y. *Chem. Soc. Rev.* 2015, *44*, 3295−3346.
(21) Saito, N.; Haniu, H.; Usui, Y.; Aoki, K.; Hara, K.; Takanashi, S.; Shimizu, M.; Narita, N.; Okamoto, M.; Kobayashi, S.; et al. *Chem. Rev.* 2014, *114*, 6040−6079.
(22) Dyke, C. A.; Tour, J. M. *J. Phys. Chem. A* 2004, *108*, 11151−11159.
(23) Sun, Y.-P.; Fu, K.; Lin, Y.; Huang, W. *Acc. Chem. Res.* 2002, *35*, 1096−1104.
(24) Prato, M.; Kostarelos, K.; Bianco, A. *Acc. Chem. Res.* 2008, *41*, 60−68.
(25) Marcus, Y.; Smith, A. L.; Korobov, M. V.; Mirakyan, A. L.; Avramenko, N. V.; Stukalin, E. B. *J. Phys. Chem. B* 2001, *105*, 2499−2506.

(26) Duque, J. G.; Parra-Vasquez, A. N. G.; Behabtu, N.; Green, M. J.; Higginbotham, A. L.; Price, B. K.; Leonard, A. D.; Schmidt, H. K.; Lounis, B.; Tour, J. M.; et al. *ACS Nano* 2010, 4, 3063–3072.

(27) Criado, A.; Gómez-Escalonilla, M. J.; Fierro, J. L. G.; Urbina, A.; Peña, D.; Guitián, E.; Langa, F. *Chem. Commun.* 2010, 46, 7028–7030.

(28) McHedlov-Petrossyan, N. O. *Chem. Rev.* 2013, 113, 5149–5193.

(29) Tasis, D.; Tagmatarchis, N.; Bianco, A.; Prato, M. *Chem. Rev.* 2006, 106, 1105–1136.

(30) Yang, T.; Zhao, X.; Nagase, S. *J. Comput. Chem.* 2013, 34, 2223–2232.

(31) Martín, N. *Chem. Commun.* 2006, 2093–2104.

(32) Chaur, M. N.; Melin, F.; Ortiz, A. L.; Echegoyen, L. *Angew. Chem., Int. Ed.* 2009, 48, 7514–7538.

(33) Yamada, M.; Akasaka, T.; Nagase, S. *Acc. Chem. Res.* 2010, 43, 92–102.

(34) Osuna, S.; Swart, M.; Solà, M. *Phys. Chem. Chem. Phys.* 2011, 13, 3585–35603.

(35) Popov, A. A.; Yang, S.; Dunsch, L. *Chem. Rev.* 2013, 113, 5989–6113.

(36) Kumar, I.; Rana, S.; Cho, J. W. *Chem. - Eur. J.* 2011, 17, 11092–11101.

(37) Hoke, S. H.; Molstad, J.; Dilettato, D.; Jay, M. J.; Carlson, D.; Kahr, B.; Cooks, R. G. *J. Org. Chem.* 1992, 57, 5069–5071.

(38) Ishida, T.; Shinozuka, K.; Nogami, T.; Sasaki, S.; Iyoda, M. *Chem. Lett.* 1995, 24, 317–318.

(39) Nakamura, Y.; Takano, N.; Nishimura, T.; Yashima, E.; Sato, M.; Kudo, T.; Nishimura, J. *Org. Lett.* 2001, 3, 1193–1196.

(40) Kim, G.; Lee, K. C.; Kim, J.; Lee, J.; Lee, S. M.; Lee, J. C.; Seo, J. H.; Choi, W.-Y.; Yang, C. *Tetrahedron* 2013, 69, 7354–7359.

(41) Darwish, A. D.; Abdul-Sada, A. K.; Langley, G. J.; Kroto, H. W.; Taylor, R.; Walton, D. R. M. *J. Chem. Soc., Chem. Commun.* 1994, 2133–2134.

(42) Darwish, A. D.; Avent, A. G.; Taylor, R.; Walton, D. R. M. *J. Chem. Soc., Perkin Trans. 2* 1996, 2079–2084.

(43) Meier, M. S.; Wang, G.-W.; Haddon, R. C.; Brock, C. P.; Lloyd, M. A.; Selegue, J. P. *J. Am. Chem. Soc.* 1998, 120, 2337–2342.

(44) Lu, X.; Xu, J.; He, X.; Shi, Z.; Gu, Z. *Chem. Mater.* 2004, 16, 953–955.

(45) Lu, X.; Nikawa, H.; Tsuchiya, T.; Akasaka, T.; Toki, M.; Sawa, H.; Mizorogi, N.; Nagase, S. *Angew. Chem., Int. Ed.* 2010, 49, 594–597.

(46) Li, F.-F.; Pinzón, J. R.; Mercado, B. Q.; Olmstead, M. M.; Balch, A. L.; Echegoyen, L. *J. Am. Chem. Soc.* 2011, 133, 1563–1571.

(47) Rivera-Nazario, D. M.; Pinzón, J. R.; Stevenson, S.; Echegoyen, L. A. *J. Phys. Org. Chem.* 2013, 26, 194–205.

(48) Wang, G.-W.; Liu, T.-X.; Jiao, M.; Wang, N.; Zhu, S.-E.; Chen, C.; Yang, S.; Bowles, F. L.; Beavers, C. M.; Olmstead, M. M.; Mercado, B. Q.; Balch, A. L. *Angew. Chem., Int. Ed.* 2011, 50, 4658–4662.

(49) Fagan, S. B.; da Silva, A. J. R.; Mota, R.; Baierle, R. J.; Fazzio, A. *Phys. Rev. B: Condens. Matter Mater. Phys.* 2003, 67, 033405.

(50) Bettinger, H. F.; Kudin, K. N.; Scuseria, G. E. *J. Am. Chem. Soc.* 2001, 123, 12849–12856.

(51) Osuna, S.; Torrent-Sucarrat, M.; Solà, M.; Geerlings, P.; Ewels, C. P.; Lier, G. V. *J. Phys. Chem. C* 2010, 114, 3340–3345.

(52) Ogunro, O. O.; Nicolas, C. I.; Mintz, E. A.; Wang, X.-Q. *ACS Macro Lett.* 2012, 1, 524–528.

(53) Globus, A.; Bauschlicher, C. W.; Han, J.; Jaffe, R. L.; Levit, C.; Srivastava, D. *Nanotechnology* 1998, 9, 192–199.

(54) Criado, A.; Vizuete, M.; Gómez-Escalonilla, M. J.; García-Rodriguez, S.; Fierro, J. L. G.; Cobas, A.; Peña, D.; Guitián, E.; Langa, F. *Carbon* 2013, 63, 140–148.

(55) Yang, T.; Zhao, X.; Nagase, S. *Org. Lett.* 2013, 15, 5960–5963.

(56) te Velde, G.; Bickelhaupt, F. M.; Baerends, E. J.; Fonseca Guerra, C.; van Gisbergen, S. J. A.; Snijders, J. G.; Ziegler, T. *J. Comput. Chem.* 2001, 22, 931–967.

(57) Snijders, J. G.; Swart, M. *Theor. Chem. Acc.* 2003, 110, 34–41.

(58) Swart, M.; Snijders, J. G. *Theor. Chem. Acc.* 2004, 111, 56–56.

(59) Lenthe, E. v.; Baerends, E. J.; Snijders, J. G. *J. Chem. Phys.* 1993, 99, 4597–4610.

(60) van Lenthe, E.; van Leeuwen, R.; Baerends, E. J.; Snijders, J. G. *Int. J. Quantum Chem.* 1996, 57, 281–293.

(61) Becke, A. D. *Phys. Rev. A: At., Mol., Opt. Phys.* 1988, 38, 3098–3100.

(62) Perdew, J. *Phys. Rev. B: Condens. Matter Mater. Phys.* 1986, 33, 8822–8824.

(63) Grimme, S. *J. Comput. Chem.* 2006, 27, 1787–1799.

(64) Osuna, S.; Swart, M.; Solà, M. *J. Phys. Chem. A* 2011, 115, 3491–3496.

(65) Swart, M.; Bickelhaupt, F. M. *J. Comput. Chem.* 2008, 29, 724–734.

(66) Swart, M.; Bickelhaupt, F. M. *Int. J. Quantum Chem.* 2006, 106, 2536–2544.

(67) Cao, Y.; Osuna, S.; Liang, Y.; Haddon, R. C.; Houk, K. N. *J. Am. Chem. Soc.* 2013, 135, 17643–17649.

(68) Kawase, T.; Kurata, H. *Chem. Rev.* 2006, 106, 5250–5273.

(69) Pincak, R.; Pudlak, M. 2007, arXiv:cond-mat/0703580v1 [cond-mat.mtrl-sci] e-Print archive. http://arxiv.org/abs/cond-mat/0703580v1.

(70) Ando, T. *J. Phys. Soc. Jpn.* 2000, 69, 1757–1763.

(71) Smotlacha, J.; Pincak, R.; Pudlak, M. *Eur. Phys. J. B* 2011, 84, 255–264.

(72) Pincak, R.; Smotlacha, J.; Pudlak, M. *Eur. Phys. J. B* 2015, 88, 17.

(73) Pincak, R.; Smotlacha, J.; Osipov, V. A. *Phys. B* 2015, 475, 61–65.

(74) Yang, T.; Nagase, S.; Akasaka, T.; Poblet, J. M.; Houk, K. N.; Ehara, M.; Zhao, X. *J. Am. Chem. Soc.* 2015, 137, 6820–6828.

(75) Cases, M.; Duran, M.; Mestres, J.; Martín, N.; Solà, M. In *Fullerenes for the New Millennium*; Kamat, P. V., Kadish, K. M., Guldi, D. M., Eds.; The Electrochemical Society Inc., Pennington, NJ, 2011; Vol. 11, 244–269.

(76) Matsuo, Y.; Tahara, K.; Nakamura, E. *Org. Lett.* 2003, 5, 3181–3184.

(77) Baldoni, M.; Sgamellotti, A.; Mercuri, F. *Org. Lett.* 2007, 9, 4267–4270.

(78) Baldoni, M.; Selli, D.; Sgamellotti, A.; Mercuri, F. *J. Phys. Chem. C* 2009, 113, 862–866.

(79) Clar, E. *The Aromatic Sextet*; Wiley: New York, 1972.

(80) Solà, M. *Front. Chem.* 2013, 1, 22.

(81) Martín-Martínez, F. J.; Melchor, S.; Dobado, J. A. *Phys. Chem. Chem. Phys.* 2011, 13, 12844–12857.

(82) Garcia-Borràs, M.; Osuna, S.; Luis, J. M.; Swart, M.; Solà, M. *Chem. Soc. Rev.* 2014, 43, 5089–5105.

(83) Martín-Martínez, F. J.; Melchor, S.; Dobado, J. A. *Org. Lett.* 2008, 10, 1991–1994.

(84) Zhao, J.; Balbuena, P. B. *J. Phys. Chem. C* 2008, 112, 3482–3488.

(85) Pierrefixe, S. C. A. H.; Bickelhaupt, F. M. *Chem. - Eur. J.* 2007, 13, 6321–6328.

(86) Pierrefixe, S. C. A. H.; Bickelhaupt, F. M. *Chem. - Eur. J.* 2007, 13, 8371–8371.

(87) Hammouri, M.; Jha, S. K.; Vasiliev, I. *J. Phys. Chem. C* 2015, 119, 18719–18728.

(88) van Zeist, W.-J.; Bickelhaupt, F. M. *Org. Biomol. Chem.* 2010, 8, 3118–3127.

(89) Bickelhaupt, F. M. *J. Comput. Chem.* 1999, 20, 114–128.

(90) Fernández, I.; Bickelhaupt, F. M. *Chem. Soc. Rev.* 2014, 43, 4953–4967.

(91) Wolters, L. P.; Bickelhaupt, F. M. *WIREs Comput. Mol. Sci.* 2015, 5, 324–343.

(92) Houk, K. N.; Gandour, R. W.; Strozier, R. W.; Rondan, N. G.; Paquette, L. A. *J. Am. Chem. Soc.* 1979, 101, 6797–6802.

(93) Ess, D. H.; Houk, K. N. *J. Am. Chem. Soc.* 2007, 129, 10646–10647.

(94) Cao, Y.; Liang, Y.; Zhang, L.; Osuna, S.; Hoyt, A.-L. M.; Briseno, A. L.; Houk, K. N. *J. Am. Chem. Soc.* 2014, 136, 10743–10751.

(95) Osuna, S.; Houk, K. N. *Chem. - Eur. J.* 2009, 15, 13219–13231.

(96) Hammond, G. S. *J. Am. Chem. Soc.* 1955, 77, 334–338.

Chapter 5

Metal-Catalyzed Reactions

with Fullerene C$_{60}$

5.1 On the Reaction Mechanism of the Rhodium-Catalyzed Arylation of Fullerene (C_{60}) with Organoboron Compounds in the Presence of Water
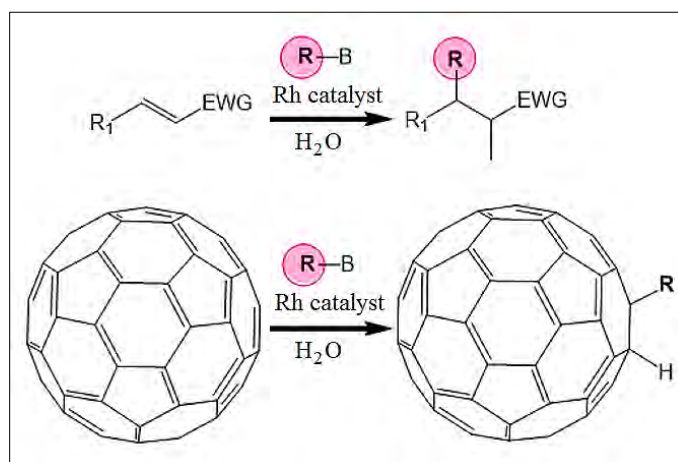
J.P.M. participated in the design of the project, performed all the calculations, analyzed the results, and co-wrote the manuscript.

VIP

On the Reaction Mechanism of the Rhodium-Catalyzed Arylation of Fullerene (C$_{60}$) with Organoboron Compounds in the Presence of Water

Juan Pablo Martínez, Miquel Solà, and Albert Poater*[a]

Dedicated to the memory of our colleague Prof. Dr. Tom Ziegler

Density functional theory (DFT) calculations were carried out to study the reaction mechanism of the Suzuki–Miyaura rhodium-catalyzed hydroarylation of fullerene (C$_{60}$) by phenylboronic acid in the presence of water. As found experimentally, our results confirm that addition of the phenyl group and the hydrogen atom in C$_{60}$ occurs at the [6,6] bond. The rate-determining step corresponds to the simultaneous transfer of a hydrogen atom from a water molecule to C$_{60}$ and the recovery of the active species. The use of 2-phenyl-1,3,2-dioxaborinane and the 4,4,5,5-tetramethyl-2-phenyl-1,3,2,-dioxaborolane instead of phenylboronic acid as organoborate agents does not lead to great modifications of the energy profile. The possible higher steric hindrance of 4,4,5,5-tetramethyl-2-phenyl-1,3,2,-dioxaborolane should not inhibit its use in the hydroarylation of C$_{60}$. Overall, we show how organoboron species arylate C$_{60}$ in rhodium-based catalysis assisted by water as a source of protons.

Introduction

After thirty years since it was discovered,[1] fullerene C$_{60}$ is still an attractive nanocarbon-based material due to its unique structure,[2] specific properties, and numerous derivatives that enable potential applications in biology, medicine, electronics, photovoltaics, and cosmetic industries.[3,4] The reactivity of fullerenes is rich;[5] the most important synthetic pathways used to functionalize C$_{60}$ are not only pericyclic reactions, such as cyclopropanations,[6] Diels–Alder reactions, and 1,3-dipolar cycloadditions,[7] but also the addition of free radicals or nucleophiles.[8]

The hydroalkylation and hydroarylation of C$_{60}$ have also been fascinating areas of research.[9] In this framework, organolithium and Grignard compounds are used to form intermediate anions (RC$_{60}^-$), which undergo protonation to yield hydroalkylated or hydroarylated derivatives.[3] Following the advance in rhodium(I) and palladium(II) catalysis of organoboron-based hydroarylation chemistry,[10–12] Itami et al. provided a catalytic pathway for the hydroalkylation and hydroarylation of C$_{60}$

(Scheme 1).[13,14] Their work was inspired by the work of Miyaura et al., who discovered the rhodium-catalyzed conjugate addition of organoboron compounds to enones in aqueous solution.[11,12,15,16] They also established the basis of the mechanism to carry out the addition of aryl- or 1-alkenylboronic acids to enones. In this case, the catalytic cycle encompasses transmetalation between rhodium(I) enolates and arylboronic acids to produce arylrhodium(I) species followed by insertion of enones into Ar–Rh bonds.[17] The mechanistic pathway of the addition of organoboron compounds to electron-deficient alkenes such as C$_{60}$ catalyzed by rhodium complexes remains rather unknown.[18] Itami et al.[14,19] proposed a general catalytic cycle, based on the work of Miyaura et al.,[11] for the hydroarylations of C$_{60}$ fullerene, and the details of the reaction mechanism and the function of water are missing or incomplete. For

[a] J. P. Martínez, Prof. M. Solà, Dr. A. Poater
Institut de Química Computacional i Catàlisi and Departament de Química
Universitat de Girona, Campus Montilivi
17071 Girona, Catalonia (Spain)
E-mail: albert.poater@udg.edu

R = aryl, heteroaryl, alkenyl
B = B(OH)$_2$, B(pin), BF$_3$K
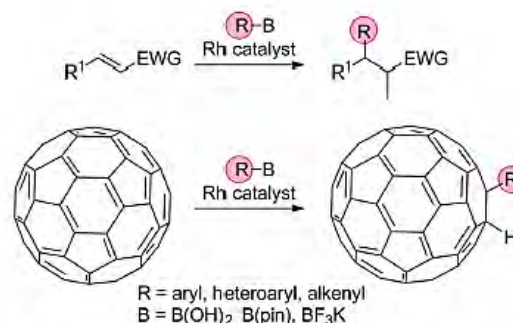
Scheme 1. Hydroarylation of electron-deficient alkenes (EWG: electron-withdrawing group) and fullerenes by means of organoborates and rhodium-based catalysts.

this reason, here we aim to unravel the role of each agent in the Suzuki–Miyaura-like reaction catalyzed by rhodium complexes of C$_{60}$ and organoborates as cocatalysts in the presence of water. In order to do so, we explore the catalytic cycle that leads to the hydroarylation of C$_{60}$ via density functional theory (DFT) methods.

Results and Discussion

The reaction pathway is divided into four main different parts (see Figure 1): 1) transmetalation of Rh–OH species with water and the organoborate to generate the Ar–RhB(OH)$_3$ complex (A→C); 2) elimination of B(OH)$_3$ to give the Rh–Ar species (C→D); 3) insertion or arylrhodation of Ar–Rh to C$_{60}$ (D→F); 4) protonation of Ar–C$_{60}$ through a water molecule and release of the Rh–OH species to conclude the hydroarylation process of C$_{60}$.

The catalytic species A is obtained from the precatalytic species [Rh(cod)(MeCN)$_2$]BF$_4$ (cod = 1,5-cyclooctadiene) through the dissociation of an acetonitrile ligand followed by the coordination of the hydroxy group from a water molecule releasing a proton that, with the initial counter anion BF$_4^-$, yields HBF$_4$. This step has an energetic cost of 24.3 kcal mol^{-1},[20] and is a common step for all organoborates.[14, 19] First, we discuss the reaction mechanism of the Suzuki–Miyaura rhodium-catalyzed hydroarylation of C$_{60}$ by phenylboronic acid in the presence of water. The neutral species [Rh(cod)(MeCN)(OH)] (A) can release an acetonitrile ligand and coordinate Ph–B(OH)$_2$ in a slightly exergonic process (0.6 kcal mol^{-1}) to give B. Then species B overcomes a barrier of 6.6 kcal mol^{-1} to transfer the phenyl

group from boron to rhodium to yield Ph(cod)RhB(OH)$_3$ (complex C).

Release of B(OH)$_3$ from C results in D with an energetic cost of only 6.2 kcal mol^{-1}. In D, rhodium is surrounded by the cod and phenyl ligands. η^2-Coordination of D to C$_{60}$ to form E is favorable by 11.8 kcal mol^{-1}, in agreement with previous experimental[21] and computational insights,[22] with slightly longer Rh–C bonds (2.28 and 2.31 Å) to be compared with 2.20 Å for RhH(CO)(PH$_3$)$_2$(C$_{60}$) in part due to the sterically demanding cod ligand. From E, the transfer of the phenyl group to the adjacent carbon atom requires to overcome a relatively low barrier of 12.8 kcal mol^{-1}, driving to the next intermediate F, which is quite stable (11.3 kcal mol^{-1} more stable than its precursor E). The resulting attacked bond in F is a [6,6] bond as experimentally found.[14,19] We also examined the attack to a [5,6] bond of C$_{60}$ in E and confirmed that the transition state and the resulting complex are less stable by 3.6 and 7.5 kcal mol^{-1}, respectively. Moreover, we were not able to obtain an optimized structure with η^5 and η^6 coordination of the PhRh(cod) in E or Rh(cod) in F to C$_{60}$.

Finally, in order to get the organic substituted C$_{60}$ product and regenerate the catalyst, a coordination of a water molecule to rhodium occurs to yield G. This complex (G) is transformed into H via the transfer of a hydrogen atom from water to the carbon atom of C$_{60}$ bonded to rhodium and concomitant release of (cod)Rh–OH. The role of water is then to provide the hydrogen atom for the formation of the phenyl(hydro)[60]fullerene and the OH group to recover the (cod)Rh–OH species.[14,19] The structure, acidity, and aromaticity of this phenyl(hydro)[60]fullerene species were discussed previously by Geerlings and co-workers.[23] The complete G→H transformation has a Gibbs energy barrier of 12.9 kcal mol^{-1}. In the next step, Rh in H coordinates a new entering Ph–B(OH)$_2$ molecule, which is a reactant in excess, to recover the catalytic species B again and close the catalytic cycle. The energy difference between species B at the beginning and at the end of the catalytic cycle in Figure 1 corresponds to the Gibbs reaction energy of the transformation of C$_{60}$, H$_2$O, and PhB(OH)$_2$ into B(OH)$_3$ and C$_{60}$PhH in a process that is exergonic by 27.9 kcal mol^{-1}.

For 2-phenyl-1,3,2.dioxaborinane and 4,4,5,5-tetramethyl-2-phenyl-1,3,2-dioxaborolane, the Gibbs reaction energies are the same: −27.9 kcal mol^{-1}. Apart from the relatively high energy cost to generate the catalytic species A from the precatalytic species [Rh(cod)(MeCN)$_2$]BF$_4$, for
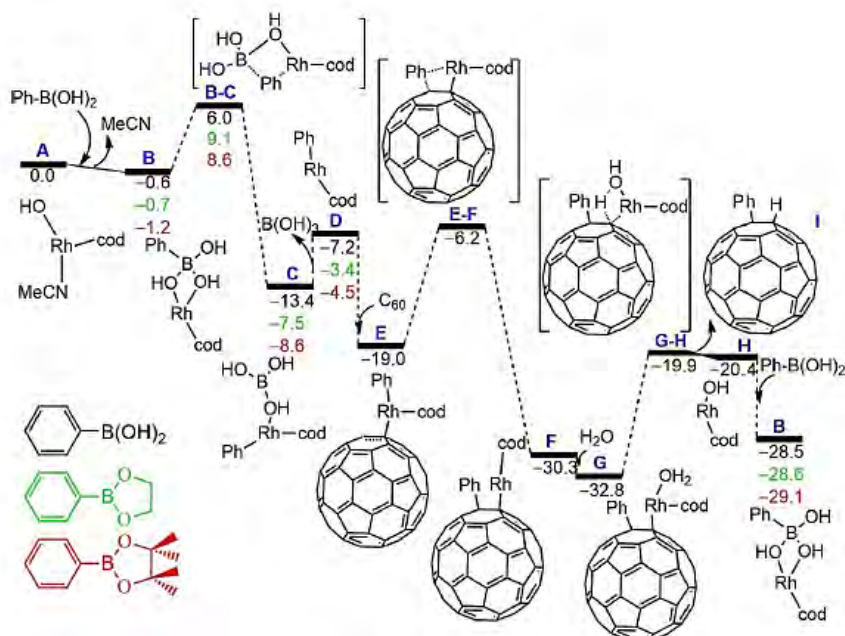
Figure 1. Gibbs energy reaction profiles for the rhodium-catalyzed addition to fullerene (C$_{60}$) of phenylboronic acid (black), 2-phenyl-1,3,2-dioxaborinane (green), and 4,4,5,5-tetramethyl-2-phenyl-1,3,2,-dioxaborolane (red) in ortho-dichlorobenzene solution. Values for the Gibbs energy are given in kcal mol^{-1}. Schematic drawings of molecules refer to the reaction with phenylboronic acid.

Figure 2. Density functional theory (DFT)-optimized geometries for the transition states of the transformations **E→F** (left) and **G→H** (right); key distances are given in Å.

the catalytic cycle, the **G** to **H** conversion is the rate determining step. However, the phenyl transfer in **E→F** is in competition, being the corresponding barrier of the transition state just 0.1 kcal mol^{-1} lower in energy (see Figure 2).[24]

On the other hand, considering the non-stoichiometric amount of C_{60} with respect to the metal catalyst, the coordination of a second C_{60} molecule substituting the cod ligand in the intermediate species displayed in Figure 1 was also investigated (see Figure S1 in the Supporting Information). This alternative path for the transformation of **A** to **H** implies the loss of acetonitrile and cod, the attack of RhOH to C_{60}, and subsequent addition of PhB(OH)$_2$. Overall, this path to **H** has to surmount a Gibbs energy barrier higher than 40 kcal mol^{-1} and, therefore, it is not operative and can be ruled out.

The Gibbs energy profiles corresponding to alternative organoborates, such as 2-phenyl-1,3,2,-dioxaborinane and 4,4,5,5-tetramethyl-2-phenyl-1,3,2,-dioxaborolane, are similar to that obtained with the phenylboronic acid (Figure 1). The fact that 2-phenyl-1,3,2,-dioxaborinane gives a nearly identical energy profile to that of phenylboronic acid concurs with the experimental result that this organoborate also results in the formation of the corresponding aryl(hydro)fullerene. However, for the 4,4,5,5-tetramethyl-2-phenyl-1,3,2,-dioxaborolane, no yield is observed experimentally. This is unexpected because the different organoborates share the same rate-determining step. Maybe it could be related to the somewhat more energetically difficult **B** to **C** transformation. What is clear is that steric hindrance seems not to be the cause of the decreased reactivity of 4,4,5,5-tetramethyl-2-phenyl-1,3,2,-dioxaborolane.

Conclusions

We have investigated by DFT calculations the reaction mechanism of the Suzuki–Miyaura rhodium-catalyzed hydroarylation of C_{60} by phenylboronic acid in the presence of water. Our results show that the until now unknown role of water is to coordinate the PhC$_{60}$Rh(cod) complex to provide the hydrogen atom for the formation of the phenyl(hidro)[60]fullerene and

the OH group to recover the (cod)Rh–OH species. This step is the rate-determining step of the whole catalytic cycle.

Our results with alternative organoborates, such as dioxaborinane and 4,4,5,5-tetramethyl-2-phenyl-1,3,2,-dioxaborolane, showed no remarkable differences for the phenyl transfer to the metal center, thus excluding the steric hindrance of the organoborate as a key factor to tune and improve the yield of the Suzuki–Miyaura reaction of C_{60} as a substrate, rhodium as a catalyst, and organoborate as cocatalysts. Water turns out to be a key reactant.

Experimental Section

All DFT calculations were completed with the Gaussian09 set of programs.[25] For geometry optimizations, the well-established and computationally fast hybrid-GGA functional B3LYP was used.[26] Geometry optimizations were performed without symmetry constraints, and the located stationary points were characterized by analytical frequency calculations. The electronic configuration of the molecular systems was described with the Gaussian 6-31G(d) basis set with a polarization function for H, C, N, B, and O.[27]

For rhodium, we used the small-core, quasi-relativistic Stuttgart/Dresden (SDD) effective core potential with an associated valence contracted basis set (standard SDD keywords in Gaussian 09).[28] Zero-point energies (ZPEs) and thermal corrections were calculated at the B3LYP level. Single-point energy calculations with the M06 functional[29] in solution were performed with the 6-311G(d,p) basis set for main group atoms,[30] and again the same SDD pseudopotential for rhodium.[31] Solvent effects were included with the polarizable continuous solvation model polarizable continuum model (PCM) using ortho-dichlorobenzene (o-DCB) as a solvent (the solvent employed in experimental studies is a 9:1 mixture of o-DCB and water). The Gibbs energy profiles in water are given in the Supporting Information. Relative Gibbs energy differences in water and in o-DCB are lower than 2.0 kcal mol^{-1}.

The M06 energy calculations were carried out with the scf=tight and integral(grid=ultrafinegrid) keywords. Reported energies are M06/6-311G(d,p)~SDD//B3LYP/6-31G(d)~SDD electronic energies corrected with ZPEs, thermal energies, and entropy effects calculated at 298 K using the B3LYP/6-31G(d)~SDD method. We also corrected the energy for solvation effects present in an o-DCB solution that were calculated at the M06/6-311G(d,p)~SDD//B3LYP/6-31G(d)~SDD level with the PCM method.[32] Finally, we applied a concentration correction of 1.89 kcal mol^{-1} for the Gibbs energies in solution to account for the condition change from 1 atm to 1 M concentration when going from gas phase to solution.[33] For water, the correction was 4.27 kcal mol^{-1}. Furthermore, for the aqueous solvation free energy of the proton, we assumed the value of −262.2 kcal mol^{-1} from the literature.[34]

[1] H. W. Kroto, J. R. Heath, S. C. O'Brien, R. F. Curl, R. E. Smalley, *Nature* **1985**, *318*, 162–163.

[2] a) *Fullerenes: Chemistry, Physics, and Technology*, (Eds.: K. M. Kadish, R. S. Ruoff), Wiley, New York, **2000**; b) *Fullerenes: Principles and Applications*, (Eds.: F. Langa, J.-F. Nierengarten), RSC, Cambridge, **2007**; c) N. Martín, *Chem. Commun.* **2006**, 2093–2104; d) N. Martín, M. Altable, S. Filippone, A. Martín-Domenech, *Synlett* **2007**, 3077–3095.

[3] J. Tong, M. C. Zimmerman, S. Li, X. Yi, R. Luxenhofer, R. Jordan, A. V. Kabanov, *Biomaterials* **2011**, *32*, 3654–3665.

[4] a) S. Kato, H. Taira, H. Aoshima, Y. Saitoh, N. Miwa, *J. Nanosci. Nanotechnol.* **2010**, *10*, 6769–6774; b) S. Jennepalli, S. G. Pyne, P. A. Keller, *RSC Adv.* **2014**, *4*, 46383–46398; c) M. Hosseini, D. M. Rivera-Nazario, L. A. Echegoyen, *ACS Appl. Mater. Interfaces* **2014**, *6*, 3712–3720; d) S. W. Cho, L. F. J. Piper, A. DeMasi, A. R. H. Preston, K. E. Smith, K. V. Chauhan, P. Sullivan, R. A. Hatton, T. S. Jones, *J. Phys. Chem. C* **2010**, *114*, 1928–1933.

[5] a) C. Bingel, *Chem. Ber.* **1993**, *126*, 1957–1959; b) J.-F. Nierengarten, V. Gramlich, F. Cardullo, F. Diederich, *Angew. Chem. Int. Ed. Engl.* **1996**, *35*, 2101–2103; *Angew. Chem.* **1996**, *108*, 2242–2244; c) X. Camps, A. Hirsch, *J. Chem. Soc. Perkin Trans. 1* **1997**, 1595–1596; d) J.-F. Nierengarten, D. Felder, J.-F. Nicoud, *Tetrahedron Lett.* **1998**, *39*, 2747–2750; e) F. Cheng, X. Yang, H. Zhu, Y. Song, *Tetrahedron Lett.* **2000**, *41*, 3947–3950; f) N. Martín, M. Altable, S. Filippone, A. Martin-Domenech, A. Poater, M. Solà, *Chem. Eur. J.* **2005**, *11*, 2716–2729; g) N. Alegret, A. Rodriguez-Fortea, J. M. Poblet, *Chem. Eur. J.* **2013**, *19*, 5061–5069; h) E. E. Maroto, S. Filippone, M. Suarez, R. Martinez-Alvarez, A. de Cozar, F. P. Cossio, N. Martin, *J. Am. Chem. Soc.* **2014**, *136*, 705–712; i) E. E. Maroto, J. Mateos, M. García-Borràs, S. Osuna, S. Filippone, M. A. Herranz, M. Solà, N. Martín, *J. Am. Chem. Soc.* **2014**, *137*, 1190–1197.

[6] a) V. M. Rotello, J. B. Howard, T. Yadav, M. M. Conn, E. Viani, L. M. Giovane, A. L. Lafleur, *Tetrahedron Lett.* **1993**, *34*, 1561–1562; b) M. Tsuda, T. Ishida, T. Nogami, S. Kurono, M. Ohashi, *J. Chem. Soc. Chem. Commun.* **1993**, 1296–1297; c) K. Komatsu, Y. Murata, N. Sugita, K. Takeuchi, T. S. M. Wan, *Tetrahedron Lett.* **1993**, *34*, 8473–8476; d) I. Lamparth, C. Maichle-Mössmer, A. Hirsch, *Angew. Chem. Int. Ed. Engl.* **1995**, *34*, 1607–1609; *Angew. Chem.* **1995**, *107*, 1755–1757; e) Y. Murata, N. Kato, K. Fujiwara, K. Komatsu, *J. Org. Chem.* **1999**, *64*, 3483–3488; f) K. Mikami, S. Matsumoto, T. Tonoi, Y. Okubo, T. Suenobu, S. Fukuzumi, *Tetrahedron Lett.* **1998**, *39*, 3733–3736; g) J. L. Segura, N. Martín, *Chem. Rev.* **1999**, *99*, 3199–3246; h) Y. Takaguchi, T. Tajima, K. Ohta, J. Motoyoshiya, H. Aoyama, T. Wakahara, T. Akasaka, M. Fujitsuka, O. Ito, *Angew. Chem. Int. Ed.* **2002**, *41*, 817–819; *Angew. Chem.* **2002**, *114*, 845–847.

[7] a) M. Maggini, G. Scorrano, M. Prato, *J. Am. Chem. Soc.* **1993**, *115*, 9798–9799; b) M. Prato, M. Maggini, *Acc. Chem. Res.* **1998**, *31*, 519–526; c) H. Imahori, H. Norieda, H. Yamada, Y. Nishimura, I. Yamazaki, Y. Sakata, S. Fukuzumi, *J. Am. Chem. Soc.* **2001**, *123*, 100–110; d) G.-W. Wang, T.-H. Zhang, E.-H. Hao, L.-J. Jiao, Y. Murata, K. Komatsu, *Tetrahedron* **2003**, *59*, 55–60; e) G.-W. Wang, J.-X. Li, Y.-J. Li, Y.-C. Liu, *J. Org. Chem.* **2006**, *71*, 680–684; f) A. Alvarez, E. Ochoa, Y. Verdecia, M. Suárez, M. Solà, N. Martín, *J. Org. Chem.* **2005**, *70*, 3256–3262.

[8] a) A. Hirsch, M. Brettreich, *Fullerenes: Chemistry and Reactions*, Wiley-VCH, Weinheim, **2005**; b) M. Izquierdo, S. Osuna, S. Filippone, A. Martín-Domenech, M. Solà, N. Martín, *J. Org. Chem.* **2009**, *74*, 1480–1487; c) M. Izquierdo, S. Osuna, S. Filippone, N. Martín-Domenech, M. Solà, N. Martín, *J. Org. Chem.* **2009**, *74*, 6253–6259; d) M. Izquierdo, S. Osuna, S. Filippone, A. Martín-Domenech, M. Solà, N. Martín, *Eur. J. Org. Chem.* **2009**, 6231–6238; e) K. M. Keshavarz-K, B. Knight, G. Srdanov, F. Wudl, *J. Am. Chem. Soc.* **1995**, *117*, 11371–11372; f) M. Nambo, A. Wakamiya,

[8] (continued) Yamaguchi, K. Itami, *J. Am. Chem. Soc.* **2009**, *131*, 15112–15113; g) A. Hirsch, Q. Li, F. Wudl, *Angew. Chem. Int. Ed. Engl.* **1991**, *30*, 1309–1310; *Angew. Chem.* **1991**, *103*, 1339–1341.

[9] M. D. Tzirakis, M. Orfanopoulos, *Chem. Rev.* **2013**, *113*, 5262–5321.

[10] a) C. S. Cho, S. Motofusa, K. Ohe, S. Uemura, S. C. Shim, *J. Org. Chem.* **1995**, *60*, 883–888; b) T. Zhang, M. Shi, *Chem. Eur. J.* **2008**, *14*, 3759–3764; c) M. Nambo, A. Wakamiya, K. Itami, *Chem. Sci.* **2012**, *3*, 3474–3481.

[11] Y. Takaya, M. Ogasawara, T. Hayashi, M. Sakai, N. Miyaura, *J. Am. Chem. Soc.* **1998**, *120*, 5579–5580.

[12] T. Hayashi, K. Yamasaki, *Chem. Rev.* **2003**, *103*, 2829–2844.

[13] S. Mori, M. Nambo, L. C. Chi, J. Bouffard, K. Itami, *Org. Lett.* **2008**, *10*, 4609–4612.

[14] M. Nambo, R. Noyori, K. Itami, *J. Am. Chem. Soc.* **2007**, *129*, 8080–8081.

[15] a) N.-W. Tseng, J. Mancuso, M. Lautens, *J. Am. Chem. Soc.* **2006**, *128*, 5338–5338; b) K. Tonogaki, K. Itami, J. Yoshida, *Org. Lett.* **2006**, *8*, 1419–1422; c) T. Miura, M. Murakami, *Chem. Commun.* **2007**, 217–224; d) T. Kurahashi, H. Shinokubo, A. Osuka, *Angew. Chem. Int. Ed.* **2006**, *45*, 6336–6338; *Angew. Chem.* **2006**, *118*, 6484–6486; e) K. Ueura, S. Miyamura, T. Satoh, M. Miura, *J. Organomet. Chem.* **2006**, *691*, 2821–286; f) K. Ukai, M. Aoki, J. Takaya, N. Iwasawa, *J. Am. Chem. Soc.* **2006**, *128*, 8706–8707.

[16] Recent examples of rhodium-catalyzed 1,4-addition of arylboronic acids to α,β-unsaturated carbonyl compounds: a) J.-F. Paquin, C. Defieber, C. R. J. Stephenson, E. M. Carreira, *J. Am. Chem. Soc.* **2005**, *127*, 10850–10851; b) C. Walter, G. Auer, M. Oestreich, *Angew. Chem. Int. Ed.* **2006**, *45*, 5675–5677; *Angew. Chem.* **2006**, *118*, 5803–5805; c) W.-L. Duan, H. Iwamura, R. Shintani, T. Hayashi, *J. Am. Chem. Soc.* **2007**, *129*, 2130–2138; d) R. Mariz, X. Luan, M. Gatti, A. Linden, R. Dorta, *J. Am. Chem. Soc.* **2008**, *130*, 2172–2173; e) T. Nishimura, J. Wang, M. Nagaosa, K. Okamoto, R. Shintani, F.-Y. Kwong, W.-Y. Yu, A. S. C. Chan, T. Hayashi, *J. Am. Chem. Soc.* **2010**, *132*, 464–465.

[17] a) M. Sakai, H. Hayashi, N. Miyaura, *Organometallics* **1997**, *16*, 4229–4231; b) A. Poater, F. Ragone, R. Mariz, R. Dorta, L. Cavallo, *Chem. Eur. J.* **2010**, *16*, 14348–14353.

[18] K. Fagnou, M. Lautens, *Chem. Rev.* **2003**, *103*, 169–196.

[19] M. Nambo, Y. Segawa, A. Wakamiya, K. Itami, *Chem. Asian J.* **2011**, *6*, 590–598.

[20] A. Poater, S. V. C. Vummaleti, L. Cavallo, *Organometallics* **2013**, *32*, 6330–6336.

[21] a) Y. Ishii, Y. Hoshi, Y. Hamada, M. Hidai, *Chem. Lett.* **1994**, *23*, 801–804; b) R. E. Douthwaite, M. L. H. Green, A. H. H. Stephens, J. F. C. Turner, *J. Chem. Soc. Chem. Commun.* **1993**, 1522–1523.

[22] A. Ikeda, Y. Kameno, Y. Nakao, H. Sato, S. Sakaki, *J. Organomet. Chem.* **2007**, *692*, 299–306.

[23] a) G. Van Lier, B. Safi, P. Geerlings, *J. Phys. Chem. Solids* **1997**, *58*, 1719–1727; b) M. C. Amat, G. Van Lier, M. Solà, M. Duran, P. Geerlings, *J. Org. Chem.* **2004**, *69*, 2374–2380.

[24] S. Kozuch, S. Shaik, *Acc. Chem. Res.* **2011**, *44*, 101–110.

[25] Gaussian 09, Revision C.01, M. J. Frisch, G. W. Trucks, H. B. Schlegel, G. E. Scuseria, M. A. Robb, J. R. Cheeseman, G. Scalmani, V. Barone, B. Mennucci, G. A. Petersson, H. Nakatsuji, M. Caricato, X. Li, H. P. Hratchian, A. F. Izmaylov, J. Bloino, G. Zheng, J. L. Sonnenberg, M. Hada, M. Ehara, K. Toyota, R. Fukuda, J. Hasegawa, M. Ishida, T. Nakajima, Y. Honda, O. Kitao, H. Nakai, T. Vreven, J. A. Montgomery, Jr., J. E. Peralta, F. Ogliaro, M. Bearpark, J. J. Heyd, E. Brothers, K. N. Kudin, V. N. Staroverov, R. Kobayashi, J. Normand, K. Raghavachari, A. Rendell, J. C. Burant, S. S. Iyengar, J. Tomasi, M. Cossi, N. Rega, J. M. Millam, M. Klene, J. E. Knox, J. B. Cross, V. Bakken, C. Adamo, J. Jaramillo, R. Gomperts, R. E. Stratmann, O. Yazyev, A. J. Austin, R. Cammi, C. Pomelli, J. W. Ochterski, R. L. Martin, K. Morokuma, V. G. Zakrzewski, G. A. Voth, P. Salvador, J. J. Dannenberg, S. Dapprich, A. D. Daniels, Ö. Farkas, J. B. Foresman, J. V. Ortiz, J. Cioslowski, D. J. Fox, Gaussian, Inc., Wallingford, CT, USA, **2009**.

[26] a) A. D. Becke, *J. Chem. Phys.* **1993**, *98*, 5648–5652; b) C. Lee, W. Yang, R. G. Parr, *Phys. Rev. B* **1988**, *37*, 785–789; c) P. Stephens, F. J. Devlin, C. F. Chabalowski, M. J. Frisch, *J. Phys. Chem.* **1994**, *98*, 11623–11627.

[27] a) W. J. Hehre, R. Ditchfield, J. A. Pople, *J. Chem. Phys.* **1972**, *56*, 2257–2261; b) W. J. Hehre, L. Radom, P. v. R. Schleyer, J. A. Pople, *Ab Initio Molecular Orbital Theory*; Wiley, New York, **1986**.

[28] a) U. Häussermann, M. Dolg, H. Stoll, H. Preuss, P. Schwerdtfeger, R. M. Pitzer, *Mol. Phys.* **1993**, *78*, 1211–1224; b) W. Küchle, M. Dolg, H. Stoll,

H. Preuss, *J. Chem. Phys.* **1994**, *100*, 7535–7542; c) T. Leininger, A. Nicklass, H. Stoll, M. Dolg, P. Schwerdtfeger, *J. Chem. Phys.* **1996**, *105*, 1052–1059.

[29] Y. Zhao, D. G. Truhlar, *Theor. Chem. Acc.* **2008**, *120*, 215–241.

[30] A. J. H. Wachters, *J. Chem. Phys.* **1970**, *52*, 1033–1036.

[31] R. Mariz, X. Luan, A. Poater, M. Gatti, S. Blumentritt, E. Drinkel, A. Linden, J. J. Bürgi, L. Cavallo, R. Dorta, *Chem. Eur. J.* **2010**, *16*, 14335–14347.

[32] a) V. Barone, M. Cossi, *J. Phys. Chem. A* **1998**, *102*, 1995–2001; b) T. Tomasi, M. Persico, *Chem. Rev.* **1994**, *94*, 2027–2094.

[33] a) C. P. Kelly, C. J. Cramer, D. G. Truhlar, *J. Chem. Theory Comput.* **2005**, *1*, 1133–1152; b) C. P. Kelly, C. J. Cramer, D. G. Truhlar, *J. Phys. Chem. B* **2006**, *110*, 16066–16081; c) V. S. Bryantsev, M. S. Diallo, W. A. Goddard III, *J. Phys. Chem. B* **2008**, *112*, 9709–9719.

[34] G. J. Tawa, I. A. Topol, S. K. Burt, R. A. Caldwell, A. A. Rashin, *J. Chem. Phys.* **1998**, *109*, 4852–4963.
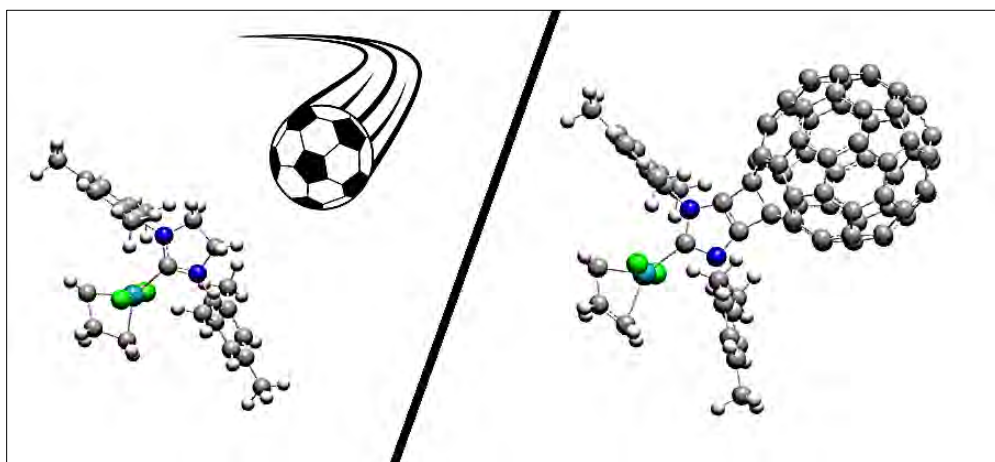
5.2 In Silico Olefin Metathesis with Ru-Based Catalysts Containing N-Heterocyclic Carbenes Bearing C_{60} Fullerenes

J.P.M. participated in the design of the project, performed all the calculations, analyzed the results, and co-wrote the manuscript.

▌Metathesis

In Silico Olefin Metathesis with Ru-Based Catalysts Containing N-Heterocyclic Carbenes Bearing C$_{60}$ Fullerenes

Juan Pablo Martínez,[a] Sai Vikrama Chaitanya Vummaleti,[b] Laura Falivene,[b] Steven P. Nolan,[c, d] Luigi Cavallo,[b] Miquel Solà,[a] and Albert Poater*[a]

In memory of our colleague Yves Chauvin

Abstract: Density functional theory calculations have been used to explore the potential of Ru-based complexes with 1,3-bis(2,4,6-trimethylphenyl)imidazolin-2-ylidene (SIMes) ligand backbone (A) being modified in silico by the insertion of a C$_{60}$ molecule (B and C), as olefin metathesis catalysts. To this end, we investigated the olefin metathesis reaction catalyzed by complexes A, B, and C using ethylene as the substrate, focusing mainly on the thermodynamic stability of all possible reaction intermediates. Our results suggest that complex B bearing an electron-withdrawing N-heterocyclic carbene improves the performance of unannulated complex A. The efficiency of complex B is only surpassed by complex A when the backbone of the N-heterocyclic carbene of complex A is substituted by two amino groups. The particular performance of complexes B and C has to be attributed to electronic factors, that is, the electronic-donating capacity of modified SIMes ligand rather than steric effects, because the latter are predicted to be almost identical for complexes B and C when compared to those of A. Overall, this study indicates that such Ru-based complexes B and C might have the potential to be effective olefin metathesis catalysts.

Introduction

Olefin metathesis is one of the most important tools for the formation of carbon–carbon bonds in modern synthetic chemistry.[1] Among its various industrial applications, the metathesis reaction is used mainly in the preparation of fine chemicals,[2] biologically active compounds,[3] new functionalized materials and polymers.[4] Although there exists other metal-based complexes, ruthenium has occupied a prominent role in olefin metathesis during the last decade. This preference for a second-row transition metal is due to the high reactivity and tolerance towards group functionalization that they offer.[5, 6]

The metathesis reaction mechanism proposed by Chauvin in the early 1970s considers the metal carbene complex as the active catalyst and the respective four-membered metallacycle derivatives as the crucial intermediates leading to the desired products.[7] The presence of a ruthenacycle intermediate has been studied experimentally[8] and theoretically[9] since the late 1990s. In these studies, density functional theory (DFT) calculations have been extensively used to clarify many aspects of Ru-catalyzed olefin metathesis,[10,11] and efforts have been also made to achieve highly accurate and less expensive computational recipes to acquire new mechanistic knowledge to feed into catalyst design efforts.[12,13]

Focusing on the Ru-based systems, the activity of the "first-generation" phosphine-based catalysts was significantly improved with the discovery of a "second-generation" catalysts, in which an N-heterocyclic carbene (NHC) was used to replace one phosphine ligand.[14] In the last decade, many variants of the Ru-based catalysts have been disclosed.[1,15]

Despite the numerous studies in the past two decades,[8–12] there is still the absence of a "universal" catalyst for all olefin metathesis applications; however, there are smart particular solutions.[1] Additionally, there is no rule of thumb to predict exactly why Ru-based catalysts with certain NHCs and phosphine ligands show catalytic activity, whereas with other ligands (including variants of NHCs and phosphines) they display poor performance.[16]

[a] J. P. Martínez, Prof. Dr. M. Solà, Dr. A. Poater
    Institut de Química Computacional i Catàlisi
    and Departament de Química, Universitat de Girona
    Campus Montilivi, 17071, Girona, Catalonia (Spain)
    E-mail: albert.poater@udg.edu

[b] Dr. S. V. C. Vummaleti, Dr. L. Falivene, Prof. Dr. L. Cavallo
    KAUST Catalysis Center, Physical Sciences and Engineering Division
    King Abdullah University of Science and Technology
    Thuwal 23955-6900 (Saudi Arabia)

[c] Prof. Dr. S. P. Nolan
    Department of Inorganic and Physical Chemistry
    Universiteit Gent, Krijgslaan 281 - S3
    9000 Gent (Belgium)

[d] Prof. Dr. S. P. Nolan
    Chemistry Department, College of Science
    King Saud University, P.O. Box 2455, Riyadh 11451 (Saudi Arabia)

   Supporting information for this article and ORCID for some of the authors
   are available on the WWW under
   http://dx.doi.org/10.1002/chem.201600383.

Research and industrial interest in fullerenes has been translated into a recent high number of applications.[17] Apart from being able to produce solar cells painting simply a surface, or store hydrogen as a green energy source or killers of bacteria in membranes in water systems, these nanotechnological species are prone to trap free radicals,[18] thus are suitable to act as active agents to block the inflammation generated by an allergy, or to fight against the deterioration of motor function due to multiple sclerosis. Here we envisaged fullerenes as a new supporting ligand that could facilitate olefin metathesis processes. The combination of organometallic chemistry and fullerenes is relatively scarce.[19,20] Very recently, Stang et al. have synthesized a series of supramolecular platinum(II) complexes in which the metal is attached to macrocycles containing pyrrolidine rings that are connected to C₆₀.[20] To our knowledge, NHC ligands bearing fullerene moieties have not been reported yet,[21] apart from a recent study bearing C₈₀.[21b]

In the present study, we use DFT calculations to explore the potential of Ru-based complexes with SIMes (SIMes = 1,3-bis[2,4,6-(trimethyl)phenyl]imidazolidin-2-ylidene) ligand backbone (A) being modified in silico by the insertion of a C₆₀ molecule (B and C), and its activity as an olefin metathesis catalyst (see Scheme 1). In principle, this modification of the SIMes
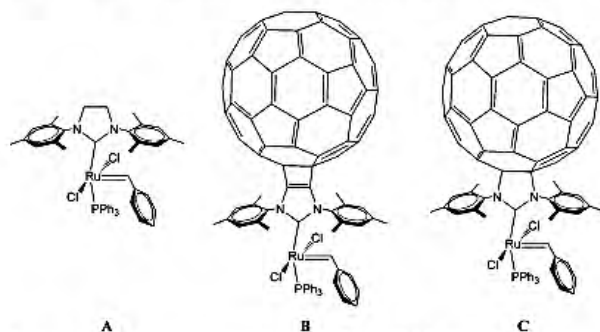
Scheme 1. Ru-based complex with SIMes (1,3-bis(2,4,6-trimethylphenyl)imidazolin-2-ylidene) ligand backbone (A) and in silico modifications by the insertion of a C₆₀ molecule (B and C) as olefin metathesis catalysts.

ligand will increase its steric hindrance by either replacing the methylene H atoms by a fullerene (complex B) or replacing both methylene C and H atoms (complex C).

The approach to use computational techniques as a tool to screen new catalyst architectures more rapidly and examine their potential as efficient catalysts for a certain reaction is nowadays very popular. This can be understood if one considers that the experimental exploration of the catalytic space to find new and better catalysts is a tedious task often driven by a trial and error approach. In this sense, Poater et al. recently reported the in silico prediction of new Fe- and Rh-based olefin metathesis catalyst activities.[22] Additionally, this in silico approach has been extended to predict promising new starting materials as well.[23, 24]

Results and Discussion

For this study we computed the olefin metathesis reaction mechanism for the Ru-based complexes A, B, and C using eth-
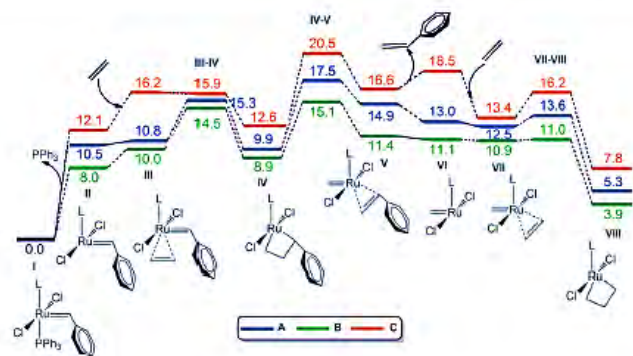
Figure 1. Computed thermodynamic stability of reaction intermediates II–VIII relative to that of species I for the studied olefin metathesis reaction catalyzed by Ru-based complexes A–C using ethylene as the substrate. L = NHC. Gibbs energies in CH₂Cl₂ solvent are given in kcal mol⁻¹.

ylene as the substrate. The main focus is on the differential thermodynamic stability of the reaction intermediates of complexes A, B, and C. Figure 1 collects the Gibbs energies relative to species I of intermediates II to VIII and the key transition state structures for the studied Ru-based complexes A–C. For systems B and C, C₆₀ is connected to the NHC moiety through a [6,6] bond junction (see Figure 2). It is worth mentioning here that complexes B and C attached to the C₆₀ molecule through the [5,6] bond are found to be about 18.0 kcal mol⁻¹ higher in energy than those connected through the [6,6] bond. It is evident from Figure 1 that the relative stability of all other intermediates for complexes B and C are nearly identical when compared to the respective intermediates of complex A, with the maximum energy difference amounting to less than 5.5 kcal mol⁻¹ (for intermediate VI).

As can be seen in Figure 1, the rate-determining transition state[25] in this process is the IV–V, corresponding to the breaking of the ruthenacyclobutane complex. Indeed, once species V is generated the Gibbs energy profile follows an energetically slight downhill trajectory without high-energy barriers or highly stabilized intermediates that follow the classical steps described in a number of previous reports.[26] Overall, our results indicate that for the studied olefin metathesis reaction, complex B presents the lowest energy barrier (15.1 kcal mol⁻¹) followed by complex A (17.5 kcal mol⁻¹), whereas complex C has the highest energy barrier (20.5 kcal mol⁻¹).

The formation of a stable ruthenacyclobutane IV by the metathesis of ethylene with the Ru–alkylidene bond is considered fundamental to describe a successful olefin metathesis catalyst.[16,27] The ruthenacyclobutane is a relatively stable key intermediate of each metathesis event, and it has been characterized experimentally.[28] Furthermore, the less substituted the metallacycle, the higher its stability is. Nolan et al. reported in a recent study that the substitution of the SIMes ligand in the Ru-based catalyst by a phosphine resulted in the destabilization of metallacycle IV by 8.4 kcal mol⁻¹ with respect to the previous ethylene coordination intermediate III,[16] compared with just 0.4 kcal mol⁻¹ for the system containing SIMes. The studied olefin metathesis reaction was with methyl vinyl ether as a substrate instead of ethylene. Experimentally, a Ru-based complex containing SIMes ligand was found to be catalytically

active, but it showed poor catalytic performance when substituted with phosphine. This poor catalytic activity observed was attributed to the low stability of ruthenacyclobutane IV. The possible difficulty in the evolution of the catalytic process can be also related to a high thermodynamic stability of the metallacycle intermediate. Thus, Schrock catalysts with highly stable metallacycles showed poor catalytic performances.[29] These insights allow us to confirm the relationship between the stability of the ruthenacyclobutane and the potential catalytic activity of the corresponding Ru-catalyst species. For the catalysis to be efficient, the ruthenacyclobutane should be moderately stable. Going back to the present study, for complexes B and C, the metallacycle IV is 1.1 and 3.6 kcal mol^{-1} more stable than the former coordination intermediate III, respectively, and comparable to the relative stability of metallacycle for complex A (0.9 kcal mol^{-1}), thus the values fit perfectly with the active catalysts in olefin metathesis.[30] Thus, taking into account that a too high stability of the ruthenacyclobutane intermediate might be a bottleneck in olefin metathesis catalysis, this new family of catalysts overcomes this hurdle.

We have studied in detail the steric and electronic properties of species I and II for complexes A, B, and C (see Figure 2). Focusing on the steric properties, we calculated the buried volume (%V_{Bur}) of the three NHC ligands A, B, and C using the SambVca package developed by Cavallo et al.[31] This program analyzes the first coordination sphere around the metal, which is the place where catalysis occurs, and the buried volume is the amount of the first coordination sphere of the metal occupied by a given ligand.[32] We performed also a more detailed analysis by evaluating the %V_{Bur} in the single quadrants around the Ru center and plotted them as steric contour steric maps (Figure 3 and Table 1), see the Supporting Information for further details. Splitting the total %V_{Bur} into quadrant contributions quantifies any asymmetry in the way the ligand wraps around the metal. Here, this analysis will show how the shape of the reactive pocket is modified[33] when moving from A to B or C.

It is evident from Figure 3 that for the studied Ru-based complexes A–C, species I presents quite similar sterics, thus neither B nor C are significantly more sterically congested than A. In detail, the calculated percent buried volume (%V_{Bur}) for complexes B (32.5%) and C (33.3%) are comparable to the %V_{Bur} of A (32.8%) (see Table 1). Similarly, for species II, the predicted %V_{Bur} values are nearly the same despite the potential relaxation of NHC ligand after the dissociation of phosphine ligand. Nevertheless, species II of complex C displayed a somewhat more sterically hindered environment next to the metal, being three out of four quadrants generously occupied.

Figure 2. DFT optimized geometry of intermediates I and II for the Ru-complexes A, B, and C (selected distances in Å).

Taken together, these observations confirm that the sterics for the studied complexes A–C are quite similar and indeed none of them preclude coordination of bulky substrates.

To understand the effect of the bulky C$_{60}$ fullerene on the binding of NHC to the Ru metal, we decomposed the total bond energy, BE, of the NHC-Ru bond in species I for the studied Ru-complexes A–C as shown in Equation (1)

$$-BE = E_{Def} + E_{Int} \tag{1}$$

in which E_{Def} is the deformation energy associated with the change in the geometry of the free NHC and of the Ru metal fragment, to the geometry they have in the complex, whereas E_{Int} is the interaction energy between the NHC and the metal fragment frozen at the geometry they have in the complex.

The E_{Int} is negative because it is the energy gain associated with placing together the two deformed fragments, whereas the E_{Def} is positive as it corresponds to the energetic cost of deforming the two fragments to the geometry they have in

Table 1. Total %V_{Bur} and quadrant %V_{Bur} (numbers in brackets) values for species I and II for the considered Ru-based complexes A–C.

Complex	Sterics (%V_{Bur}) I	II
A	32.8 (41.0/31.5/31.9/26.7)	32.8 (36.3/33.0/31.0/30.6)
B	32.5 (44.0/32.3/27.3/26.4)	31.8 (37.0/36.1/27.6/26.4)
C	33.3 (40.0/34.5/29.8/28.6)	33.6 (36.9/35.0/32.2/30.2)
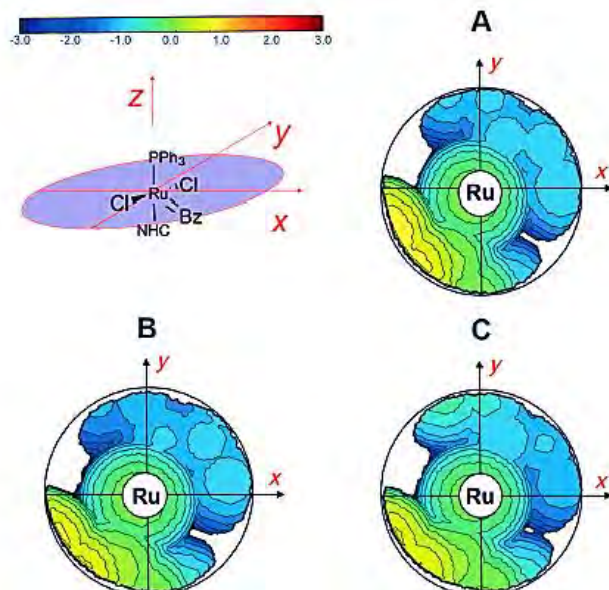
Figure 3. Topographic steric maps of the NHC ligands of species **I** for the studied Ru-complexes **A–C**. %V_{Bur} is the percent of buried volume. The Ru atom is at the origin and the P atom is on the z axis. The isocontour curves of the steric maps are given in Å.

for the energy decomposition given by Equation (1), the energy data for transition state III–IV, together with the corresponding values for the former intermediate III, referred to II, are collected in Table 2. Fragments considered are the incom-

Table 2. Energy decomposition analysis of reaction intermediates **III** plus the transition state **III–IV** relative to that of species **II** for the studied olefin metathesis reaction catalyzed by complex **A** and its analogues with the C$_{60}$ annulated NHC backbone, **B** and **C**. Gibbs energies in CH$_2$Cl$_2$ solvent are given in kcalmol^{-1}.

Species	BE	E_{int}	E_{def}	$E_{def\,complex\,I}$	$E_{def\,ethylene}$
A					
III	0.3	−5.9	6.2	5.7	0.5
III–IV	4.8	−21.2	26.0	15.3	10.7
B					
III	2.0	−13.3	15.3	11.5	3.8
III–IV	6.5	−24.3	30.8	19.3	11.5
C					
III	4.1	−15.9	20.0	16.0	4.0
III–IV	3.8	−23.5	26.3	17.4	9.9

the complex. Within this framework, the E_{Int} in species **I** is −59.8 kcalmol^{-1} for **A**, whereas it is 3.7 and 2.0 kcalmol^{-1} lower (in absolute value) in the cases of complexes **B** and **C**, respectively. The lower interaction energy for complexes **B** and **C** is likely due to the electron-withdrawing capacity of the C$_{60}$ group that makes the electron pair of the NHC less available for the interaction with the metal. The lower NHC-Ru interaction energy of the **B** complex is attributed to the fact that the NHC moiety of **B** interacts with the π-system of C$_{60}$ through the C=C double bond more effectively than that of the **A** complex that does not have such a π-system. On the other hand, the E_{Def} of NHC with C$_{60}$ is similar in energy (2.8 and 2.1 kcal mol^{-1} for complexes **B** and **C**, respectively) with respect to the standard NHC, that is, SIMes (1.9 kcalmol^{-1} for complex **A**). The E_{Def} of the metal fragment is not significant (for complex **A** just 0.1 kcalmol^{-1} more distorted). Overall, the calculated BE is 4.5 and 2.2 kcalmol^{-1} less stabilizing for complexes **B** and **C**, respectively, than for complex **A**. To summarize, the presence of the C$_{60}$ molecule reduces the strength of the Ru-NHC bond, and this observation is further supported by the shorter Ru–C$_{NHC}$ bond length for complex **A** when compared with those of complexes **B** and **C** (see Figure 2).

The activation strain model (ASM)[34] was also used to analyze the first steps of the reaction. Basically, this model establishes the desired causal relationship between reaction barriers, on one hand, and the properties of reactants and characteristics of reaction mechanisms, on the other hand. Here the ASM cannot be applied to the rate-determining step described by IV–V because of the too different nature of the latter transition state with respect to II,[35] but only to the barrier described by the closure of the metallacycle, that is, III–IV, to provide insight about how the balance between sterics and electronics drives the reaction to the metallacycle. Following the same Scheme

ing ethylene and complex **II**. As to intermediate III, the interaction of the entering olefin is electronically favored for the systems bearing an annulated C$_{60}$. This more stabilizing interaction energy concurs with the higher electrophilicity of intermediate II for complexes **B** and **C** (see above) and is partially compensated by the higher deformation suffered by the latter systems, mainly centered in the metallic fragment. The same trends are observed for the transition state III–IV, pointing out that E_{int} for system **A** converges nearly to the corresponding values for **B** and **C**, and thus the differences between the three studied complexes decrease.

Because of slight differences in the charge analysis (see the Supporting Information, Table S1),[36] we envisaged an additional conceptual DFT analysis to get more insights into the electronic contribution of the NHCs. The electrophilicity of the complexes was evaluated as the Parr electrophilicity index shown in Equation (2).[37]

$$\omega = \frac{\mu^2}{2\eta} \tag{2}$$

in which μ and η are the chemical potential and the molecular hardness, respectively. In the framework of DFT,[38] μ and η for a N-electron system with total electronic energy E are defined as the first and second derivatives of the energy with respect to N at a fixed external potential[39] In numerical applications, μ and η are calculated with the finite difference formulas of Equations (3) and (4), which are based on Koopmans' approximation[40]

$$\mu \cong \frac{1}{2}(\varepsilon_L + \varepsilon_H) \tag{3}$$

and

$$\eta \cong \frac{1}{2}(\varepsilon_L - \varepsilon_H) \tag{4}$$

in which ε_H and ε_L are the energies of the highest occupied molecular orbital (HOMO) and the lowest unoccupied molecular orbital (LUMO), respectively.[41]

To this end, we obtained the values of chemical hardness (η) and Parr electrophilicity index (ω) for the species **I** and **II**.[42] For **A**, ω was calculated from the HOMO and LUMO orbital energies (see Figure 4). Whereas for a direct comparison between
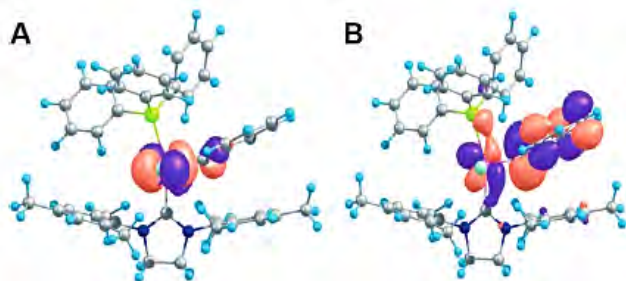
Figure 4. Frontier molecular orbitals for species **I** for the Ru-based complex **A**: (a) HOMO and (b) LUMO.

A and C$_{60}$-based complexes **B** and **C**, we had to look for the appropriate frontier molecular orbitals of the former complexes (see the Supporting Information, Figure S1 for further details). For the studied Ru-based complexes **A–C**, the predicted η values are quite constant and do not show a clear trend (see Table 3), whereas the predicted ω values increase (166.2,

Table 3. Computed electronic properties of species **I** and **II** for the considered Ru-complexes **A–C**; H = HOMO; L = LUMO; η = chemical hardness and ω = Parr electrophilicity index (in kcal mol^{-1}).

Complex	H		L		η		ω	
	I	II	I	II	I	II	I	II
A	−91.1	−105.7	−57.8	−61.8	16.7	22.0	166.2	159.5
B[a]	−95.5	−106.6	−61.2	−65.5	17.1	20.6	179.3	180.0
C[a]	−90.7	−109.5	−60.8	−65.3	16.2	22.1	181.1	172.8

[a] For **B** and **C**, the energies of the corresponding orbitals, analogous to HOMO and LUMO of **A**.

179.3, and 181.1 kcal mol^{-1}, respectively, for species **I** for the considered Ru-complexes **A–C**) with significant quantitative differences. The reason for the high electrophilicity of **B** and **C** has to be attributed mainly to their larger chemical potential, that is, the energy released when the number of electrons increases as a result of a more accessible LUMO. Moreover, the predicted higher ω values for complexes **B** and **C** than for that of **A** suggest that the former complexes will be more prone to nucleophilic substrate attacks, and thus more reactive than **A**. In summary, our results indicate that a reduced electron-donating capability of the SIMes ligand with a backbone annulated by a C$_{60}$ molecule together with higher ω values make complexes **B** and **C** potentially active catalysts for olefin metathesis.

Finally, to better understand the electronic properties of the C$_{60}$-based NHCs in complexes **B** and **C**, we replaced the methylene H atoms in complex **A** by either NH$_2$ or NO$_2$ groups to simulate NHCs with different electron-donor capabilities.[43] Table 4 reports the Gibbs energies relative to species **I** of intermediates **II** to **VIII** and the key transition structures for the studied Ru-complex **A** and its derivatives, **A+2NH$_2$**, **A+2NO$_2$**, and **A+4NO$_2$**. The catalyst with lowest barriers is **A+2NH$_2$**. This catalyst shows a performance similar to that of complex **B**.

Table 4. Computed thermodynamic stability of reaction intermediates **II–VIII** relative to that of species **I** for the studied olefin metathesis reaction catalyzed by complex **A** and its analogues with the modified NHC backbone, **A+2NH$_2$**, **A+2NO$_2$** and **A+4NO$_2$**. Gibbs energies in CH$_2$Cl$_2$ solvent are given in kcal mol^{-1}.

Species	A	A+2NH$_2$	A+2NO$_2$	A+4NO$_2$
I	0.0	0.0	0.0	0.0
II	10.5	9.5	7.9	11.4
III	10.8	10.1	10.1	12.9
III–IV	15.3	12.4	14.6	16.8
IV	9.9	6.0	12.7	12.1
IV–V	17.5	14.7	17.0	17.6
V	14.9	13.4	15.5	14.9
VI	13.0	11.5	15.5	16.5
VII	12.5	9.6	11.9	11.9
VII–VIII	13.6	10.0	14.0	12.4
VIII	5.3	1.1	5.9	7.8

Conclusion

We have used DFT calculations to explore the potential of Ru-based complexes having SIMes ligand (complex **A**) and C$_{60}$ annulated SIMes ligand (complexes **B** and **C**) as olefin metathesis catalysts using ethylene as the substrate. Our results show that for complexes **B** and **C**, the thermodynamic stability of the reaction intermediates is similar to the respective intermediates of complex **A**, being the maximum energy difference ≤ 6.0 kcal mol^{-1}. However, for the studied olefin metathesis reaction, complex **B** presented the lowest energy barriers (15.1 kcal mol^{-1}) followed by complex **A** (17.5 kcal mol^{-1}), whereas complex **C** presented the highest energy barriers (20.5 kcal mol^{-1}). The predicted steric properties are almost similar for the studied complexes **A–C**, suggesting that sterics have no significant role in the observed differential catalytic activity of the Ru-based complexes under study. On the other hand, the lower electron-donating nature of the C$_{60}$ annulated SIMes ligand, revealed by a significant increase of electrophilicity of complexes **B** and **C**, change the nature of the available olefin metathesis catalysts, making the catalysis more efficient in the case of complex **B**. Therefore, our results show that the tuning of the electron-donating capacity of the NHC ligand by annulation at the NHC backbone substantially modifies the catalytic activity of Ru-based catalysts. The inclusion of C$_{60}$ into the structure of the NHC provides a potential path to be explored in the quest for more effective catalysts for olefin metathesis. Overall, this type of work might guide catalyst design efforts. In as such, this contribution aims to inspire and provoke interest in this specific catalyst architecture.

Experimental Section

All DFT static calculations were performed with the Gaussian set of programs.[44] The electronic configuration of the molecular systems was described with the standard split-valence basis set with a polarization function of Ahlrichs and co-workers for H, C, N, and Cl (SVP keyword in Gaussian 09).[45] For Ru we used the small-core, quasi-relativistic Stuttgart/Dresden effective core potential, with an associated valence basis set contracted (standard SDD keywords in Gaussian 09).[46] The geometry optimizations were carried out without symmetry constraints, and the characterization of the located stationary points was performed by analytical frequency calculations. The M06L functional was employed in geometry optimizations and frequency calculations. Gibbs energies, ΔG, were built through single point energy calculations on the M06L/SVP geometries using the M06 functional[47] and the triple-ζ valence plus polarization on main group atoms (TZVP keyword in Gaussian).[48] Solvent effects were included with the PCM model using CH$_2$Cl$_2$ as the solvent.[49] To these M06/TZVP electronic energies in solvent, zero point energy and thermal and entropic corrections were included from the gas phase frequency calculations at the M06L/SVP level of theory.

%V_{Bur} Calculations

The buried volume calculations were performed with the SambVca package developed by Cavallo et al.[31] The radius of the sphere around the metal center was set to 3.5 Å, whereas for the atoms we adopted the Bondi radii scaled by 1.17, and a mesh of 0.1 Å was used to scan the sphere for buried voxels. The steric maps were evaluated with a development version of the SambVca package.[32]

[1] a) R. H. Grubbs, *Handbook of Olefin Metathesis*, Wiley-VCH, Weinheim, **2003**; b) G. C. Vougioukalakis, R. H. Grubbs, *Chem. Rev.* **2009**, *109*, 1746–1787; c) C. Samojowicz, M. Bieniek, K. Grela, *Chem. Rev.* **2009**, *109*, 3708–3742; d) A. Fürstner, *Angew. Chem. Int. Ed.* **2000**, *39*, 3012–3043; *Angew. Chem.* **2000**, *112*, 3140–3172; e) B. K. Keitz, K. Endo, P. R. Patel, M. B. Herbert, R. H. Grubbs, *J. Am. Chem. Soc.* **2012**, *134*, 693–699.

[2] a) S. J. Connon, S. Blechert, *Angew. Chem. Int. Ed.* **2003**, *42*, 1900–1923; *Angew. Chem.* **2003**, *115*, 1944–1968; b) F. Pozgan, P. H. Dixneuf, *Metathesis Chemistry: From Nanostructure Design to Synthesis of Advanced*

Materials, Vol. 243, Springer, Dordrecht, **2007**, pp. 195–222; c) G. Mele, J. Li, G. Vasapollo, *Chim. Oggi* **2008**, *26*, 72–74.

[3] a) R. E. Giudici, A. H. Hoveyda, *J. Am. Chem. Soc.* **2007**, *129*, 3824–3825; b) B. K. Keitz, R. H. Grubbs, *Organometallics* **2010**, *29*, 403–408; c) B. Stenne, J. Timperio, J. Savoie, T. Dudding, S. K. Collins, *Org. Lett.* **2010**, *12*, 2032–2035; d) B. Schmidt, L. Staude, *J. Org. Chem.* **2009**, *74*, 9237–9240.

[4] a) A. Leitgeb, J. Wappel, C. Slugovc, *Polymer* **2010**, *51*, 2927–2946; b) C. W. Bielawski, R. H. Grubbs, *Prog. Polym. Sci.* **2007**, *32*, 1–29; c) J. C. Mol, *J. Mol. Catal. A* **2004**, *213*, 39–45; d) T. W. Baughman, K. B. Wagener, *Adv. Polym. Sci.* **2005**, *176*, 1–42.

[5] C. Adlhart, P. Chen, *J. Am. Chem. Soc.* **2004**, *126*, 3496–3510.

[6] a) J. A. Tallarico, P. J. Bonitatebus Jr., M. L. Snapper, *J. Am. Chem. Soc.* **1997**, *119*, 7157–7158; b) D. R. Anderson, D. D. Hickstein, D. J. O'Leary, R. H. Grubbs, *J. Am. Chem. Soc.* **2006**, *128*, 8386–8387.

[7] P. J. L. Hérisson, Y. Chauvin, *Die Makromol. Chem.* **1971**, *141*, 161–176.

[8] a) E. L. Dias, S. T. Nguyen, R. H. Grubbs, *J. Am. Chem. Soc.* **1997**, *119*, 3887–3897; b) M. S. Sanford, M. Ulman, R. H. Grubbs, *J. Am. Chem. Soc.* **2001**, *123*, 749–750; c) M. S. Sanford, J. A. Love, R. H. Grubbs, *J. Am. Chem. Soc.* **2001**, *123*, 6543–6554; d) C. Adlhart, C. Hinderling, H. Baumann, P. Chen, *J. Am. Chem. Soc.* **2000**, *122*, 8204–8214; e) C. Adlhart, P. Chen, *Helv. Chim. Acta* **2000**, *83*, 2192–2196.

[9] a) S. E. Vyboishchikov, M. Bühl, W. Thiel, *Chem. Eur. J.* **2002**, *8*, 3962–3975; b) L. Cavallo, *J. Am. Chem. Soc.* **2002**, *124*, 8965–8973; c) O. M. Aagaard, R. J. Meier, F. Buda, *J. Am. Chem. Soc.* **1998**, *120*, 7174–7182; d) F. Bernardi, A. Bottoni, G. P. Miscione, *Organometallics* **2000**, *19*, 5529–5532; e) C. Adlhart, P. Chen, *Angew. Chem. Int. Ed.* **2002**, *41*, 4484–4487; *Angew. Chem.* **2002**, *114*, 4668–4671; f) S. Manzini, C. A. Urbina-Blanco, A. Poater, A. M. Z. Slawin, L. Cavallo, S. P. Nolan, *Angew. Chem. Int. Ed.* **2012**, *51*, 1042–1045; *Angew. Chem.* **2012**, *124*, 1066–1069; g) S. Manzini, A. Poater, D. J. Nelson, L. Cavallo, A. M. Z. Slawin, S. P. Nolan, *Angew. Chem. Int. Ed.* **2014**, *53*, 8995–8999; *Angew. Chem.* **2014**, *126*, 9141–9145.

[10] a) I. C. Stewart, D. Benitez, D. J. O'Leary, E. Tkatchouk, M. W. Day, W. A. Goddard III, R. H. Grubbs, *J. Am. Chem. Soc.* **2009**, *131*, 1931–1938; b) W. Janse van Rensburg, P. J. Steynberg, W. H. Meyer, M. M. Kirk, G. S. Forman, *J. Am. Chem. Soc.* **2004**, *126*, 14332–14333.

[11] a) A. Correa, L. Cavallo, *J. Am. Chem. Soc.* **2006**, *128*, 13352–13353; b) C. E. Webster, *J. Am. Chem. Soc.* **2007**, *129*, 7490–7491; c) D. Benitez, E. Tkatchouk, W. A. Goddard III., *Chem. Commun.* **2008**, 6194–6196; d) J. Mathew, N. Koga, C. H. Suresh, *Organometallics* **2008**, *27*, 4666–4670; e) M. Barbasiewicz, A. Szadkowska, R. Bujok, K. Grela, *Organometallics* **2006**, *25*, 3599–3604; f) A. Poater, L. Cavallo, *J. Mol. Catal. A* **2010**, *324*, 75–79; g) F. Nuñez-Zarur, J. Poater, L. Rodríguez-Santiago, X. Solans-Monfort, M. Solà, M. Sodupe, *Comput. Theor. Chem.* **2012**, *996*, 57–67; h) F. Nuñez-Zarur, X. Solans-Monfort, L. Rodríguez-Santiago, M. Sodupe, *ACS Catal.* **2013**, *3*, 206–218; i) L. Falivene, A. Poater, C. S. J. Cazin, C. Slugovc, L. Cavallo, *Dalton Trans.* **2013**, *42*, 7312–7317; j) X. Bantreil, A. Poater, C. A. Urbina-Blanco, Y. D. Bidal, L. Falivene, R. A. M. Randall, L. Cavallo, A. M. Z. Slawin, C. S. J. Cazin, *Organometallics* **2012**, *31*, 7415–7426; k) A. Poater, N. Bahri-Lalehac, L. Cavallo, *Chem. Commun.* **2011**, *47*, 6674–6676; l) D. Benitez, W. A. Goddard III, *J. Am. Chem. Soc.* **2005**, *127*, 12218–12219; m) P. Liu, X. Xu, X. Dong, B. K. Keitz, M. B. Herbert, R. H. Grubbs, K. N. Houk, *J. Am. Chem. Soc.* **2012**, *134*, 1464–1467; n) C. Costabile, A. Mariconda, L. Cavallo, P. Longo, V. Bertolasi, F. Ragone, F. Grisi, *Chem. Eur. J.* **2011**, *17*, 8618–8629; p) F. Nuñez-Zarur, X. Solans-Monfort, L. Rodríguez-Santiago, M. Sodupe, *Organometallics* **2012**, *31*, 4203–4215; o) F. Núñez-Zarur, X. Solans-Monfort, R. Pleixats, L. Rodríguez-Santiago, M. Sodupe, *Chem. Eur. J.* **2013**, *19*, 14553–14565.

[12] a) A. D. Kulkarni, D. G. Truhlar, *J. Chem. Theory Comput.* **2011**, *7*, 2325–2332; b) Y. Zhao, D. G. Truhlar, *J. Chem. Theory Comput.* **2009**, *5*, 324–333; c) Y. Zhao, D. G. Truhlar, *Org. Lett.* **2007**, *9*, 1967–1970; d) Y. Zhao, D. G. Truhlar, *Chem. Phys. Lett.* **2011**, *502*, 1–13; e) Y. Zhao, D. G. Truhlar, *Acc. Chem. Res.* **2008**, *41*, 157–167; f) G. Occhipinti, H.-R. Bjørsvik, V. R. Jensen, *J. Am. Chem. Soc.* **2006**, *128*, 6952–6954; g) Y. Minenkov, A. Singstad, G. Occhipinti, V. R. Jensen, *Dalton Trans.* **2012**, *41*, 5526–5541; h) A. C. Tsipis, A. G. Orpen, J. N. Harvey, *Dalton Trans.* **2005**, 2849–2858; i) G. Occhipinti, F. R. Hansen, K. W. Törnroos, V. R. Jensen, *J. Am. Chem. Soc.* **2013**, *135*, 3331–3334; j) E. Pump, A. Poater, M. Zirngast, A. Torvisco, R. Fischer, L. Cavallo, C. Slugovc, *Organometallics* **2014**, *33*, 2806–2813.

[13] A. Poater, E. Pump, S. V. C. Vummaleti, L. Cavallo, *J. Chem. Theory Comput.* **2014**, *10*, 4442–4448.

[14] a) T. Weskamp, W. C. Schattenmann, M. Spiegler, W. A. Herrmann, *Angew. Chem. Int. Ed.* **1998**, *37*, 2490–2493; *Angew. Chem.* **1998**, *110*, 2631–2633; b) J. Huang, E. D. Stevens, J. L. Petersen, S. P. Nolan, *J. Am. Chem. Soc.* **1999**, *121*, 2674–2678; c) M. Scholl, S. Ding, C. W. Lee, R. H. Grubbs, *Org. Lett.* **1999**, *1*, 953–956.

[15] A. Leitgeb, M. Abbas, R. C. Fischer, A. Poater, L. Cavallo, C. Slugovc, *Catal. Sci. Technol.* **2012**, *2*, 1640–1643.

[16] C. A. Urbina-Blanco, A. Poater, T. Lebl, S. Manzini, A. M. Z. Slawin, L. Cavallo, S. P. Nolan, *J. Am. Chem. Soc.* **2013**, *135*, 7073–7079.

[17] a) A. A. Popov, S. Yang, L. Dunsch, *Chem. Rev.* **2013**, *113*, 5989–6113; b) X. Lu, L. Feng, T. Akasaka, S. Nagase, *Chem. Soc. Rev.* **2012**, *41*, 7723–7760; c) D. M. Rivera-Nazario, J. R. Pinzón, S. Stvenson, L. A. Echegoyen, *J. Phys. Org. Chem.* **2013**, *26*, 194–205; d) M. Rudolf, S. Wolfrum, D. M. Guldi, L. Feng, T. Tsuchiya, T. Akasaka, L. Echegoyen, *Chem. Eur. J.* **2012**, *18*, 5136–5148; e) M. Yamada, T. Akasaka, S. Nagase, *Acc. Chem. Res.* **2010**, *43*, 92–102; f) M. N. Chaur, F. Melin, A. L. Ortiz, L. Echegoyen, *Angew. Chem. Int. Ed.* **2009**, *48*, 7514–7538; *Angew. Chem.* **2009**, *121*, 7650–7675; g) F. Giacalone, N. Martín, *Chem. Rev.* **2006**, *106*, 5136–5190.

[18] a) R. Bakry, R. M. Vallant, M. Najam-ul-Haq, M. Rainer, Z. Szabo, C. W. Huck, G. K. Bonn, *Int. J. Nanomed.* **2007**, *2*, 639–649; b) J. Heath, *Nat. Mater.* **2010**, *9*, 876–877.

[19] a) F. L. Bowles, M. M. Olmstead, A. L. Balch, *J. Am. Chem. Soc.* **2014**, *136*, 3338–3341; b) J. P. Martínez, M. Solà, A. Poater, *ChemistryOpen* **2015**, *4*, 774–778; c) M. Nambo, Y. Segawa, A. Wakamiya, K. Itami, *Chem. Asian J.* **2011**, *6*, 590–598; d) N. Martín, M. Altable, S. Filippone, A. Martín-Domenech, A. Poater, M. Solà, *Chem. Eur. J.* **2005**, *11*, 2716–2729.

[20] V. S. P. K. Neti, M. L. Saha, X. Yan, X. Zhou, P. J. Stang, *Organometallics* **2015**, *34*, 4813–4815.

[21] a) M.-C. Li, M.-D. Su, *Theor. Chem. Acc.* **2015**, *134*, 38–46; b) M.-G. Chen, L. Bao, M. Ai, W.-G. Shena, X. Lu, *Chem. Sci.* **2016**, *7*, 2331–2334 (the latter work was published after submission of the present paper).

[22] a) A. Poater, S. V. C. Vummaleti, E. Pump, L. Cavallo, *Dalton Trans.* **2014**, *43*, 11216–12220; b) A. Poater, *Molecules* **2016**, *21*, 177; c) A. Poater, E. Pump, S. V. C. Vummaleti, L. Cavallo, *Chem. Phys. Lett.* **2014**, *610–611*, 29–32.

[23] a) A. Poater, R. Credendino, C. Slugovc, L. Cavallo, *Dalton Trans.* **2013**, *42*, 7271–7275; b) J. Wappel, R. C. Fischer, L. Cavallo, C. Slugovc, A. Poater, *Beilstein J. Org. Chem.* **2016**, *12*, 154–165.

[24] a) G. Hautier, C. C. Fischer, A. Jain, T. Mueller, G. Ceder, *Chem. Mater.* **2010**, *22*, 3762–3767; b) F. Rissner, M. Y. Ma, O. T. Hofmann, C. Slugovc, Z. Shuai, E. Zojer, *J. Mater. Chem.* **2012**, *22*, 4269–4272; c) Y. Chu, W. Heyndrickx, G. Occhipinti, V. R. Jensen, *J. Am. Chem. Soc.* **2012**, *134*, 8885–8895; d) A. Poater, L. Falivene, C. A. Urbina-Blanco, S. Manzini, S. P. Nolan, L. Cavallo, *Dalton Trans.* **2013**, *42*, 7433–7439.

[25] S. Kozuch, S. Shaik, *Acc. Chem. Res.* **2011**, *44*, 101–110.

[26] R. Credendino, A. Poater, F. Ragone, L. Cavallo, *Catal. Sci. Technol.* **2011**, *1*, 1287–1297.

[27] A. Poater, L. Cavallo, *Beilstein J. Org. Chem.* **2015**, *11*, 1767–1780.

[28] a) P. E. Romero, W. E. Piers, *J. Am. Chem. Soc.* **2007**, *129*, 1698–1704; b) E. F. van der Eide, W. E. Piers, *Nat. Chem.* **2010**, *2*, 571–576.

[29] a) X. Solans-Monfort, *Dalton Trans.* **2014**, *43*, 4573–4586; b) A. Poater, X. Solans-Monfort, E. Clot, C. Copéret, O. Eisenstein, *Dalton Trans.* **2006**, 3077–3087; c) A. Poater, X. Solans-Monfort, E. Clot, C. Copéret, O. Eisenstein, *J. Am. Chem. Soc.* **2007**, *129*, 8207–8216.

[30] A. Poater, F. Ragone, A. Correa, A. Cavallo, *Dalton Trans.* **2011**, *40*, 11066–11069.

[31] A. Poater, B. Cosenza, A. Correa, S. Giudice, F. Ragone, V. Scarano, L. Cavallo, *Eur. J. Inorg. Chem.* **2009**, 1759–1766.

[32] a) L. Cavallo, A. Correa, C. Costabile, H. Jacobsen, *J. Organomet. Chem.* **2005**, *690*, 5407–5413; b) A. Poater, F. Ragone, S. Giudice, C. Costabile, R. Dorta, S. P. Nolan, L. Cavallo, *Organometallics* **2008**, *27*, 2679–2681; c) A. Poater, L. Cavallo, *Dalton Trans.* **2009**, 8878–8883; d) H. Jacobsen, A. Correa, A. Poater, C. Costabile, L. Cavallo, *Coord. Chem. Rev.* **2009**, *253*, 687–703.

[33] a) F. Ragone, A. Poater, L. Cavallo, *J. Am. Chem. Soc.* **2010**, *132*, 4249–4258; b) C. J. Richmond, R. Matheu, A. Poater, L. Falivene, J. Benet-Buch-

holz, X. Sala, L. Cavallo, A. Llobet, *Chem. Eur. J.* **2014**, *20*, 17282–17286; c) C. Di Giovanni, A. Poater, J. Benet-Buchholz, L. Cavallo, M. Solà, A. Llobet, *Chem. Eur. J.* **2014**, *20*, 3898–3902; d) A. Poater, F. Ragone, R. Mariz, R. Dorta, L. Cavallo, *Chem. Eur. J.* **2010**, *16*, 14348–14353; e) S. M. Ahmed, A. Poater, M. I. Childers, P. C. B. Widger, A. M. LaPointe, E. B. Lobkovsky, G. W. Coates, L. Cavallo, *J. Am. Chem. Soc.* **2013**, *135*, 18901–18911.

[34] a) F. M. Bickelhaupt, *J. Comput. Chem.* **1999**, *20*, 114–128; b) I. Fernández, F. M. Bickelhaupt, *Chem. Soc. Rev.* **2014**, *43*, 4953–4967; c) D. H. Ess, K. N. Houk, *J. Am. Chem. Soc.* **2007**, *129*, 10646–10647; d) W.-J. Van Zeist, F. M. Bickelhaupt, *Org. Biomol. Chem.* **2010**, *8*, 3118–3127; e) G. T. de Jong, F. M. Bickelhaupt, *J. Chem. Theory Comput.* **2007**, *3*, 514–529; f) G. T. de Jong, F. M. Bickelhaupt, *ChemPhysChem* **2007**, *8*, 1170; g) I. Fernández, M. Solà, F. M. Bickelhaupt, *Chem. Eur. J.* **2013**, *19*, 7416–7422; h) I. Fernández, F. M. Bickelhaupt, F. P. Cossío, *Chem. Eur. J.* **2014**, *20*, 10791–10801.

[35] J. P. Martínez, F. Langa, F. M. Bickelhaupt, S. Osuna, M. Solà, *J. Phys. Chem. C* **2016**, *120*, 1716–1726.

[36] S. Manzini, C. A. Urbina-Blanco, D. J. Nelson, A. Poater, T. Lebl, S. Meiries, A. M. Z. Slawin, L. Falivene, L. Cavallo, S. P. Nolan, *J. Organomet. Chem.* **2015**, *780*, 43–48.

[37] R. G. Parr, L. von Szentpaly, S. Liu, *J. Am. Chem. Soc.* **1999**, *121*, 1922–1924.

[38] P. Geerlings, F. De Proft, W. Langenaeker, *Chem. Rev.* **2003**, *103*, 1793–1873.

[39] a) R. G. Parr, W. Yang, *Density Functional Theory of Atoms and Molecules*, Oxford University Press, New York, **1989**; b) R. G. Parr, R. A. Donnelly, M. Levy, W. E. Palke, *J. Chem. Phys.* **1978**, *68*, 3801–3807.

[40] T. Koopmans, *Physica* **1934**, *1*, 104–113.

[41] a) M. Costas, X. Ribas, A. Poater, J. M. L. Valbuena, R. Xifra, A. Company, M. Duran, M. Solà, A. Llobet, M. Corbella, M. A. Uson, J. Mahia, X. Solans, X. P. Shan, J. Benet-Buchholz, *Inorg. Chem.* **2006**, *45*, 3569–3581; b) A. Poater, A. Gallegos Saliner, R. Carbó-Dorca, J. Poater, M. Solà, L. Cavallo, A. P. Worth, *J. Comput. Chem.* **2009**, *30*, 275–284; c) A. Poater, A. Gallegos Saliner, M. Solà, L. Cavallo, A. P. Worth, *Expert Opin. Drug Delivery* **2010**, *7*, 295–305.

[42] R. G. Parr, R. G. Pearson, *J. Am. Chem. Soc.* **1983**, *105*, 7512–7516.

[43] S. V. C. Vummaleti, D. J. Nelson, A. Poater, A. Gomez-Suarez, D. B. Cordes, A. M. Z. Slawin, S. P. Nolan, L. Cavallo, *Chem. Sci.* **2015**, *6*, 1895–1904.

[44] Gaussian 09, Revision D.01, M. J. Frisch, G. W. Trucks, H. B. Schlegel, G. E. Scuseria, M. A. Robb, J. R. Cheeseman, G. Scalmani, V. Barone, B. Mennucci, G. A. Petersson, H. Nakatsuji, M. Caricato, X. Li, H. P. Hratchian, A. F. Izmaylov, J. Bloino, G. Zheng, J. L. Sonnenberg, M. Hada, M. Ehara, K. Toyota, R. Fukuda, J. Hasegawa, M. Ishida, T. Nakajima, Y. Honda, O. Kitao, H. Nakai, T. Vreven, J. A. Montgomery, Jr., J. E. Peralta, F. Ogliaro, M. Bearpark, J. J. Heyd, E. Brothers, K. N. Kudin, V. N. Staroverov, R. Kobayashi, J. Normand, K. Raghavachari, A. Rendell, J. C. Burant, S. S. Iyengar, J. Tomasi, M. Cossi, N. Rega, J. M. Millam, M. Klene, J. E. Knox, J. B. Cross, V. Bakken, C. Adamo, J. Jaramillo, R. Gomperts, R. E. Stratmann, O. Yazyev, A. J. Austin, R. Cammi, C. Pomelli, J. W. Ochterski, R. L. Martin, K. Morokuma, V. G. Zakrzewski, G. A. Voth, P. Salvador, J. J. Dannenberg, S. Dapprich, A. D. Daniels, Ö. Farkas, J. B. Foresman, J. V. Ortiz, J. Cioslowski, D. J. Fox, Gaussian, Inc., Wallingford CT, **2009**.

[45] A. Schäfer, H. Horn, R. Ahlrichs, *J. Chem. Phys.* **1992**, *97*, 2571–2577.

[46] a) U. Häusermann, M. Dolg, H. Stoll, H. Preuss, *Mol. Phys.* **1993**, *78*, 1211–1224; b) W. Küchle, M. Dolg, H. Stoll, H. Preuss, *J. Chem. Phys.* **1994**, *100*, 7535–7542; c) T. Leininger, A. Nicklass, H. Stoll, M. Dolg, P. Schwerdtfeger, *J. Chem. Phys.* **1996**, *105*, 1052–1059.

[47] Y. Zhao, D. G. Truhlar, *Theor. Chem. Acc.* **2008**, *120*, 215–241.

[48] F. Weigend, R. Ahlrichs, *Phys. Chem. Chem. Phys.* **2005**, *7*, 3297–3305.

[49] a) V. Barone, M. Cossi, *J. Phys. Chem. A* **1998**, *102*, 1995–2001; b) J. Tomasi, M. Persico, *Chem. Rev.* **1994**, *94*, 2027–2094.

Chapter 6

Electron Transfer in Fullerene

Dye-Sensitized Solar Cells

6.1 Extent of Charge Separation and Exciton Delocalization for Electronically Excited States in a Triphenylamine-C$_{60}$ Donor-Acceptor Conjugate: a Combined Molecular Dynamics and TD-DFT Study

J.P.M. participated in the design of the project, performed all the calculations, analyzed the results, and co-wrote the manuscript.

Abstract

Triphenylamine-pyrrolidine-C_{60} is a potential material to construct high-efficient dye-sensitized solar cells. A combined molecular dynamics and time-dependent density functional theory study has been carried out to analyze charge separation and exciton delocalization in excited states of two constitutional isomers of this compound. Insight into the intrinsic structure of the excited states is provided. The presence of states with a hybrid excitonic and charge-transfer character is suggested to promote the direct charge separation process by excitation, which could have a significant impact on the efficiency of the light-harvesting species. A greater amount of such hybrid states is found at short distances between the triphenylamine fragment and the C_{60} cage.

Keywords

6.2 Theoretical Estimation of the Rate of Photoinduced Charge Transfer Reactions in Triphenylamine C$_{60}$ Donor-Acceptor Conjugate

J.P.M. participated in the design of the project, performed all the calculations, analyzed the results, and co-wrote the manuscript.

Journal of COMPUTATIONAL CHEMISTRY

Theoretical Estimation of the Rate of Photoinduced Charge Transfer Reactions in Triphenylamine C$_{60}$ Donor–Acceptor Conjugate

Juan Pablo Martínez,[a] Miquel Solà,*[a] and Alexander A. Voityuk*[a,b]

Fullerene-based molecular heterojunctions such as the [6,6]-pyrrolidine-C$_{60}$ donor–acceptor conjugate containing triphenylamine (TPA) are potential materials for high-efficient dye-sensitized solar cells. In this work, we estimate the rate constants for the photoinduced charge separation and charge recombination processes in TPA-C$_{60}$ using the unrestricted and time-dependent DFT methods. Different schemes are applied to evaluate excited state properties and electron transfer parameters (reorganization energies, electronic couplings, and Gibbs energies). The use of open-shell singlet or triplet states, several density functionals, and continuum solvation models is discussed. Strengths and limitations of the computational approaches are highlighted. The present benchmark study provides an overview of the expected performance of DFT-based methodologies in the description of photoinduced charge transfer reactions in fullerene heterojunctions. © 2016 Wiley Periodicals, Inc.

DOI: 10.1002/jcc.24355

Introduction

Fullerenes are probably one of the most promising materials for the construction of organic dye-sensitized solar cells (DSSCs).[1–8] The interest in fullerene DSSCs is mainly due to the fact that they are a low-cost replacement for silicon-based solar cells and they are associated to profitable manufacturing and negligible toxicity.[9–14]

The reference system for fullerene DSSCs is the blend of poly(3-hexylthiophene) (P3HT) and [6,6]-phenyl-C$_{61}$-butyric acid methyl ester (PCBM). It has been extensively studied experimentally and theoretically.[12,15–21] For instance, rate constants (k_{ct}, subscript ct stands for charge transfer; it can be turned into subscripts cs and cr standing for charge separation and charge recombination, respectively) for photoinduced charge transfer (CT) reactions occurring in P3HT-PCBM reveal the potential of such materials in the construction of efficient DSSCs. Based on quantum chemistry methods, these k_{ct} have been demonstrated[22] to be tunable by a few parameters so that the power conversion efficiency may be increased,[23–25] which highlights, in fact, the importance of theoretical developments for the understanding and design of DSSCs with improved efficiency.[26]

At the molecular level, blends such as P3HT-PCBM are classified into the so called bulk heterojunctions[27] (BHJs), where the donor and acceptor moieties are not covalently connected, and molecular heterojunctions[28] (mHJs) with covalently linked donor and acceptor. The use of mHJs allows a better control of their structure and the charge mobility. Also, mHJs represent a remarkable advantage for computational modeling of underlying CT processes.[28] In particular, the theoretical computation of the different parameters determining k_{ct} in fullerene DSSCs can be conveniently performed for these systems.

In this work, we study the mHJ of triphenylamine (TPA) (electron donor) and C$_{60}$ (electron acceptor; see Fig. 1) to eval-

uate the performance of density functional theory (DFT) quantum chemical methodology in predicting CT parameters and k_{ct} in the donor–acceptor dyads.

TPA and its derivatives have been used as photoactive molecules during several decades and their applicability in the construction of DSSCs is also of technological interest.[29–34] The molecules were considered in several experimental and (TD)DFT computational studies related to the mHJ approach. TPA is able to confine cationic charge and hamper aggregation between molecules, which induces self-quenching and reduces the electron injection efficiency.[31,33] Conversely, C$_{60}$ is an excellent electron acceptor[35–38] that can react with a variety of chemical agents.[39–44]

Recently, based on electrochemical and photophysical studies, Echegoyen et al.[45] determined k_{ct} for the TPA-C$_{60}$ and TPA-Sc$_3$N@I_h-C$_{80}$ donor–acceptor conjugates and showed that (i) ultrafast charge separation (CS) reactions occur at the molecular interface, thus giving evidence of CT activity; (ii) TPA-Sc$_3$N@I_h-C$_{80}$ generates longer-lived photoinduced charge transfer states (CTSs) than does TPA-C$_{60}$; (iii) increasing the

Figure 1. Structure of triphenylamine-[6,6]-pyrrolidine-C_{60} conjugate. Carbon, nitrogen, and hydrogen atoms are represented by gray, cherry, and blue spheres.

distance of the donor–acceptor interface produces longer-lived CTSs; (iv) nonpolar solvents bring about lack of CT activity; on the contrary, more polar solvents can slow down the charge recombination (CR) reaction; (v) a smaller value of k_{ct} for the CR reaction with $Sc_3N@I_h-C_{80}$ in comparison with C_{60} was found, which was attributed to a smaller value of the driving force.

In this work we aim to assess the performance of DFT-based methodology for the description of CT reactions occurring in the TPA-C_{60} donor–acceptor complex. In view of that, different schemes to estimate the reorganization energy and driving forces are analyzed. We are aware of the challenges concerning the understanding of CT processes at the molecular level.[46] In particular, electronic couplings and driving forces can be significantly affected by structural fluctuations on the donor–acceptor interface and the accurate description of localization/delocalization dynamics of a photogenerated electron-hole pair is quite difficult. Additionally, some studies have underlined a possible role of two-electron excitations in excited states of cyanine-like structures such as TPA, which may represent a limitation for DFT.[47,48] Nevertheless, our results may be a useful reference for future investigations of CT phenomena in (endohedral) fullerene DSSCs.

Methods

General

All of the quantum chemical calculations were completed with the program Gaussian09.[49] Unless otherwise specified, the (U)CAM-B3LYP/6-31G* and TD-CAM-B3LYP/6-31G* level of theories[50] coupled to the conductor-like screening model[51] with benzonitrile as the solvent (COSMO:bzn) in equilibrium solvation were used for the calculations of single-point energies, geometry optimizations, and molecular properties of both solvated ground and excited states. Henceforth, let us

refer these methods by using the abbreviations U-DFT and TD-DFT, respectively. Despite the good performance of hybrid functionals in the calculation of intramolecular electronic excitations,[52,53] the range separated functional CAM-B3LYP is expected to provide a more reliable description of CTSs. In particular, CAM-B3LYP yields reasonable oscillator strength values and relatively accurate excitation energies for Rydberg and intermolecular CT transitions (within an error of 0.5 eV).[54,55] Although this work is mainly focused on U-DFT and TD-DFT via CAM-B3LYP coupled to COSMO in equilibrium solvation, through the manuscript we discuss the use of other theoretical frameworks, density functionals, and continuum solvation models, as well as the effect of different solvents on excitation energies; all of them are explicitly specified in due course for reasons of clarity.

Structure of the interface TPA-C_{60}

Only one optimized geometry of TPA-C_{60} was taken into consideration. It corresponds to the ground-state (GS) equilibrium geometry optimized in the implicit presence of benzonitrile. In a previous work,[56] we demonstrated that the structural variability of the TPA-C_{60} interface modeled by molecular dynamics simulations does not have a significant impact on the intrinsic nature of excited states. Accordingly, all our estimations of excited states are always done at the geometry of GS schematized in Figure 1, unless otherwise specified.

Analysis of excited states

For the analysis of excited states,[57,58] we make use of the extent of excitation delocalization in the excited state ψ_i which can be measured as:

$$X_{ii}(F) = \frac{1}{2} \sum_{\alpha,\beta \in F} \left[(SP^{0i})_{\alpha\beta} (P^{0i}S)_{\alpha\beta} \right], \quad (1)$$

where the sums run over all atomic orbitals centered in fragment F, S is the atomic orbital overlap matrix, and P^{0i} is the symmetrized one-electron transition density matrix between the GS ψ_0 and the excited state ψ_i in the atomic orbital representation. The overall charge separation Δq between fragments F_1 and F_2 is estimated as:

$$\Delta q = \sum_{\substack{\alpha \in F_1 \\ \beta \in F_2}} \left[(SP^{0i})_{\alpha\beta}(P^{0i}S)_{\alpha\beta} + (SP^{0i})_{\beta\alpha}(P^{0i}S)_{\beta\alpha} \right] \quad (2)$$

These quantities $X_{ii}(F)$ (being F either C_{60} or TPA) and Δq are computed by means of linear-response[59] TD-CAM-B3LYP/6-31G* in the gas phase.

Rate constant expression for charge transfer reactions, k_{ct}

Assuming a weak electronic coupling between the donor and acceptor moieties, the theory of nonadiabatic electron transfer is taken into account for the description of the CT processes.

In view of that, we use the standard formulation developed by Marcus:[60,61]

$$k_{ct} = \frac{2\pi}{\hbar} V_{ij}^2 \frac{1}{\sqrt{4\pi\lambda k_B T}} \exp\left(-\frac{(\lambda+\Delta G^0)^2}{4\lambda k_B T}\right), \tag{3}$$

where λ is the total reorganization energy, ΔG^0 is the Gibbs energy difference between the initial and final states, V_{ij} is the electronic coupling between the initial and final states, T is the temperature, k_B is the Boltzmann constant, and $\hbar$ is the reduced Planck constant.

Total reorganization energy, λ

The total reorganization energy λ is usually decomposed into two terms, the internal reorganization energy λ_{int} and the external reorganization energy λ_{ext}, so that $\lambda = \lambda_{int} + \lambda_{ext}$.[60]

Internal reorganization energy, λ_{int}. The energy required to rearrange all the nuclei of the system due to a CT reaction leading from a neutral state to a CTS is computed as follows:

$$\lambda_{int} = \frac{1}{2}\left(E'_n - E_n + E'_{CTS} - E_{CTS}\right) \tag{4}$$

where $E_{n(CTS)}$ is the energy of the neutral (CTS) state computed in the equilibrium geometry of the neutral (CTS) state and $E'_{n(CTS)}$ is the energy of the neutral (CTS) state computed in the equilibrium geometry of the CTS (neutral state). Nevertheless, λ_{int} can be also calculated by considering isolated donor and acceptor fragments as a separated contribution to the internal organization of each fragment:

$$\lambda_{int} = \lambda_D + \lambda_A \tag{5}$$

$$\lambda_{D(A)} = \frac{1}{2}\left(E'_n - E_n + E'_{ion} - E_{ion}\right) \tag{6}$$

where $\lambda_{D(A)}$ is the reorganization energy of either the donor or the acceptor. $E_{n(ion)}$ is the energy of the neutral (ionic) state computed in the equilibrium geometry of the neutral (ionic) state; and $E'_{n(ion)}$ is the energy of the neutral (ionic) state computed in the equilibrium geometry of the ionic (neutral) state. The ionic states are $+1e^-$ cation and $-1e^-$ anion states for the donor and acceptor fragments, respectively.

External reorganization energy, λ_{ext}. Changes in solvent polarization, λ_{ext}, is one of the parameters that introduces more uncertainty to the estimation of k_{ct}. In this work, we present three different approaches to calculate λ_{ext} as follows:

(i) Two-sphere Marcus model, λ_{ext} (M).[62-64]

$$\lambda_{ext}(M) = \frac{1}{4\pi\varepsilon_0}\Delta e^2\left(\frac{1}{2a_1} + \frac{1}{2a_2} - \frac{1}{R}\right)\left(\frac{1}{\varepsilon_{OP}} - \frac{1}{\varepsilon_s}\right) \tag{7}$$

where ε_o and Δe are respectively the vacuum permittivity and the amount of transferred charge; a_1, a_2, and R are respectively the donor and acceptor sphere radii and the distance between the sphere centers. We use the contact distance, defined as

$R = a_1 + a_2$; wherein the sphere radii were calculated by computing the molecular volume of each fragment, defined as the volume inside a contour of 0.001 electrons/Bohr density which was determined from a gas-phase CAM-B3LYP/6-31G* calculation. ε_{OP} and ε_s are the optical and zero-frequency dielectric constants of the surrounding media obtained from the literature.[49]

(ii) Nonequilibrium versus equilibrium solvation, λ_{ext} (E_{noneq}-E_{eq}). The difference between nonequilibrium and equilibrium solvation naturally arises from excited state calculations in solution. That is to say, a very fast process occurs when the solvent polarizes its electron distribution (electronic polarization); but the solvent may be reoriented (dipole polarization; e.g., rotation), which is a much slower process. If the solvent does not have enough time to fully respond, like in a vertical electronic excitation, then the situation is described by nonequilibrium solvation (E_{noneq}). In contrast, if the solvent does have enough time to fully respond to the solute in both ways (electronic and dipole polarizations) then the situation is described by equilibrium solvation (E_{eq}). Accordingly, λ_{ext} is simply the energy difference between E_{noneq} and E_{eq}.[49]

(iii) Dynamic polarization response, λ_{ext} ($E_{noneq}(\omega)$-E_{eq}). In this approach, E_{eq} is exactly the same as explained in (ii); that is, the time or frequency (ω) to reach E_{eq} is such that the electronic and dipole polarizations can be completed. In this regard, molecular movements depend on ω of the change of direction of the electric field; in fact, as ω increases the dipole polarization effect tends to vanish and ε_s shall be only dependent on the electronic polarization, as a result the nonequilibrium effects shall appear subsequently in the different contributions to the polarization (i.e., orientational, atomic, and electronic polarization). The vanishing dipole polarization effect can be conveniently simulated by setting a calculation in which $\varepsilon_s = \varepsilon_{OP}$; thus obtaining $E_{noneq}(\omega)$. Then λ_{ext} is simply the energy difference between $E_{noneq}(\omega)$ and E_{eq}.[49,65]

Electronic coupling

There are a number of studies focused on the development of theoretical frameworks for the evaluation of the electronic coupling.[66-68] Previous studies discussed the implications of using a particular level of theory,[69,70] basis set,[71] and methods.[72] We applied the Fragment Charge Difference method (FCD) to derive the coupling values from excited states of the system calculated with TD-DFT.[73]

Changes in Gibbs energy, ΔG_{ct}. The CT reactions under study are given as follows:

$$TPA-C_{60} + h\nu \rightarrow TPA-C_{60}^* \tag{8}$$

$$TPA-C_{60}^* \rightarrow TPA^+ - C_{60}^- \tag{9}$$

$$TPA^+ - C_{60}^- \rightarrow TPA-C_{60} \tag{10}$$
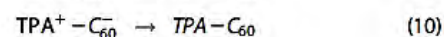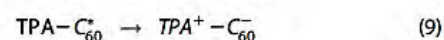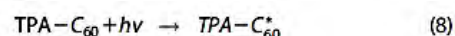
The initial formation of a molecular exciton state is represented by eq. (8), the CS and CR reactions are respectively eq. (9) and eq. (10). Observe that eq. (8) is not the common

LUMO+1

LUMO

HOMO

HOMO-1
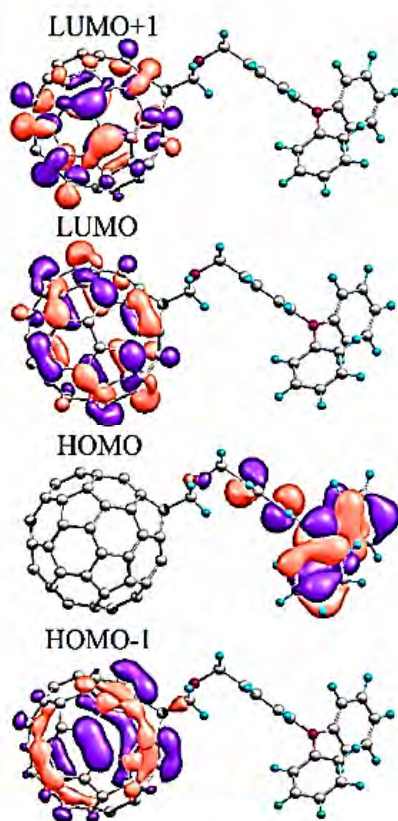
Figure 2. Frontier molecular orbitals in TPA-C_{60}.

approach wherein the photon absorption mainly occurs in the donor fragment.[22,74] The reason is due to the many lowest excited states that are mostly localized in C_{60}. Assuming a negligible entropic component, changes in electronic energy ΔE_{ct} for the CT reactions nearly correspond to ΔG_{ct} ($\Delta E_{ct} \approx \Delta G_{ct}$). Franck–Condon excitations and excited-state properties of every excited state represented in eq. (9) and eq. (10) were computed via the TD-DFT framework. Conversely, we also use the U-DFT formalism to obtain Franck–Condon and relaxed CTSs by interchanging one alpha HOMO localized in TPA with one alpha LUMO located in C_{60} such that a self-consistent field solution is searched;[49] in other words, constraining the self-consistent field process to a solution of the type $TPA^+ - C_{60}^-$. To this end, we first perform a RCAM-B3LYP/6-31G* calculation to obtain the equilibrium geometry and relaxed wavefunction of GS; then, we use the Gaussian09 standard keyword *Guess=(Read,Alter)* to obtain either a Franck–Condon or relaxed CTS by following the next process: (i) *Guess = Read* recovers the GS wavefunction, (ii) *Guess = Alter* specifies orbitals to be alternated from the GS wavefunction (from Fig. 2, it should be understood that interchanging alpha HOMO by alpha LUMO must lead to a CT situation, that is $TPA^+ - C_{60}^-$), and (iii) we perform a UCAM-B3LYP/6-31G* calculation keeping the modified wavefunction so as to reach a self-consistent field solution for both cases: the geometry-relaxed or the Franck–Condon CTS. As mentioned before, we make use of

the abbreviation U-DFT for every calculation performed in the unrestricted formalism for either CTSs or some other exciton state. That is, by following the same procedure, neutral excited states can be also modeled by U-DFT by interchanging alpha HOMO-1 and alpha LUMO since this alteration does not lead to a CT situation in view of both orbitals are fully localized in C_{60} [see TPA-C_{60}* in eq. (9)]. Observe that the restricted formalism is only used for GS.

Results and Discussion

This section initiates with the introduction of the electronic transitions under study with their respective oscillator strength value and orbital contributions, along with the extent of exciton delocalization $X_{ii}(F)$ and amount of charge separation Δq, so as to provide a comprehensive description of the excited states of interest. Then, a detailed evaluation of reorganization energies and electronic couplings is reported; wherein the external reorganization energy is the main subject to discuss in view of the difficulties associated to the calculation of such a parameter. To account for Gibbs energies, we first aim to describe the initial formation of a molecular exciton from which charge separation can occur; after that Gibbs energies of charge separation and recombination reactions are given. The variation of the dielectric constant as a function of the excitation energy is also analyzed so that the lack of charge transfer activity in nonpolar solvents is explained. In line with this subject, we briefly discuss alternative approaches for the description of CT activity such as the use of other density functionals, other continuum solvation models, triplet states, or even other theoretical approximations. Finally, the most relevant results are collected to calculate the rate constants for the photoinduced charge transfer reactions under consideration; then the results are compared to the experimental evidence. At the end, a brief justification of the lack of nuclear degrees of freedom in the current study is explicated.

Extent of charge separation and exciton delocalization for electronically excited states

Our discussion begins with the analysis of the most relevant electronic excited states. In Figure 2 some frontier molecular orbitals (MOs) in TPA-C_{60} are depicted. As a matter of fact, most frontier MOs are entirely localized at the fullerene cage; therefore, the lowest-energy electronic transitions are expected to be mainly localized at the fullerene moiety.

An electronic transition exclusively occurring in the cage leads to the formation of a localized excited state (LES). Conversely, since HOMO is fully localized at the TPA fragment, an electronic transition in which the main contribution is a HOMO to LUMO + X (in C_{60}) excitation leads to the formation of a CTS. In Table 1 the two lowest in energy LESs and CTSs are reported as calculated via gas-phase TD-CAM-B3LYP/6-31G*. The HOMO-1-to-LUMO transition leads to the excited state lowest in energy (LES$_1$) that lies at 2.46 eV with respect to the gas-phase GS. It is an orbitally forbidden transition as indicated by the vanishing value of the oscillator strength.

Table 1. Franck–Condon excitation energies *Ex* in eV (nm), oscillator strengths *f*, corresponding HOMO→LUMO (H→L) transitions (coefficients), extent of exciton delocalization $X_{ii}(F)$ in each fragment, and amount of charge separation Δq (in electrons) for the two lowest-energy localized (LES) and charge transfer (CTS) states.[a]

Parameter	Excited State			
	LES$_1$	LES$_2$	CTS$_1$	CTS$_2$
Ex	2.457 (504.5)	2.544 (487.3)	3.477 (356.6)	3.630 (341.5)
f	0.003	0.000	0.001	0.000
Transition	H-1 → L (0.92)	H-1 → L+1 (0.67)	H → L (0.98)	H → L+1 (0.96)
X_{ii} (TPA)	0.00	0.00	0.00	0.00
X_{ii} (C$_{60}$)	0.99	0.99	0.00	0.02
Δq	0.01	0.00	0.99	0.98

[a] All the results refer to the gas phase. *Ex* is the difference between the energy of that excited state and the ground state.

Furthermore, we can observe that TPA has no contribution in the formation of LES$_1$ because this molecular exciton state is not extended through this fragment, X_{ii}(TPA) = 0.0. However, this state is clearly originated from a transition fully localized at the C$_{60}$ moiety as shown by the X_{ii}(C$_{60}$) = 1.0 value and the lack of charge separation (Δq = 0.0). Exactly the same conclusions are attained for LES$_2$; which are in good agreement with the experimental spectrum of C$_{60}$, wherein the 2.0 to 3.0 eV energy range corresponds only to forbidden transitions.[75,76] In view of that, other LESs are expected to be inaccessible by photon absorption within the mentioned energy range.

The excitation corresponding to a HOMO-to-LUMO transition lies at 3.48 eV and leads to the CTS lowest in energy. Nevertheless, CTSs can be only accessed after dissociation of a Frenkel exciton; from which an electron may be migrated to a phase boundary through spatial translation of such an exciton. As a result, electronic transitions leading to a CTS by direct photon absorption are either completely forbidden or only weakly allowed. Observe that this is indeed the case for CTS$_1$ and CTS$_2$ in view of their vanishing oscillator strengths. These exciton states with strong charge transfer character are mainly characterized by the amount of donor-to-acceptor charge separation, Δq = 1.0, and their notable exciton delocalization through the whole complex; that is to say, CTS$_1$ and CTS$_2$ are neither localized at TPA nor C$_{60}$ since X_{ii}(TPA) and X_{ii}(C$_{60}$) are both null.

Further discussion is focused in the electronic excited states reported in Table 1. For our purposes, CT reactions can be consistently described by those states; although the reader should keep in mind that other states of different nature might contribute to the CS process; like those exciton states

with partial charge separation where some amount of charge ($\Delta q \sim 0.5$) is transferred from the donor to the acceptor. Such partial CTSs were analyzed in detail by us for the TPA-C$_{60}$ dyad,[56] although other works describing such partial CTSs in fullerene DSSCs can be found in the literature.[77–79] In addition, conformational changes in TPA-C$_{60}$ were demonstrated to have no significant impact in the intrinsic nature of excited states, therefore the analysis done in this subsection in a single (the most stable) conformation for the GS remains valid.[56]

Internal and external reorganization energies

The appropriate selection of CTSs is crucial for the evaluation of the CT parameters affecting the rate constant. Nuclei are rearranged to compensate the structural stress caused by the excess of charge generated through the entire system. However, geometry relaxation of CTSs is a challenging task for large-sized systems; as a matter of fact, in TPA-C$_{60}$, excited states are scarcely separated by *ca.* 0.1 eV (see complete details in Supporting Information Table S1), which hinders the geometry optimization of a CTS since the procedure rather leads to a neutral excited state because LESs are more abundant. In view of that, we make use of a low-cost methodology to perform a geometry relaxation of CTSs with no geometrical constraints; that is, open-shell singlet CTSs are relaxed by constraining an excess of charge in the donor and acceptor fragments. This strategy can be accomplished by U-DFT as explained in the Methodology section; where we have reached a geometry-relaxed CTS by interchanging alpha HOMO in TPA by alpha LUMO in C$_{60}$ (see Fig. 2);[49] then the calculation of λ_{int} through eq. (4) can be conveniently done. In Table 2, we compare this result with the ones obtained through eq. (5). In this latter case, we optimized the isolated fragments C$_{60}$, C$_{60}^-$, TPA, and TPA$^+$ in the gas phase and in solution. Observe that there is no significant difference between all λ_{int} results; therefore we use the average value for λ_{int} for the estimation of k_{ct} in view of the small standard deviation.

Table 2 lists also λ_{ext} values. Unlike λ_{int}, the uncertainty of the estimations of λ_{ext} is large since our results diverge within a 0.4 eV energy range. As mentioned before, the reliable evaluation of this parameter is difficult to achieve. Some authors set the value of λ_{ext} as an adjustable parameter;[80,81] conversely, the direct evaluation of λ_{ext} can be consistently performed via QM/MM[82] or a polarizable force field.[83] It is expected that

Table 2. Internal and external reorganization energies in eV for the TPA-C$_{60}$ complex.

Approach	Energy
λ_{int} eq. (4)	0.161
λ_{int} eq. (5)	0.160
λ_{int} eq. (5)[a]	0.154
Average	0.158
Standard deviation	0.004
λ_{ext} (M)	0.492
λ_{ext} (E_{noneq}-E_{eq})	0.605
λ_{ext} ($E_{noneq}(\omega)$-E_{eq})	0.869

[a] Calculated in the gas phase.

Table 3. Electronic couplings for photoinduced CT reactions in the TPA-C_{60} complex.

CT reaction	$|V_{ij}|$, eV
$LES_1 \rightarrow CTS_1$	0.0024
$LES_1 \rightarrow CTS_2$	0.0005
$CTS_1 \rightarrow GS$	0.0206
$CTS_2 \rightarrow GS$	0.0108

QM/MM would provide a more accurate value for λ_{ext}, yet it is required that the polarizability of the molecular fragments can be validated through experiments; a condition that is not fulfilled for the system under study. Additionally, the lack of detailed information on the interface and surroundings makes us consider the methods reported in Table 2; indeed, we keep in mind that, in some cases, neither implicit nor explicit solvent models are sufficient enough to reproduce experimental observations as shown for paracyclophane chromophores and, therefore, one might expect different results from different modeling of the solvent.[84] However, it is worth to mention that the approaches that we use to calculate λ_{ext} are completely different (two-sphere against continuum solvation models), but the missing reproducibility must be solved; this issue shall be analyzed at the end of the manuscript.

Electronic couplings

The calculated values of electronic couplings are listed in Table 3. Because the values are sufficiently small, the nonadiabatic approach, eq. (3), may be applied to estimate the corresponding k_{ct}. The coupling is rather sensitive to localization of excited state density. In particular, because of the coupling difference, the $LES_1 \rightarrow CTS_1$ charge separation is expected to be faster than $LES_1 \rightarrow CTS_2$ by a factor of ~ 25.

Energetics of CT reactions

Initial formation of a molecular exciton state on light absorption. The initial formation of LES_1 represented in eq. (8) by direct light absorption corresponds to a dipole-forbidden transition as discussed in Extent of charge separation and exciton delocalization for electronically excited states section. Dipole-allowed LESs of higher-energy populated by light absorbance are expected to relax very fast to LES_1. To prove that charge separation can indeed occur from LES_1 quantum dynamics simulations are required.[59] This type of calculation is out of the scope of the present work. There are some experimental and theoretical works wherein real-time dynamics of CS states in fullerene DSSCs were described.[85,86] For our purposes we highlight the study carried out by Li et al.[87,88] where simulations based on real-time dynamics were performed for a C_{60} fragment (the acceptor) covalently linked to an aniline derivative (the donor). Regardless the oscillator strength, they show the population of LUMO, depopulation of HOMO and population/depopulation of HOMO-1 (coincidently, those MOs resemble the ones in Fig. 2) in a femtosecond (fs) scale after photoinduction. The interesting point of their study is that the population of LUMO (in C_{60}) by one electron can be actually originated from

a HOMO-1→LUMO transition; however, while the time evolves HOMO-1 (the photogenerated hole in C_{60}) is populated again at the time HOMO (in the donor) is depopulated by one electron bringing about charge separation, a process that occurs coherently as the hole in C_{60} is generated/dissociated in an oscillating way (see Fig. 3). Moreover, they observed that the CR reaction takes place after ca. 80 fs as a result of the declination of the LUMO population. In higher-energy and short-time scales they also analyzed the initial molecular excitation formed in the donor fragment, where the charge separation barely lasted 5 fs. In both processes the electron-hole recombination was demonstrated to be dominant. Based on the similitudes in the molecular and electronic structure of the system studied by Li et al. and ours (the donors are cyanine-like structures linked to a pyrrolidine-like ring as the bridge, and the acceptor is C_{60}), we extrapolate their results to our system and infer that charge separation can occur from the initial formation of LES_1.

Charge transfer reactions. The relative energy of LES_1 lies at 2.68 eV as calculated through gas-phase linear-response TD-CAM-B3LYP/6-31G* and 2.42 eV as computed via state-specific (COSMO:bzn)TD-CAM-B3LYP/6-31G* in equilibrium solvation (recall that these and subsequent Franck–Condon excitation energies are relative to the energy of GS; unless otherwise specified). Continuum solvation models implemented under the state-specific framework are claimed to be more accurate than the linear-response approach; we refer the reader to the seminal papers dealing with this subject.[89–94] Unfortunately, the improvements of time-dependent state-specific calculations could not be observed in the calculation of CTSs since we had many difficulties trying to obtain a physically reasonable excitation energy for a solvated CTS in TPA-C_{60}, with no success (CTSs become more stable than the GS). In view of that, we had to resort to the U-DFT approach to obtain the Gibbs energy of solvation ΔG_{sol} of CTSs.

The U-DFT Franck–Condon excited states reported in Table 4 were modeled by moving one alpha electron of the HOMO-1 (in C_{60}) or HOMO (in TPA) to the LUMO + X (in C_{60}). We verified that dipole moments (μ), summations of all the atomic Mulliken charges on a fragment (Q_F where the values +1, 0, or −1 e^-, respectively, means that the complete fragment F is in a cation, neutral or anion state), and the expected values of $<S^2>$ correspond to the excited state under consideration (see Supporting Information Table S2). That is to say, in neutral states, μ for GS are 4.1 and 4.8 debye in the gas phase and in solution, respectively; and analogously 5.1 and 6.7 debye for LES_1. Besides, we distinguish three fragments: the donor TPA, the bridge, and the acceptor C_{60}. For a neutral state, Q_F are +0.1, 0.0, and −0.1 e^- for TPA, the bridge, and C_{60}, respectively. Conversely, μ for CTSs ranges from 47.7 to 49.4 and from 56.1 to 59.5 debye in the gas phase and in solution, respectively. Moreover, Q_F are +1.0, 0.0, and −1.0 e^- for TPA, the bridge, and C_{60}; which confirms the correct simulation of the CTSs since TPA appears as a cation and C_{60} as an anion. In all the cases, the open-shell singlet character was also verified since $<S^2>$ is ca. 1.05 (see also the frontier MOs depicted in Supporting Information Table S3 for every excited state under
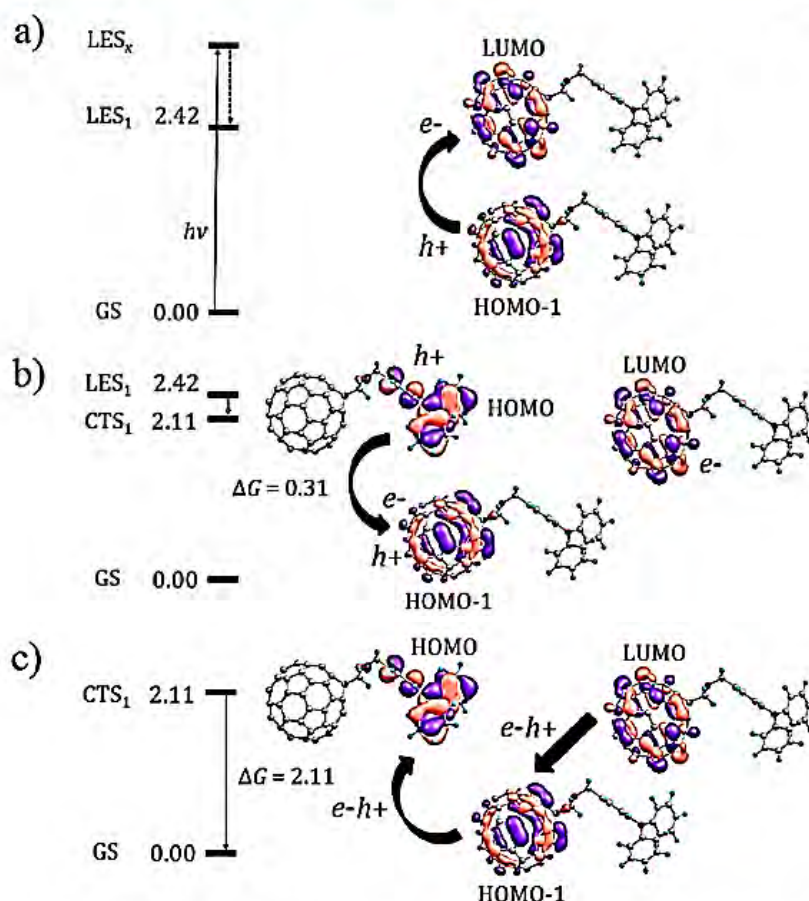
Figure 3. Schematization of Franck–Condon excitations in solution (in eV) and photoinduced charge transfer reactions in TPA-C$_{60}$. a) Formation of the lowest-energy molecular exciton where an electron-hole ($e^{-}h+$) pair is photogenerated in C$_{60}$ by light absorption hv; b) charge separation reaction in which one electron is transferred from TPA to C$_{60}$; the $e^{-}h+$ pair is separated; c) charge recombination reaction in which the ground state is recovered; the $e^{-}h+$ pair is dissociated. Gibbs energies ΔG in solution (in eV) for the CT reactions are also depicted. [Color figure can be viewed in the online issue, which is available at wileyonlinelibrary.com.]

consideration). U-DFT therefore predicts the average value of −1.58 eV for ΔG_{sol} of CTSs with a standard deviation of 0.03 eV. We use this value for the evaluation of the solvated TD-DFT CTS$_1$. The energy of CTS$_1$ lies at 3.69 eV as calculated through gas-phase linear-response TD-CAM-B3LYP/6-31G*; as a result the energy of CTS$_1$ in solution lies at 2.11 eV (compare this value with the one of U-DFT CTS$_1$ in Table 4). In Figure 3, we provide a schematization of our calculations and CT processes.

Our results lead to a ΔG_{cs} of −0.31 eV, which is exactly the experimentally reported value.[45] This value is obtained from the 2.42 eV corresponding to LES$_1$ obtained with state-specific (COSMO:bzn)TD-CAM-B3LYP/6-31G* and the 2.11 eV of the CTS$_1$ calculated from the gas-phase TD-CAM-B3LYP/6-31G* together with the U-DFT solvation energy of the singlet open-shell CTS. However, the neutral singlet excited state energy is reported to be 1.76 eV, which results in an overestimation of 0.66 eV when compared to the energy calculated for LES$_1$. As a matter of fact, $\Delta G_{cr} = -2.11$ eV is also overestimated as compared to the experimental value by exactly the same 0.66 eV.[45] This overestimation constitutes another source of error for the theoretical prediction of k_{cr}. This issue shall be analyzed in detail at the end of the manuscript together with λ_{ext}.

Quenched charge transfer reactions. The solvent plays an important role in the CT activity. So far, all our calculations are performed by taking into account benzonitrile ($\varepsilon_s = 25.6$). Nonetheless, in Figure 4 the variation of the excitation energy in solution of LES$_1$ and CTS$_1$ as a function of ε_s is examined via U-DFT. As ε_s decrease, CTS$_1$ becomes less stable than LES$_1$ and

Table 4. U-DFT relative energies[a] in eV with respect to the solvated ground state (GS) for electronically excited states and their respective Gibbs energy of solvation ΔG_{sol} in eV.

| State | Transition | E_{rel} | | ΔG_{sol} |
		COSMO:bzn	gas-phase	
GS	none	0.000	0.218	−0.218
LES$_1$	H-1 → L	2.364	2.598	−0.234
CTS$_1$	H → L	2.192	3.756	−1.563
CTS$_2$	H → L+1	2.332	3.893	−1.562
CTS$_3$	H → L+2	2.530	4.142	−1.611

[a] All the excited states were calculated at the equilibrium geometry of GS.

Figure 4. Variation of the vertical energies of LES$_1$ and CTS$_1$ in solution as a function of the dielectric constant ε_s. [Color figure can be viewed in the online issue, which is available at wileyonlinelibrary.com.]

the CS reaction does not occur because it corresponds to an endergonic process. These results concur with the experimental evidence in which steady-state fluorescence measurements confirmed the absent of CT activity in toluene ($\varepsilon_s = 2.4$) and carbon disulfide ($\varepsilon_s = 2.6$). Moreover, CT activity can be observed even in tetrahydrofuran (THF, $\varepsilon_s = 7.4$) despite of the slightly favorable driving force, which is calculated to be only 0.02 eV (0.09 eV experimental); unlike less polar solvents.[45]

The use of hybrid functionals for gas-phase TD-DFT calculations should be avoided since they predict CTS$_1$ to be the lowest-energy excited state, which is in contradiction with Figure 4 and experimental results. Indeed, the similar results obtained through linear-response TD-B3LYP/6-31G* coupled to the PCM,[65] COSMO, and SMD[95] solvation models suggest that, when compared to the gas-phase results, failures in the determination of CTS energies are not originated from the continuum solvation model, but from the inherent problems of the theory (see Supporting Information Table S4). The use of range separated functionals are supposed to be a better alternative in the determination of CTSs.[96] Accordingly, our results at the TD-ωB97XD/6-31G* level of theory[97] were compared to the analogous TD-CAM-B3LYP ones. Unlike hybrid functionals, range separated functionals do reproduce the correct order of excited state energies since CTSs are calculated to be lying ∼1.5 eV above the lowest localized excited state in the gas phase; in agreement with the U-DFT ΔG_{sol} estimated for CTSs in benzonitrile (see Supporting Information Table S5).

This trend was also observed by using the Tamm–Dancoff approximation[59] (see Supporting Information Table S1). Unfortunately, solvent effects could not be observed by means of linear-response TD-DFT coupled to continuum solvation models since energies in solution r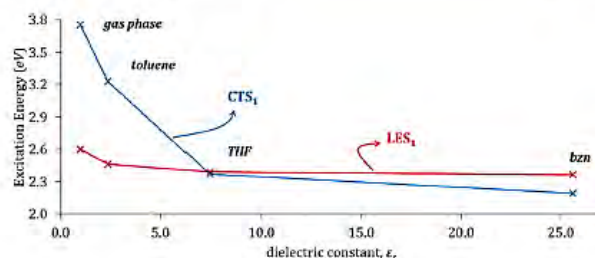esult in exactly the same quantity as in the gas phase; and in the case of state-specific TD-DFT, CTS energies were highly underestimated so that negative excitation energies were calculated[49] (i.e., CTSs were determined to be lying below the GS). Both approaches therefore could not reproduce the trends observed in Figure 4 despite the use of range separated density functionals. We assume that a possible reason of the failure of linear-response TD-DFT to calculate solvated CTSs is due to the vanishing predicted transition dipole moments.

As a final remark, it has been purposed the alternative use of U-DFT triplet excited states instead of TD-DFT in the determination of excitation energies and properties of CTSs in fullerene DSSCs.[22,79] However, the formation of low-energy triplet excited states in donor–acceptor pairs have been proved to be a loss mechanism;[98,99] which may be attributed to the dipole-forbidden transitions. The justification of the use of U-DFT triplet states lies in the fact that it is a low-cost alternative to reach reliable energies of CTSs in fullerene DSSCs; that is, the unpaired electrons are well separated such that the exchange interaction is negligible, therefore singlet and triplet CTSs are expected to be nearly structurally and energetically equivalent. In fact, the relative energy with respect to GS of a geometry-relaxed triplet CTS is 1.88 eV; only 0.15 eV lower in energy than the relaxed singlet CTS$_1$. Moreover, the triplet CTS has $\lambda_{int} = 0.16$ eV in good agreement with our previous results for singlet CTSs (see Supporting Information Table S6 for more details).

Rate constants of photoinduced charge transfer reactions

In previous sections, we discussed the evaluation of λ_{int}, λ_{ext}, V_{ij} and ΔG_{ct} concerning different drawbacks related to the intrinsic problems of the theoretical methodologies under consideration. We were able to anticipate the sources of error with a bigger impact in the estimation of k_{ct}; which are λ_{ext} and ΔG_{cr} (i.e., the energy of CTS$_1$); therefore, let us conduct this section around these two parameters.

In Table 5, k_{ct} is estimated as a function of λ_{ext}. In the case of the CS reaction, the value of ΔG_{cs} is in excellent agreement with the experimental reference; as a result, it seems that a two-sphere model (i.e., λ_{ext} (M)) might be the best alternative in the estimation of k_{ct} since our theoretical values resemble the experimental value of k_{cs}. However, to avoid misleading observations, we consider that consistent conclusions related to the appropriate evaluation of λ_{ext} can be only attained by simultaneously taking into account both CT reactions. In this regard, by using a two-sphere model, k_{cr} drastically vanishes; as a result this approach is not suitable for the calculation of k_{ct} in the system under consideration.

ΔG_{cr} also introduces uncertainty. In Table 5, k_{cr} is reported as a function of ΔG_{cr}. We note that our estimation of ΔG_{cr} can be used together with λ_{ext} ($E_{noneq}(\omega)$-E_{eq}) so as to better reproduce the experimental trends of k_{cr} within deviations of

Table 5. Rate constants (in 1/s) for CT reactions as a function of the external reorganization energy λ_{ext}. Thermal energy $k_BT = 0.026$ eV; $\lambda_{int} = 0.158$ eV; V_{ij} for the CS and CR reactions are respectively 0.0024 and 0.0206 eV.

λ_{ext}[a]	k_{cs}; $\Delta G_{cs} = -0.31$[b]	k_{cr}; $\Delta G_{cr} = -2.11$[c]	k_{cr}; $\Delta G_{cr} = -1.45$[d]
0.492	3.51×10^9	2.44×10^{-2}	9.94×10^7
0.605	1.35×10^9	1.33×10^2	3.16×10^9
0.869	1.23×10^8	1.86×10^7	2.07×10^{11}
	6.00×10^{10}[e]	1.90×10^9[e]	

[a] In agreement with the Methodology section, in descending order this parameter respectively corresponds to λ_{ext} (M), λ_{ext} (E_{noneq}-E_{eq}), and λ_{ext} ($E_{noneq}(\omega)$-E_{eq}). [b] ΔG_{cs} calculated as the energy difference between LES$_1$ (state-specific (COSMO:bzn)TD-CAM-B3LYP/6-31G*) and CTS$_1$ (gas-phase linear-response TD-CAM-B3LYP/6-31G* with U-DFT solvent corrections). [c] ΔG_{cr} calculated as the energy difference between CTS$_1$ described in footnote b and the solvated ground state GS. [d] Experimental value of ΔG_{cr}. [e] Experimental values of k_{ct}.

less than two order of magnitudes. Similarly, the experimental value of ΔG_{cr} can be used together with λ_{ext} (E_{noneq}-E_{eq}). Those observations suggest that solvent reorganization can be better simulated[49] by continuum solvation models than by the two-sphere model. The limitation of the latter may be attributed to the fact that the condition $R \gg a_1 + a_2$ is not fulfilled for our system.

As a final remark, it might be proposed that the lack of structural variability could alter our estimations; and also the use of the Marcus–Levich–Jortner equation might be a better approach to include the effect of quantum vibrational modes, wherein the nuclear relaxation caused by CT is expected to involve intramolecular (high-frequency) modes.[100,101] Nevertheless, we infer that the role of nuclear degrees of freedom in the system under study can be ignored and still the physics of the CT process can be described satisfactorily. Our deduction is supported by the fact that we have previously described the intrinsic nature of excited states for a number of thermally accessible structures of the TPA-C$_{60}$ interface as simulated by molecular dynamics; from which we concluded that geometrical variations do not significantly change the intrinsic nature and distribution of excited states.[56] As a matter of fact, through the manuscript we show the similitudes in structure and energetics between Franck–Condon and geometry-relaxed CTSs. Moreover, in an interesting discussion by Troisi,[102] it is suggested that CS reactions in organic photovoltaic interfaces are mostly purely electronic processes which is in line with our conclusions.

Conclusions

We have assessed the performance of U-CAM-B3LYP and TD-CAM-B3LYP with the 6-31G* basis set for estimating the rate constant of photoinduced charge transfer reactions using the molecular heterojunction triphenylamine C$_{60}$ donor–acceptor conjugate as the reference system with the following conclusions:

i. Electronic couplings have been computed using multiconfigurational excited states as generated by TD-DFT. The applied scheme does not use orbital approximation to represent locally excited and CT states and thus provides more accurate values.

ii. Franck–Condon and relaxed charge transfer states can be conveniently modeled by a U-DFT approach coupled to a continuum solvation model to explain experimental data or predict trends in CT properties of related systems. Due to the large separation of the unpaired electrons, either singlet or triplet states with charge transfer character can be used to estimate the internal and external reorganization energies as well as the energetics of charge transfer reactions. Conversely, both linear-response and state-specific time-dependent solvation models were unable to provide a reasonable estimate of the energy of solvated charge transfer states.

iii. The evaluation of external reorganization energies can be properly performed by continuum solvation models.

The use of the two-sphere model may be limited for systems with relatively small donor–acceptor distance.

iv. The lack of charge transfer activity experimentally observed in nonpolar solvents is attributed to the destabilization of charge transfer states relative to the lowest excited state localized on the dye (TPA). This result can be only reproduced by time-dependent range separated functionals (CAM-B3LYP). In addition, a good performance of U-DFT has been found: the obtained variation of excitation energies as a function of the dielectric constant reproduces well the experimental data.

v. We have provided a benchmark for the strengths and weaknesses of computational schemes used for modeling photoinduced charge separation and charge recombination processes in fullerene-based molecular heterojunctions.

[1] D. Jariwala, V. K. Sangwan, L. J. Lauhon, T. J. Marks, M. C. Hersam, *Chem. Soc. Rev.* **2013**, *42*, 2824.
[2] S. Günes, H. Neugebauer, N. S. Sariciftci, *Chem. Rev.* **2007**, *107*, 1324.
[3] J. Yan, B. R. Saunders, *RSC Adv.* **2014**, *4*, 43286.
[4] B. R. Saunders, M. L. Turner, *Adv. Colloid Interface Sci.* **2008**, *138*, 1.
[5] S. A. Berhe, H. B. Gobeze, S. D. Pokharel, E. Park, W. J. Youngblood, *ACS Appl. Mater. Interfaces* **2014**, *6*, 10696.
[6] G. Chen, J. Seo, C. Yang, P. N. Prasad, *Chem. Soc. Rev.* **2013**, *42*, 8304.
[7] J. L. Delgado, P. A. Bouit, S. Filippone, M. A. Herranz, N. Martín, *Chem. Commun.* **2010**, *46*, 4853.
[8] C. A. Echeverry, R. Cotta, E. Castro, A. Ortiz, L. Echegoyen, B. Insuasty, *RSC Adv.* **2015**, *5*, 60823.
[9] M. S. Mauter, M. Elimelech, *Environ. Sci. Technol.* **2008**, *42*, 5843.
[10] P. Kumar, S. Chand, *Prog. Photovoltaics Res. Appl.* **2012**, *20*, 377.
[11] G. Yu, J. Gao, J. C. Hummelen, F. Wudl, A. J. Heeger, *Science* **1995**, *270*, 1789.
[12] B. C. Thompson, J. M. J. Fréchet, *Angew. Chem. Int. Ed.* **2008**, *47*, 58.
[13] P. W. M. Blom, V. D. Mihailetchi, L. J. A. Koster, D. E. Markov, *Adv. Mater.* **2007**, *19*, 1551.
[14] J. Peet, J. Y. Kim, N. E. Coates, W. L. Ma, D. Moses, A. J. Heeger, G. C. Bazan, *Nat. Mater.* **2007**, *6*, 497.
[15] J. Guo, H. Ohkita, H. Benten, S. Ito, *J. Am. Chem. Soc.* **2010**, *132*, 6154.
[16] C. Groves, O. G. Reid, D. S. Ginger, *Acc. Chem. Res.* **2010**, *43*, 612.
[17] G. Li, V. Shrotriya, J. Huang, Y. Yao, T. Moriarty, K. Emery, Y. Yang, *Nat. Mater.* **2005**, *4*, 864.
[18] H. Ohkita, S. Cook, Y. Astuti, W. Duffy, S. Tierney, W. Zhang, M. Heeney, I. McCulloch, J. Nelson, D. D. C. Bradley, J. R. Durrant, *J. Am. Chem. Soc.* **2008**, *130*, 3030.
[19] I. W. Hwang, D. Moses, A. J. Heeger, *J. Phys. Chem. C* **2008**, *112*, 4350.
[20] X. Ai, M. C. Beard, K. P. Knutsen, S. E. Shaheen, G. Rumbles, R. J. Ellingson, *J. Phys. Chem. B* **2006**, *110*, 25462.
[21] G. Sauvé, R. Fernando, *J. Phys. Chem. Lett.* **2015**, *6*, 3770.
[22] T. Liu, A. Troisi, *J. Phys. Chem. C* **2011**, *115*, 2406.
[23] D. M. González, V. Körstgens, Y. Yao, L. Song, G. Santoro, S. V. Roth, P. Müller-Buschbaum, *Adv. Energy Mater.* **2015**, *5*, 1401770.

[24] W. Y. Wong, X. Z. Wang, Z. He, A. B. Djurisić, C. T. Yip, K. Y. Cheung, H. Wang, C. S. K. Mak, W. K. Chan, *Nat. Mater.* **2007**, *6*, 521.

[25] J. C. Bijleveld, A. P. Zoombelt, S. G. J. Mathijssen, M. M. Wienk, M. Turbiez, D. M. de Leeuw, R. A. J. Janssen, *J. Am. Chem. Soc.* **2009**, *131*, 16616.

[26] L. M. Peter, *J. Phys. Chem. C* **2007**, *111*, 6601.

[27] Y. Huang, E. J. Kramer, A. J. Heeger, G. C. Bazan, *Chem. Rev.* **2014**, *114*, 7006.

[28] J. L. Segura, N. Martin, D. M. Guldi, *Chem. Soc. Rev.* **2005**, *34*, 31.

[29] A. S. D. Sandanayaka, H. Sasabe, Y. Araki, Y. Furusho, O. Ito, T. Takata, *J. Phys. Chem. A* **2004**, *108*, 5145.

[30] V. Coropceanu, J. Cornil, D. A. da Silva Filho, Y. Olivier, R. Silbey, J. L. Brédas, *Chem. Rev.* **2007**, *107*, 926.

[31] J. Preat, *J. Phys. Chem. C* **2010**, *114*, 16716.

[32] G. Wu, F. Kong, Y. Zhang, X. Zhang, J. Li, W. Chen, W. Liu, Y. Ding, C. Zhang, B. Zhang, J. Yao, S. Dai, *J. Phys. Chem. C* **2014**, *118*, 8756.

[33] J. Xu, L. Wang, G. Liang, Z. Bai, L. Wang, W. Xu, X. Shen, *Bull. Korean Chem. Soc.* **2010**, *31*, 2531.

[34] Z. Ning, Q. Zhang, W. Wu, H. Pei, B. Liu, H. Tian, *J. Org. Chem.* **2008**, *73*, 3791.

[35] N. Martin, L. Sánchez, B. Illescas, I. Pérez, *Chem. Rev.* **1998**, *98*, 2527.

[36] F. D'Souza, R. Chitta, A. S. D. Sandanayaka, N. K. Subbaiyan, L. D'Souza, Y. Araki, O. Ito, *J. Am. Chem. Soc.* **2007**, *129*, 15865.

[37] K. Stranius, V. Iashin, T. Nikkonen, M. Muuronen, J. Helaja, N. Tkachenko, *J. Phys. Chem. A* **2014**, *118*, 1420.

[38] B. M. Illescas, N. Martin, *J. Org. Chem.* **2000**, *65*, 5986.

[39] N. Martin, *Chem. Commun.* **2006**, 2093.

[40] C. Thilgen, F. Diederich, *Chem. Rev.* **2006**, *106*, 5049.

[41] N. Martin, I. Pérez, L. Sánchez, C. Seoane, *J. Org. Chem.* **1997**, *62*, 5690.

[42] Z. Zhou, P. A. Magriotis, *Org. Lett.* **2005**, *7*, 5849.

[43] S. H. Hoke, J. Molstad, D. Dilettato, M. J. Jay, D. Carlson, B. Kahr, R. G. Cooks, *J. Org. Chem.* **1992**, *57*, 5069.

[44] C. Bingel, *Chem. Ber.* **1993**, *126*, 1957.

[45] J. R. Pinzón, D. C. Gasca, S. G. Sankaranarayanan, G. Bottari, T. Torres, D. M. Guldi, L. Echegoyen, *J. Am. Chem. Soc.* **2009**, *131*, 7727.

[46] J. L. Brédas, J. E. Norton, J. Cornil, V. Coropceanu, *Acc. Chem. Res.* **2009**, *42*, 1691.

[47] A. E. Masunov, *Int. J. Quantum Chem.* **2010**, *110*, 3095.

[48] R. Send, O. Valsson, C. Filippi, *J. Chem. Theory Comput.* **2011**, *7*, 444.

[49] M. J. Frisch, G. W. Trucks, H. B. Schlegel, G. E. Scuseria, M. A. Robb, J. R. Cheeseman, G. Scalmani, V. Barone, B. Mennucci, G. A. Petersson, H. Nakatsuji, M. Caricato, X. Li, H. P. Hratchian, A. F. Izmaylov, J. Bloino, G. Zheng, J. L. Sonnenberg, M. Hada, M. Ehara, K. Toyota, R. Fukuda, J. Hasegawa, M. Ishida, T. Nakajima, Y. Honda, O. Kitao, H. Nakai, T. Vreven, J. Montgomery, J. A., J. E. Peralta, F. Ogliaro, M. Bearpark, J. J. Heyd, E. Brothers, K. N. Kudin, V. N. Staroverov, R. Kobayashi, J. Normand, K. Raghavachari, A. Rendell, J. C. Burant, S. S. Iyengar, J. Tomasi, M. Cossi, N. Rega, J. M. Millam, M. Klene, J. E. Knox, J. B. Cross, V. Bakken, C. Adamo, J. Jaramillo, R. Gomperts, R. E. Stratmann, O. Yazyev, A. J. Austin, R. Cammi, C. Pomelli, J. W. Ochterski, R. L. Martin, K. Morokuma, V. G. Zakrzewski, G. A. Voth, P. Salvador, J. J. Dannenberg, S. Dapprich, A. D. Daniels, Ö. Farkas, J. B. Foresman, J. V. Ortiz, J. Cioslowski, D. J. Fox, Gaussian 09, Rev. C.01; Gaussian, Inc.: Wallingford, CT, **2009**.

[50] T. Yanai, D. P. Tew, N. C. Handy, *Chem. Phys. Lett.* **2004**, *393*, 51.

[51] A. Klamt, *J. Phys. Chem.* **1995**, *99*, 2224.

[52] M. R. Silva-Junior, M. Schreiber, S. P. A. Sauer, W. Thiel, *J. Chem. Phys.* **2008**, *129*, 104103.

[53] D. Jacquemin, B. Mennucci, C. Adamo, *Phys. Chem. Chem. Phys.* **2011**, *13*, 16987.

[54] M. J. G. Peach, T. Helgaker, P. Sałek, T. W. Keal, O. B. Lutnaes, D. J. Tozer, N. C. Handy, *Phys. Chem. Chem. Phys.* **2006**, *8*, 558.

[55] Y. Tawada, T. Tsuneda, S. Yanagisawa, T. Yanai, K. Hirao, *J. Chem. Phys.* **2004**, *120*, 8425.

[56] J. P. Martínez, S. Osuna, M. Solà, A. Voityuk, *Theor. Chem. Acc.* **2015**, *134*, 12.

[57] F. Plasser, H. Lischka, *J. Chem. Theory Comput.* **2012**, *8*, 2777.

[58] A. V. Luzanov, O. A. Zhikol, *Int. J. Quantum Chem.* **2010**, *110*, 902.

[59] M. A. L. Marques, N. T. Maitra, F. M. S. Nogueira, E. K. U. Gross, A. Rubio, Fundamentals of Time-Dependent Density Functional Theory; Springer-Verlag: Berlin, Heidelberg, **2012**.

[60] P. F. Barbara, T. J. Meyer, M. A. Ratner, *J. Phys. Chem.* **1996**, *100*, 13148.

[61] R. A. Marcus, *Rev. Mod. Phys.* **1993**, *65*, 599.

[62] R. A. Marcus, *J. Chem. Phys.* **1956**, *24*, 966.

[63] R. A. Marcus, *Annu. Rev. Phys. Chem.* **1964**, *15*, 155.

[64] R. A. Marcus, N. Sutin, *Biochim. Biophys. Acta Rev. Bioenerg.* **1985**, *811*, 265.

[65] J. Tomasi, B. Mennucci, R. Cammi, *Chem. Rev.* **2005**, *105*, 2999.

[66] R. J. Cave, M. D. Newton, *Chem. Phys. Lett.* **1996**, *249*, 15.

[67] A. A. Voityuk, N. Rösch, *J. Chem. Phys.* **2002**, *117*, 5607.

[68] Q. Wu, T. Van Voorhis, *Phys. Rev. A* **2005**, *72*, 024502.

[69] C. P. Hsu, *Acc. Chem. Res.* **2009**, *42*, 509.

[70] S. Yeganeh, T. Van Voorhis, *J. Phys. Chem. C* **2010**, *114*, 20756.

[71] J. Huang, M. Kertesz, *Chem. Phys. Lett.* **2004**, *390*, 110.

[72] J. Huang, M. Kertesz, *J. Chem. Phys.* **2005**, *122*, 234707.

[73] A. A. Voityuk, *J. Phys. Chem. C* **2013**, *117*, 2670.

[74] I. Gutiérrez-González, B. Molina-Brito, A. W. Götz, F. L. Castillo-Alvarado, J. I. Rodríguez, *Chem. Phys. Lett.* **2014**, *612*, 234.

[75] S. Leach, M. Vervloet, A. Després, E. Bréheret, J. P. Hare, T. John Dennis, H. W. Kroto, R. Taylor, D. R. M. Walton, *Chem. Phys.* **1992**, *160*, 451.

[76] G. Orlandi, F. Negri, *Photochem. Photobiol. Sci.* **2002**, *1*, 289.

[77] Y. Kanai, J. C. Grossman, *Nano Lett.* **2007**, *7*, 1967.

[78] S. Few, J. M. Frost, J. Kirkpatrick, J. Nelson, *J. Phys. Chem. C* **2014**, *118*, 8253.

[79] T. Liu, D. L. Cheung, A. Troisi, *Phys. Chem. Chem. Phys.* **2011**, *13*, 21461.

[80] S. Di Motta, E. Di Donato, F. Negri, G. Orlandi, D. Fazzi, C. Castiglioni, *J. Am. Chem. Soc.* **2009**, *131*, 6591.

[81] S. E. Koh, C. Risko, D. A. da Silva Filho, O. Kwon, A. Facchetti, J. L. Brédas, T. J. Marks, M. A. Ratner, *Adv. Funct. Mater.* **2008**, *18*, 332.

[82] J. E. Norton, J. L. Brédas, *J. Am. Chem. Soc.* **2008**, *130*, 12377.

[83] D. P. McMahon, A. Troisi, *J. Phys. Chem. Lett.* **2010**, *1*, 941.

[84] A. Masunov, S. Tretiak, J. W. Hong, B. Liu, G. C. Bazan, *J. Chem. Phys.* **2005**, *122*, 224505.

[85] A. A. Bakulin, S. D. Dimitrov, A. Rao, P. C. Y. Chow, C. B. Nielsen, B. C. Schroeder, I. McCulloch, H. J. Bakker, J. R. Durrant, R. H. Friend, *J. Phys. Chem. Lett.* **2013**, *4*, 209.

[86] J. Jakowski, S. Irle, B. G. Sumpter, K. Morokuma, *J. Phys. Chem. Lett.* **2012**, *3*, 1536.

[87] C. T. Chapman, W. Liang, X. Li, *J. Phys. Chem. Lett.* **2011**, *2*, 1189.

[88] C. T. Chapman, W. Liang, X. Li, *J. Phys. Chem. A* **2013**, *117*, 2687.

[89] R. Cammi, S. Corni, B. Mennucci, J. Tomasi, *J. Chem. Phys.* **2005**, *122*, 104513.

[90] R. Improta, G. Scalmani, M. J. Frisch, V. Barone, *J. Chem. Phys.* **2007**, *127*, 074504.

[91] R. Cammi, B. Mennucci, J. Tomasi, *J. Phys. Chem. A* **2000**, *104*, 5631.

[92] B. Mennucci, C. Cappelli, C. A. Guido, R. Cammi, J. Tomasi, *J. Phys. Chem. A* **2009**, *113*, 3009.

[93] M. Cossi, V. Barone, *J. Chem. Phys.* **2001**, *115*, 4708.

[94] C. A. Guido, D. Jacquemin, C. Adamo, B. Mennucci, *J. Chem. Theory Comput.* **2015**, *11*, 5782.

[95] A. V. Marenich, C. J. Cramer, D. G. Truhlar, *J. Phys. Chem. B* **2009**, *113*, 6378.

[96] P. Wiggins, J. A. G. Williams, D. J. Tozer, *J. Chem. Phys.* **2009**, *131*, 091101.

[97] J. D. Chai, M. Head-Gordon, *Phys. Chem. Chem. Phys.* **2008**, *10*, 6615.

[98] C. Dyer-Smith, L. X. Reynolds, A. Bruno, D. D. C. Bradley, S. A. Haque, J. Nelson, *Adv. Funct. Mater.* **2010**, *20*, 2701.

[99] R. Schueppel, C. Uhrich, M. Pfeiffer, K. Leo, E. Brier, E. Reinold, P. Baeuerle, *ChemPhysChem* **2007**, *8*, 1497.

[100] N. R. Kestner, J. Logan, J. Jortner, *J. Phys. Chem.* **1974**, *78*, 2148.

[101] J. Jortner, *J. Chem. Phys.* **1976**, *64*, 4860.

[102] A. Troisi, *Faraday Discuss.* **2013**, *163*, 377.

Chapter 7

Results and Discussion

This chapter has been divided into three main subjects with the aim of providing a better comprehension of the goals attained in the current manuscript. Firstly, the chemo- and regioselective of cycloadditions to carbon nanostructures is outlined; thus emphasizing in the (2+1) addition to a paramagnetic endohedral metallofullerene with 24 nonequivalent carbon atoms (i.e. La@C_{2v}-C_{82}), and the (2+2) and (4+2) cycloadditions of benzyne as a function of the curvature of the nanostructure; that is, from fullerenes to zig-zag single-walled carbon nanotubes (Chapter 4). Then, metal-catalyzed reactions with fullerenes are discussed so as to explain the Suzuki-Miyaura-like arylation of C_{60} catalyzed by a rhodium complex; as well as the contribution of C_{60} in ruthenium-based catalysts synthesized *in silico* for the metathesis of olefins (Chapter 5). Finally, the triphenylamine-C_{60} donor-acceptor conjugate is analyzed in detail in order to predict its potential application in the construction of fullerene-based dye-sensitized solar cells (Chapter 6). This thesis therefore encompasses a complete exploration of (metal-catalyzed) chemical reactions and electron transfer in carbon nanostructures.

7.1 Chemo- and Regioselectivity of Cycloadditions to Carbon Nanostructures

According to the *Gold Book* of the International Union of Pure and Applied Chemistry, IUPAC,[365] the exact definition of chemoselectivity refers to the selective reactivity of one functional group in the presence of others. A reagent has a high chemoselectivity if reaction occurs with only a limited number of different functional groups. On the other hand, a regioselective reaction is the one in which one direction of bond making or breaking occurs preferentially over all other possible directions. The chemo- and regioselectivity of cycloaddition reactions to carbon nanostructures can be explained taking as an example the BH addition to nitride clusters inside the icosahedral cage of C_{80} under mild conditions; that is, $Y_3N@I_h$-C_{80}, $Er_3N@I_h$-C_{80}, $Sc_3N@I_h$-C_{80}, and $Lu_3N@I_h$-C_{80}. It is found that the BH addition is chemoselective since diethyl bromomalonate only reacts with the two former cages; besides, it is also regioselective because the addition preferably occurs at a [6,6] bond of the cage.[159,366] Particularly, in the following subsections the chemo- and regioselectivity of cycloadditions to fullerenes and carbon nanotubes are the main subjects of study with the aim of explaining experimental observations and providing a systematic understanding of the reactions under consideration.

7.1.1 The special case of the Bingel-Hirsch addition to La@C_{2v}-C_{82}

The La@C_{2v}-C_{82} cage is a special case study because the paramagnetic nature of the structure may lead to different mechanistic pathways. Additionally, there are 24 nonequivalent carbon atoms associated to 35 bonds (19 [6,6] bonds are denoted with numbers from *1* to *19*, and 16 [5,6] bonds are labeled with letters from *a* to *p* as schematized in Figure 7.1a). As a result, 35 methanofullerenes and 35 methanofulleroids can be distinguished. Furthermore, La@C_{2v}-C_{82}, or La^{3+}@C_{2v}-$C_{82}$$^{3-}$ in agreement with the ionic model, is an IPR structure in which bond types are classified according to the structure of four-fused polycyclic aromatic hydrocarbons: type A or pyracylene, type B, type C or pyrene, and type D or corannulene (see also Figure 7.1a).[367–370]

In the first step of the BH addition studied in the current thesis, 1,8-diazabicycloundec-7-ene (DBU), the base, subtracts the acidic proton of dimethyl bromomalonate to generate the carbanion, **dmbm⁻**. Consequently, the cyclopropanation reaction begins when **dmbm⁻** attacks the bond **γ**, which is the bond formed by the carbon atoms Cα and Cβ, leading to the formation of a singly-bonded derivative defined as $\mathbf{I_{C\alpha,\gamma}}$, given that the initial attack occurred in carbon atom Cα. This intermediate structure has to overcome an energy barrier represented by a transition state (TS) structure, $\mathbf{TS_{C\alpha,\gamma}}$, which leads to the formation of a methanofullerene $\mathbf{*P_{C\alpha C\beta,\gamma}}$ or a methanofulleroid $\mathbf{P_{C\alpha C\beta,\gamma}}$ (see details in Figure 7.1b). Analogously, the formation of either $\mathbf{*P_{C\alpha C\beta,\gamma}}$ or $\mathbf{P_{C\alpha C\beta,\gamma}}$ can be not only attained by the attack of **dmbm⁻** to carbon atom Cα but the reaction can also evolve from the carbon atom Cβ through the stationary structures $\mathbf{I_{C\beta,\gamma}}$ and $\mathbf{TS_{C\beta,\gamma}}$.

7.1.1.1 Classification of the 65 available reaction pathways

In an $\mathbf{I_{C\alpha,\gamma}}$ structure, **dmbm⁻** can freely rotate to form three different orientational isomers defined by the alignment of bromine and the bond **γ**; therefore, three BH adducts may be formed. However, only two orientational isomers can be distinguished when **dmbm⁻** is linked to carbon atoms C2, C3, C5, C8, C17, C20, and C24 because of symmetry arguments. Every single nonequivalent carbon atom represents one reaction site, and the formation of distinct orientational isomers of every $\mathbf{I_{C\alpha,\gamma}}$ structure gives rise to 65 different reaction pathways, some of them leading to the same product (e.g., cyclopropanation to bond **1** can be achieved from either C1 or C2, as can be seen by observing Figure 7.1a).

Under typical conditions and in the case of EMFs, the BH reaction occurs under kinetic control.[371,372] In view of that, a complete DFT-based study must be performed through the 65 different reaction pathways available in La@C_{2v}-C_{82}. Nonetheless, in the current study, a strategy is designed so that the definition of three different profiles of the BH addition to La@C_{2v}-C_{82} is introduced with the aim of reducing the computational effort by excluding those energetically impeded reaction pathways.
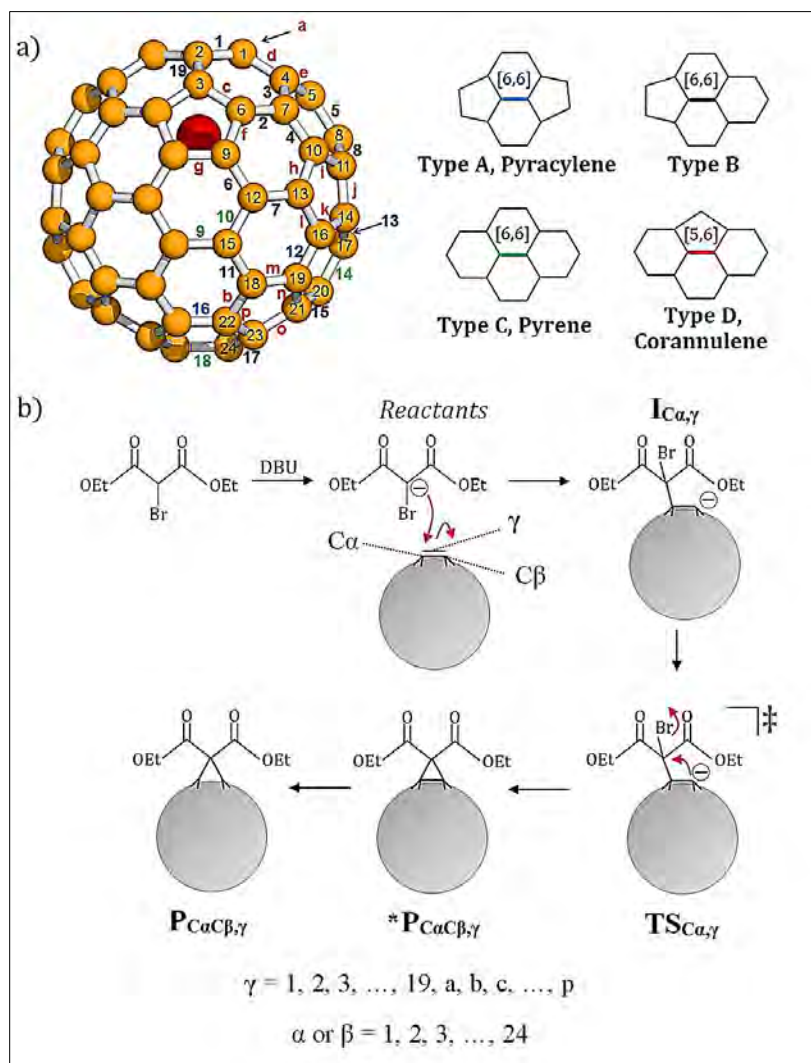
Figure 7.1 a) The 24 nonequivalent carbon atoms and the 35 different bonds of La@C_{2v}-C$_{82}$. For bonds, numbers denote [6,6] bonds and lower-case letters denote [5,6] bonds. Bond types are distinguished by color code (type A: blue, type B: black, type C: green, type D: red). Labels as assigned in a previous study.[132] b) General mechanism of the nucleophilic (2+1) Bingel-Hirsch addition to La@C_{2v}-C$_{82}$. Nomenclature used in the current work is also provided. The attack on a bond γ formed between adjacent carbon atoms Cα and Cβ leads to the formation of an intermediate, either **I$_{C\alpha,\gamma}$** or **I$_{C\beta,\gamma}$**; thus proceeding to the respective transition state, either **TS$_{C\alpha,\gamma}$** or **TS$_{C\beta,\gamma}$**, which leads to the formation of a methanofullerene ***P$_{C\alpha C\beta,\gamma}$** or methanofulleroid **P$_{C\alpha C\beta,\gamma}$**.

The definition of three different profiles in terms of Gibbs energies relative to the reactants in toluene, ΔG_{tol}, is stated as follows: profile type I is defined as the energy profile in which both reaction pathways lead to a BH product that is more stable than the two possible intermediate precursors (**I$_{C\alpha,\gamma}$** and **I$_{C\beta,\gamma}$**). If one or two reaction pathways could be reverted, then profiles type II or type III are defined where the BH product is less stable than one or two of the intermediate precursors, respectively. In these latter cases, the BH retro-reaction will happen and the BH product will not be accumulated. The schematic representation of such a strategy is depicted in Figure 7.2.
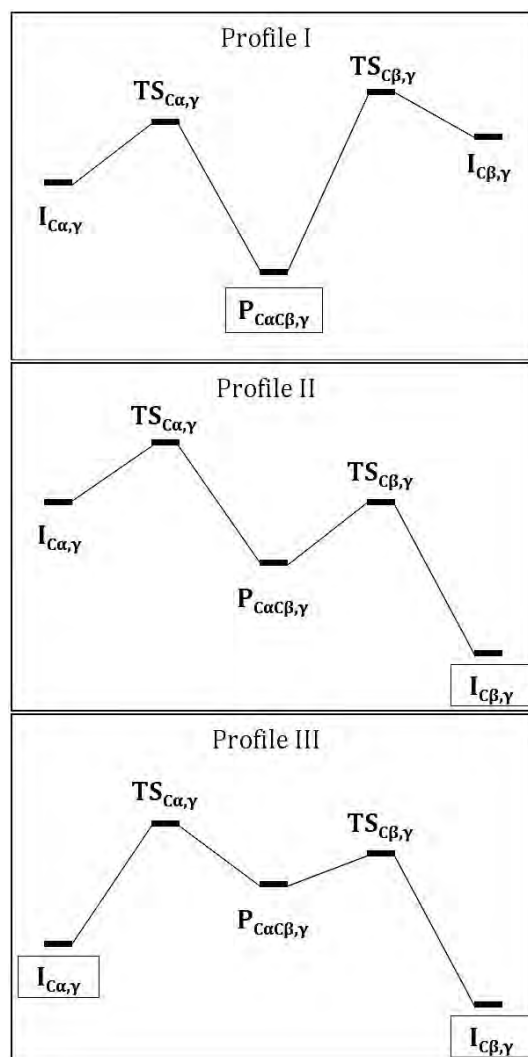
Figure 7.2 Representation of the two reaction pathways leading to the formation of a Bingel-Hirsch adduct as a methanofulleroid or a methanofullerene through the attack on bond γ with adjacent reaction centers $C\alpha$ and $C\beta$. The energy profile in which the retro-Bingel-Hirsch addition is hampered is classified as profile type I. On the contrary, if one or two reaction pathways can be regressed to a singly-bonded derivative then the resulting profiles are respectively classified as II or III. For every diagram, the most likely structure to be experimentally accumulated is enclosed in a rectangular box.

Table 7.1 accounts for ΔG_{tol} for the formation of the 65 different $\mathbf{I}_{C\alpha,\gamma}$ structures and the 35 most stable BH adducts (mostly $\mathbf{P}_{C\alpha C\beta,\gamma}$ adducts due to the fulleroid structure was generally found to be more stable than the methanofullerene $\mathbf{*P}_{C\alpha C\beta,\gamma}$). Based on Figure 7.2 and the values of ΔG_{tol} for the structures related to a single pathway, it is possible to define the profile type in which that reaction pathway can be classified (e.g. for the attack on bond **1**, $\mathbf{P}_{C1C2,1}$ is more stabilized than $\mathbf{I}_{C1,1}$ and $\mathbf{I}_{C2,1}$; therefore, the situation is described by profile type I).

Table 7.1 Classification based on energetic stability (in kcal/mol) of $\mathbf{I_{C\alpha,\gamma}}$, $\mathbf{I_{C\beta,\gamma}}$, and $\mathbf{P_{C\alpha C\beta,\gamma}}$, of all possible Gibbs energy profiles for the Bingel-Hirsch addition to La@C_{2v}-C_{82} in toluene. The structural classification of bond γ is also given. Marked in italics the most stable intermediates (criterion: $\Delta G_{tol} < -10.0$ kcal/mol).

γ	Bond type	Cα	Cβ	$\mathbf{I_{C\alpha,\gamma}}$	$\mathbf{I_{C\beta,\gamma}}$	$\mathbf{P_{C\alpha C\beta,\gamma}}$	Profile
					ΔG_{tol}		
1	B	1	*2*	-7.82	*-13.49*	-15.40	I
2	B	6	7	-8.15[a]	*-10.38*	-9.71	II
3	B	4	7	-8.78	*-10.86*	-12.37	I
4	B	7	10	-8.96	-8.03[a]	-7.96[b]	III
5	B	5	8	-3.58[a]	-7.81[a]	-2.89	III
6	B	9	12	-5.67[a]	-7.40	-0.48	III
7	B	12	*13*	-7.84	*-10.59*	-12.39	I
8	B	8	*11*	-7.81	*-11.54*	-6.03	III
9	C	15	15	0.69	0.69	-15.93	I
10	C	12	15	-7.91	2.18	-11.97	I
11	B	15	18	-0.15	-9.46	-15.40	I
12	A	16	*19*	-3.59[a]	*-11.16*	-9.93[b]	II
13	B	14	17	-8.05	-6.44	-10.66	I
14	C	17	20	-6.99	3.87	-16.56	I
15	B	20	*21*	5.09	*-10.88*	-9.56	II
16	A	22	22	-6.48	-6.48	-10.09[b]	I
17	B	*23*	24	*-13.46*	1.92	-7.86	II
18	C	24	24	2.42	2.42	-18.04	I
19	B	*2*	3	*-14.92*	-7.63	-18.52	I
a	D	1	1	-7.76	-7.76	-15.58	I
b	D	*18*	22	*-11.28*	-6.48[a]	-4.49	III
c	D	3	6	-8.09	-7.81	-7.27	III
d	D	1	4	-7.82[a]	-9.47	-8.79	II
e	D	4	5	-9.58	-3.58	-9.45	II
f	D	6	9	-8.15	-5.67	-12.42	I
g	D	9	9	-5.67[a]	-5.67[a]	2.10[b]	III
h	D	10	*13*	-7.23	*-10.73*	-10.77	I
i	D	10	*11*	-8.03	*-10.40*	-12.71	I
j	D	*11*	14	*-11.55*	-9.09	-9.26	II
k	D	14	16	-9.11	-3.59	-0.29	III
l	D	*13*	16	*-11.30*	-3.59[a]	-4.93	II
m	D	*18*	*19*	*-10.28*	*-10.58*	-7.23	III
n	D	*19*	*21*	*-11.68*	*-10.49*	-9.86	III
o	D	*21*	23	*-11.14*	*-13.74*	-10.30	III
p	D	22	*23*	-4.63	*-12.37*	-8.87	II

[a] ΔG_{tol} for these intermediates was estimated from the energy of the most stable orientational isomer for that specific reaction site. For instance, the energy of $\mathbf{I_{C9,6}}$ is not calculated, but it is taken as the energy of $\mathbf{I_{C9,f}}$ since orientational isomers are energetically very similar. Moreover, from the energy of $\mathbf{I_{C12,6}}$ it is possible to anticipate that bond **6** is not indeed involved in a profile type I.

[b] Only in these four cases, *$\mathbf{P_{C7C10,4}}$, *$\mathbf{P_{C9C9,g}}$, *$\mathbf{P_{C16C19,12}}$, and *$\mathbf{P_{C22C22,16}}$, the most stable Bingel-Hirsch adduct is a methanofullerene instead of a methanofulleroid structure.

After analyzing the profile type for all the 65 available reaction pathways, it is found that only 15 attacks out of 35 are of profile type I. These 15 attacks can occur through 26 different pathways (Cα = Cβ for bonds **9**, **16**, **18**, and **a**) and generate relatively stable BH products. Reaction pathways with profile type I are only taken into account because in this situation the BH adduct is going to be accumulated. Accordingly, the kinetic study is based on the 26 reaction pathways related to profile type I.

7.1.1.2 Product characterization: accumulation of Bingel-Hirsch adducts

The experimental evidence provided by Nagase et al. revealed the isolation and characterization of five different structures with the following product distribution (in percentage): 55.4, 22.1, 5.5, 5.1, and 11.9.[373] Based on electron spin resonance and NMR analyses, the former four adducts were assigned to be singly-bonded derivatives and the latter, the one obtained with a yield of 11.9%, was determined to be a methanofulleroid. The two singly-bonded derivatives with the highest yields are assigned to be the most stable intermediates which are generated at the C2 and C23 positions. The orientational isomers of I_{C2} and I_{C23} are connected to the corresponding addition products via relatively high energy transition states. Indeed, $TS_{C2,1}$, $TS_{C2,19}$, $TS_{C23,17}$, $TS_{C23,o}$, and $TS_{C23,p}$ are associated with energy barriers of 13.1, 15.8, 13.5, 21.5 and 15.2 kcal/mol, respectively. Moreover, the reaction pathways involving the intermediates formed at C23 are classified into profiles II or III. Consequently, the formation of the three products concerning I_{C23} are kinetically hampered, thus resulting in an accumulation of this intermediate as the major product instead of the cyclopropanated derivative. This is in good agreement with the experimental observations since I_{C23} was the only structure confirmed by X-ray and had the highest yield (55.4%). Additionally, the reaction pathways through the bonds around C2 are also associated with activation energies higher than 13 kcal/mol. In view of that, one might expect the same yield for I_{C2} and I_{C23}. Nonetheless, unlike C23, reaction pathways around C2 do actually produce well-stabilized fulleroids and they are classified into profile I; in fact, the global minimum is $P_{C2C3,19}$. Subsequently, a portion of I_{C2} may be consumed to produce $P_{C2C3,19}$ during the BH reaction, thus being the second most abundant singly-bonded adduct (22.1%). Relatively stable singly-bonded derivatives are also formed at C7, C11, C13, C18, C19, and C21 positions. The I_{C19} and I_{C21} species may be accumulated because they are related to profile types II and III, thus characterizing the species with the yields of 5.5% and 5.1%. However, the attacks on the other positions cannot be fully discarded. In conclusion, and in line with experimental observations, La@C_{2v}-C_{82} is not particularly regioselective under Bingel-Hirsch conditions.

The fulleroid (yield of 11.9%) is related to the reaction pathways with the lowest energy barriers, which are calculated to be 5.7 and 6.3 kcal/mol for $\mathbf{TS_{C15,11}}$ and $\mathbf{TS_{C3,19}}$, respectively (see Figure 7.3). Nonetheless, the formation of $\mathbf{I_{C15,11}}$ is hindered because of $\Delta G_{tol} = -0.2$ kcal/mol; therefore, the most favored reaction pathway rather occurs at bond **19** (although the attack on bond **11** cannot be totally dismissed). The other competitive reaction pathway leads to $\mathbf{*P_{C22C22,16}}$, a methanofullerene, yet the formation of a methanofullerene does not resemble the experimentally observed fulleroid; as a result, bond **16** is discarded.
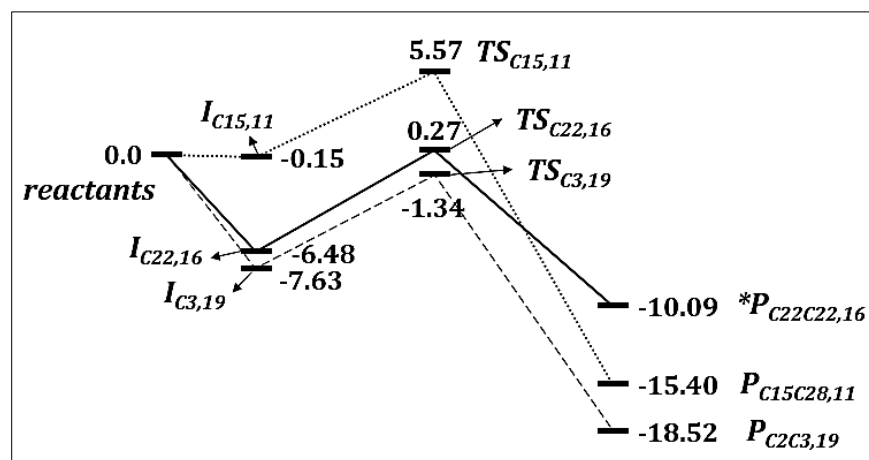
Figure 7.3 Comparison of the Gibbs energy profiles (in kcal/mol) for the lowest-barrier pathways occurring at C15 on bond **11** (dotted line), C3 on bond **19** (dashed-line), and C22 on bond **16** (solid line).

It is interesting to notice that additions with the lowest energy barriers produce well-stabilized fulleroids; indeed, the most stable fulleroid is $\mathbf{P_{C2C3,19}}$ which is produced with one of the lowest energy barrier. The great stability of $\mathbf{P_{C2C3,19}}$ is in line with the experimentally tested thermal stability of the isolated fulleroid.[373] In general, it is observed that the cyclopropanation between **dmbm⁻** and a [6,6] bond is favored when a 5-MR is adjacent to the initially functionalized carbon atom, as shown for bond types A and B.

7.1.2 Cycloadditions as a function of the curvature of the carbon nanostructure

In this subsection, (2+2) and (4+2) pericyclic reactions of benzyne with fullerene C_{60} and a series of zig-zag SWCTNs with diameters ranging from 6.3 to 14.1 Å are studied with the intention of accounting for the effect of the curvature of the nanostructure on the chemical reactivity. As a matter of fact, experiments have revealed that benzyne can react with fullerenes[46,374–377] and EMFs[37,378–380] through (2+2) cycloadditions that occur preferentially at [6,6] bonds, although there are several examples of [5,6] attacks.[381–383] It has been claimed that small-diameter carbon nanostructures like fullerenes promote better the (2+2) cycloaddition.[46,375] For SWCNTs, cycloadditions of benzyne can produce both (2+2) and (4+2) adducts depending on the shape and curvature of the nanotube, as well as their intrinsic electronic nature.[221–223] The mechanistic details of the benzyne cycloaddition (BC) to all these nanostructures of carbon have not been entirely elucidated yet, and the reasons for the chemoselectivity (preference of the (2+2) over the (4+2) BC) and regioselectivity (the [6,6] attack is more frequently found than the [5,6] addition in fullerenes) of the BC have not been discussed to date. In the following subsections these issues are analyzed.
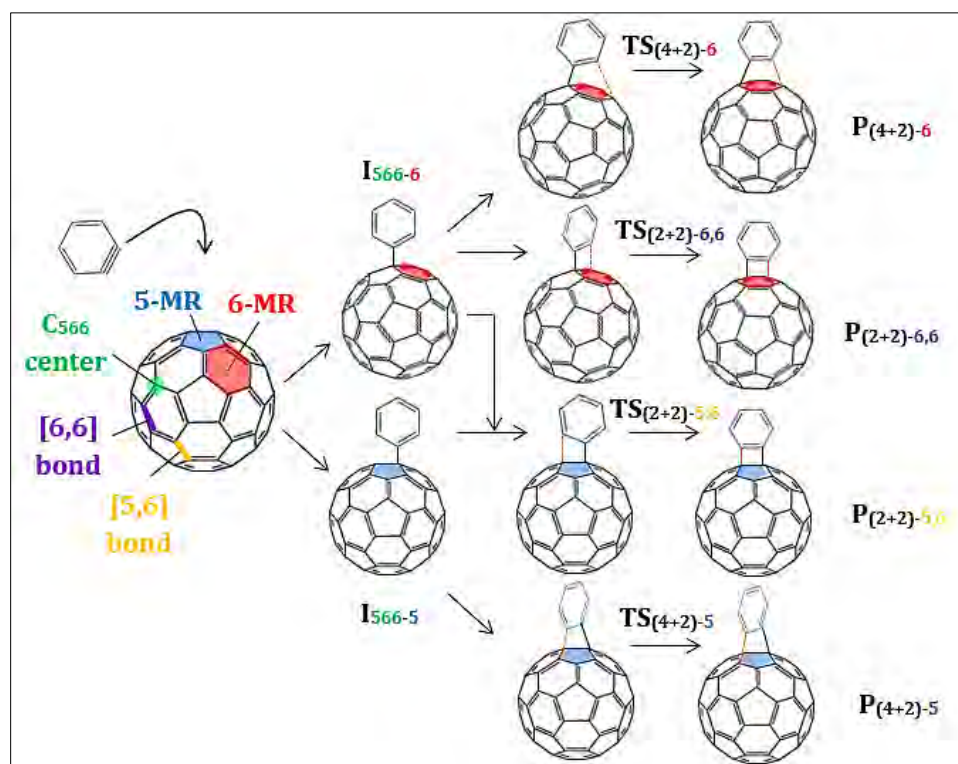
Figure 7.4 Generalized representation of the benzyne cycloaddition to C_{60}. Biradical singly-bonded intermediates are represented as **I**; transition states and final products are labeled as **TS** and **P**, respectively. Two subscripts separated by a dash are used to indicate how the species are formed; in fact, they refer to chemoselectivity-regioselectivity. The left subscript takes the values of "(4+2)" or "(2+2)" to denote whether the 1,4- or 1,2-addition takes place, respectively; but it also acquires the value of "566" indicating the formation of biradical singly-bonded structures related to the attack on a 566 carbon center (i.e. a C_{566} center, see green dot in the fullerene structure). The right subscript takes the values of "5" or "6" to indicate whether a 5- or 6-membered ring (see 5-MR in blue, and 6-MR in red) is under attack; but it can also have the values of "5,6" or "6,6" to denote whether a [5,6] or [6,6] bond is attacked (see respectively orange and purple labels).

7.1.2.1 Benzyne cycloaddition to C_{60}

A generalization of the reaction mechanisms of the BC to C_{60} is depicted in Figure 7.4; wherein the terminology used to identify every structure under study is schematized. In the first stage of the reaction mechanism (see Figure 7.5), a reactant complex (**RC**) is formed followed by the first TS structure, **TS$_{566-6}$**, that leads to a biradical singly-bonded intermediate, **I$_{566-6}$** or the isoenergetic isomer **I$_{566-5}$**. The description of the (2+2) and (4+2) BC to C_{60} can be consistently done from the idea of a rotating benzyne in **I$_{566}$**; being the formation of this latter the rate-determining step for the (2+2) BC (but not for the (4+2) BC).
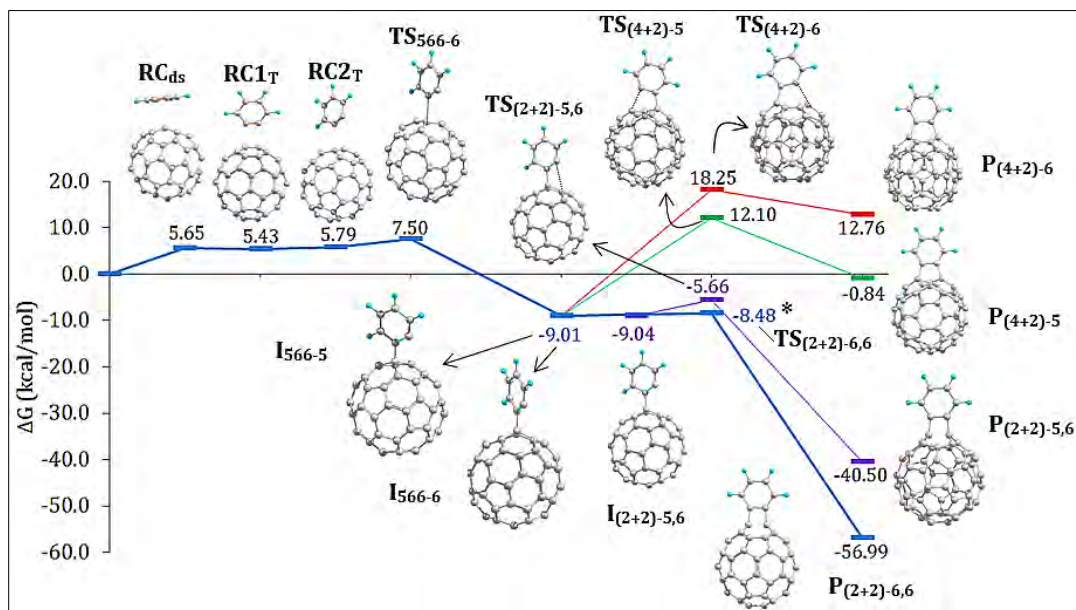
Figure 7.5 Gibbs energy profiles (in kcal/mol) for the (2+2) (in blue and purple) and (4+2) (in red and green) benzyne cycloadditions to fullerene C_{60}. The energy for the TS involving the rotation toward a [6,6] bond marked with a star (*), **TS$_{(2+2)-6,6}$**, corresponds to an upper bound limit. Blue and purple colored ΔG values stand for open-shell singlet structures.

In the (4+2) BC, the ring closure leading to **P$_{(4+2)-5}$** and **P$_{(4+2)-6}$** is respectively generated from **I$_{566-5}$** and **I$_{566-6}$**. However, the (4+2) BC to C_{60} is kinetically hampered in view of the larger energy barriers as compared to its (2+2) BC counterpart. Moreover, the formation of **P$_{(4+2)-6}$** is an endergonic process. On the other hand, the free rotation of benzyne in **I$_{566-5}$** and **I$_{566-6}$** leads to the (2+2) cycloadducts. **P$_{(2+2)-5,6}$** can be only formed from **I$_{566-5}$**; but both **P$_{(2+2)-5,6}$** and **P$_{(2+2)-6,6}$** are produced from **I$_{566-6}$**. In the first case, the ring closure towards **P$_{(2+2)-5,6}$** is hampered by an energy barrier of 3.4 kcal/mol calculated with **TS$_{(2+2)-5,6}$**, which is associated to the ring closure of a 4-MR. In the second case, the ring closure towards **P$_{(2+2)-6,6}$** proceeds with no energy barrier; therefore the (2+2) BC to the [6,6] bond of C_{60} is the most kinetically and thermodynamically favored reaction pathway. However, the (2+2) BC to a [5,6] bond may also occur in view of the relatively small energy barrier. These results are in line with the experimental observations that only (2+2) BC are observed in fullerenes and that the additions to both [6,6] and [5,6] bonds have been reported in the literature, with the [6,6] case being more frequently observed than the [5,6] one.[46,374,376,377,381]

7.1.2.2 Benzyne cycloaddition to zig-zag single-walled carbon nanotubes

SWCNTs constructed under the Clar theory have been named finite-length Clar cells (FLCC, see also Subsection 1.3.3).[174,175,177–179] In this subsection, fully benzenoid FLCC structures with chiral indices (9,0)-, (12,0)-, and (18,0)-SWCNT are studied. Additionally, some FLCC structures lacking completeness of the Clar network such as (8,0)- and (13,0)-SWCNT are also taken into consideration. The reaction mechanism of the BC to zig-zag SWCNTs is only outlined for the case of (9,0)-SWCNT since the mechanistic details are exactly the same for all the SWCNTs under study. The nomenclature of every structure follows the same terminology used in the previous case of C_{60} (see Figure 7.4).

The reaction mechanism depicted in Figure 7.6 starts with the formation of a reactant complex RC_{ds} followed by TS structures for either the (4+2) or (2+2) BC. The energy barrier of 9.8 kcal/mol calculated from TS_{666-6} is associated to the formation of the biradical intermediate I_{666-6}, where benzyne can be rotated toward either a parallel p or an oblique o orientation with respect to the nanotube axis. In this regard, the parallel-oriented (2+2) BC evolves with the rotation of benzyne toward the ring closure to generate $P_{(2+2)-p}$ with an energy cost of 3.7 kcal/mol given by TS_{666-p}. The ring closure in the oblique-oriented (2+2) BC is described by the stationary point $TS_{(2+2)-o}$ with an energy cost of 2.6 kcal/mol. In view of these results, the (2+2) BC can equally proceed at the parallel and oblique positions and the rate-determining step is the formation of I_{666-6}. In the case of the (4+2) BC, $P_{(4+2)-o}$ is highly destabilized since its energy lies 9.2 kcal/mol above the energy of the reactants; on the other hand, the $TS_{(4+2)-p}$ structure is a concerted TS leading to $P_{(4+2)-p}$ with a Gibbs energy barrier of only 4.9 kcal/mol. Therefore, the parallel-oriented (4+2) BC to (9,0)-SWCNT is the most kinetically and thermodynamically favored reaction pathway.
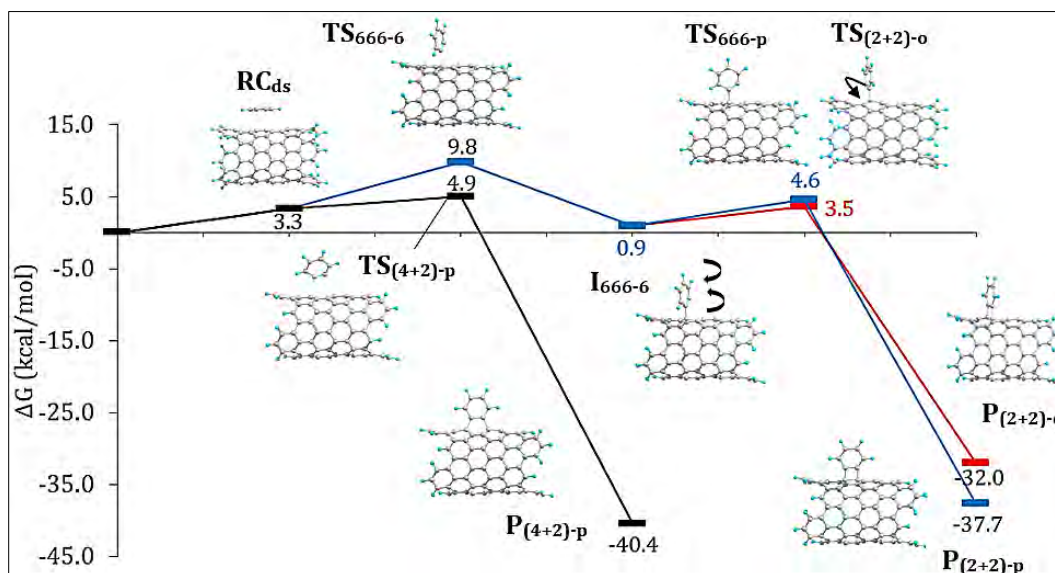
Figure 7.6 Gibbs energy profiles for the (2+2) (for blue and red lines benzyne is respectively added in parallel and oblique position with respect to the nanotube axis) and (4+2) (black line) benzyne cycloadditions to (9,0)-SWCNT. Blue and red colored ΔG values stand for open-shell singlet structures.

7.1.2.3 Reaction energies and barriers as a function of the diameter of the nanostructure

The mechanism as formulated for (9,0)-SWCNT can be also applied for the rest of the structures under consideration. In Table 7.2 it is reported reaction energies in terms of electronic energies (ΔE) for the formation of parallel-oriented benzyne cycloadducts as well as the initial activation energy E_a^1 (i.e. the energy barrier from the reactant complex to the following TS). These results demonstrate that the (4+2) BC is always the preferred reaction pathway for finite-diameter zig-zag SWCNTs because of the substantially lower E_a^1. It is also observed that the larger the curvature of the SWCNT, the lower the energy barriers and the larger the exothermicity[384] of the (2+2) and (4+2) BC. Moreover, **P(4+2)-p** is the most stabilized product in all the cases, and thus the kinetics and thermodynamics correspond to the same addition.

Table 7.2 Initial activation energies (E_a^1) and reaction energies (ΔE) in terms of electronic energy (kcal/mol) as a function of the diameter of the structure (Å).[a]

(n,m)	diameter	E_a^1		ΔE	
		(4+2)	(2+2)	(4+2)	(2+2)
(8,0)	6.26	1.25	4.74	-61.68	-59.49
(9,0)	7.05	1.32	5.67	-57.39	-53.92
(12,0)	9.39	2.36	7.94	-47.88	-45.17
(13,0)	10.18	2.42	7.81	-47.28	-42.61
(18,0)	14.09	5.22	8.90	-39.54	-37.81

[a] ΔE is the energy difference between products and reactants.
E_a^1 is the energy difference between the first transition state and the reactant complex.

Nagase and co-workers[385] concluded that the activation energy for large-diameter armchair (n,n)-SWCNTs (above 10 Å) is lower for the (4+2) BC; but the (2+2) products are always the most stable. The results in Table 7.2 show that a gradual increase of the diameter of the SWCNT causes a steady increase in E_a^1 and ΔE for both types of BC. This trend resembles the tendency observed by Nagase et al.[385] In zig-zag SWCNTs, however, the (4+2) addition is for all diameters preferred kinetically and thermodynamically over the (2+2) one.

7.1.2.4 Structural deformation as a key factor determining the course of the reaction
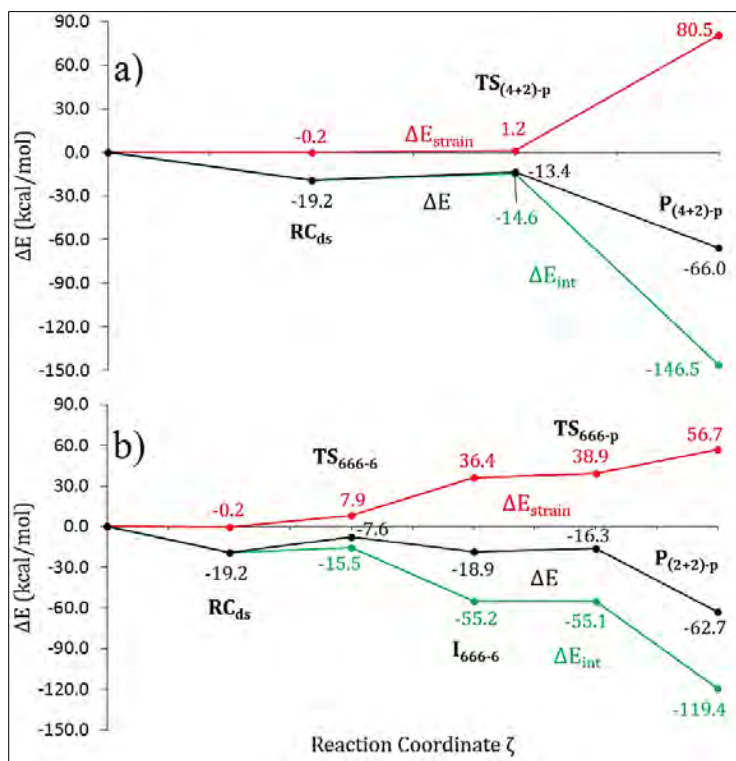
Figure 7.7 Schematic representation of the activation strain model for the cycloadditions of benzyne to (9,0)-SWCNT. a) Parallel (4+2) BC; b) parallel (2+2) BC. Red, green, and black lines respectively correspond to strain, interaction, and total energies.

The activation strain model (ASM) for the BC to (9,0)-SWCNT is depicted in Figure 7.7. The (4+2) BC evolves with practically no deformation of the reactants; while the (2+2) BC involves the formation of intermediate structures in which the reactants are significantly deformed before the ring closure. Despite of the fact that the (4+2) BC generates a more deformed 6-MR adduct (ΔE_{strain} = 80.5 kcal/mol for **P(4+2)-p**), the formation of the less-strained 4-MR adduct produced through the (2+2) BC (ΔE_{strain} = 56.7 kcal/mol for **P(2+2)-p**) is not favored because the preceding formation of a biradical singly-bonded TS (ΔE_{strain} = 7.9 kcal/mol for **TS666-6**), which cannot compete with the unstrained concerted TS in the (4+2) BC (ΔE_{strain} = 1.2 kcal/mol for **TS(4+2)-p**). Since the interaction energy is nearly the same at the first TS of both BC [-14.6 and -15.5 kcal/mol for the (4+2) and (2+2) BC, respectively], it is concluded that the strain energy determines the course of the reaction. Therefore, those cycloadducts produced via a less strained reaction pathway will be favored. The same conclusion was reached by Houk and Osuna in a study of a series of (4+2) cycloadditions to polyaromatic hydrocarbons.[386]
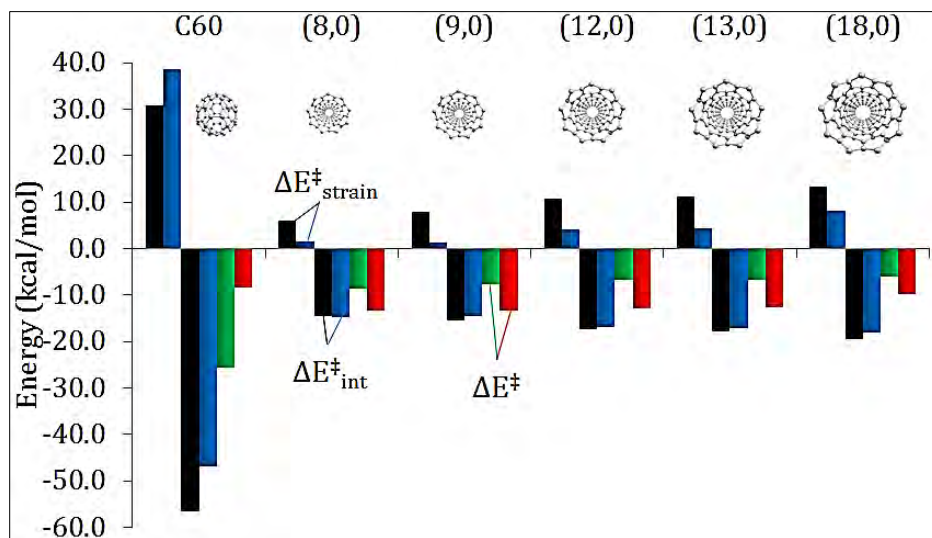
Figure 7.8 Strain energy $\Delta E^{\ddagger}_{strain}$ (top) and transition state interaction $\Delta E^{\ddagger}_{int}$ (bottom) as a function of the diameter and shape of the carbon nanostructure. Black and blue bars respectively correspond to the (2+2) and (4+2) BC. Green and red bars account for the TS energy ($\Delta E^{\ddagger} = \Delta E^{\ddagger}_{strain} + \Delta E^{\ddagger}_{int}$) for the (2+2) and (4+2) BC, respectively. In the case of C_{60}, the values correspond to **TS$_{(2+2)-5,6}$** and **TS$_{(4+2)-5}$**. For SWCNTs, the first (2+2) TS is compared to the (4+2) TS.

In Figure 7.8 the evolution of $\Delta E^{\ddagger}_{strain}$ and $\Delta E^{\ddagger}_{int}$ as a function of the diameter and shape of the nanostructure is illustrated. In C_{60}, comparisons are referred to the TS related to the ring closure, **TS$_{(2+2)}$** and **TS$_{(4+2)}$**, because the first TS, **TS$_{566-6}$**, is common for both BC. Accordingly, the (4+2) TS involves a larger deformation by 7.8 kcal/mol as compared to the (2+2) TS due to the higher distortion of C_{60} required for the formation of a 6-MR ring. Furthermore, the interaction energy for the (2+2) TS is more favored by 9.6 kcal/mol; as a result, the (4+2) BC to C_{60} is not only disfavored by the structural strain but also by the interaction energy. In the case of the tube-shaped nanostructures, there is more interaction between reactants at the first (2+2) TS, from 3.9 to 0.4 kcal/mol, as compared to the (4+2) case. However, there is more deformation of the reactants in the (2+2) TS, being from 6.8 to 4.4 kcal/mol more strained than the (4+2) case, which in fact hinders the course of the (2+2) BC. The large difference in $\Delta E^{\ddagger}_{strain}$ and $\Delta E^{\ddagger}_{int}$ between C_{60} and SWCNTs is because of the already formed covalent bond between C_{60} and benzyne in the TS under study. These results certainly confirm that the structural strain is the main factor determining the reactivity of the carbon nanostructure. The origin of the increased distortion in the TS as the diameter of the SWCNT increases is due to the more pyramidalized carbon atoms in the nanotubes with larger diameters as a consequence of the closer distance with benzyne. That is to say, the reacting carbon atoms in the nanotube have to adopt a closer situation to a sp^3-type geometrical configuration, which causes more deformation.

7.2 Reactions Catalyzed by Metal Complexes Involving C_{60}

In Section 7.1 the functionalization of fullerenes through pericyclic reactions was described in depth; however, the synthesis of many other fullerene adducts can be also reached via organometallic catalysis. That is to say, direct coordination of metallic centers to fullerenes has mainly led to the isolation of compounds with η^2-coordination.[105] The η^5- and η^6-coordination to fullerenes can be achieved by the inclusion of specific organometallic fragments which lead to vanish the unfavorable interactions brought about π-orbitals dispersed through either the 5-MR or 6-MR.[85,387,388] In this section, the rhodium-catalyzed hydroarylation of C_{60} with organoboron compounds in the presence of water is studied in detail. The η^x-coordination (x=1, 2, 5, and 6) of rhodium to C_{60} is analyzed through the whole pathway, as well as the double η^2-coordination of C_{60} referring to the coordination of rhodium to two C_{60} molecules. The aim of the study is to provide the mechanistic details of the Suzuki-Miyaura-like reaction that leads to the hydroarylation of C_{60}, thus explaining experimental observations. The second analysis presented in this section encompasses the metathesis of ethylene catalyzed by complexes synthesized *in silico* to include C_{60}, N-heterocyclic carbenes, and ruthenium as the metallic center; thus describing the catalytic role of fullerene C_{60} in such reactions.
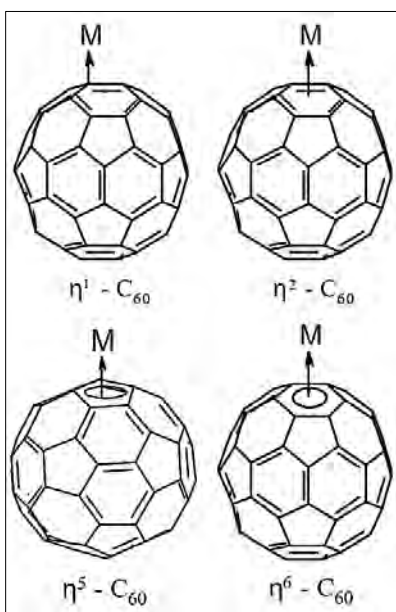
Figure 7.9 Some metal η^x-coordination ($x = 1, 2, 5,$ and 6) compounds with C_{60}.

7.2.1 Rhodium-catalyzed hydroarylation of C_{60}

The Rh-catalyzed arylation of C_{60} with organoboron compounds in the presence of water was firstly described by Itami et al.[76] The addition of various functional groups to C_{60} is possible by this new synthetic method which leads to functional fullerenes. The most productive and selective catalyst turned out to be [Rh-(cod)(MeCN)$_2$]BF$_4$. A highly regioselective mono-addition for the formation of an arylated hydrofullerene was observed; wherein water is essential for the course of the reaction. Several experimental parameters were analyzed which are summarized as follows:

(i)   *Effect of catalyst components*: Among the several catalysts that were studied, [Rh-(cod)$_2$]B(3,5-bis(trifluoromethyl)phenyl)$_4$, [Rh-(cod)$_2$]PF$_6$, and [Rh-(cod)$_2$]OTf were unable to complete the hydroarylation of C_{60}. On the other hand, the best yield was achieved with [Rh-(cod)(MeCN)$_2$]BF$_4$.

(ii)   *Effect of protic additives*: Acidic phenol, methanol, and tert-butanol were found to hamper the reaction. On the other hand, the addition of water was demonstrated to be essential. It is worth mentioning that methanol and tert-butanol have similar pK_a values as water.

(iii)   *Effect of substituents on the boron atom*: Among the several phenylboron compounds, the use of phenylboronic acid produced the arylated hydrofullerene with a yield of 45%. On the other hand, the yield obtained with 2-phenyl-1,3,2-dioxaborinane was 39%, in contrast to 4,4,5,5-tetramethyl-2-phenyl-1,3,2-dioxaborolane for which no yield was observed.

(iv)   *Effect of ortho-substituents on arylboronic acids*: Despite *ortho*-substituents may be though to hinder the reaction because of the steric hindrance, in fact they promote better the reaction than *para*-substituents. This was demonstrated by the introduction of *o*-tolylboronic acid resulting in a yield of 46% of the arylated hydrofullerene, thus contrasting the yield of 12% obtained with *p*-tolylboronic.[76]

Based on the Rh-catalyzed arylation of C_{60} with organoboron compounds experimentally studied by Itami et al., in this subsection a reaction mechanism is developed so as to explicate some of the effects that promote or hinder the course of the reaction; particularly the role of water [point (ii)) and steric hindrance (point (iii)], as well as the coordination sphere of rhodium, are detailed.

7.2.1.1 Arylation in four steps: transmetalation, elimination, arylrhodation, and protonation

The Suzuki-Miyaura reaction[389–392] can be understood in terms of three main consecutive steps depicted in Figure 7.10: oxidative addition, transmetalation, and reductive elimination. The oxidative addition of palladium (Pd^0) to an alkyl halide (R_2-X) leads to the formation of a halogenated organopalladium species, R_2-Pd^{II}-X. Then, the halogen is displaced as NaX via reaction between the halogenated organopalladium species and a sodium-based base (NaO^tBu) resulting in an oxidized organopalladium species, R_2-Pd^{II}-O^tBu. After that, an organoborate complex $Na^+(R_1$-$B(Y)_2$-$O^tBu)^-$ undergoes transmetalation with R_2-Pd^{II}-O^tBu to form R_1-Pd^{II}-R_2. Finally, a reductive elimination recovers the catalyst Pd^0 with the simultaneous formation of a new carbon-carbon bond, R_1-R_2.[393]
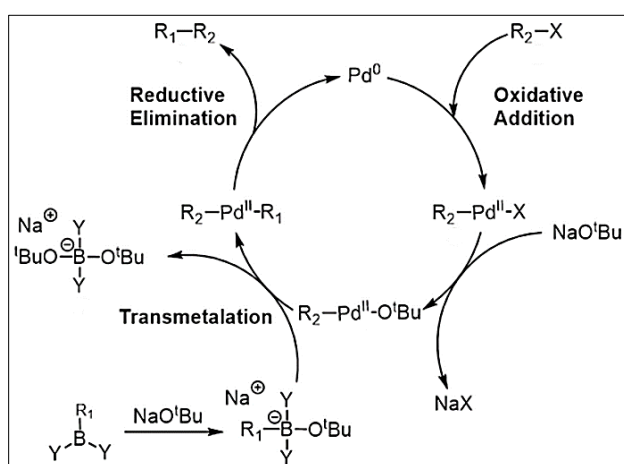
Figure 7.10 The Suzuki-Miyaura reaction mechanism.

The reaction mechanism for the rhodium-catalyzed hydroarylation of C_{60} can be consistently formulated by following a Suzuki-Miyaura-like reaction. Accordingly, four steps are highlighted as follows (see Figure 7.11): first step, transmetalation of Rh-OH species with water and the organoborate to generate the Ph-$RhB(OH)_3$ complex (see **A→C**); second step, elimination of $B(OH)_3$ to give the Rh-Ph species (**C→D**); third step, insertion of Rh-Ph to C_{60} or arylrhodation (**D→F**); and final step, protonation of Ph-C_{60} by means of a water molecule and release of the Rh-OH species to conclude the hydroarylation process of C_{60}.

The catalytic species **A** is obtained from the precatalytic species $[Rh(cod)(MeCN)_2]BF_4$ (cod=1,5-cyclooctadiene) through the dissociation of an acetonitrile ligand followed by the coordination of the hydroxyl group from a water molecule releasing a proton that, with the initial counteranion BF_4^-, yields HBF_4. This step has an energetic cost of 24.3 kcal/mol. This is a common step for all organoborates.[76,394]
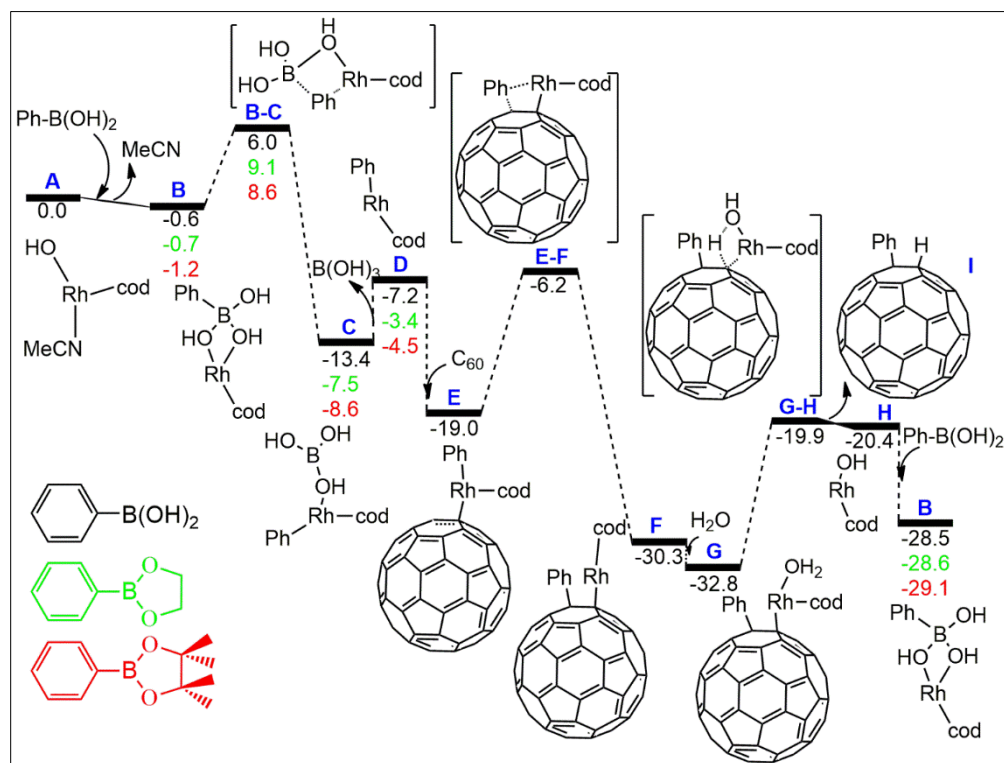
Figure 7.11 Gibbs energy reaction profiles (in kcal/mol) for the Rh-catalyzed addition to C_{60} of phenylboronic acid (black), 2-phenyl-1,3,2-dioxaborinane (green), and 4,4,5,5-tetramethyl-2-phenyl-1,3,2-dioxaborolane (red) in *o*-dichlorobenzene. Schematic drawings of molecules refer to the reaction with phenylboronic acid.

The neutral species [Rh(cod)(MeCN)(OH)], **A**, can release an acetonitrile ligand and coordinate Ph-B(OH)$_2$ in a slightly exergonic process to give **B**. Then, species **B** overcomes a barrier of 6.6 kcal/mol to transfer the phenyl group from boron to rhodium thus yielding the Ph(cod)RhB(OH)$_3$ complex, **C**. Releasing B(OH)$_3$ from **C** results in **D** with an energetic cost of 6.2 kcal/mol. In **D**, rhodium is only surrounded by the cod and phenyl ligands. The η^2-coordination of **D** to C_{60} to form **E** is favorable by 11.8 kcal/mol, in agreement with previous experimental[106] and computational[395] studies. From **E**, the transfer of Ph to the adjacent carbon atom requires to overcome a relatively low barrier of 12.8 kcal/mol, leading to the next relatively stable η^1-coordinated intermediate **F** (11.3 kcal/mol more stable than its precursor **E**). The resulting attacked bond in **F** is a [6,6] bond as experimentally found. Furthermore, the attack to a [5,6] bond of C_{60} in **E** involves a higher energy barrier (3.6 kcal/mol higher than the attack on a [6,6] bond) resulting in a less stable complex by 7.5 kcal/mol. On the other hand, minima corresponding to η^5- and η^6-coordination of the PhRh(cod) in **E** or Rh(cod) in **F** to C_{60} could not be located. Finally, in order to get the organic substituted C_{60} product and regenerate the catalyst, a coordination of a water molecule to rhodium occurs to yield **G**. This complex **G** is transformed into **H** via the transfer of a hydrogen atom from water to the carbon atom of C_{60} bonded to rhodium, thus leading to the release of (cod)Rh-OH.

In addition, considering the non-stoichiometric amount of C_{60} with respect to the metal catalyst, the η^2-coordination of rhodium to a second C_{60} structure where the cod ligand is substituted in the intermediate species was also investigated. This alternative path for the transformation of **A** to **H** implies the loss of acetonitrile and the cod, the attack of RhOH to C_{60}, and subsequent addition of PhB(OH)$_2$. Overall, this reaction pathway has to overcome a Gibbs energy barrier higher than 40 kcal/mol and, therefore, it is not operative.

7.2.1.2 The role of water as a key factor instead of steric hindrance

The role of water is to provide a proton for the formation of the phenyl(hydro)[60]fullerene and, in turn, the OH group to recover the catalyst as (cod)Rh-OH. The complete **G**→**H** transformation has a Gibbs energy barrier of 12.9 kcal/mol. In the next step, Rh in **H** coordinates a new entering Ph-B(OH)$_2$ molecule, which is a reactant in excess, to recover the catalytic species **B** again and close the catalytic cycle. The energy difference between species **B** at the beginning and at the end of the catalytic cycle corresponds to the Gibbs reaction energy of the transformation of C_{60}, H_2O, and PhB(OH)$_2$ into B(OH)$_3$ and C_{60}PhH in a process that is exergonic by 27.9 kcal/mol. For 2-phenyl-1,3,2-dioxaborinane and 4,4,5,5-tetramethyl-2-phenyl-1,3,2-dioxaborolane the Gibbs reaction energies are the same, -27.9 kcal/mol. Moreover, the closure of the catalytic cycle, the **G**→**H** conversion, is the rate-determining step of the reaction. However, the transfer of the phenyl in the **E**→**F** step is also in competition. The Gibbs energy profiles corresponding to the alternative organoborates are similar to that obtained with the phenylboronic acid. The fact that 2-phenyl-1,3,2-dioxaborinane gives a nearly identical energy profile to that of phenylboronic acid concurs with the experimental result that this organoborate also leads to the formation of the corresponding aryl(hydro)fullerene. However, for the 4,4,5,5-tetramethyl-2-phenyl-1,3,2-dioxaborolane no yield is observed experimentally. This is unexpected because the different organoborates share the same rate-determining step. In view of that, the role of water is rather a key factor instead of the steric hindrance, and factors beyond this latter should be considered to explain the chemical activity of the different organoboron compounds.

7.2.2 The role of C_{60} in ruthenium-based catalysts for olefin metathesis

Among the metal-based complexes used in chemical catalysis, ruthenium has occupied a prominent role in olefin metathesis during the last decade.[396–398] Regarding the Ru-based systems, the activity of the *first-generation* phosphine-based catalysts was significantly improved with the discovery of *second-generation* catalysts, where an N-heterocyclic carbene (NHC) was used to replace one phosphine ligand.[399–401] Despite the numerous studies in the past two decades,[402–413] there is still the absence of a *universal* catalyst for all olefin metathesis applications. There are no simple rules to predict exactly why Ru-based catalysts with certain NHC and phosphine ligands show catalytic activity, while other ligands (including variants of NHC and phosphines) display poor performance.[414] In this subsection, fullerene C_{60} is investigated as a novel supporting ligand that could facilitate olefin metathesis processes. This study is based on the reaction mechanism proposed by Chauvin in the early 1970s, which considers the metal carbene complex as the active catalyst and the respective four-membered metallacycle derivatives as the crucial intermediates leading to the desired products.[415] The presence of a ruthenacycle intermediate has been studied experimentally[402–406] and theoretically[407–411] since the late 1990s. The reaction mechanism depicted in Figure 7.12 shows all the possible intermediates formed through the reaction coordinate of the olefin metathesis. Such a reaction mechanism is taken into account with the aim of providing *in silico* new synthesized ruthenium catalysts containing C_{60} and NHC in the backbone of the structure; thus demonstrating the advantages of including fullerenes in these catalyzed reactions.
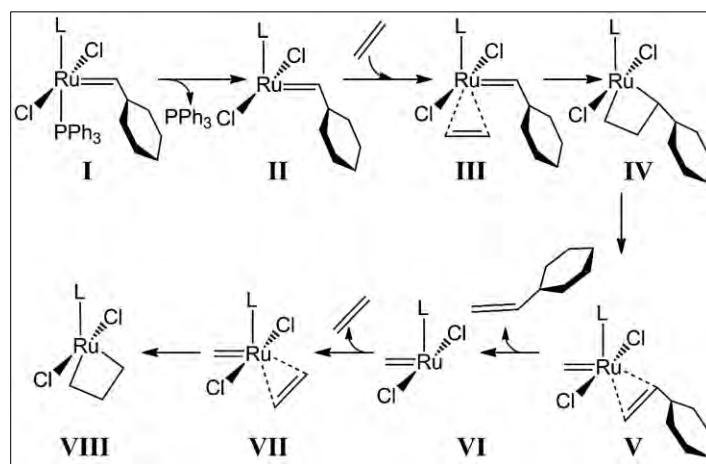
Figure 7.12 Ru-based catalysis of olefin metathesis.

7.2.2.1 Potential energy surface for the catalyzed olefin metathesis

The PES for the metathesis of ethylene catalyzed by Ru-based complexes with the SIMes (SIMes=1,3-bis[2,4,6-(trimethyl)phenyl]imidazolidin-2-ylidene) ligand backbone (complex **A**) being modified *in silico* by the insertion of a C$_{60}$ molecule (complexes **B** and **C**; see Figure 7.13) is depicted in Figure 7.14.
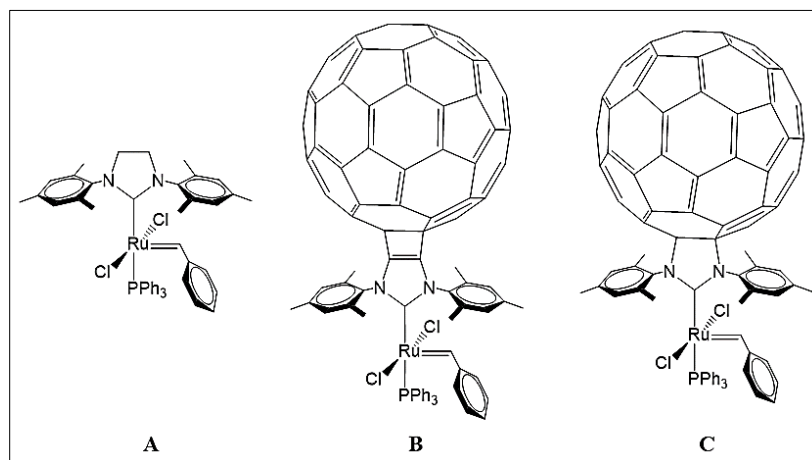
Figure 7.13 Ru-based olefin metathesis catalyst bearing a SIMes (1,3-bis(2,4,6-trimethylphenyl)imidazolin-2-ylidene) ligand (**A**), and *in silico* modification of its backbone by the annulation of a C$_{60}$ (**B** and **C**).

The relative thermodynamic stability of the reaction intermediates of complexes **A**, **B**, and **C** is the main subject of study. Figure 7.14 reports the Gibbs energies relative to species **I** for the intermediates **II** to **VIII** and the key TS structures for the studied Ru-based complexes **A-C**. Complexes **B** and **C** with the C$_{60}$ annulated through the [5,6] bond are about 18.0 kcal/mol higher in energy than the analogous ones in a [6,6] bond. The relative stability of all other intermediates for complexes **B** and **C** is nearly identical within an energy range of 5.5 kcal/mol when compared with the respective intermediates of complex **A**. The rate-determining intermediate and TS are those corresponding to the **IV**-**V** conversion,[416] which is associated to the breaking of the ruthenacyclobutane. After **V**, the Gibbs energy profile follows an energetically slight downhill trajectory without high-energy barriers or highly stabilized intermediates in agreement with previous reports.[417] Moreover, complex **B** presents the lowest energy barrier (15.1 kcal/mol) followed by complex **A** (17.5 kcal/mol), while complex **C** has the highest energy barrier (20.5 kcal/mol).

The formation of a stable ruthenacyclobutane **IV** by the metathesis of ethylene with the Ru-alkylidene bond is considered fundamental to describe a successful olefin metathesis catalyst.[414,418] The ruthenacyclobutane is a relatively stable key intermediate of each metathesis event, and it has been characterized experimentally.[414,419,420] For an efficient catalysis, the ruthenacyclobutane should be moderately stable. In complexes **B** and **C**, the metallacycle **IV** is 1.1 and 3.6 kcal/mol more stable than **III**, respectively, and comparable to the relative stability of the metallacycle for complex **A** (0.9 kcal/mol), thus the values fit perfectly with the active catalysts in olefin metathesis.[421] Thus, taking into account that a

highly stabilization of the ruthenacyclobutane intermediate might be a bottleneck in olefin metathesis catalysis, this new family of catalysts overcomes this impediment.
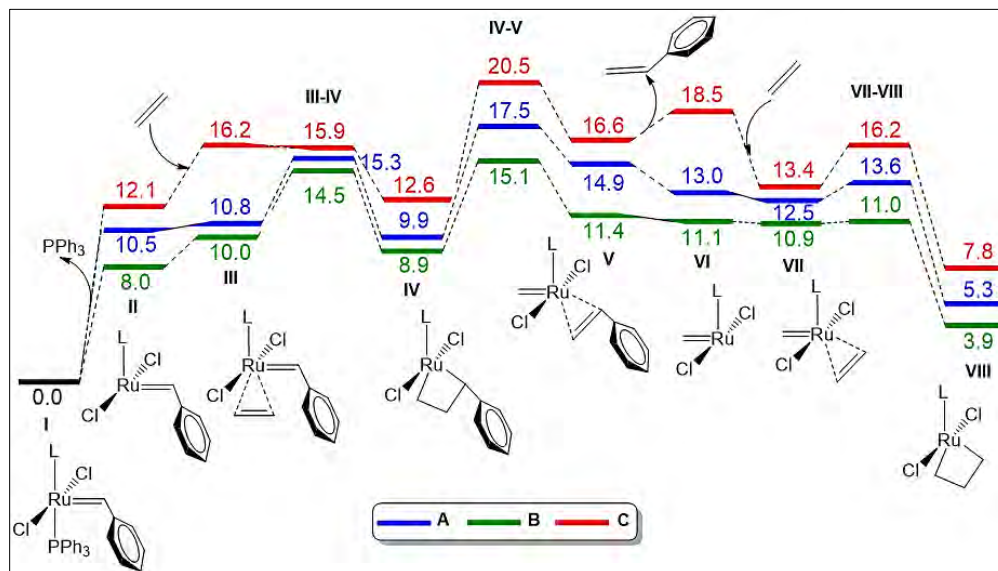
Figure 7.14 Computed thermodynamic stability of reaction intermediates **II–VIII** relative to species **I** for the studied olefin metathesis reaction catalyzed by Ru-based complexes **A-C** using ethylene as the substrate. L = NHC. Gibbs energies in CH_2Cl_2 solvent are given in kcal/mol.

7.2.2.2 Steric hindrance, binding energies, and Parr electrophilicity index

With the intention of better comprehending the Ru-based catalysts with NHC containing C_{60}, the steric hindrance and electronic properties of the species **I** and **II** for complexes **A**, **B**, and **C** were analyzed in detail.

Steric hindrance

Differences between the steric hindrance of the NHC ligand in **A**, **B**, and **C** can be quantified by calculating the buried volume of a given ligand, which is a number that quantifies the amount of the first coordination sphere of the metal occupied by this ligand.[422,423] The *SambVca* code[424] was used. From Table 7.3, the calculated percent buried volume (%V_{Bur}) for complexes **B** (32.5%) and **C** (33.3%) are comparable to the %V_{Bur} of **A** (32.8%). Similarly, for species **II**, the predicted %V_{Bur} values are nearly the same despite the potential relaxation of NHC ligand after the dissociation of the phosphine ligand. Nevertheless, species **II** of complex **C** displayed a somewhat more sterically hindered environment next to the metal. These observations corroborate that the steric hindrance for the complexes **A-C** are quite similar and, in turn, none of them preclude coordination of bulky substrates.

Table 7.3 Total $\%V_{Bur}$ values for species **I** and **II**
for the considered Ru-based complexes **A-C**.

Sterics ($\%V_{Bur}$)		
Complex	I	II
A	32.8	32.8
B	32.5	31.8
C	33.3	33.6

Binding energies

The analysis of binding energies can be conveniently done via the ASM; particularly, the main target is structure **I**. Accordingly, ΔE_{int} in species **I** is -59.8, -63.5, and -61.8 kcal/mol for **A**, **B**, and **C**, respectively. The better interaction between reactants for complexes **B** and **C** is likely due to the electron-withdrawing capacity of the C_{60} group that makes the electron pair of the NHC less available for the interaction with the metal. The lower NHC-Ru interaction energy of complex **B** is attributed to the fact that the NHC moiety of **B** interacts more effectively with the π-system of C_{60} through the carbon-carbon double bond than that of the complex **A** which does not have such a π-system. On the other hand, ΔE_{strain} of NHC with C_{60} is similar in energy (2.8 and 2.1 kcal/mol for complexes **B** and **C**, respectively) with respect to the standard NHC, i.e. SIMes (1.9 kcal/mol for complex **A**). Moreover, differences in ΔE_{strain} of the metal fragment are negligible. Generally, the binding energies, that is $\Delta E = \Delta E_{int} + \Delta E_{strain}$, are 4.5 and 2.2 kcal/mol less stabilizing for complexes **B** and **C**, respectively, than is it for complex **A**.

Parr electrophilicity index

Additionally, insights into the electronic contribution of the NHC can be attained by making use of the values of Parr electrophilicity index (ω) for species **I**.[425] Accordingly, ω of Ru-based complexes **A-C** increase with significant quantitative differences (respectively, 166.2, 179.3, and 181.1 kcal/mol for species **I**). The predicted higher ω values for complexes **B** and **C** with respect to **A** suggest that the former complexes shall be more prone to nucleophilic attacks, and thus more reactive than **A**. In summary, these results indicate that complexes **B** and **C** are potentially active catalysts for the metathesis of olefins in view of their reduced electron donating capability of the SIMes ligand.

7.3 Triphenylamine-C$_{60}$, a Promising Dye-Sensitized Solar Cell

The chemical functionalization of carbon nanostructures described in previous sections results in adducts with potential applications in the field of organic photovoltaics since these chemical species can be used in the construction of dye-sensitized solar cells (DSSCs). A DSSC is a photovoltaic cell created from low- to medium-purity materials through low-cost processes that exhibits a commercially realistic energy-conversion efficiency as compared to existing commercial devices. The large current densities (greater than 12 mA/cm^2) and exceptional stability, as well as the low cost, make practical applications feasible.[426] Fullerenes can be used in the design and construction of DSSCs;[427] as a matter of fact, in this section the main subject of study is the elucidation of the electron transfer (ET) problem in a fullerene-based dye with the purpose of explicating and, in turn, predicting the applicability of this carbon nanostructure in the production of higher-efficient organic solar cells. The reference system under consideration is triphenylamine (TPA) covalently linked to the electron acceptor C$_{60}$ via a pyrrolidine ring as the anchoring group (TPA-C$_{60}$). In this regard, TPA is able to confine cationic charge and hamper aggregation between molecules, which induces self-quenching and reduces the electron injection efficiency.[428,429] Besides, C$_{60}$ is an excellent electron acceptor[430–433] able to react with a variety of chemical agents.[46,54,55,434–436] The current section encompasses the examination of electronic transitions in TPA-C$_{60}$ through different thermally accessible conformations of the donor-acceptor conjugate. A detailed analysis of the estimation of ET parameters is provided with the aim of determining consistent values of rate constants, k_{et}, for photoinduced CT reactions. This latter is particularly important since the efficiency of the DSSC depends upon k_{et}.
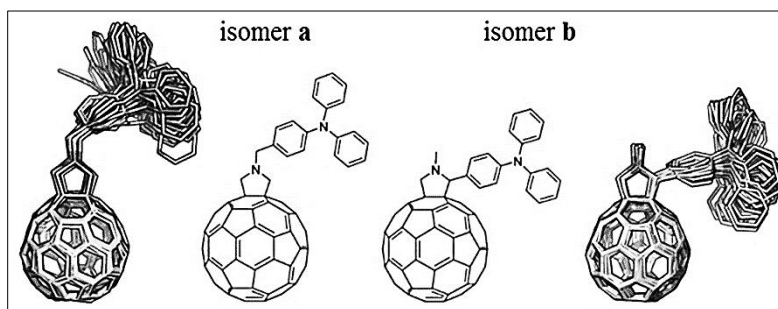

Figure 7.15 Structures of two constitutional isomers of triphenylamine-C$_{60}$ **a** and **b** and overlay of 50 snapshots obtained every 2 ps from MD simulations.

7.3.1 Description of exciton states

In agreement with the *Gold Book* of the IUPAC, when an electronic excitation is considered as a quasi-particle capable of migrating, the term to be used is exciton.[365] An exciton is a bound state of an electron, e^-, and an electron hole, h^+, which are attracted to each other by the electrostatic Coulomb force. This neutral-charged quasiparticle can exist in insulators, semiconductors and in some liquids.[437] Among the several types of excitons in which they can be classified, in this subsection we are particularly interested in molecular and charge-transfer excitons.

The analysis of excited states[438,439] can be achieved by the use of the extent of exciton delocalization in the excited state ψ_i which can be measured as:

$$X_{ii}(F) = \frac{1}{2} \sum_{\alpha,\beta \in F} \left[\left(SP^{0i} \right)_{\alpha\beta} \left(P^{0i}S \right)_{\alpha\beta} \right] \tag{7.1}$$

where the sums run over all atomic orbitals centered in fragment F, S is the atomic orbital overlap matrix and P^{0i} is the symmetrized one-electron transition density matrix between the ground state ψ_0 and the excited state ψ_i in the atomic orbital representation. The overall charge separation Δq between fragments F_1 and F_2 is estimated as:

$$\Delta q = \sum_{\substack{\alpha \in F_1 \\ \beta \in F_2}} \left[\left(SP^{0i} \right)_{\alpha\beta} \left(P^{0i}S \right)_{\alpha\beta} + \left(SP^{0i} \right)_{\beta\alpha} \left(P^{0i}S \right)_{\beta\alpha} \right] \tag{7.2}$$

These quantities $X_{ii}(F)$ (being F either C_{60} or TPA) and Δq are computed by means of linear response (LR) TD-CAM-B3LYP/6-31G* in the gas phase. The parameters $X_{ii}(F)$ and Δq are useful descriptors of the intrinsic structure of electronic transitions from which, depending on their value, we distinguish three different excitations that can give rise to a molecular exciton or localized excited state (LES), a charge transfer state (CTS), or a hybrid state (HS). In the TPA-C_{60} system, the nature of a particular excited state ψ_i depends upon the contributions of the states $(F_{C60})^*$, $(F_{TPA})^*$, $(F_{C60})^-(F_{TPA})^+$, and $(F_{C60})^+(F_{TPA})^-$; from which the two former terms, respectively, stand for excitations localized at either the C_{60} or TPA fragments, and the two latter ones represent excited states with strong CT character. Figure 7.16 schematizes the distribution of $X_{ii}(F)$ and Δq as a function of the excitation energy.

Localized excited states, LES. A pure molecular exciton has no CT character. However, Figure 7.16 shows that $X_{ii}(F_{TPA}) = 0.0$, thus reflecting no contribution of TPA for all the excited states. Therefore, molecular excitons are mainly characterized by single-molecule excitations in C_{60}, LES, since $X_{ii}(F_{C60}) = 0.9\text{-}1.0$ and $\Delta q = 0.0\text{-}0.1$. Only LES are populated at the 2.0-2.5 eV range. Nevertheless, while 97% of the excitations in isomer **a** remain to be LES in the 2.5-3.0 range, this population decreases by a factor of 0.74 in isomer **b**. Excitations above 3.0 eV give rise to states with mixed character, and the amount of LES is diminished to 79 and 84 % in isomers **a** and **b**, respectively.
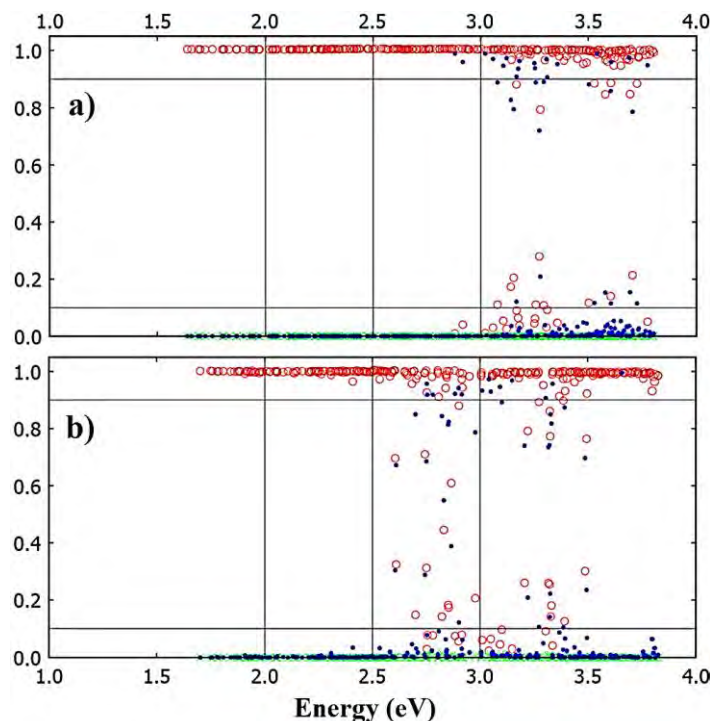
Figure 7.16 Distribution of $X_{ii}(F_{C60})$ (white-filled red circles), $X_{ii}(F_{TPA})$ (green X), and Δq (blue-filled circles) as a function of the excitation energy. a) Results for isomer **a**, b) results for isomer **b**. Every plot contains the 30 lowest excited states calculated for 10 different MD structures of the corresponding isomer.

Charge transfer states, CTS. The main contribution to form an exciton with CT character comes from $(F_{TPA})^+(F_{C60})^-$; $X_{ii}(F_{C60}) = 0.0\text{-}0.1$ and $\Delta q = 0.9\text{-}1.0$. At the 2.0-2.5 eV range no CTS is observed; however, only 3% and 9% of the excitations correspond to the formation of a CTS in isomers **a** and **b** at the 2.5-3.0 eV range. Besides, above 3.0 eV there are almost three times more CTS (10 %) as compared to the former energy range in isomer **a**, although the amount of CTS in **b** is reduced to 6 %.

Hybrid states, HS. These excitons are characterized by their partial CT character.[360,363,364] In the TPA-C_{60} system, there are some excitations with contributions given by $(F_{TPA})^+(F_{C60})^-$ and $(F_{C60})^*$; that is, $X_{ii}(F_{TPA}) = 0.0$, $X_{ii}(F_{C60}) = 0.1\text{-}0.9$ and $\Delta q = 0.1\text{-}0.9$. Figure 7.17 shows a graphical representation of how an exciton with partial CT character might look like. There are no HS in isomer **a** at the 2.0-3.0 eV range, and HS appear in isomer **b** at the 2.5-3.0 eV range with a population of 17%. Above 3.0 eV, isomers **a** and **b** show the same population of 10 %. From these results, due to the larger distance between TPA and C_{60} in isomer **a**, it is inferred that CT reactions are slower in this isomer because it produces a fewer amount of HS, which are supposed to promote the charge separation (CS) at the donor-acceptor interface. This could have a direct impact in the design of high-efficient DSSCs as materials may be engineered such that their excitations lead to a small number of HS, thus avoiding a premature charge recombination (CR). As a matter of fact, Echegoyen et al.[440] found that isomer **a** generates longer-lived charge transfer states (CTS) as compared to isomer **b**; indeed, they also reported slightly slower k_{et} for CT reactions in isomer **a**; thus being in line with our conclusions.
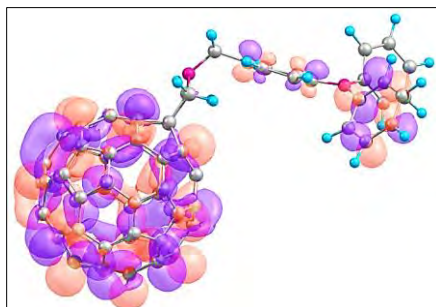
Figure 7.17 Probable schematization of an exciton
state with partial charge transfer character.

7.3.2 Electron transfer parameters

In Table 7.4, reorganization energies (λ_{int} and λ_{ext}), electronic couplings (V_{ij}), and changes in Gibss energy (ΔG_{ct}) for photoinduced CT reactions (equations 7.3 and 7.4) occurring in TPA-C$_{60}$ (isomer **a**) are reported. The lowest-energy molecular and charge-transfer excitons are represented by TPA-C$_{60}$* and TPA$^+$-C$_{60}^-$, respectively, and the ground state is TPA-C$_{60}$.

$$TPA - C_{60}^* \quad \rightarrow \quad TPA^+ - C_{60}^- \tag{7.3}$$

$$TPA^+ - C_{60}^- \quad \rightarrow \quad TPA - C_{60} \tag{7.4}$$
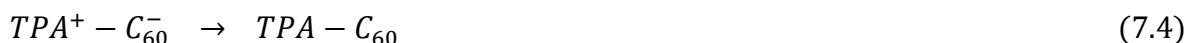
Table 7.4 Electron transfer parameters for
photoinduced charge transfer reactions in TPA-C$_{60}$.

Parameter	Energy (eV)
λ_{int}	0.158
$\lambda_{ext}(M)$	0.492
$\lambda_{ext}(E_{noneq}\text{-}E_{eq})$	0.605
$\lambda_{ext}(E_{noneq}(\omega)\text{-}E_{eq})$	0.869
CS V_{ij}	0.0024
CR V_{ij}	0.0206
ΔG_{cs}	-0.31
ΔG_{cr}	-2.11

In agreement with Section 2.14, λ_{int} was estimated as the average value, with a standard deviation of 4 meV, calculated from equations 2.103 and 2.104. However, the direct application of equation 2.103 involves the geometry relaxation of an open-shell singlet CTS. The use of U-DFT turns out to be a proper alternative for the determination of excited states, including those with CT character. TD-DFT is prone to fail in the geometry relaxation of a CTS but not for the excited states in TPA-C$_{60}$ that are mostly LES and are scarcely separated (within 0.1 eV, see Figure 7.16). Indeed, during the development of this study it was possible to obtain several Franck-Condon and geometry-relaxed exciton states with either neutral or CT character via (COSMO:benzonitrile) UCAM-B3LYP/6-31G*. The U-DFT geometry-relaxed CTS is the one included in equation 2.103. On the contrary, $\lambda_{ext}(M)$ corresponds to

the value of equation 2.106, and the others were evaluated by implicitly treating the solvent effects as explained in Section 2.14. The uncertainty of the estimations of λ_{ext} is large since the results diverge within a 0.4 eV energy range. The reliable evaluation of this parameter is difficult to achieve as discussed in Section 2.14. Nonetheless, it is worth to mention that the several approaches that are used to calculate λ_{ext} are completely different (two-sphere, $\lambda_{ext}(M)$, against continuum solvation models, $\lambda_{ext}(E_{noneq}-E_{eq})$ or $\lambda_{ext}(E_{noneq}(\omega)-E_{eq})$), but the missing reproducibility must be solved; this issue shall be discussed in the following subsection.

The determination of V_{ij} was done via the fragment charge difference method from excited states of the system under study calculated with TD-CAM-B3LYP/6-31G*.[347] Because the values are sufficiently small, the nonadiabatic approach may be applied to estimate the corresponding k_{ct}.
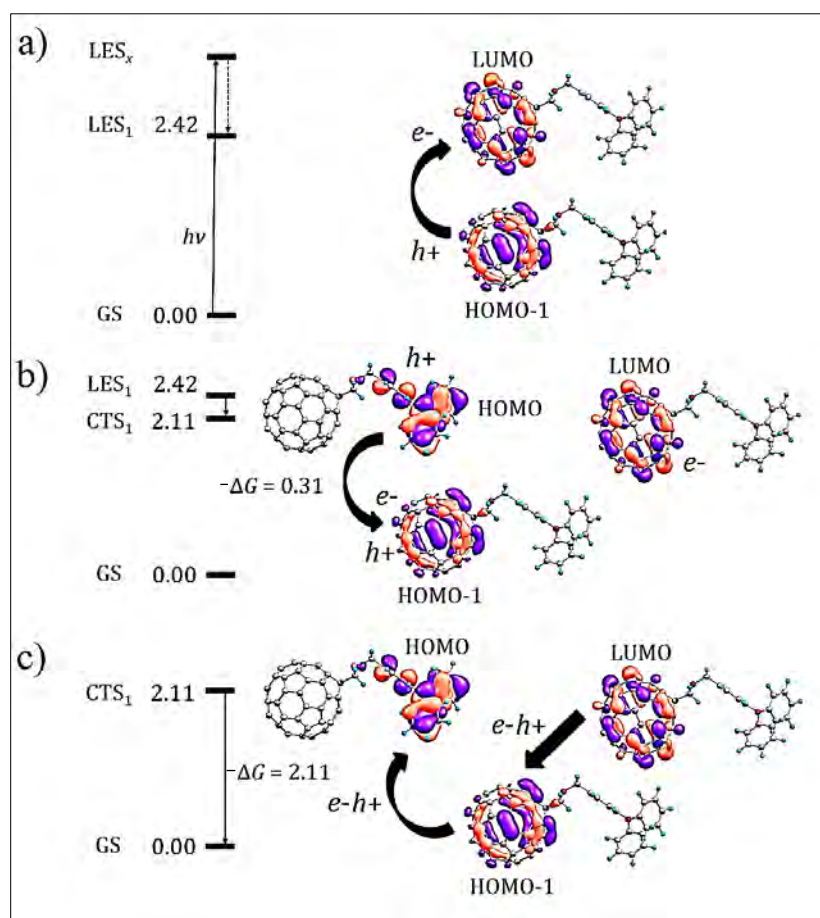
Figure 7.18 Schematization of Franck-Condon excitations in solution (in eV) and photoinduced charge transfer reactions in TPA-C$_{60}$. a) Formation of the lowest-energy molecular exciton where an electron-hole (e^-h^+) pair is photogenerated in C$_{60}$ by light absorption hv; b) charge separation reaction in which one electron is transferred from TPA to C$_{60}$; the e^-h^+ pair is separated; c) charge recombination reaction in which the ground state is recovered; the e^-h^+ pair is recombined. Gibbs energies ΔG in solution (in eV) for the charge transfer reactions are also depicted.

Changes in electronic energy ΔE_{ct} for the CT reactions nearly correspond to ΔG_{ct} ($\Delta E_{ct} \approx \Delta G_{ct}$) assuming a negligible entropic component. The initial formation of TPA-C$_{60}$* by direct light absorption corresponds to a dipole-forbidden transition. Dipole-allowed transitions of higher-energy populated by light absorbance are expected to relax very fast to the lowest-energy LES (see Figure 7.18). The Franck-Condon transition to TPA-C$_{60}$* lies at 2.68 eV as calculated through gas-phase linear response (LR) TD-CAM-B3LYP/6-31G* and 2.42 eV as computed via state-specific (COSMO:benzonitrile)TD-CAM-B3LYP/6-31G* in equilibrium solvation. Furthermore, the energy of the lowest-energy Franck-Condon TPA^{+}-C$_{60}^{-}$ excited state lies at 3.69 eV in the gas phase. Unfortunately, solvent effects for a CTS could not be determined by either LR or state-specific TD-DFT. However, the free energy of solvation, ΔG_{sol}, of a CTS can be calculated by means of U-DFT, which turns out in -1.58 eV; as a result, the lowest-energy Franck-Condon CTS lies at 2.11 eV, then ΔG_{cs} = -0.31 eV in excellent agreement with the experimental value.[440] However, the neutral singlet excited state energy is reported to be 1.76 eV, which results in an overestimation of 0.66 eV when compared to the energy of TPA-C$_{60}$*. As a matter of fact, ΔG_{cr} = -2.11 eV is also overestimated as compared to the experimental value by exactly the same 0.66 eV.[440] This overestimation constitutes another source of error for the theoretical prediction of k_{cr}. This issue shall be analyzed in detail in the following subsection together with λ_{ext}.

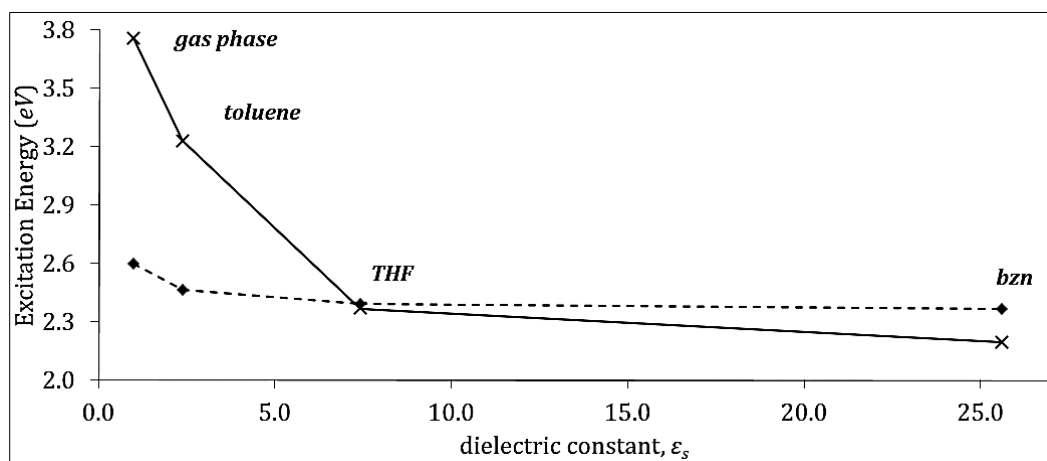## 7.3.2.1 Charge transfer activity

Figure 7.19 Variation of the vertical energies of TPA-C$_{60}$* (dashed line) and TPA^{+}-C$_{60}^{-}$ (solid line) in solution as a function of the dielectric constant ε_s.

The variation of the Franck-Condon excitation energies of TPA-C_{60}^* and TPA$^+$-C_{60}^- as a function of ε_s is schematized in Figure 7.19. As ε_s decreases, TPA$^+$-C_{60}^- becomes less stable than TPA-C_{60}^* and the CS reaction does not occur because it corresponds to an endergonic process. These results concur with the experimental evidence in which steady-state fluorescence measurements confirmed the absent of CT activity in toluene ($\varepsilon_s = 2.4$) and carbon disulfide ($\varepsilon_s = 2.6$). Moreover, CT activity can be observed even in tetrahydrofuran (THF, $\varepsilon_s = 7.4$) despite of the slightly favorable driving force, which is calculated to be only 0.02 eV (0.09 eV experimental); unlike less polar solvents.[440]

7.3.2.2 Nonadiabatic rate constants

The sources of error that more affect the assessment of k_{ct} are λ_{ext} and ΔG_{cr}. In view of that, k_{ct} is reported as a function of those ET parameters in Table 7.5. In the use of $\lambda_{ext}(M)$, one assumes that the donor and acceptor are spheres of radii a_1 and a_2 separated by the distance R, then the condition of $R >> a_1 + a_2$ has to be fulfilled. In the current study the contact distance was used, $R = a_1 + a_2$, and this may be the reason of the unreasonable value determined for k_{cr} with $\lambda_{ext}(M)$. The best estimation of k_{ct}, within less than two orders of magnitude as compared to experimental evidence, is achieved with $\lambda_{ext}(E_{noneq}(\omega)-E_{eq})$. Those results suggest that λ_{ext} can be better simulated by continuum solvation models. Additionally, it might be proposed that the use of the Marcus-Levich-Jortner equation might be a better approach to include the effect of quantum vibrational modes.[332,334] Nevertheless, the role of nuclear degrees of freedom in the system under study can be ignored and still the physics of the CT process can be described satisfactorily. This deduction is supported by the fact that geometrical variations in TPA-C_{60} do not significantly change the intrinsic nature and distribution of excited states as previously demonstrated.[441] Moreover, it was suggested that CS reactions for organic photovoltaic interfaces are mostly purely electronic processes which is in line with the conclusions attained in the current thesis.[442]

Finally, the ultrafast CT reactions described in this section certainly point out that the inclusion of fullerenes in the design of a DSSC may increase the efficiency of the device. In view of that, the current thesis provides an overview for the engineering of fullerene-based DSSCs:

(i)   A closer distance between the donor and acceptor fragments brings about faster CT reactions; a fact that is attributed to the population of excitons with partial CT character.

(ii)   Despite the CR process is dominant, dyes with diminished driving force can slow down this reaction so that longer-lived CTS can be generated.

(iii)   The CT activity of the dye depends also on the polarity of the solvent. Nonpolar solvents cause lack of CT activity, yet a more polar solvent has a more stabilizing effect on CTS, which results in slower CR reactions.

Table 7.5 Rate constants (in $1/s$) for CT reactions as a function of λ_{ext} and ΔG_{cr}. Thermal energy $k_B T = 0.026$ eV; $\lambda_{int} = 0.158$ eV; V_{ij} for the CS and CR reactions are respectively 0.0024 and 0.0206 eV.

λ_{ext} [a]	k_{cs} ; $\Delta G_{cs} = -0.31$ [b]	k_{cr} ; $\Delta G_{cr} = -2.11$ [c]	k_{cr} ; $\Delta G_{cr} = -1.45$ [d]
0.492	3.51 x 10^9	2.44 x 10^{-2}	9.94 x 10^7
0.605	1.35 x 10^9	1.33 x 10^2	3.16 x 10^9
0.869	1.23 x 10^8	1.86 x 10^7	2.07 x 10^{11}
	6.00 x 10^{10} [e]	1.90 x 10^9 [e]	

[a] In agreement with Section 2.14, in descending order this parameter respectively corresponds to $\lambda_{ext}(M)$, $\lambda_{ext}(E_{noneq}\text{-}E_{eq})$, and $\lambda_{ext}(E_{noneq}(\omega)\text{-}E_{eq})$.
[b] ΔG_{cs} calculated as the energy difference between TPA-C$_{60}$* [state-specific (COSMO:bzn) TD-CAM-B3LYP/6-31G*] and TPA$^+$-C$_{60}^-$ (gas-phase linear-response TD-CAM-B3LYP/6-31G* with U-DFT solvent corrections).
[c] ΔG_{cr} calculated as the energy difference between TPA$^+$-C$_{60}^-$ described in footnote b and the solvated ground state.
[d] Experimental value of ΔG_{cr}.
[e] Experimental values of k_{ct}.

Chapter 8

Conclusions

The main achievements attained in the current manuscript are outlined as follows:

1. **Cycloaddition reactions to carbon nanostructures**

The nucleophilic (2+1) Bingel-Hirsch addition of dimethyl bromomalonate to the endohedral metallofullerene La@C_{2v}-C_{82} was studied in detail in the current thesis. The formation of one fulleroid at bond **19** emerges as the kinetically and thermodynamically most favorable Bingel-Hirsch adduct in agreement with the experimental evidence; even though the fulleroid at bond **11** is in direct competition. On the other hand, experiments also report the formation of four singly-bonded derivatives; two of them, the ones with the highest yields, are assigned to carbon atoms C2 and C23. These positions generate the most thermodynamically stable intermediates associated to kinetically hampered cyclopropanation reactions; thus leading to the accumulation of these chemical species. Based on the thermodynamic stability, the other two singly bonded derivatives can be formed on C7, C11, C13, C18, C19, and C21; therefore, the Bingel-Hirsch addition to La@C_{2v}-C_{82} is not regioselective and the formation of at least ten products can be expected, even under relatively mild reaction conditions.

Cycloadditions of benzyne to different carbon nanostructures is also another case study. The achieved goal is the elucidation of the chemoselectivity [(2+2) vs (4+2) additions] and regioselectivity ([5,6] vs [6,6] in fullerenes or parallel vs oblique addition in zig-zag single-walled carbon nanotubes) of the reactions. Reaction mechanisms for the benzyne cycloaddition to carbon nanostructures were quantum-chemically formulated, wherein the formation of a singly-bonded biradical intermediate determines the course of the reactions. These results demonstrate that the (2+2) benzyne cycloaddition to a [6,6] bond of C_{60} is the most thermodynamically and kinetically favored reaction pathway in excellent agreement with experimental observations, yet the attack on a [5,6] bond kinetically competes with the attack on a [6,6] bond. Therefore, a [5,6]-cycloaddition product can be also observed as suggested by indirect experimental evidence. Moreover, for the (2+2) benzyne cycloaddition to the endohedral metallofullerenes $X_3N@C_{80}$ (X = Sc, Y), both [5,6] and [6,6] attacks also compete each other.[443] In contrast, the most thermodynamically and kinetically preferred reaction pathway in zig-zag single-walled carbon nanotubes is the (4+2) benzyne cycloaddition; even though, in the case of armchair single-walled carbon nanotubes, the cycloaddition depends upon the diameter. However, in both cases of carbon nanotubes, it is

generally observed that the energy barrier increases and the exothermicity of the reaction decreases as the diameter of the nanostructure increases. As a final remark, changes in chemoselectivity and regioselectivity can be explained in terms of structural strain and interaction between reactants as determined by the activation strain model, wherein reaction pathways involving less or negligible structural deformation shall be favored.

To sum up, the chemo- and regioselectivity of the (2+1), (2+2), and (4+2) cycloadditions to (endohedral)fullerenes and carbon nanotubes have been determined in detail so as to provide a systematic understanding of the chemical functionalization of carbon nanostructures. As a result, the outcomes of the current thesis are guidelines in the characterization, prediction, and even design of innovative cycloadducts of carbon nanostructures.

2. Reactions catalyzed by transition metals involving fullerene C_{60}

The analysis of reactions involving C_{60} and catalysts based on transition metals performed in this thesis is twofold: one encompasses the quantum-chemical development of the reaction mechanism that leads to the formation of an arylated hydrofullerene with the aim of rationalizing experimental observations; and the other provides the *in silico* synthesis of catalysts including C_{60} for the metathesis of olefins.

In the first study, it is formulated a Suzuki-Miyaura-like reaction mechanism of the hydroarylation of C_{60} with organoboron compounds catalyzed by a rhodium complex in the presence of water. The rate-determining step is described as the coordination of water to the $PhC_{60}Rh(cod)$ complex to provide the hydrogen atom for the formation of the phenyl(hydro)[60]fullerene and the OH group to recover the catalyst. Therefore, the unknown role of water is consistently explained in this study, which turns out to be essential for the success of the reaction, thus discarding the steric hindrance as a key factor as previously suggested.

In the second study, it was developed a quantum-chemical exploration of the potential energy surface of the metathesis of ethylene catalyzed by complexes based on ruthenium as the metallic center and N-heterocyclic carbenes containing C_{60}. Three catalysts were discussed; complexes **B** and **C** bear a C_{60} annulated in the backbone of the NHC ligand. Despite the thermodynamic stability among the three complexes **A**, **B**, and **C** is similar, complex **B** shows the lowest energy barriers for olefin metathesis, thus demonstrating that the inclusion of C_{60} increases the catalytic power. Indeed, steric hindrance of **B** is similar to **A** in spite of the relatively large-sized fullerene structure. The activation strain model shows better reactant interactions for species of **B**, and this latter also has more electrophilicity. All these attributes certainly indicate a better performance of C_{60}-based catalysts for olefin metathesis.

3. Fullerene-based dye-sensitized solar cells

The investigation of electron transfer phenomena in the triphenylamine-C_{60} donor-acceptor conjugate is included in this manuscript in order to better comprehend the photovoltaics behind fullerene-based solar cells. This is accomplished by the description of electronic transitions in triphenylamine-C_{60} and the evaluation of electron transfer parameters of photoinduced charge transfer reactions occurring at the donor-acceptor interface. In the case of electronic transitions, an exciton characterized by a partial charge separation is described with the intention of explaining how the rate of charge transfer reactions varies. In this regard, the population of excitons with partial charge transfer character produce faster charge transfer reactions, and vice versa, which resembles experimental results. It is also observed that a closer distance between the donor-acceptor fragments promotes the formation of an exciton with partial charge separation. Therefore, highly efficient dye-sensitized solar cells can be engineered by avoiding the population of these excitons, which turns out in slower charge recombination reactions due to the formation of longer-lived charge transfer states.

In the case of the evaluation of the rate of charge transfer reactions, the estimations of the external reorganization energy and the energy of a solvated charge transfer state are key factors to reach reliable, consistent values of rate constants. Moreover, the importance of the solvent effects lies in the fact that the polarity of the solvent determines the charge transfer events; that is to say, nonpolar solvents cause lack of charge transfer activity due to they cannot stabilize the formation of a charge transfer state. In contrast, more polar solvents stabilize charge transfer states and, as a consequence, they are longer-lived and the charge recombination reaction is delayed. Accordingly, the stabilization of charge transfer states is reflected in higher-efficient dye-sensitized solar cells.

In general, the description, forecasting, and even design of functionalized carbon nanostructures with interesting physical and chemical properties, as well as potential applications in the construction of photovoltaic devices, are faced and proved through the current thesis.

Bibliography

(1)   Kroto, H. W.; Heath, J. R.; O'Brien, S. C.; Curl, R. F.; Smalley, R. E. *Nature* **1985**, *318*, 162–163.

(2)   Guldi, D. M.; Martín, N. *Fullerenes: From Synthesis to Optoelectronic Properties*; Kluwer Academic Publishers: Dordrecht, The Netherlands, **2002**.

(3)   Hirsch, A.; Bettreich, M. *Fullerenes, Chemistry and Reactions*; Wiley-VCH: Weinheim, Germany, **2005**.

(4)   Ros, T. Da; Prato, M. *Chem. Commun.* **1999**, 663–669.

(5)   Krätschmer, W.; Lamb, L. D.; Fostiropoulos, K.; Huffman, D. R. *Nature* **1990**, *347*, 354–358.

(6)   Haddon, R. C. *Science* **1993**, *261*, 1545–1550.

(7)   Langa, F.; Nierengarten, J.-F. *Fullerenes. Principles and Applications*; Royal Society of Chemistry: Cambridge, United Kingdom, **2011**.

(8)   Martín, N.; Nierengarten, J.-F. *Supramolecular Chemistry of Fullerenes and Carbon Nanotubes*; Wiley-VCH: Germany, **2012**.

(9)   Kroto, H. W. *Nature* **1987**, *329*, 529–531.

(10)   Schmalz, T. G.; Seitz, W. A.; Klein, D. J.; Hite, G. E. *Chem. Phys. Lett.* **1986**, *130*, 203–207.

(11)   Martín, N. *Angew. Chem. Int. Ed.* **2011**, *50*, 5431–5433.

(12)   Wang, C. R.; Kai, T.; Tomiyama, T.; Yoshida, T.; Kobayashi, Y.; Nishibori, E.; Takata, M.; Sakata, M.; Shinohara, H. *Nature* **2000**, *408*, 426–427.

(13)   Kato, H.; Taninaka, A.; Sugai, T.; Shinohara, H. *J. Am. Chem. Soc.* **2003**, *125*, 7782–7783.

(14)   Hart, G. W. Leonardo da Vinci's Polyhedra http://www.georgehart.com/virtual-polyhedra/leonardo.html.

(15)   Dresselhaus, M. S.; Dresselhaus, G.; Eklund, P. C. *Science of Fullerenes and Carbon Nanotubes: Their Properties and Applications*; Academic Press: United States of America, **1996**.

(16)   Mostofizadeh, A.; Li, Y.; Song, B.; Huang, Y. *J. Nanomater.* **2011**, 685081.

(17)   Abraham, M. H.; Green, C. E.; Acree, Jr., W. E. *J. Chem. Soc. Perkin Trans. 2* **2000**, 281–286.

(18)   Haddon, R. C.; Hebard, A. F.; Rosseinsky, M. J.; Murphy, D. W.; Duclos, S. J.; Lyons, K. B.; Miller, B.; Rosamilia, J. M.; Fleming, R. M.; Kortan, A. R.; Glarum, S. H.; Makhija, A. V.; Muller, A. J.; Eick, R. H.; Zahurak, S. M.; Tycko, R.; Dabbagh, G.; Thiel, F. A. *Nature* **1991**, *350*, 320–322.

(19)   Hebard, A. F.; Rosseinsky, M. J.; Haddon, R. C.; Murphy, D. W.; Glarum, S. H.; Palstra, T. T. M.; Ramirez, A. P.; Kortan, A. R. *Nature* **1991**, *350*, 600–601.

(20)   Rosseinsky, M.; Ramirez, A.; Glarum, S.; Murphy, D.; Haddon, R.; Hebard, A.; Palstra, T.; Kortan, A.; Zahurak, S.; Makhija, A. *Phys. Rev. Lett.* **1991**, *66*, 2830–2832.

(21)   Haufler, R. E.; Conceicao, J.; Chibante, L. P. F.; Chai, Y.; Byrne, N. E.; Flanagan, S.; Haley, M. M.; O'Brien, S. C.; Pan, C.; Xiao, Z.; Billups, W. E.; Ciufolini, M. A.; Hauge, R. H.; Margrave, J. L.; Wilson, L. J.; Curl, R. F.; Smalley, R. E. *J. Phys. Chem.* **1990**, *94*, 8634–8636.

(22)   Allemand, P. M.; Koch, A.; Wudl, F.; Rubin, Y.; Diederich, F.; Alvarez, M. M.; Anz, S. J.; Whetten, R. L. *J. Am. Chem. Soc.* **1991**, *113*, 1050–1051.

(23)   Cox, D. M.; Behal, S.; Disko, M.; Gorun, S. M.; Greaney, M.; Hsu, C. S.; Kollin, E. B.; Millar, J.; Robbins, J. *J. Am. Chem. Soc.* **1991**, *113*, 2940–2944.

(24)   Jehoulet, C.; Bard, A. J.; Wudl, F. *J. Am. Chem. Soc.* **1991**, *113*, 5456–5457.

(25)   Dubois, D.; Kadish, K. M.; Flanagan, S.; Haufler, R. E.; Chibante, L. P. F.; Wilson, L. J. *J. Am. Chem. Soc.* **1991**, *113*, 4364–4366.

(26)   Xie, Q.; Perez-Cordero, E.; Echegoyen, L. *J. Am. Chem. Soc.* **1992**, *114*, 3978–3980.

(27)   Eiermann, M.; Wudl, F.; Prato, M.; Maggini, M. *J. Am. Chem. Soc.* **1994**, *116*, 8364–8365.

(28)   Suzuki, T.; Li, Q.; Khemani, K. C.; Wudl, F.; Almarsson, O. *J. Am. Chem. Soc.* **1992**, *114*, 7300–7301.

(29)   Taliani, C.; Ruani, G.; Zamboni, R.; Danieli, R.; Rossini, S.; Denisov, V. N.; Burlakov, V. M.; Negri, F.; Orlandi, G.; Zerbetto, F. *J. Chem. Soc. Chem. Commun.* **1993**, 220–222.

(30)   Tutt, L. W.; Kost, A. *Nature* **1992**, *356*, 225–226.

(31)   Wang, Y. *Nature* **1992**, *356*, 585–587.
(32)   Sariciftci, N. S.; Smilowitz, L.; Heeger, A. J.; Wudl, F. *Science* **1992**, *258*, 1474–1476.
(33)   Morita, S.; Zakhidov, A. A.; Yoshino, K. *Solid State Commun.* **1992**, *82*, 249–252.
(34)   Dunk, P. W.; Mulet-Gas, M.; Nakanishi, Y.; Kaiser, N. K.; Rodríguez-Fortea, A.; Shinohara, H.; Poblet, J. M.; Marshall, A. G.; Kroto, H. W. *Nat. Commun.* **2014**, *5*, 5844.
(35)   Zhang, J.; Bowles, F. L.; Bearden, D. W.; Ray, W. K.; Fuhrer, T.; Ye, Y.; Dixon, C.; Harich, K.; Helm, R. F.; Olmstead, M. M.; Balch, A. L.; Dorn, H. C. *Nat. Chem.* **2013**, *5*, 880–885.
(36)   Stephan, I.; Zheng, G.; Elstner, M.; Morokuma, K. **2003**, *3*, 1657–1664.
(37)   Rivera-Nazario, D. M.; Pinzón, J. R.; Stevenson, S.; Echegoyen, L. A. *J. Phys. Org. Chem.* **2013**, *26*, 194–205.
(38)   Krätschmer, W.; Fostiropoulos, K.; Huffman, D. R. *Chem. Phys. Lett.* **1990**, *170*, 167–170.
(39)   Taylor, R.; Walton, D. R. M. *Nature* **1993**, *363*, 685–693.
(40)   Fernández, I.; Solà, M.; Bickelhaupt, F. M. *Chem. Eur. J.* **2013**, *19*, 7416–7422.
(41)   Prato, M. *J. Mater. Chem.* **1997**, *7*, 1097–1109.
(42)   Diederich, F.; Isaacs, L.; Philp, D. *Chem. Soc. Rev.* **1994**, *23*, 243–255.
(43)   Wudl, F. *Acc. Chem. Res.* **1992**, *25*, 157–161.
(44)   Tsuda, M.; Ishida, T.; Nogami, T.; Kurono, S.; Ohashi, M. *Tetrahedron Lett.* **1993**, *34*, 6911–6912.
(45)   Zhang, X.; Foote, C. S. *J. Am. Chem. Soc.* **1995**, *117*, 4271–4275.
(46)   Hoke, S. H.; Molstad, J.; Dilettato, D.; Jay, M. J.; Carlson, D.; Kahr, B.; Cooks, R. G. *J. Org. Chem.* **1992**, *57*, 5069–5071.
(47)   Prato, M.; Suzuki, T.; Foroudian, H.; Li, Q.; Khemani, K.; Wudl, F.; Leonetti, J.; Little, R. D.; White, T. *J. Am. Chem. Soc.* **1993**, *115*, 1594–1595.
(48)   Shiu, L.-L.; Lin, T.-I.; Peng, S.-M.; Her, G.-R.; Ju, D. Der; Lin, S.-K.; Hwang, J.-H.; Mou, C. Y.; Luh, T.-Y. *J. Chem. Soc. Chem. Commun.* **1994**, 647–648.
(49)   Meier, M. S.; Poplawska, M. *J. Org. Chem.* **1993**, *58*, 4524–4525.
(50)   Muthu, S.; Maruthamuthu, P.; Ragunathan, R.; Vasudeva Rao, P. R.; Mathews, C. K. *Tetrahedron Lett.* **1994**, *35*, 1763–1766.
(51)   Rubin, Y.; Khan, S.; Freedberg, D. I.; Yeretzian, C. *J. Am. Chem. Soc.* **1993**, *115*, 344–345.
(52)   Belik, P.; Gügel, A.; Kraus, A.; Spickermann, J.; Enkelmann, V.; Frank, G.; Müllen, K. *Adv. Mater.* **1993**, *5*, 854–856.
(53)   Grösser, T.; Prato, M.; Lucchini, V.; Hirsch, A.; Wudl, F. *Angew. Chem. Int. Ed.* **1995**, *34*, 1343–1345.
(54)   Thilgen, C.; Diederich, F. *Chem. Rev.* **2006**, *106*, 5049–5135.
(55)   Bingel, C. *Chem. Ber.* **1993**, *126*, 1957–1959.
(56)   Merlic, C. A.; Bendorf, H. D. *Tetrahedron Lett.* **1994**, *35*, 9529–9532.
(57)   Fabre, T. S.; Treleaven, W. D.; McCarley, T. D.; Newton, C. L.; Landry, R. M.; Saraiva, M. C.; Strongin, R. M. *J. Org. Chem.* **1998**, *63*, 3522–3523.
(58)   Dragoe, N.; Shimotani, H.; Wang, J.; Iwaya, M.; de Bettencourt-Dias, A.; Balch, A. L.; Kitazawa, K. *J. Am. Chem. Soc.* **2001**, *123*, 1294–1301.
(59)   Schuster, D. I.; Cao, J.; Kaprinidis, N.; Wu, Y.; Jensen, A. W.; Lu, Q.; Wang, H.; Wilson, S. R. *J. Am. Chem. Soc.* **1996**, *118*, 5639–5647.
(60)   Vassilikogiannakis, G.; Orfanopoulos, M. *J. Org. Chem.* **1999**, *64*, 3392–3393.
(61)   Jensen, A. W.; Khong, A.; Saunders, M.; Wilson, S. R.; Schuster, D. I. *J. Am. Chem. Soc.* **1997**, *119*, 7303–7307.
(62)   Bernstein, R.; Foote, C. S. *Tetrahedron Lett.* **1998**, *39*, 7051–7054.
(63)   Maggini, M.; Scorrano, G.; Prato, M. *J. Am. Chem. Soc.* **1993**, *115*, 9798–9799.
(64)   Padwa, A.; Pearson, W. H. *Synthetic Applications of 1,3-Dipolar Cycloaddition Chemistry Toward Heterocycles and Natural Products, Volume 59*; John Wiley & Sons, Inc: New York, **2003**.
(65)   Martin, N.; Segura, J. L.; Wudl, F. In *Fullerenes: From Synthesis to Optoelectronic Properties*; Kluver Academic Publishers: Dordrecht, The Netherlands, **2002**.
(66)   Segura, J. L.; Martín, N. *Chem. Rev.* **1999**, *99*, 3199–3246.
(67)   Beer, E.; Feuerer, M.; Knorr, A.; Mirlach, A.; Daub, J. *Angew. Chem. Int. Ed.* **1994**, *33*, 1087–1089.
(68)   Holczer, K.; Klein, O.; Huang, S.-M.; Kaner, R. B.; Fu, K.-J.; Whetten, R. L.; Diederich, F. *Science* **1991**, *252*, 1154–1157.
(69)   Fagan, P. J.; Calabrese, J. C.; Malone, B. *Science* **1991**, *252*, 1160–1161.
(70)   Song, L.-C.; Wang, G.-F.; Liu, P.-C.; Hu, Q.-M. *Organometallics* **2003**, *22*, 4593–4598.
(71)   Song, L.-C.; Yu, G.-A.; Su, F.-H.; Hu, Q.-M. *Organometallics* **2004**, *23*, 4192–4198.

(72)   Nagashima, H.; Nakaoka, A.; Saito, Y.; Kato, M.; Kawanishi, T.; Itoh, K. *J. Chem. Soc. Chem. Commun.* **1992**, 377–379.

(73)   Song, L.-C.; Yu, G.-A.; Wang, H.-T.; Su, F.-H.; Hu, Q.-M.; Song, Y.-L.; Gao, Y.-C. *Eur. J. Inorg. Chem.* **2004**, 866–871.

(74)   Song, L.-C.; Su, F.-H.; Hu, Q.-M.; Grigiotti, E.; Zanello, P. *Eur. J. Inorg. Chem.* **2006**, 422–429.

(75)   Usatov, A. V.; Kudin, K. N.; Vorontsov, E. V.; Vinogradova, L. E.; Novikov, Y. N. *J. Organomet. Chem.* **1996**, *522*, 147–153.

(76)   Nambo, M.; Segawa, Y.; Wakamiya, A.; Itami, K. *Chem. Asian J.* **2011**, *6*, 590–598.

(77)   Balch, A. L.; Catalano, V. J.; Lee, J. W. *Inorg. Chem.* **1991**, *30*, 3980–3981.

(78)   Usatov, A. V.; Martynova, E. V.; Dolgushin, F. M.; Peregudov, A. S.; Antipin, M. Y.; Novikov, Y. N. *Eur. J. Inorg. Chem.* **2002**, 2565–2567.

(79)   Balch, A. L.; Catalano, V. J.; Lee, J. W.; Olmstead, M. M.; Parkin, S. R. *J. Am. Chem. Soc.* **1991**, *113*, 8953–8955.

(80)   Balch, A. L.; Ginwalla, A. S.; Lee, J. W.; Noll, B. C.; Olmstead, M. M. *J. Am. Chem. Soc.* **1994**, *116*, 2227–2228.

(81)   Thompson, D. M.; Jones, M.; Baird, M. C. *Eur. J. Inorg. Chem.* **2003**, 175–180.

(82)   Song, H.; Lee, K.; Park, J. T.; Choi, M.-G. *Organometallics* **1998**, *17*, 4477–4483.

(83)   Lee, K.; Hsu, H.-F.; Shapley, J. R. *Organometallics* **1997**, *16*, 3876–3877.

(84)   Guldi, D. M.; Aminur Rahman, G. M.; Marczak, R.; Matsuo, Y.; Yamanaka, M.; Nakamura, E. *J. Am. Chem. Soc.* **2006**, *128*, 9420–9427.

(85)   Sawamura, M.; Kuninobu, Y.; Toganoh, M.; Matsuo, Y.; Yamanaka, M.; Nakamura, E. *J. Am. Chem. Soc.* **2002**, *124*, 9354–9355.

(86)   Song, L.-C.; Liu, J.-T.; Hu, Q.-M.; Weng, L.-H. *Organometallics* **2000**, *19*, 1643–1647.

(87)   Crane, J. D.; Hitchcock, P. B.; Kroto, H. W.; Taylor, R.; Walton, D. R. M. *J. Chem. Soc. Chem. Commun.* **1992**, 1764–1765.

(88)   Crane, J. D.; Hitchcock, P. B. *J. Chem. Soc. Dalton Trans.* **1993**, 2537–2538.

(89)   Olmstead, M. M.; Costa, D. A.; Maitra, K.; Noll, B. C.; Phillips, S. L.; Van Calcar, P. M.; Balch, A. L. *J. Am. Chem. Soc.* **1999**, *121*, 7090–7097.

(90)   Iyoda, M.; Sultana, F.; Sasaki, S.; Butenschön, H. *Tetrahedron Lett.* **1995**, *36*, 579–582.

(91)   Herranz, M. Á.; Illescas, B.; Martín, N.; Luo, C.; Guldi, D. M. *J. Org. Chem.* **2000**, *65*, 5728–5738.

(92)   Sun, Y.; Drovetskaya, T.; Bolskar, R. D.; Bau, R.; Boyd, P. D. W.; Reed, C. A. *J. Org. Chem.* **1997**, *62*, 3642–3649.

(93)   Wijnkoop, M. van; Meidine, M. F.; Avent, A. G.; Darwish, A. D.; Kroto, H. W.; Taylor, R.; Walton, D. R. M. *J. Chem. Soc. Dalton Trans.* **1997**, 675–678.

(94)   Sawamura, M.; Iikura, H.; Nakamura, E. *J. Am. Chem. Soc.* **1996**, *118*, 12850–12851.

(95)   Martín, N.; Altable, M.; Filippone, S.; Martín-Domenech, A. *Chem. Commun.* **2004**, 1338–1339.

(96)   Martín, N.; Altable, M.; Filippone, S.; Martín-Domenech, A.; Poater, A.; Solà, M. *Chem. Eur. J.* **2005**, *11*, 2716–2729.

(97)   Tuktarov, A. R.; Korolev, V. V.; Dzhemilev, U. M. *Russ. J. Org. Chem.* **2010**, *46*, 588–589.

(98)   Nair, V.; Sethumadhavan, D.; Sheela, K. .; Nair, S. M.; Eigendorf, G. K. *Tetrahedron* **2002**, *58*, 3009–3013.

(99)   Martín, N.; Altable, M.; Filippone, S.; Martín-Domenech, A.; Echegoyen, L.; Cardona, C. M. *Angew. Chem. Int. Ed.* **2005**, *45*, 110–114.

(100)   Lukoyanova, O.; Cardona, C. M.; Altable, M.; Filippone, S.; Martín Domenech, A.; Martín, N.; Echegoyen, L. *Angew. Chem. Int. Ed.* **2006**, *45*, 7430–7433.

(101)   Sinbandhit, S.; Hamelin, J. *J. Chem. Soc. Chem. Commun.* **1977**, 768–769.

(102)   Filippone, S.; Barroso, M. I.; Martín-Domenech, A.; Osuna, S.; Solà, M.; Martín, N. *Chem. Eur. J.* **2008**, *14*, 5198–5206.

(103)   Martín, N.; Altable, M.; Filippone, S.; Martín-Domenech, A.; Martínez-Alvarez, R.; Suarez, M.; Plonska-Brzezinska, M. E.; Lukoyanova, O.; Echegoyen, L. *J. Org. Chem.* **2007**, *72*, 3840–3846.

(104)   Lee, J. W.; Olmstead, M. M.; Vickery, J. S.; Balch, A. L. *J. Clust. Sci.* **2000**, *11*, 67–77.

(105)   Balch, A. L.; Olmstead, M. M. *Chem. Rev.* **1998**, *98*, 2123–2166.

(106)   Douthwaite, R. E.; Green, M. L. H.; Stephens, A. H. H.; Turner, J. F. C. *J. Chem. Soc. Chem. Commun.* **1993**, 1522–1523.

(107)   Lee, K.; Song, H.; Kim, B.; Park, J. T.; Park, S.; Choi, M.-G. *J. Am. Chem. Soc.* **2002**, *124*, 2872–2873.

(108)   Sawamura, M.; Kuninobu, Y.; Nakamura, E. *J. Am. Chem. Soc.* **2000**, *122*, 12407–12408.

(109)   Park, J. T.; Cho, J.-J.; Song, H. *J. Chem. Soc. Chem. Commun.* **1995**, 15–16.

(110)   Park, J. T.; Cho, J.-J.; Song, H.; Jun, C.-S.; Son, Y.; Kwak, J. *Inorg. Chem.* **1997**, *36*, 2698–2699.

(111)   Song, H.; Lee, K.; Lee, C. H.; Park, J. T.; Chang, H. Y.; Choi, M.-G. *Angew. Chem. Int. Ed.* **2001**, *40*, 1500–1502.

(112)   Song, H.; Lee, C. H.; Lee, K.; Park, J. T. *Organometallics* **2002**, *21*, 2514–2520.

(113)   Braun, T.; Wohlers, M.; Belz, T.; Nowitzke, G.; Wortmann, G.; Uchida, Y.; Pfänder, N.; Schlögl, R. *Catal. Lett.* **1997**, *43*, 167–173.

(114)   Braun, T.; Wohlers, M.; Belz, T.; Schlögl, R. *Catal. Lett.* **1997**, *43*, 175–180.

(115)   Pradeep, T.; Kulkarni, G. U.; Kannan, K. R.; Row, T. N. G.; Rao, C. N. R. *J. Am. Chem. Soc.* **1992**, *114*, 2272–2273.

(116)   Patel, D. K.; Thompson, D. M.; Baird, M. C.; Thompson, L. K.; Preston, K. F. *J. Organomet. Chem.* **1997**, *545-546*, 607–610.

(117)   Huang, Y.; Freiser, B. S. *J. Am. Chem. Soc.* **1991**, *113*, 8186–8187.

(118)   Król, S.; Łapiński, A.; Graja, A. *Adv. Mater. Opt. Electron.* **1996**, *6*, 255–260.

(119)   Billaud, D.; Lemont, S.; Ghanbaja, J. *Fullerene Sci. Techn.* **1996**, *4*, 1119–1154.

(120)   Popov, A. A.; Yang, S.; Dunsch, L. *Chem. Rev.* **2013**, *113*, 5989–6113.

(121)   Lu, X.; Bao, L.; Akasaka, T.; Nagase, S. *Chem. Commun.* **2014**, *50*, 14701–14715.

(122)   Lu, X.; Feng, L.; Akasaka, T.; Nagase, S. *Chem. Soc. Rev.* **2012**, *41*, 7723–7760.

(123)   Rodríguez-Fortea, A.; Balch, A. L.; Poblet, J. M. *Chem. Soc. Rev.* **2011**, *40*, 3551–3563.

(124)   Shi, Z.-Q.; Wu, X.; Wang, C.-R.; Lu, X.; Shinohara, H. *Angew. Chem. Int. Ed.* **2006**, *45*, 2107–2111.

(125)   Rodríguez-Fortea, A.; Alegret, N.; Balch, A. L.; Poblet, J. M. *Nat. Chem.* **2010**, *2*, 955–9561.

(126)   Garcia-Borràs, M.; Osuna, S.; Swart, M.; Luis, J. M.; Solà, M. *Angew. Chem. Int. Ed.* **2013**, *52*, 9275–9278.

(127)   Chai, Y.; Guo, T.; Jin, C.; Haufler, R. E.; Chibante, L. P. F.; Fure, J.; Wang, L.; Alford, J. M.; Smalley, R. E. *J. Phys. Chem.* **1991**, *95*, 7564–7568.

(128)   Lu, X.; Nakajima, K.; Iiduka, Y.; Nikawa, H.; Mizorogi, N.; Slanina, Z.; Tsuchiya, T.; Nagase, S.; Akasaka, T. *J. Am. Chem. Soc.* **2011**, *133*, 19553–19558.

(129)   Manolopoulos, D. E.; Fowler, P. W. *An Atlas of Fullerenes*; Clarendon: Oxford: United Kingdom, **1995**.

(130)   Akasaka, T.; Wakahara, T.; Nagase, S.; Kobayashi, K.; Waelchli, M.; Yamamoto, K.; Kondo, M.; Shirakura, S.; Maeda, Y.; Kato, T.; Kako, M.; Nakadaira, Y.; Gao, X.; Van Caemelbecke, E.; Kadish, K. M. *J. Phys. Chem. B* **2001**, *105*, 2971–2974.

(131)   Muthukumar, K.; Larsson, J. A. *J. Phys. Chem. A* **2008**, *112*, 1071–1075.

(132)   Garcia-Borràs, M.; Luis, J. M.; Swart, M.; Solà, M. *Chem. Eur. J.* **2013**, *19*, 4468–4479.

(133)   Garcia-Borràs, M.; Osuna, S.; Luis, J. M.; Swart, M.; Solà, M. *Chem. Soc. Rev.* **2014**, *43*, 5089–5105.

(134)   Feng, L.; Nakahodo, T.; Wakahara, T.; Tsuchiya, T.; Maeda, Y.; Akasaka, T.; Kato, T.; Horn, E.; Yoza, K.; Mizorogi, N.; Nagase, S. *J. Am. Chem. Soc.* **2005**, *127*, 17136–17137.

(135)   Akasaka, T.; Nagase, S.; Kobayashi, K.; Suzuki, T.; Kato, T.; Yamamoto, K.; Funasaka, H.; Takahashi, T. *J. Chem. Soc. Chem. Commun.* **1995**, 1343–1344.

(136)   Maeda, Y.; Miyashita, J.; Hasegawa, T.; Wakahara, T.; Tsuchiya, T.; Feng, L.; Lian, Y.; Akasaka, T.; Kobayashi, K.; Nagase, S.; Kako, M.; Yamamoto, K.; Kadish, K. M. *J. Am. Chem. Soc.* **2005**, *127*, 2143–2146.

(137)   Akasaka, T.; Wakahara, T.; Nagase, S.; Kobayashi, K.; Waelchli, M.; Yamamoto, K.; Kondo, M.; Shirakura, S.; Okubo, S.; Maeda, Y.; Kato, T.; Kako, M.; Nakadaira, Y.; Nagahata, R.; Gao, X.; Van Caemelbecke, E.; Kadish, K. M. *J. Am. Chem. Soc.* **2000**, *122*, 9316–9317.

(138)   Nishibori, E.; Takata, M.; Sakata, M.; Tanaka, H.; Hasegawa, M.; Shinohara, H. *Chem. Phys. Lett.* **2000**, *330*, 497–502.

(139)   Yang, S.; Dunsch, L. *Angew. Chem. Int. Ed.* **2006**, *45*, 1299–1302.

(140)   Stevenson, S.; Rice, G.; Glass, T.; Harich, K.; Cromer, F.; Jordan, M. R.; Craft, J.; Hadju, E.; Bible, R.; Olmstead, M. M.; Maitra, K.; Fisher, A. J.; Balch, A. L.; Dorn, H. C. *Nature* **1999**, *401*, 55–57.

(141)   Olmstead, M. M.; de Bettencourt-Dias, A.; Duchamp, J. C.; Stevenson, S.; Dorn, H. C.; Balch, A. L. *J. Am. Chem. Soc.* **2000**, *122*, 12220–12226.

(142)   Stevenson, S.; Fowler, P. W.; Heine, T.; Duchamp, J. C.; Rice, G.; Glass, T.; Harich, K.; Hajdu, E.; Bible, R.; Dorn, H. C. *Nature* **2000**, *408*, 427–428.

(143)   Olmstead, M. M.; Lee, H. M.; Duchamp, J. C.; Stevenson, S.; Marciu, D.; Dorn, H. C.; Balch, A. L. *Angew. Chem. Int. Ed.* **2003**, *42*, 900–903.

(144) Olmstead, M. M.; de Bettencourt-Dias, A.; Duchamp, J. C.; Stevenson, S.; Marciu, D.; Dorn, H. C.; Balch, A. L. *Angew. Chem. Int. Ed.* **2001**, *40*, 1223–1225.

(145) Stevenson, S.; Lee, H. M.; Olmstead, M. M.; Kozikowski, C.; Stevenson, P.; Balch, A. L. *Chem. Eur. J.* **2002**, *8*, 4528–4535.

(146) Iezzi, E. B.; Duchamp, J. C.; Fletcher, K. R.; Glass, T. E.; Dorn, H. C. *Nano Lett.* **2002**, *2*, 1187–1190.

(147) Krause, M.; Kuzmany, H.; Georgi, P.; Dunsch, L.; Vietze, K.; Seifert, G. *J. Chem. Phys.* **2001**, *115*, 6596.

(148) Shinohara, H. *Rep. Prog. Phys.* **2000**, *63*, 843–892.

(149) Dunsch, L.; Krause, M.; Noack, J.; Georgi, P. *J. Phys. Chem. Solids* **2004**, *65*, 309–315.

(150) Krause, M.; Dunsch, L. *Angew. Chem. Int. Ed.* **2005**, *44*, 1557–1560.

(151) Yang, S.; Dunsch, L. *J. Phys. Chem. B* **2005**, *109*, 12320–12328.

(152) Yang, S.; Dunsch, L. *Chem. Eur. J.* **2005**, *12*, 413–419.

(153) Krause, M.; Wong, J.; Dunsch, L. *Chem. Eur. J.* **2005**, *11*, 706–711.

(154) Stevenson, S.; Phillips, J. P.; Reid, J. E.; Olmstead, M. M.; Rath, S. P.; Balch, A. L. *Chem. Commun.* **2004**, 2814–2815.

(155) Krause, M.; Dunsch, L. *ChemPhysChem* **2004**, *5*, 1445–1449.

(156) Iezzi, E. B.; Duchamp, J. C.; Harich, K.; Glass, T. E.; Lee, H. M.; Olmstead, M. M.; Balch, A. L.; Dorn, H. C. *J. Am. Chem. Soc.* **2002**, *124*, 524–525.

(157) Lee, H. M.; Olmstead, M. M.; Iezzi, E.; Duchamp, J. C.; Dorn, H. C.; Balch, A. L. *J. Am. Chem. Soc.* **2002**, *124*, 3494–3495.

(158) Iezzi, E. B.; Cromer, F.; Stevenson, P.; Dorn, H. C. *Synth. Met.* **2002**, *128*, 289–291.

(159) Cardona, C. M.; Kitaygorodskiy, A.; Echegoyen, L. *J. Am. Chem. Soc.* **2005**, *127*, 10448–10453.

(160) Stevenson, S.; Stephen, R. R.; Amos, T. M.; Cadorette, V. R.; Reid, J. E.; Phillips, J. P. *J. Am. Chem. Soc.* **2005**, *127*, 12776–12777.

(161) Shu, C.; Cai, T.; Xu, L.; Zuo, T.; Reid, J.; Harich, K.; Dorn, H. C.; Gibson, H. W. *J. Am. Chem. Soc.* **2007**, *129*, 15710–15717.

(162) Alvarez, L.; Pichler, T.; Georgi, P.; Schwieger, T.; Peisert, H.; Dunsch, L.; Hu, Z.; Knupfer, M.; Fink, J.; Bressler, P.; Mast, M.; Golden, M. S. *Phys. Rev. B* **2002**, *66*, 035107.

(163) Krause, M.; Liu, X.; Wong, J.; Pichler, T.; Knupfer, M.; Dunsch, L. *J. Phys. Chem. A* **2005**, *109*, 7088–7093.

(164) Liu, X.; Krause, M.; Wong, J.; Pichler, T.; Dunsch, L.; Knupfer, M. *Phys. Rev. B* **2005**, *72*, 085407.

(165) Shiozawa, H.; Rauf, H.; Pichler, T.; Grimm, D.; Liu, X.; Knupfer, M.; Kalbac, M.; Yang, S.; Dunsch, L.; Büchner, B.; Batchelor, D. *Phys. Rev. B* **2005**, *72*, 195409.

(166) Osuna, S.; Valencia, R.; Rodríguez-Fortea, A.; Swart, M.; Solà, M.; Poblet, J. M. *Chem. Eur. J.* **2012**, *18*, 8944–8956.

(167) Iijima, S. *Nature* **1991**, *354*, 56–58.

(168) Iijima, S.; Ichihashi, T. *Nature* **1993**, *363*, 603–605.

(169) Bethune, D. S.; Klang, C. H.; de Vries, M. S.; Gorman, G.; Savoy, R.; Vazquez, J.; Beyers, R. *Nature* **1993**, *363*, 605–607.

(170) Kaempgen, M.; Dettlaff, U.; Roth, S. *Synth. Met.* **2003**, *135-136*, 761–762.

(171) Dresselhaus, M. S.; Dresselhaus, G.; Saito, R. *Carbon* **1995**, *33*, 883–891.

(172) Ogunro, O. O.; Nicolas, C. I.; Mintz, E. A.; Wang, X.-Q. *ACS Macro Lett.* **2012**, *1*, 524–528.

(173) Cabria, I.; Mintmire, J. W.; White, C. T. *Phys. Rev. B* **2003**, *67*, 121406.

(174) Clar, E. *The Aromatic Sextet*; Wiley: New York, **1972**.

(175) Solà, M. *Front. Chem.* **2013**, *1*, 22.

(176) Martín-Martínez, F. J.; Melchor, S.; Dobado, J. A. *Org. Lett.* **2008**, *10*, 1991–1994.

(177) Baldoni, M.; Sgamellotti, A.; Mercuri, F. *Org. Lett.* **2007**, *9*, 4267–4270.

(178) Baldoni, M.; Selli, D.; Sgamellotti, A.; Mercuri, F. *J. Phys. Chem. C* **2009**, *113*, 862–866.

(179) Matsuo, Y.; Tahara, K.; Nakamura, E. *Org. Lett.* **2003**, *5*, 3181–3184.

(180) Ormsby, J. L.; King, B. T. *J. Org. Chem.* **2004**, *69*, 4287–4291.

(181) Lu, J. P. *Phys. Rev. Lett.* **1997**, *79*, 1297–1300.

(182) Wong, E. W.; Sheehan, P. E.; Lieber, C. M. *Science* **1997**, *277*, 1971–1975.

(183) Krishnan, A.; Dujardin, E.; Ebbesen, T. W.; Yianilos, P. N.; Treacy, M. M. J. *Phys. Rev. B* **1998**, *58*, 14013.

(184) Treacy, M. M. J.; Ebbesen, T. W.; Gibson, J. M. *Nature* **1996**, *381*, 678–680.

(185) Yang, Y. H.; Li, W. Z. *Appl. Phys. Lett.* **2011**, *98*, 041901.

(186)   Pop, E.; Mann, D.; Wang, Q.; Goodson, K.; Dai, H. *Nano Lett.* **2006**, *6*, 96–100.

(187)   White, C. T.; Todorov, T. N. *Nature* **1998**, *393*, 240–242.

(188)   Ebbesen, T. W.; Lezec, H. J.; Hiura, H.; Bennett, J. W.; Ghaemi, H. F.; Thio, T. *Nature* **1996**, *382*, 54–56.

(189)   Javey, A.; Guo, J.; Wang, Q.; Lundstrom, M.; Dai, H. *Nature* **2003**, *424*, 654–657.

(190)   Javey, A.; Kim, H.; Brink, M.; Wang, Q.; Ural, A.; Guo, J.; McIntyre, P.; McEuen, P.; Lundstrom, M.; Dai, H. *Nat. Mater.* **2002**, *1*, 241–246.

(191)   Wind, S. J.; Appenzeller, J.; Martel, R.; Derycke, V.; Avouris, P. *J. Vac. Sci. Technol. B* **2002**, *20*, 2798.

(192)   Krüger, M.; Buitelaar, M. R.; Nussbaumer, T.; Schönenberger, C.; Forró, L. *Appl. Phys. Lett.* **2001**, *78*, 1291.

(193)   Zhaoa, J.; Xieb, R.-H. *J. Nanosci. Nanotechnol.* **2003**, *3*, 459–478.

(194)   Henrard, L.; Hernández, E.; Bernier, P.; Rubio, A. *Phys. Rev. B* **1999**, *60*, R8521–R8524.

(195)   Cotiuga, I.; Picchioni, F.; Agarwal, U. S.; Wouters, D.; Loos, J.; Lemstra, P. J. *Macromol. Rapid Commun.* **2006**, *27*, 1073–1078.

(196)   Qiao, R.; Ke, P. C. *J. Am. Chem. Soc.* **2006**, *128*, 13656–13657.

(197)   Tasis, D.; Tagmatarchis, N.; Georgakilas, V.; Prato, M. *Chem. Eur. J.* **2003**, *9*, 4000–4008.

(198)   Sinani, V. A.; Gheith, M. K.; Yaroslavov, A. A.; Rakhnyanskaya, A. A.; Sun, K.; Mamedov, A. A.; Wicksted, J. P.; Kotov, N. A. *J. Am. Chem. Soc.* **2005**, *127*, 3463–3472.

(199)   Thess, A.; Lee, R.; Nikolaev, P.; Dai, H.; Petit, P.; Robert, J.; Xu, C.; Lee, Y.; Kim, S.; Rinzler, A.; Colbert, D.; Scuseria, G.; Tomanek, D.; Fischer, J.; Smalley, R. *Science* **1996**, *273*, 483–487.

(200)   Nikolaev, P.; Bronikowski, M. J.; Bradley, R. K.; Rohmund, F.; Colbert, D. T.; Smith, K. .; Smalley, R. E. *Chem. Phys. Lett.* **1999**, *313*, 91–97.

(201)   Journet, C.; Maser, W. K.; Bernier, P.; Loiseau, A.; de la Chapelle, M. L.; Lefrant, S.; Deniard, P.; Lee, R.; Fischer, J. E. *Nature* **1997**, *388*, 756–758.

(202)   José-Yacamán, M.; Miki-Yoshida, M.; Rendón, L.; Santiesteban, J. G. *Appl. Phys. Lett.* **1993**, *62*, 657.

(203)   Guo, T.; Nikolaev, P.; Rinzler, A. G.; Tomanek, D.; Colbert, D. T.; Smalley, R. E. *J. Phys. Chem.* **1995**, *99*, 10694–10697.

(204)   Tian, Y.; Hu, Z.; Yang, Y.; Wang, X.; Chen, X.; Xu, H.; Wu, Q.; Ji, W.; Chen, Y. *J. Am. Chem. Soc.* **2004**, *126*, 1180–1183.

(205)   Matthews, K. D.; Lemaitre, M. G.; Kim, T.; Chen, H.; Shim, M.; Zuo, J.-M. *J. Appl. Phys.* **2006**, *100*, 044309.

(206)   Dai, H. *Acc. Chem. Res.* **2002**, *35*, 1035–1044.

(207)   Zhang, J.; Zou, H.; Qing, Q.; Yang, Y.; Li, Q.; Liu, Z.; Guo, X.; Du, Z. *J. Phys. Chem. B* **2003**, *107*, 3712–3718.

(208)   Li, Y.; Zhang, X.; Luo, J.; Huang, W.; Cheng, J.; Luo, Z.; Li, T.; Liu, F.; Xu, G.; Ke, X.; Li, L.; Geise, H. J. *Nanotechnology* **2004**, *15*, 1645–1649.

(209)   Holzinger, M.; Vostrowsky, O.; Hirsch, A.; Hennrich, F.; Kappes, M.; Weiss, R.; Jellen, F. *Angew. Chem. Int. Ed.* **2001**, *40*, 4002–4005.

(210)   Hirsch, A. *Angew. Chem. Int. Ed.* **2002**, *41*, 1853–1859.

(211)   Chen, R. J.; Zhang, Y.; Wang, D.; Dai, H. *J. Am. Chem. Soc.* **2001**, *123*, 3838–3839.

(212)   Tasis, D.; Tagmatarchis, N.; Bianco, A.; Prato, M. *Chem. Rev.* **2006**, *106*, 1105–1136.

(213)   Hu, H.; Bhowmik, P.; Zhao, B.; Hamon, M. .; Itkis, M. .; Haddon, R. . *Chem. Phys. Lett.* **2001**, *345*, 25–28.

(214)   Dresselhaus, M. S.; Dresselhaus, G.; Avouris, P. *Carbon Nanotubes*; Topics in Applied Physics Volume 80; Springer Berlin Heidelberg: Germany, **2001**.

(215)   Saito, R.; Grüneis, A.; Samsonidze, G. G.; Dresselhaus, G.; Dresselhaus, M. S.; Jorio, A.; Cançado, L. G.; Pimenta, M. A.; Souza Filho, A. G. *Appl. Phys. A* **2004**, *78*, 1099–1105.

(216)   Georgakilas, V.; Voulgaris, D.; Vázquez, E.; Prato, M.; Guldi, D. M.; Kukovecz, A.; Kuzmany, H. *J. Am. Chem. Soc.* **2002**, *124*, 14318–14319.

(217)   Kürti, J.; Zólyomi, V.; Grüneis, A.; Kuzmany, H. *Phys. Rev. B* **2002**, *65*, 165433.

(218)   Zólyomi, V.; Kürti, J.; Grüneis, A.; Kuzmany, H. *Phys. Rev. Lett.* **2003**, *90*, 157401.

(219)   Fagan, S. B.; da Silva, A. J. R.; Mota, R.; Baierle, R. J.; Fazzio, A. *Phys. Rev. B* **2003**, *67*, 033405.

(220)   Bettinger, H. F.; Kudin, K. N.; Scuseria, G. E. *J. Am. Chem. Soc.* **2001**, *123*, 12849–12856.

(221)   Criado, A.; Gómez-Escalonilla, M. J.; Fierro, J. L. G.; Urbina, A.; Peña, D.; Guitián, E.; Langa, F. *Chem. Commun.* **2010**, *46*, 7028–7030.

(222) Globus, A.; Bauschlicher, C. W.; Han, J.; Jaffe, R. L.; Levit, C.; Srivastava, D. *Nanotechnology* **1998**, *9*, 192–199.

(223) Criado, A.; Vizuete, M.; Gómez-Escalonilla, M. J.; García-Rodriguez, S.; Fierro, J. L. G.; Cobas, A.; Peña, D.; Guitián, E.; Langa, F. *Carbon* **2013**, *63*, 140–148.

(224) Dyke, C. A.; Tour, J. M. *J. Phys. Chem. A* **2004**, *108*, 11151–11159.

(225) Prato, M.; Kostarelos, K.; Bianco, A. *Acc. Chem. Res.* **2008**, *41*, 60–68.

(226) Sun, Y.-P.; Fu, K.; Lin, Y.; Huang, W. *Acc. Chem. Res.* **2002**, *35*, 1096–1104.

(227) De Broglie, L. *Matter and Light: The New Physics*; Dover Publications Inc.: New York, **1939**.

(228) Heisenberg, W. *Z. Phys.* **1927**, *43*, 172–198.

(229) Levine, I. N. *Quantum Chemistry*, 5th ed.; Prentice Hall: Englewood Cliffs, **2000**.

(230) Schrödinger, E. *Ann. Phys.* **1926**, *384*, 361–376.

(231) Born, M.; Oppenheimer, R. *Ann. Phys.* **1927**, *389*, 457–484.

(232) Head-Gordon, M. *J. Phys. Chem.* **1996**, *100*, 13213–13225.

(233) Slater, J. C. *Phys. Rev.* **1951**, *81*, 385–390.

(234) Szabo, A.; Ostlund, N. S. *Modern Quantum Chemistry: Introduction to Advanced Electronic Structure Theory*; Dover Publications Inc.: New York, **1989**.

(235) Mortimer, R. G. *Mathematics for Physical Chemistry*, 3rd ed.; Elsevier: United States of America, **2005**.

(236) Davidson, E. R.; Feller, D. *Chem. Rev.* **1986**, *86*, 681–696.

(237) Baxter, C. A.; Cook, D. B. *Electron. J. Theor. Chem.* **1997**, *2*, 66–70.

(238) Dewar, M. J. S.; Storch, D. M. *J. Am. Chem. Soc.* **1985**, *107*, 3898–3902.

(239) Cramer, C. J. *Essentials of Computational Chemistry: Theories and Models*, 2nd ed.; John Wiley & Sons, Inc: London, **2004**.

(240) Foresman, J. B.; Frisch, M. J. *Exploring Chemistry with Electronic Structure Methods*, 2nd ed.; Gaussian, Inc., Wallingford CT, **2007**.

(241) Ditchfield, R.; Hehre, W. J.; Pople, J. A. *J. Chem. Phys.* **1971**, *54*, 724.

(242) Schwerdtfeger, P. *ChemPhysChem* **2011**, *12*, 3143–3155.

(243) Hinchliffe, A.; Pyykkö, P.; Stoll, H. *Chemical Modelling: Applications and Theory. Relativistic Pseudopotential Calculations*; Hinchliffe, A., Ed.; Chemical Modelling; Royal Society of Chemistry: Cambridge, Vol. 1, **2000**.

(244) Hay, P. J.; Wadt, W. R. *J. Chem. Phys.* **1985**, *82*, 270.

(245) Frisch, M. J.; Trucks, G. W.; Schlegel, H. B.; Scuseria, G. E.; Robb, M. A.; Cheeseman, J. R.; Scalmani, G.; Barone, V.; Mennucci, B.; Petersson, G. A.; Nakatsuji, H.; Caricato, M.; Li, X.; Hratchian, H. P.; Izmaylov, A. F.; Bloino, J.; Zheng, G.; Sonnenberg, J. L.; Hada, M.; Ehara, M.; Toyota, K.; Fukuda, R.; Hasegawa, J.; Ishida, M.; Nakajima, T.; Honda, Y.; Kitao, O.; Nakai, H.; Vreven, T.; Montgomery, J. A. J.; Peralta, J. E.; Ogliaro, F.; Bearpark, M.; Heyd, J. J.; Brothers, E.; Kudin, K. N.; Staroverov, V. N.; Kobayashi, R.; Normand, J.; Raghavachari, K.; Rendell, A.; Burant, J. C.; Iyengar, S. S.; Tomasi, J.; Cossi, M.; Rega, N.; Millam, J. M.; Klene, M.; Knox, J. E.; Cross, J. B.; Bakken, V.; Adamo, C.; Jaramillo, J.; Gomperts, R.; Stratmann, R. E.; Yazyev, O.; Austin, A. J.; Cammi, R.; Pomelli, C.; Ochterski, J. W.; Martin, R. L.; Morokuma, K.; Zakrzewski, V. G.; Voth, G. A.; Salvador, P.; Dannenberg, J. J.; Dapprich, S.; Daniels, A. D.; Farkas, Ö.; Foresman, J. B.; Ortiz, J. V.; Cioslowski, J.; Fox, D. J. Gaussian, Inc., Wallingford CT **2009**.

(246) Snijders, J. G.; Swart, M. *Theor. Chem. Acc.* **2003**, *110*, 34–41.

(247) Swart, M.; Snijders, J. G. *Theor. Chem. Acc.* **2004**, *111*, 56–56.

(248) te Velde, G.; Bickelhaupt, F. M.; Baerends, E. J.; Fonseca Guerra, C.; van Gisbergen, S. J. A.; Snijders, J. G.; Ziegler, T. *J. Comput. Chem.* **2001**, *22*, 931–967.

(249) Scientific Computing & Modelling (SCM) NV Corp. The Frozen Core Approximation http://www.scm.com/Products/Overview/frozencore.html.

(250) Parr, R. G.; Weitao, Y. *Density-Functional Theory of Atoms and Molecules*; Oxford University Press: New York, **1994**.

(251) Hohenberg, P. *Phys. Rev.* **1964**, *136*, B864–B871.

(252) Kohn, W.; Sham, L. J. *Phys. Rev.* **1965**, *140*, A1133–A1138.

(253) Kohn, W. *Phys. Rev. Lett.* **1983**, *51*, 1596–1598.

(254) Kryachko, E. S.; Ludeña, E. V. *Phys. Rev. A* **1991**, *43*, 2179–2193.

(255) Vosko, S. H.; Wilk, L.; Nusair, M. *Can. J. Phys.* **1980**, *58*, 1200–1211.

(256) Ceperley, D. M.; Alder, B. J. *Phys. Rev. Lett.* **1980**, *45*, 566–569.

(257) Lieb, E. H. *Phys. Lett. A* **1979**, *70*, 444–446.

(258) Lieb, E. H.; Oxford, S. *Int. J. Quantum Chem.* **1981**, *19*, 427–439.

(259) Perdew, J. P.; Jackson, K. A.; Pederson, M. R.; Singh, D. J.; Fiolhais, C. *Phys. Rev. B* **1992**, *46*, 6671–6687.

(260) Perdew, J. P.; Chevary, J. A.; Vosko, S. H.; Jackson, K. A.; Pederson, M. R.; Singh, D. J.; Fiolhais, C. *Phys. Rev. B* **1993**, *48*, 4978–4978.

(261) Perdew, J. P.; Burke, K.; Wang, Y. *Phys. Rev. B* **1996**, *54*, 16533–16539.

(262) Perdew, J. P.; Burke, K.; Wang, Y. *Phys. Rev. B* **1998**, *57*, 14999–14999.

(263) Becke, A. D. *Phys. Rev. A* **1988**, *38*, 3098–3100.

(264) Lee, C.; Yang, W.; Parr, R. G. *Phys. Rev. B* **1988**, *37*, 785–789.

(265) Miehlich, B.; Savin, A.; Stoll, H.; Preuss, H. *Chem. Phys. Lett.* **1989**, *157*, 200–206.

(266) Perdew, J. *Phys. Rev. B* **1986**, *33*, 8822–8824.

(267) Becke, A. D. *J. Chem. Phys.* **1993**, *98*, 5648.

(268) Levy, M.; Perdew, J. P.; Sahni, V. *Phys. Rev. A* **1984**, *30*, 2745–2748.

(269) Yanai, T.; Tew, D. P.; Handy, N. C. *Chem. Phys. Lett.* **2004**, *393*, 51–57.

(270) Dreuw, A.; Head-Gordon, M. *Chem. Rev.* **2005**, *105*, 4009–4037.

(271) Tawada, Y.; Tsuneda, T.; Yanagisawa, S.; Yanai, T.; Hirao, K. *J. Chem. Phys.* **2004**, *120*, 8425–8433.

(272) Runge, E.; Gross, E. K. U. *Phys. Rev. Lett.* **1984**, *52*, 997–1000.

(273) Casida, M. E. *J. Mol. Struct.* **2009**, *914*, 3–18.

(274) Marques, M. A. L.; Maitra, N. T.; Nogueira, F. M. S.; Gross, E. K. U.; Rubio, A. *Fundamentals of Time-Dependent Density Functional Theory*; Springer Berlin Heidelberg: Germany, **2012**.

(275) Gross, E. K. U.; Kohn, W. *Phys. Rev. Lett.* **1985**, *55*, 2850–2852.

(276) McWeeny, R. *Phys. Rev.* **1962**, *126*, 1028–1034.

(277) McWeeny, R. *Rev. Mod. Phys.* **1960**, *32*, 335–369.

(278) Stratmann, R. E.; Scuseria, G. E.; Frisch, M. J. *J. Chem. Phys.* **1998**, *109*, 8218.

(279) Metropolis, N.; Rosenbluth, A. W.; Rosenbluth, M. N.; Teller, A. H.; Teller, E. *J. Chem. Phys.* **1953**, *21*, 1087.

(280) Rahman, A. *Phys. Rev.* **1964**, *136*, A405–A411.

(281) Allen, M. P.; Tildesley, D. J. *Computer Simulation of Liquids*; Oxford University Press: New York, **1987**.

(282) Garcia de la Torre, J.; Ortega, A.; Perez Sanchez, H. E.; Hernandez Cifre, J. G. *Biophys. Chem.* **2005**, *116*, 121–128.

(283) Thompson, D. L. *Modern Methods for Multidimensional Dynamics Computations in Chemistry*; World Scientific: Singapore, **1998**.

(284) Bastida, A.; Cruz, C.; Zúñiga, J.; Requena, A.; Miguel, B. *J. Chem. Phys.* **2007**, *126*, 014503.

(285) Verlet, L. *Phys. Rev.* **1967**, *159*, 98–103.

(286) Swope, W. C. *J. Chem. Phys.* **1982**, *76*, 637.

(287) Hockney, R. W.; Goel, S. P.; Eastwood, J. W. *J. Comput. Phys.* **1974**, *14*, 148–158.

(288) Marrink, S. J.; Risselada, H. J.; Yefimov, S.; Tieleman, D. P.; de Vries, A. H. *J. Phys. Chem. B* **2007**, *111*, 7812–7824.

(289) McQuarrie, D. A. *Statistical Mechanics*; University Science Books: United States of America, **2000**.

(290) Pechukas, P. *Annu. Rev. Phys. Chem.* **1981**, *32*, 159–177.

(291) McIver, J. W.; Komornicki, A. *J. Am. Chem. Soc.* **1972**, *94*, 2625–2633.

(292) Minyaev, R. M. *Int. J. Quantum Chem.* **1994**, *49*, 105–127.

(293) Mulliken, R. S. *J. Chem. Phys.* **1955**, *23*, 1833.

(294) Fonseca Guerra, C.; Handgraaf, J.-W.; Baerends, E. J.; Bickelhaupt, F. M. *J. Comput. Chem.* **2004**, *25*, 189–210.

(295) Foster, J. P.; Weinhold, F. *J. Am. Chem. Soc.* **1980**, *102*, 7211–7218.

(296) Reed, A. E.; Weinhold, F. *J. Chem. Phys.* **1983**, *78*, 4066–4073.

(297) Reed, A. E.; Weinstock, R. B.; Weinhold, F. *J. Chem. Phys.* **1985**, *83*, 735.

(298) Reed, A. E.; Weinhold, F. *J. Chem. Phys.* **1985**, *83*, 1736.

(299) Reed, A. E.; Curtiss, L. A.; Weinhold, F. *Chem. Rev.* **1988**, *88*, 899–926.

(300) Tomasi, J.; Mennucci, B.; Cammi, R. *Chem. Rev.* **2005**, *105*, 2999–3093.

(301) Klamt, A. *J. Phys. Chem.* **1995**, *99*, 2224–2235.

(302) Barone, V.; Cossi, M. *J. Phys. Chem. A* **1998**, *102*, 1995–2001.

(303) Andzelm, J.; Kölmel, C.; Klamt, A. *J. Chem. Phys.* **1995**, *103*, 9312.

(304) Houk, K. N.; Gandour, R. W.; Strozier, R. W.; Rondan, N. G.; Paquette, L. A. *J. Am. Chem. Soc.* **1979**, *101*, 6797–6802.
(305) Ess, D. H.; Houk, K. N. *J. Am. Chem. Soc.* **2007**, *129*, 10646–10647.
(306) Cao, Y.; Liang, Y.; Zhang, L.; Osuna, S.; Hoyt, A.-L. M.; Briseno, A. L.; Houk, K. N. *J. Am. Chem. Soc.* **2014**, *136*, 10743–10751.
(307) van Zeist, W.-J.; Bickelhaupt, F. M. *Org. Biomol. Chem.* **2010**, *8*, 3118–3127.
(308) Bickelhaupt, F. M. *J. Comput. Chem.* **1999**, *20*, 114–128.
(309) Fernández, I.; Bickelhaupt, F. M. *Chem. Soc. Rev.* **2014**, *43*, 4953–4967.
(310) Wolters, L. P.; Bickelhaupt, F. M. *WIREs Comput. Mol. Sci.* **2015**, *5*, 324–343.
(311) Zhang, J.; Grubb, M.; Hansen, A. G.; Kuznetsov, A. M.; Boisen, A.; Wackerbarth, H.; Ulstrup, J. *J. Phys. Cond. Matter* **2003**, *15*, S1873–S1890.
(312) Gray, H. B.; Winkler, J. R. *Annu. Rev. Biochem.* **1996**, *65*, 537–561.
(313) Chernick, E. T.; Mi, Q.; Vega, A. M.; Lockard, J. V; Ratner, M. A.; Wasielewski, M. R. *J. Phys. Chem. B* **2007**, *111*, 6728–6737.
(314) Kurnikov, I. V.; Zusman, L. D.; Kurnikova, M. G.; Farid, R. S.; Beratan, D. N. *J. Am. Chem. Soc.* **1997**, *119*, 5690–5700.
(315) Likhtenstein, G. I.; Ishii, K.; Nakatsuji, S. *Photochem. Photobiol.* **2007**, *83*, 871–881.
(316) Likhtenshtein, G. I.; Pines, D.; Pines, E.; Khutorsky, V. *Appl. Magn. Reson.* **2009**, *35*, 459–472.
(317) Cannon, R. D. *Electron Transfer Reactions*; Butterworth and Co Ltd: England, **1980**.
(318) Marcus, R. A. *J. Chem. Phys.* **1956**, *24*, 966.
(319) Marcus, R. A. *Rev. Mod. Phys.* **1993**, *65*, 599–610.
(320) Marcus, R. A. *Annu. Rev. Phys. Chem.* **1964**, *15*, 155–196.
(321) Marcus, R. A.; Sutin, N. *Biochim. Biophys. Acta* **1985**, *811*, 265–322.
(322) Marcus, R. A. *J. Phys. Chem.* **1968**, *72*, 891–899.
(323) Hush, N. S. *J. Chem. Phys.* **1958**, *28*, 962.
(324) Fermi, E. *Nuclear Physics*; University of Chicago Press: United States of America, **1950**.
(325) Dirac, P. A. M. *Proc. R. Soc. Lond. A* **1927**, *114*, 243–265.
(326) Landau, I. *Phys. Sov. Union* **1932**, *2*, 46–51.
(327) Zener, C. *Proc. R. Soc. Lond. A* **1932**, *137*, 696–702.
(328) Marcus, R. A. *J. Electroanal. Chem.* **2000**, *483*, 2–6.
(329) Levich, V. G.; Dogonadze, R. R.; German, E. D.; Kuznetsov, A. M.; Kharkats, Y. I. *Electrochim. Acta* **1970**, *15*, 353–367.
(330) Efrima, S.; Bixon, M. *Chem. Phys. Lett.* **1974**, *25*, 34–37.
(331) Nitzan, A.; Jortner, J.; Rentzepis, P. M. *Proc. R. Soc. Lond. A* **1972**, *327*, 367–391.
(332) Kestner, N. R.; Logan, J.; Jortner, J. *J. Phys. Chem.* **1974**, *78*, 2148–2166.
(333) Costentin, C. *Chem. Rev.* **2008**, *108*, 2145–2179.
(334) Jortner, J. *J. Chem. Phys.* **1976**, *64*, 4860.
(335) DeVault, D. *Quantum Mechanical Tunneling in Biological Systems*; Cambridge University Press: Cambridge, United Kingdom, **1984**.
(336) Barbara, P. F.; Meyer, T. J.; Ratner, M. A. *J. Phys. Chem.* **1996**, *100*, 13148–13168.
(337) Cave, R. J.; Newton, M. D. *Chem. Phys. Lett.* **1996**, *249*, 15–19.
(338) Voityuk, A. A.; Rösch, N. *J. Chem. Phys.* **2002**, *117*, 5607.
(339) Wu, Q.; Van Voorhis, T. *Phys. Rev. A* **2005**, *72*, 024502.
(340) Hsu, C.-P. *Acc. Chem. Res.* **2009**, *42*, 509–518.
(341) Yeganeh, S.; Voorhis, T. Van. *J. Phys. Chem. C* **2010**, *114*, 20756–20763.
(342) Huang, J.; Kertesz, M. *Chem. Phys. Lett.* **2004**, *390*, 110–115.
(343) Huang, J.; Kertesz, M. *J. Chem. Phys.* **2005**, *122*, 234707.
(344) Voityuk, A. A. *Phys. Chem. Chem. Phys.* **2012**, *14*, 13789–13793.
(345) Voityuk, A. A. *J. Chem. Phys.* **2006**, *124*, 64505.
(346) Cave, R. J.; Newton, M. D. *J. Chem. Phys.* **1997**, *106*, 9213–9226.
(347) Voityuk, A. A. *J. Phys. Chem. C* **2013**, *117*, 2670–2675.
(348) Di Motta, S.; Di Donato, E.; Negri, F.; Orlandi, G.; Fazzi, D.; Castiglioni, C. *J. Am. Chem. Soc.* **2009**, *131*, 6591–6598.
(349) Koh, S. E.; Risko, C.; da Silva Filho, D. A.; Kwon, O.; Facchetti, A.; Brédas, J.-L.; Marks, T. J.; Ratner, M. A. *Adv. Funct. Mater.* **2008**, *18*, 332–340.
(350) Norton, J. E.; Brédas, J.-L. *J. Am. Chem. Soc.* **2008**, *130*, 12377–12384.

(351)   McMahon, D. P.; Troisi, A. *J. Phys. Chem. Lett.* **2010**, *1*, 941–946.

(352)   Masunov, A.; Tretiak, S.; Hong, J. W.; Liu, B.; Bazan, G. C. *J. Chem. Phys.* **2005**, *122*, 224505.

(353)   Cossi, M.; Barone, V. *J. Chem. Phys.* **2001**, *115*, 4708–4717.

(354)   Bakulin, A. A.; Rao, A.; Pavelyev, V. G.; van Loosdrecht, P. H. M.; Pshenichnikov, M. S.; Niedzialek, D.; Cornil, J.; Beljonne, D.; Friend, R. H. *Science* **2012**, *335*, 1340–1344.

(355)   Dewar, M. J. S.; Zoebisch, E. G.; Healy, E. F.; Stewart, J. J. P. *J. Am. Chem. Soc.* **1985**, *107*, 3902–3909.

(356)   Pople, J. A.; Beveridge, D. L.; Dobosh, P. A. *J. Chem. Phys.* **1967**, *47*, 2026.

(357)   Kawatsu, T.; Coropceanu, V.; Ye, A.; Bredas, J.-L. *J. Phys. Chem. C* **2008**, *112*, 3429–3433.

(358)   Ridley, J.; Zerner, M. *Theor. Chim. Acta* **1973**, *32*, 111–134.

(359)   Lemaur, V.; Steel, M.; Beljonne, D.; Brédas, J.-L.; Cornil, J. *J. Am. Chem. Soc.* **2005**, *127*, 6077–6086.

(360)   Kanai, Y.; Grossman, J. C. *Nano Lett.* **2007**, *7*, 1967–1972.

(361)   Kaduk, B.; Kowalczyk, T.; Van Voorhis, T. *Chem. Rev.* **2012**, *112*, 321–370.

(362)   Difley, S.; Van Voorhis, T. *J. Chem. Theory Comput.* **2011**, *7*, 594–601.

(363)   Liu, T.; Cheung, D. L.; Troisi, A. *Phys. Chem. Chem. Phys.* **2011**, *13*, 21461.

(364)   Few, S.; Frost, J. M.; Kirkpatrick, J.; Nelson, J. *J. Phys. Chem. C* **2014**, *118*, 8253–8261.

(365)   IUPAC. Compendium of Chemical Terminology, 2nd ed. (the "Gold Book"). Compiled by A. D. McNaught and A. Wilkinson. Blackwell Scientific Publications, Oxford (1997). XML on-line corrected version: http://goldbook.iupac.org (2006).

(366)   Cai, T.; Slebodnick, C.; Xu, L.; Harich, K.; Glass, T. E.; Chancellor, C.; Fettinger, J. C.; Olmstead, M. M.; Balch, A. L.; Gibson, H. W.; Dorn, H. C. *J. Am. Chem. Soc.* **2006**, *128*, 6486–6492.

(367)   Valencia, R.; Rodríguez-Fortea, A.; Poblet, J. M. *J. Phys. Chem. A* **2008**, *112*, 4550–4555.

(368)   Nagase, S.; Kobayashi, K. *Chem. Phys. Lett.* **1993**, *214*, 57–63.

(369)   Akasaka, T.; Kato, T.; Kobayashi, K.; Nagase, S.; Yamamoto, K.; Funasaka, H.; Takahashi, T. *Nature* **1995**, *374*, 600–601.

(370)   Campanera, J. M.; Bo, C.; Poblet, J. M. *Angew. Chem. Int. Ed.* **2005**, *44*, 7230–7233.

(371)   Alegret, N.; Salvadó, P.; Rodríguez-Fortea, A.; Poblet, J. M. *J. Org. Chem.* **2013**, *78*, 9986–9990.

(372)   Li, Q.-Z.; Zheng, J.-J.; Zhao, X. *J. Phys. Chem. C* **2015**, *119*, 26196–26201.

(373)   Feng, L.; Wakahara, T.; Nakahodo, T.; Tsuchiya, T.; Piao, Q.; Maeda, Y.; Lian, Y.; Akasaka, T.; Horn, E.; Yoza, K.; Kato, T.; Mizorogi, N.; Nagase, S. *Chem. Eur. J.* **2006**, *12*, 5578–5586.

(374)   Ishida, T.; Shinozuka, K.; Nogami, T.; Sasaki, S.; Iyoda, M. *Chem. Lett.* **1995**, *24*, 317–318.

375)   Nakamura, Y.; Takano, N.; Nishimura, T.; Yashima, E.; Sato, M.; Kudo, T.; Nishimura, J. *Org. Lett.* **2001**, *3*, 1193–1196.

(376)   Darwish, A. D.; Abdul-Sada, A. K.; Langley, G. J.; Kroto, H. W.; Taylor, R.; Walton, D. R. M. *J. Chem. Soc. Chem. Commun.* **1994**, 2133–2134.

(377)   Darwish, A. D.; Avent, A. G.; Taylor, R.; Walton, D. R. M. *J. Chem. Soc. Perkin Trans. 2* **1996**, 2079–2084.

(378)   Lu, X.; Xu, J.; He, X.; Shi, Z.; Gu, Z. *Chem. Mater.* **2004**, *16*, 953–955.

(379)   Li, F.-F.; Pinzón, J. R.; Mercado, B. Q.; Olmstead, M. M.; Balch, A. L.; Echegoyen, L. *J. Am. Chem. Soc.* **2011**, *133*, 1563–1571.

(380)   Wang, G.-W.; Liu, T.-X.; Jiao, M.; Wang, N.; Zhu, S.-E.; Chen, C.; Yang, S.; Bowles, F. L.; Beavers, C. M.; Olmstead, M. M.; Mercado, B. Q.; Balch, A. L. *Angew. Chem. Int. Ed.* **2011**, *50*, 4658–4662.

(381)   Kim, G.; Lee, K. C.; Kim, J.; Lee, J.; Lee, S. M.; Lee, J. C.; Seo, J. H.; Choi, W.-Y.; Yang, C. *Tetrahedron* **2013**, *69*, 7354–7359.

(382)   Meier, M. S.; Wang, G.-W.; Haddon, R. C.; Brock, C. P.; Lloyd, M. A.; Selegue, J. P. *J. Am. Chem. Soc.* **1998**, *120*, 2337–2342.

(383)   Lu, X.; Nikawa, H.; Tsuchiya, T.; Akasaka, T.; Toki, M.; Sawa, H.; Mizorogi, N.; Nagase, S. *Angew. Chem.* **2010**, *122*, 604–607.

(384)   Hammouri, M.; Jha, S. K.; Vasiliev, I. *J. Phys. Chem. C* **2015**, *119*, 18719–18728.

(385)   Yang, T.; Zhao, X.; Nagase, S. *Org. Lett.* **2013**, *15*, 5960–5963.

(386)   Osuna, S.; Houk, K. N. *Chem. Eur. J.* **2009**, *15*, 13219–13231.

(387)   Jemmis, E. D.; Manoharan, M.; Sharma, P. K. *Organometallics* **2000**, *19*, 1879–1887.

(388)   Goh, S.-K.; Marynick, D. S. *J. Comput. Chem.* **2001**, *22*, 1881–1886.

(389)   Miyaura, N.; Yamada, K.; Suzuki, A. *Tetrahedron Lett.* **1979**, *20*, 3437–3440.

(390)   Miyaura, N.; Suzuki, A. *J. Chem. Soc. Chem. Commun.* **1979**, 866–867.

(391)   Miyaura, N.; Suzuki, A. *Chem. Rev.* **1995**, *95*, 2457–2483.

(392) Suzuki, A. *Angew. Chem. Int. Ed.* **2011**, *50*, 6722–6737.
(393) Suzuki Reaction https://en.wikipedia.org/wiki/Suzuki_reaction.
(394) Nambo, M.; Noyori, R.; Itami, K. *J. Am. Chem. Soc.* **2007**, *129*, 8080–8081.
(395) Ikeda, A.; Kameno, Y.; Nakao, Y.; Sato, H.; Sakaki, S. *J. Organomet. Chem.* **2007**, *692*, 299–306.
(396) Adlhart, C.; Chen, P. *J. Am. Chem. Soc.* **2004**, *126*, 3496–3510.
(397) Tallarico, J. A.; Bonitatebus, P. J.; Snapper, M. L. *J. Am. Chem. Soc.* **1997**, *119*, 7157–7158.
(398) Anderson, D. R.; Hickstein, D. D.; O'Leary, D. J.; Grubbs, R. H. *J. Am. Chem. Soc.* **2006**, *128*, 8386–8387.
(399) Weskamp, T.; Schattenmann, W. C.; Spiegler, M.; Herrmann, W. A. *Angew. Chem. Int. Ed.* **1998**, *37*, 2490–2493.
(400) Huang, J.; Stevens, E. D.; Nolan, S. P.; Petersen, J. L. *J. Am. Chem. Soc.* **1999**, *121*, 2674–2678.
(401) Scholl, M.; Ding, S.; Lee, C. W.; Grubbs, R. H. *Org. Lett.* **1999**, *1*, 953–956.
(402) Dias, E. L.; Nguyen, S. T.; Grubbs, R. H. *J. Am. Chem. Soc.* **1997**, *119*, 3887–3897.
(403) Sanford, M. S.; Ulman, M.; Grubbs, R. H. *J. Am. Chem. Soc.* **2001**, *123*, 749–750.
(404) Sanford, M. S.; Love, J. A.; Grubbs, R. H. *J. Am. Chem. Soc.* **2001**, *123*, 6543–6554.
(405) Adlhart, C.; Hinderling, C.; Baumann, H.; Chen, P. *J. Am. Chem. Soc.* **2000**, *122*, 8204–8214.
(406) Adlhart, C.; Chen, P. *Helv. Chim. Acta* **2000**, *83*, 2192–2196.
(407) Vyboishchikov, S. F.; Bühl, M.; Thiel, W. *Chem. Eur. J.* **2002**, *8*, 3962–3975.
(408) Cavallo, L. *J. Am. Chem. Soc.* **2002**, *124*, 8965–8973.
(409) Aagaard, O. M.; Meier, R. J.; Buda, F. *J. Am. Chem. Soc.* **1998**, *120*, 7174–7182.
(410) Bernardi, F.; Bottoni, A.; Miscione, G. Pietro. *Organometallics* **2000**, *19*, 5529–5532.
(411) Adlhart, C.; Chen, P. *Angew. Chem. Int. Ed.* **2002**, *41*, 4484–4487.
(412) Stewart, I. C.; Benitez, D.; O'Leary, D. J.; Tkatchouk, E.; Day, M. W.; Goddard, W. A.; Grubbs, R. H. *J. Am. Chem. Soc.* **2009**, *131*, 1931–1938.
(413) Janse van Rensburg, W.; Steynberg, P. J.; Meyer, W. H.; Kirk, M. M.; Forman, G. S. *J. Am. Chem. Soc.* **2004**, *126*, 14332–14333.
(414) Urbina-Blanco, C. A.; Poater, A.; Lebl, T.; Manzini, S.; Slawin, A. M. Z.; Cavallo, L.; Nolan, S. P. *J. Am. Chem. Soc.* **2013**, *135*, 7073–7079.
(415) Hérisson, P. J.-L.; Chauvin, Y. *Makromol. Chem.* **1971**, *141*, 161–176.
(416) Kozuch, S.; Shaik, S. *Acc. Chem. Res.* **2011**, *44*, 101–110.
(417) Credendino, R.; Poater, A.; Ragone, F.; Cavallo, L. *Catal. Sci. Technol.* **2011**, *1*, 1287–1297.
(418) Poater, A.; Cavallo, L. *Beilstein J. Org. Chem.* **2015**, *11*, 1767–1780.
(419) Romero, P. E.; Piers, W. E. *J. Am. Chem. Soc.* **2007**, *129*, 1698–1704.
(420) van der Eide, E. F.; Piers, W. E. *Nat. Chem.* **2010**, *2*, 571–576.
(421) Poater, A.; Ragone, F.; Correa, A.; Cavallo, L. *Dalton Trans.* **2011**, *40*, 11066–11069.
(422) Cavallo, L.; Correa, A.; Costabile, C.; Jacobsen, H. *J. Organomet. Chem.* **2005**, *690*, 5407–5413.
(423) Poater, A.; Ragone, F.; Giudice, S.; Costabile, C.; Dorta, R.; Nolan, S. P.; Cavallo, L. *Organometallics* **2008**, *27*, 2679–2681.
(424) Poater, A.; Cosenza, B.; Correa, A.; Giudice, S.; Ragone, F.; Scarano, V.; Cavallo, L. *Eur. J. Inorg. Chem.* **2009**, 1759–1766.
(425) Parr, R. G.; Pearson, R. G. *J. Am. Chem. Soc.* **1983**, *105*, 7512–7516.
(426) O'Regan, B.; Grätzel, M. *Nature* **1991**, *353*, 737–740.
(427) Segura, J. L.; Martin, N.; Guldi, D. M. *Chem. Soc. Rev.* **2005**, *34*, 31–47.
(428) Preat, J. *J. Phys. Chem. C* **2010**, *114*, 16716–16725.
(429) Xu, J.; Wang, L.; Liang, G.; Bai, Z.; Wang, L.; Xu, W.; Shen, X. *Bull. Korean Chem. Soc.* **2010**, *31*, 2531–2536.
(430) Martín, N.; Sánchez, L.; Illescas, B.; Pérez, I. *Chem. Rev.* **1998**, *98*, 2527–2548.
(431) D'Souza, F.; Chitta, R.; Sandanayaka, A. S. D.; Subbaiyan, N. K.; D'Souza, L.; Araki, Y.; Ito, O. *J. Am. Chem. Soc.* **2007**, *129*, 15865–15871.
(432) Stranius, K.; Iashin, V.; Nikkonen, T.; Muuronen, M.; Helaja, J.; Tkachenko, N. *J. Phys. Chem. A* **2014**, *118*, 1420–1429.
(433) Illescas, B. M.; Martín, N. *J. Org. Chem.* **2000**, *65*, 5986–5995.
(434) Martín, N. *Chem. Commun.* **2006**, 2093–2104.
(435) Martín, N.; Pérez, I.; Sánchez, L.; Seoane, C. *J. Org. Chem.* **1997**, *62*, 5690–5695.
(436) Zhou, Z.; Magriotis, P. A. *Org. Lett.* **2005**, *7*, 5849–5851.
(437) Exciton https://en.wikipedia.org/wiki/Exciton.

(438)   Plasser, F.; Lischka, H. *J. Chem. Theory Comput.* **2012**, *8*, 2777–2789.

(439)   Luzanov, A. V.; Zhikol, O. A. *Int. J. Quantum Chem.* **2010**, *110*, 902–924.

(440)   Pinzón, J. R.; Gasca, D. C.; Sankaranarayanan, S. G.; Bottari, G.; Torres, T.; Guldi, D. M.; Echegoyen, L. *J. Am. Chem. Soc.* **2009**, *131*, 7727–7734.

(441)   Martínez, J. P.; Osuna, S.; Solà, M.; Voityuk, A. *Theor. Chem. Acc.* **2015**, *134*, 12.

(442)   Troisi, A. *Faraday Discuss.* **2013**, *163*, 377–392.

(443)   Yang, T.; Nagase, S.; Akasaka, T.; Poblet, J. M.; Houk, K. N.; Ehara, M.; Zhao, X. *J. Am. Chem. Soc.* **2015**, *137*, 6820–6828.

Appendix

Supporting Information

a. Chapter 4.1

1. Geometry Optimizations

The accurate localization of stationary points on the potential energy surface of the reaction under study is important to achieve reliable conclusions. We have carried out geometry optimizations in the gas phase for each structure reported in this chapter. However, the Bingel-Hirsch reaction takes place under some solvent environment; therefore, it is required to prove that our results are still valid. In order to do so, we have selected two transition states and monitored how energies and geometries for those structures change. Here the results at the COSMO(toluene)-BP86-D3(BJ)/TZP//BP86-D3(BJ)/DZP) level of theory in the case of geometries optimized in the gas phase (see in Table S1 the short "*solvent/gas*") and COSMO(toluene)-BP86-D3(BJ)/TZP//COSMO(toluene)-BP86-D3(BJ)/DZP) for geometries under solvent environment (short "*solvent/solvent*"):

Table S1 Comparison of electronic energies calculated at the geometry obtained in the gas phase against the geometry under solvent environment.

Structure	Approach	E_{electr} (kcal/mol)
$TS_{C2,1}$	*toluene / gas*	-19161.4
	toluene / toluene	-19161.8
$TS_{C23,o}$	*toluene / gas*	-19161.2
	toluene / toluene	-19161.5

Note: Geometrical comparisons between geometries optimized in the gas phase and in solution are reported in **Table S2**, but it is not included in this thesis because this table is large-sized. The conclusion attained from **Table S2** is that geometries are nearly identical.

2. Linear transit for transition states $TS_{C10,i}$ and $TS_{C17,14}$

In Figure S1 the linear transits (at gas-phase BP86-D3(BJ)/DZP level of theory) corresponding to the ring-closure step of the BH addition to La@C_{2v}-C_{82} is depicted for the attack on bonds **h** and **i**. The maximum points related to $TS_{C13,h}$ and $TS_{C10,i}$ are energetically and structurally very similar (absolute electronic energies are respectively -19082.81 and -19083.78 kcal/mol). The energy of $TS_{C13,h}$ after relaxation is -19082.46 kcal/mol; very close to the energy of the maximum point in the linear transit with the constrained distance d_2. We could not optimize the structure of $TS_{C10,i}$; however, since it is very similar to $TS_{C13,h}$, we decided to use the electronic, zero-point, entropy, and Gibbs energies of this latter to account for the energy barrier for the cyclopropanation on bond **i** from $I_{C10,i}$. Under the same analysis, we use all the results calculated for $TS_{C15,10}$ to report the energy barrier for the cyclopropanation on bond **14** from $I_{C17,14}$; since the maximum point in the linear transit related to $TS_{C17,14}$ matches the relaxed structure of $TS_{C15,10}$.
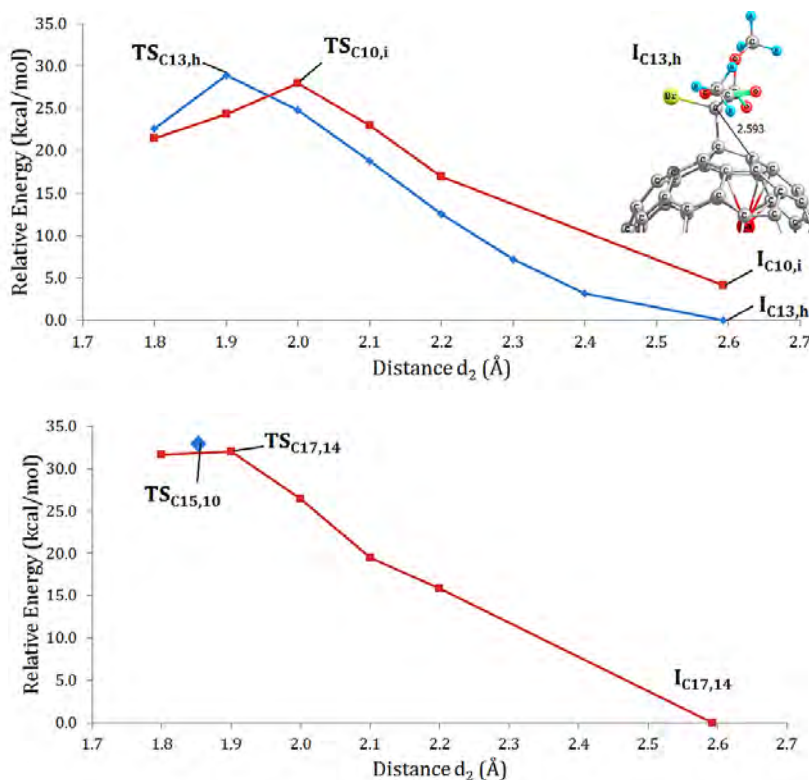
Figure S1 Linear transit for the cyclopropanation step of the Bingel-Hirsch addition to La@C_{2v}-C$_{82}$. It is schematized (top) the potential energy surface for the attack on bonds **h** and **i** involving the reaction sites C13 and C10, respectively. Similarly, bonds **10** and **14** related to carbon atoms C15 and C17 are also reported (bottom).

3. Movement of Lanthanum atom in the La@C_{2v}-C$_{82}$ cage

During the optimization process without constraints of all the structures under study the position of the lanthanum atom remained unaltered; except for the particular cases of **I**$_{C17,13}$ and **I**$_{C17,14}$. In Figure S2, the equilibrium position of the La atom for the intermediates **I**$_{C2,19}$, **I**$_{C3,19}$, **I**$_{C15,11}$, and **I**$_{C23,o}$ was deliberately moved in order to examine the movement of the La atom inside the cage. We observe that the equilibrium position of the La atom is indeed the position as experimentally determined for the pristine cage. However, in the case of **I**$_{C17,13}$ and **I**$_{C17,14}$, the movement of the La atom leads to a more stabilized structure, and we use these structures to determine the energy barriers of the reaction pathways related to the reaction site C17, as shown in Figure S3. More important, since the position of the La atom remained fixed during the optimization process for all the structures under study (i.e. all the optimized intermediates, transition states and products), we consider that our conclusions in the main manuscript are completely consistent and valid.
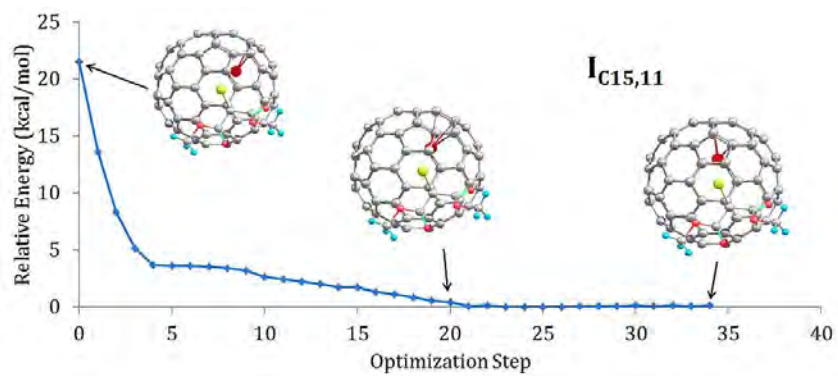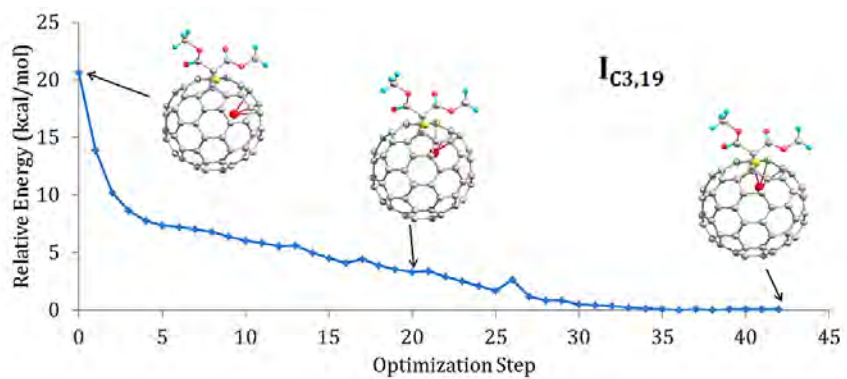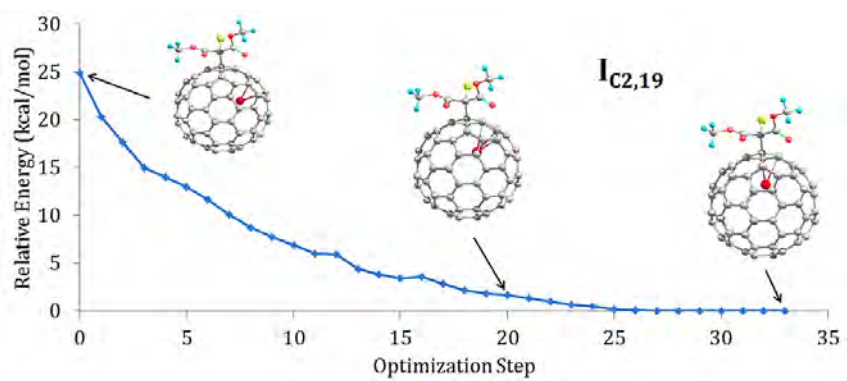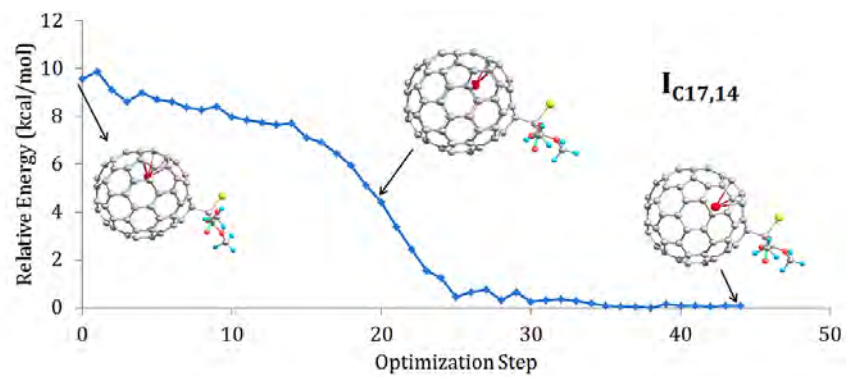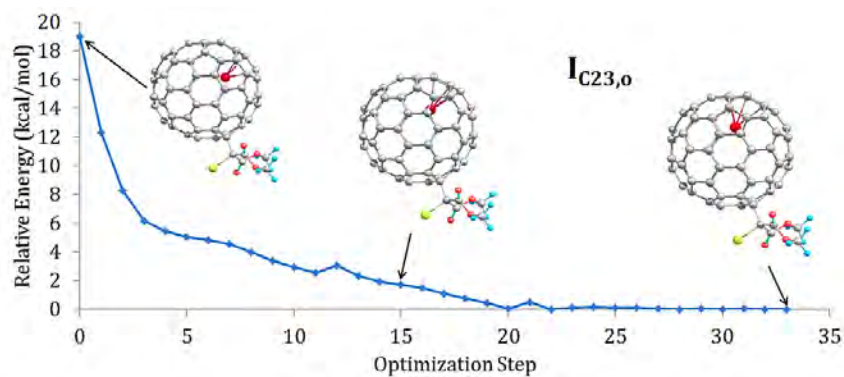
Figure S2 Geometry reoptimization of several intermediates. In the initial structure, the La atom (red atom) was intentionally moved from its equilibrium position.
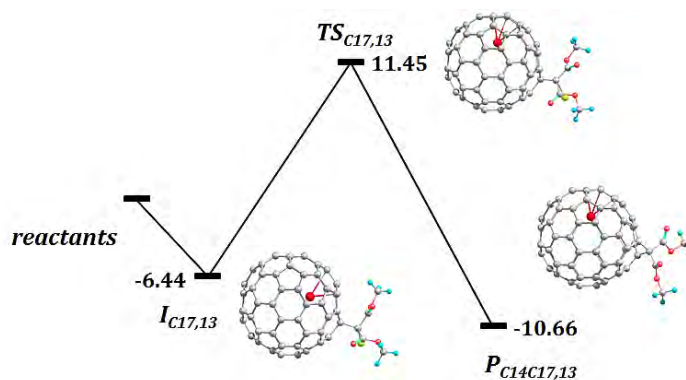

Figure S3 Gibbs energy profile for the Bingel-Hirsch addition to bond **13** through intermediate $I_{C17,13}$.

4. Fulleroids vs methanofullerenes

Table S3 Comparison in terms of Gibbs energies in toluene between fulleroids $P_{C\alpha C\beta,\gamma}$ and methanofullerenes *$P_{C\alpha C\beta,\gamma}$. $G_{relative}$ (in kcal/mol) is given as the difference between the absolute Gibbs energy in toluene G_{tol} for *$P_{C\alpha C\beta,\gamma}$ minus G_{tol} for $P_{C\alpha C\beta,\gamma}$; therefore a positive value means that the fulleroid structure is more stabilized. It was not possible to obtain both structures for the 35 available bonds in the La@C_{2v}-C_{82} cage.

γ	α	β	$G_{relative}$
6	9	12	4.02
7	12	13	5.20
8	8	11	2.03
11	15	18	6.40
13	14	17	5.34
15	20	21	3.75
17	23	24	3.23

19	2	3	11.05
b	18	22	3.32
c	3	6	5.98
d	1	4	2.41
e	4	5	3.24
g	9	9	-1.17
h	10	13	3.88
j	11	14	3.20
l	13	16	5.45
m	18	19	3.62
o	21	23	2.72

5. The activation strain model applied to other reaction pathways

Table S4 The activation strain model through several reaction pathways. Energies are given in eV at the COSMO(toluene)-BP86-D3(BJ)/TZP//BP86-D3(BJ)/DZP level of theory. Methanofulleroids ($\mathbf{P_{C\alpha C\beta,\gamma}}$) and methanofullerenes ($\mathbf{*P_{C\alpha C\beta,\gamma}}$) are reported to emphasize in the relative structural deformation and interaction of the reactants in those structures.

Structure	ASM		
	ΔE_{strain}	ΔE_{int}	ΔE
$I_{C2,1}$	1.91	-3.19	-1.27
$I_{C2,19}$	1.90	-3.17	-1.28
$I_{C12,6}$	2.24	-3.22	-0.98
$I_{C12,7}$	2.22	-3.19	-0.98
$I_{C12,10}$	2.27	-3.21	-0.94
$I_{C14,13}$	1.83	-2.80	-0.97
$I_{C18,b}$	1.94	-3.04	-1.10
$I_{C23,o}$	1.94	-3.14	-1.20
$I_{C23,p}$	1.94	-3.09	-1.15
$TS_{C2,1}$	2.90	-3.45	-0.55
$TS_{C2,19}$	2.75	-3.28	-0.53
$TS_{6C12,6}$	2.69	-3.04	-0.35

TS$_{C12,7}$	2.90	-3.02	-0.12
TS$_{C12,10}$	2.97	-3.02	-0.05
TS$_{C14,13}$	2.59	-3.00	-0.42
TS$_{C18,b}$	3.10	-3.35	-0.25
TS$_{C23,o}$	2.53	-3.07	-0.54
TS$_{C23,p}$	2.86	-2.94	-0.08
P$_{C1C2,1}$	5.57	-6.61	-1.03
***P$_{C2C3,19}$**	4.09	-4.81	-0.72
***P$_{C9C12,6}$**	4.19	-4.86	-0.66
P$_{C12C13,7}$	6.16	-6.99	-0.83
***P$_{C12C15,10}$**	4.14	-4.31	-0.17
***P$_{C14C17,13}$**	4.23	-4.78	-0.54
P$_{C18C22,b}$	5.86	-6.34	-0.49
***P$_{C21C23,o}$**	3.96	-4.68	-0.72
P$_{C22C23,p}$	5.91	-6.60	-0.69

6. Other optimized transition state structures related to profile type II or III

Table S5 Structural parameters for some selected transition states involved in reaction pathways classified as profile type II or III: distances d_n (Å) and angles θ and φ (degrees) as defined in Figure 1 of Chapter 4.1. $\Delta G_{tol}^{\ddagger}$ (kcal/mol) is the Gibbs energy barrier in toluene for the ring-closure step and it is given with respect to intermediate **I$_{C\alpha,\gamma}$**.

Cα	γ	Transition State (TS$_{C\alpha,\gamma}$)					
		d_1	d_2	d_3	θ	φ	$\Delta G_{tol}^{\ddagger}$
C12	**6**	1.535	1.810	2.828	90.6	178.2	17.55
C14	**j**	1.528	1.972	2.907	81.9	-42.0	11.86
	k	1.532	1.831	2.881	85.8	81.3	17.75
C18	**b**	1.535	1.760	2.914	95.2	-67.3	16.88
	o	1.532	1.875	2.828	87.0	-58.5	13.46
C23	**p**	1.538	1.763	2.900	95.1	64.5	21.49
	17	1.538	1.894	2.908	84.6	164.5	15.15

b. Chapter 4.2

Construction of Single-Walled Carbon Nanotubes for Quantum Computational modeling

nonFLCC models

Note: **Figure S1** is included as **Figure 1.15** of Section 1.3 in the current thesis.

Benzyne cycloaddition to the nonFLCC (9,0)-SWCNTs vs the FLCC model

The construction of structures for quantum modeling may have an impact on structural and electronic properties of the systems under study; to be precise, in order to build a SWCNT, it is computationally efficient and practical to make use of periodic-boundary conditions to eliminate interactions within neighboring replicas. Three periodic structures can be described for armchair SWCNTs by taking advantage of the Clar sextet theory. They are Kekulé, incomplete, and complete Clar networks. Chemical and electronic structures periodically oscillate as the tube is extended. The structural oscillation brings about match/mismatch of the benzene network for the armchair SWCNTs. Moreover, finite-length models based on the Clar sextet theory (FLCC) of SWCNTs are useful tools to perform high-level-of-theory calculations for such large structures. Advantages by using FLCC are (i) electronic properties of SWCNTs are uniform and consistent and (ii) there is a fast and monotonic convergence of the electronic properties to the bulk. As the length of the SWCNT is increased, the value of the band gap becomes invariable (within a value of 0.1 eV or less), and convergence is reached. The convergence of this electronic property is faster when a FLCC model is used; that is, it is required less unit cells to construct a suitable model for SWCNTs. Accordingly, not only is the diameter important to construct SWCNTs to perform quantum modeling, but the length also plays a role in the chemical reactivity.
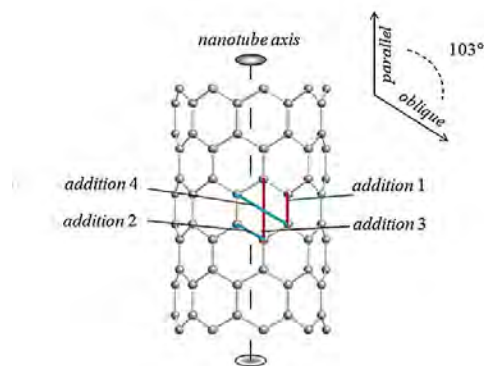

Figure S2 Possible benzyne cycloadditions to the nonFLCC (9,0)-SWCNT.

In this section we aim to compare the study of the benzyne cycloaddition to the nonFLCC (9,0)-SWCNT with its analogous FLCC model. Figure S2 shows the different additions of benzyne to the nonFLCC (9,0)-SWCNT. However, it is important to point out that the ground state in the nonFLCC model is the quintet state with the HOMO electrons localized at the nanotube edges. This difference in electronic structure has an impact on the chemical reactivity; in fact, Table S1 compares the reaction energies of some nonFLCC structures with those ones of FLCC, as calculated in terms of electronic energy at the BP86-D_2/DZP level of theory in the gas phase.

Table S1 Reaction energies ΔE_{react} (kcal/mol) for different structures

obtained with the nonFLCC and the FLCC models of (9,0)-SWCNT.

Structure	ΔE_{react} nonFLCC	ΔE_{react} FLCC
RC$_{ds}$	-19.1	-20.0
TS$_{(4+2)\text{-}p}$	-14.3	-13.1
P$_{(4+2)\text{-}p}$	-69.6	-63.8
TS$_{666\text{-}6}$	-7.4	-8.7
P$_{(2+2)\text{-}o}$	-56.6	-55.3
P$_{(2+2)\text{-}p}$	-52.8	-62.5

Observe that the results obtained with the nonFLCC model are in good agreement with the similar ones of FLCC for reactant complex and transition state structures. Nonetheless, the reaction energies calculated for the (4+2) and (2+2) adducts introduce uncertainty on the appropriate model to use; mainly due to the energy stability of the (2+2) adducts with FLCC is inverted as compared to the analogous of nonFLCC. To solve this predicament, we decided to extend the nanotube length from 3 to 6 unit cells; results are given in Table S2.

Table S2 Reaction energies ΔE_{react} (kcal/mol) for the (2+2) and (4+2) adducts obtained with nonFLCC and the FLCC models. $|\Delta\Delta E_{react}|$ is the absolute difference (kcal/mol) between the ΔE_{react} calculated with 3 and 6 cells.

Structure	nonFLCC 3 cells ΔE_{react}	nonFLCC 6 cells ΔE_{react}	$|\Delta\Delta E_{react}|$	FLCC 3 cells ΔE_{react}	FLCC 6 cells ΔE_{react}	$|\Delta\Delta E_{react}|$
P$_{(2+2)\text{-}p}$	-52.8	-57.0	4.1	-62.8	-62.6	0.1
P$_{(2+2)\text{-}o}$	-56.6	-55.8	0.9	-56.2	-55.7	0.5
P$_{(4+2)\text{-}p}$	-69.6	-66.7	2.9	-66.0	-66.5	0.5

It is concluded from Table S2 that a FLCC model is indeed a more suitable model to study chemical reactivity since consistent results can be attained with a reduced number of unit cells; this is certainly a computational advantage. Moreover, observe that Tables S1 and S2 demonstrate that the (4+2) addition of benzyne to the nonFLCC (9,0)-SWCNT through the parallel position is thermodynamically and kinetically favored; which resemble the conclusion obtained in this thesis.

Part I

Benzyne cycloaddition to C_{60}

In Chapter 4.2, Figure 1 is discussed and supported with additional information which is explained in this section. In this regard, the initial interactions between benzyne and C_{60} are schematized in Figure S3 as follows.
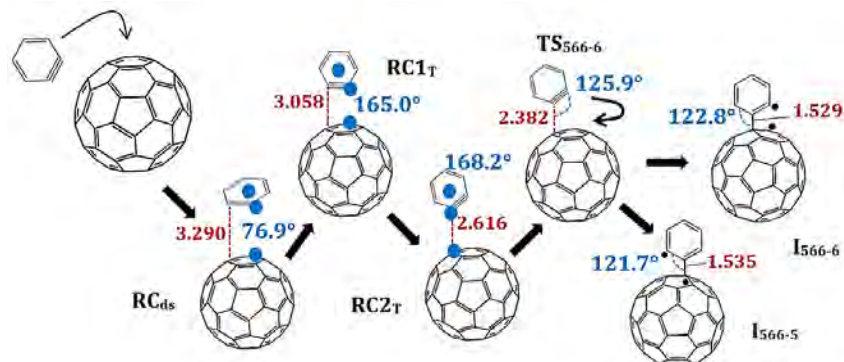

Figure S3 Schematic representation of the initial interactions between benzyne and C_{60} leading to the formation of a biradical singly-bonded intermediate. Relevant distances in Å (in red) and angles in degrees are reported (in blue).
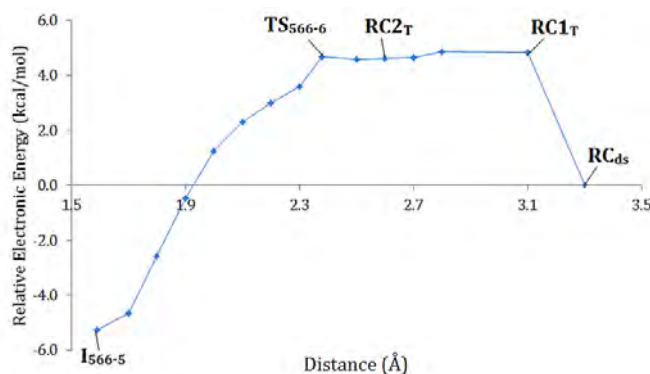
Figure S4 Formation of a biradical singly-bonded intermediate in terms of electronic energy in the gas phase as a function of the distance between benzyne and C_{60} (see Fig. S3 for details).

We determined several structures characterized to be stationary points on the PES-BC (see RC_{ds}, RC_{1T}, and RC_{2T} in Figure S3). These structures resemble a ball-shaped conjugated system in which a convex interaction between the curved surface of C_{60} and benzyne is the main noncovalent interaction. We distinguish two arrangements of benzyne with respect to the fullerene surface, RC_{ds} and R_{CT}; subscripts *ds* and *T* standing for displaced sandwiched and T-shaped configurations. In RC_{ds} the aryne triple bond is facing a 6-MR of C_{60} adjacent to a [5,6] bond. The RC_{ds}, RC_{1T}, and RC_{2T} structures present small imaginary frequencies related to small rotations of the benzyne unit. The linear transit schematized in Figure S4 shows the energy profile following the initially formed structures in terms of electronic energy in the gas phase at the BP86-D$_2$/DZP level of theory as a function of the distance between benzyne and C_{60} (see red labels in Figure S3). Observe the flatness of the potential energy surface from 3.1 to 2.4 Å. Because of the flatness of the PES-BC in this initial stage of the reaction, it was not possible to fully certify whether the small imaginary frequencies of the different reactant complexes have to be attributed to numerical noise or they correspond to true TSs. The generation of these reactant complexes is energetically favourable but when one considers the Gibbs energy their formation

is endergonic. Moreover, other stationary points may be characterized with similar energy and structural properties as RC_{ds}, RC_{1T}, and RC_{2T}. For that all these reasons, in Chapter 4.2 we mainly focus on the maximum-energy first-order saddle-point structure, TS_{566-6}, which corresponds to the TS leading to a biradical intermediate structure.

Open vs closed cage

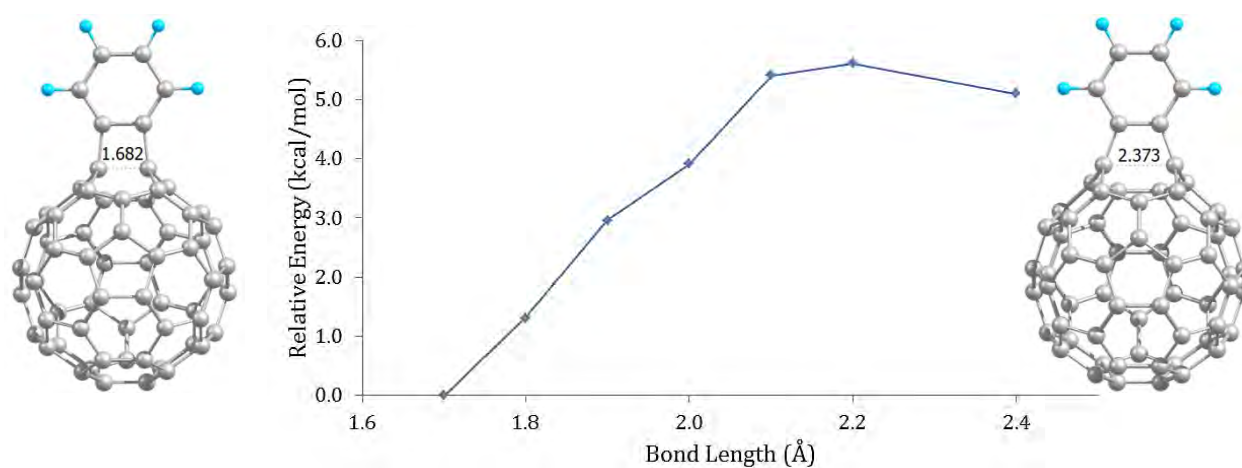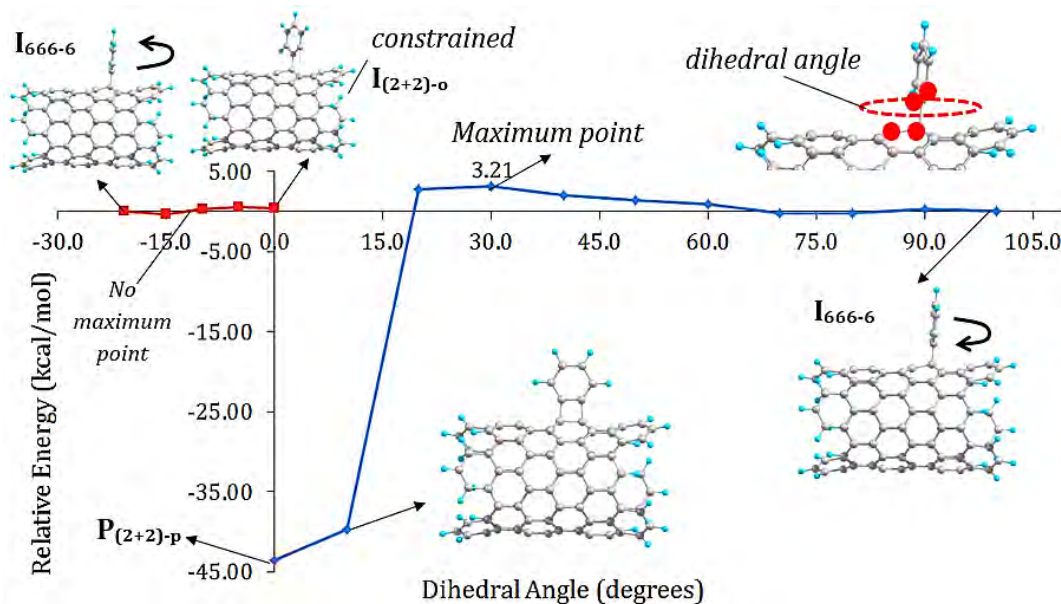**Figure S5** Relative electronic energy in the gas phase at the BP86-D$_2$/DZP as a function of the [5,6] C–C bond length in the (2+2) adduct.

Part II

Benzyne cycloaddition to SWCNTs and the curvature effect

Scanning the potential energy surface around the (2+2) and (4+2) transition states formed between benzyne and the FLCC (9,0)-SWCNT

Figure S6 Rotation of benzyne in the biradical singly-bonded intermediate I_{666-6} in terms of electronic energy in the gas phase as a function of the dihedral angle defined above in the plot (in red). From I_{666-6}, benzyne can be rotated toward the parallel (blue line) or the oblique position (red line).
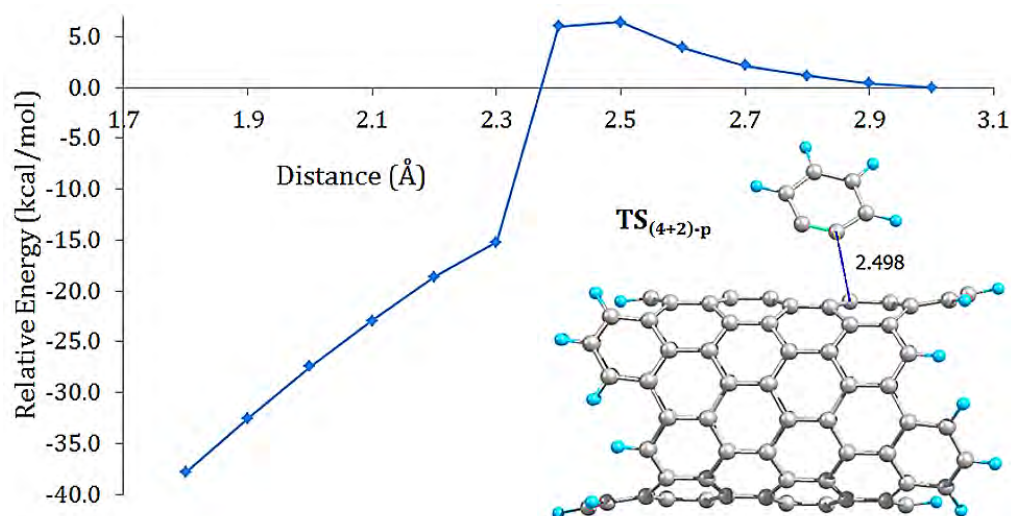
Figure S7 Linear transit for the concerted transition state for the (4+2) benzyne cycloaddition to (9,0)-SWCNT. Relative energy is given in terms of electronic energy in the gas phase at the BP86-D_2/DZP level of theory. The monitored distance is also depicted in the Figure.

Benzyne cycloaddition to non-benzenoid centers on FLCC models
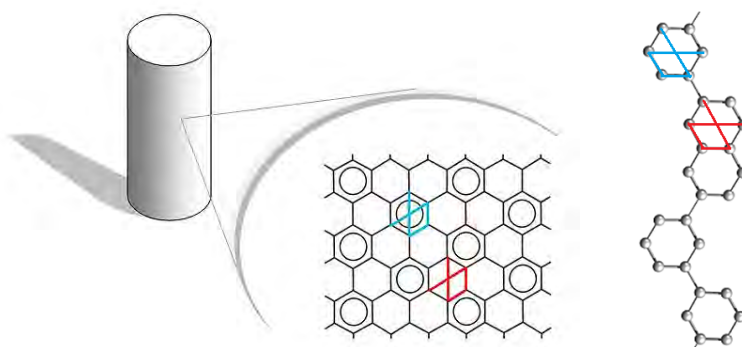
Figure S8 Benzyne cycloadditions to FLCC SWCNTs. Blue-colored lines
represent benzenoid centers, the red ones non-benzenoid centers.

Aromaticity provides stability to certain types of conjugated systems due to the nature of molecular orbitals. Complete Clar networks are fully or almost fully benzenoid structures, therefore they are more stable than their counterpart Kekulé structure. Therefore, it is expected that the benzyne addition to non-benzenoid centers breaks down two aromatic rings at once; thus decreasing the energy stability of the resulting adduct. The Clar networks of the nanotubes with chiral index (13,0) contain non-benzenoid centers; and Table S3 accounts for the differences in chemical reactivity as compared to benzenoid centers for the (13,0)-SWCNT (reaction energies in Table S3 are calculated from electronic energies at the BP86-D$_2$/DZP level of theory in the gas phase).

Table S3 Reaction energies ΔE_{react} (kcal/mol) for different structures
obtained considering the non-benzenoid and benzenoid centers in (13,0)-SWCNT.

Structure	ΔE_{react} non-benzenoid	ΔE_{react} benzenoid
RC$_{ds}$	-20.1	-20.9
TS$_{(4+2)-p}$	-12.4	-12.8
P$_{(4+2)-p}$	-56.4	-55.9
TS$_{666-6}$	-4.8	-6.7
P$_{(2+2)-o}$	-44.5	-47.8
P$_{(2+2)-p}$	-46.2	-51.4

See that the results obtained with the non-benzenoid center of (13,0)-SWCNT are in good agreement with those of the benzenoid center for all the structures reported in Table S3; except for the adduct (2+2) in parallel position, in which the non-benzenoid center gives a 5.2 kcal/mol more destabilized product. However, Table S3 demonstrates that the (4+2) addition of benzyne to the non-benzenoid center of (13,0)-SWCNT through the parallel position is thermodynamically and kinetically favored; which resemble the conclusion obtained in this thesis.

HOMO-LUMO orbital energies of reactants in TS

Table S4 HOMO and LUMO absolute energies in kcal/mol for
interacting fragments in the first TS structure of the benzyne cycloaddition.

fragment	TS$_{666-6}$; (2+2) BC		TS$_{(4+2)-p}$; (4+2) BC	
	HOMO	LUMO	HOMO	LUMO
benzyne	-0.26	-0.15	-0.26	-0.14
(8,0)-SWCNT	-0.21	-0.16	-0.21	-0.16

fragment	TS$_{666-6}$; (2+2) BC		TS$_{(4+2)-p}$; (4+2) BC	
	HOMO	LUMO	HOMO	LUMO
benzyne	-0.26	-0.16	-0.26	-0.15
(18,0)-SWCNT	-0.21	-0.16	-0.21	-0.16

c. Chapter 5.1
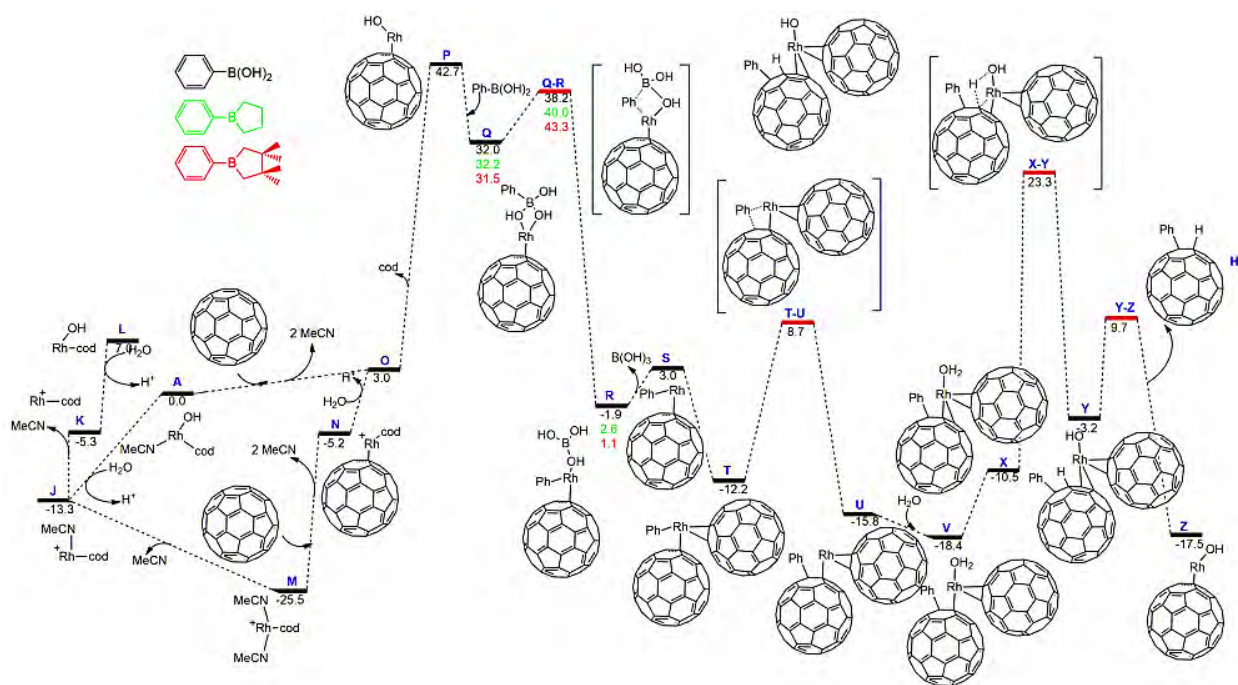
Figure S1 Alternative reaction pathways for the addition of phenyl groups or its derivatives to fullerene (C_{60}) catalyzed by rhodium (energies in kcal/mol).

d. Chapter 5.2

Steric Maps

The buried volume and the steric maps have been calculated on the NHC ligand as in the DFT optimized complexes. The points in space defining the steric map were located with the *SambVca* package. This program analyzes the first coordination sphere around the metal, which is the place where catalysis occurs. It is normally used to calculate the buried volume of a given ligand, which is a number that quantifies the amount of the first coordination sphere of the metal occupied by this ligand. Cavallo and coworkers modified *SambVca* to understand how the ligand is distributed around the metal, which is the shape of the reactive pocket. To build the steric maps reported in Figure 3 of Chapter 5.2, the optimized geometry of the complexes under analysis has been placed with the Ru center at the origin, with the Ru-PPh$_3$ aligned along the z-axis at positive z values. After this alignment step the Ru and all the other ligands except the NHC have been removed, and the first coordination sphere around the metal is analyzed. This sphere, of radius R, is sectioned by a regular 3D cubic mesh of spacing s, which defines cubic voxels v. The distance between the center of each voxel with all the atoms in the ligand is tested to check if any of the atoms is within a van der Waals distance from the center of the examined voxel. If no atom is within a van der Waals distance, the examined voxel is marked as a free voxel. Otherwise, the examined voxel is marked as buried. After all the voxels in the first coordination sphere have been marked as free or buried, for each (x,y) point within the first coordination sphere the program scans the sphere from the top (i.e. away from the ligand) to find at which z value there is the first buried voxel). This procedure results in a surface, defined as S(x,y) = zB, which represents the surface of the ligand that is exposed towards the incoming reactants. In other words, this S(x,y) = zB surface defines the shape of the reactive pocket. Positive values of zB indicate that the ligands protrude in the z > 0 half-sphere, which is the half-sphere where the reacting groups are placed. Finally, the maps are a simple 2D isocontour representation of the interaction surface S(x,y) = zB. In this work, the radius R of the sphere around the metal center was set to 3.5 Å, while for the atoms we adopted the Bondi radii scaled by 1.17, and a mesh of 0.1 Å was used to scan the sphere for buried voxels.

Conceptual DFT

Bearing conceptual DFT, the electrophilicity of the complexes is evaluated as the Parr electrophilicity index shown in eq. S1.

$$\omega = \frac{\mu^2}{2\eta} \quad S1$$

where μ and η are the chemical potential and the molecular hardness, respectively. In the framework of DFT, μ and η for an N-electron system with total electronic energy E are defined as the first and second derivatives of the energy with respect to N at a fixed external potential. In numerical applications, μ and η are calculated with the finite difference formulas of eq. S2, which are based on Koopmans' approximation,

$$\mu \cong \frac{1}{2}(\varepsilon_L + \varepsilon_H) \quad ; \quad \eta \cong \frac{1}{2}(\varepsilon_L - \varepsilon_H) \quad S2$$

where ε_H and ε_L are the HOMO and LUMO energies, respectively. Over the last years, conceptual DFT has been used to explain the reactivity pattern and, in particular, the regioselectivity in chemical reactions.

Table S1 Computed electronic properties of species **I** and **II** for the considered Ru-complexes **A-C**: q = natural population analysis charges (in electrons); and ω = Parr electrophilicity index (in kcal/mol).

Complex	q (Ru)		q (C_{NHC})		ω	
	I	**II**	**I**	**II**	**I**	**II**
A	-0.350	-0.052	0.450	0.526	166.2	159.5
B	-0.372	-0.036	0.404	0.476	179.3	180.0
C	-0.360	-0.054	0.462	0.537	181.1	172.8

Focusing on the electronic properties, it can be showed that the Ru-based catalyst bearing a para-methoxy substituted SIPr ligand (SIPrOMe) is catalytically more efficient when compared with the SIPr analogue thanks to the increased electron density on the SIPrOMe that makes it a better electron donor to Ru metal than the SIPr analogue. This feature of the NHC ligand is essential for the stabilization of the metallacycle intermediate. Having these insights on hand, we performed a natural population analysis to investigate the electron density on the Ru atom (q(Ru)) and on the carbenic C atom (q (CNHC)) for the studied Ru-complexes **A-C** (see Table S1). To sum up, the charge differences are only around 0.01 e^-, there is not a clear trend here. Further, bearing the expected electron-withdrawing capacity of the C_{60} group, the predicted more negative charge on the Ru metal for complexes **B** and **C** (-0.372 and -0.360 e^-, respectively) than **A** (-0.350 e^-) is not valid. Additionally, the calculated q(CNHC) does not follow a trend either, with a difference of about 0.05 e^- for species **I** and **II**. The ease electron donation of the NHC should be translated into a higher stability of the corresponding metallacycle.

e. Chapter 6.1

1. Computational Methods. Molecular Dynamics Simulations

Substrate parameters for the MD simulations were generated within the ANTECHAMBER module of AMBER 12 using the general AMBER force field (GAFF), with partial charges set to fit the electrostatic potential generated at the HF/6-31G(d) level by the RESP model. The charges were calculated according to the Merz-Singh-Kollman scheme using Gaussian 09. Each TPA-C_{60} isomer is immersed in a pre-equilibrated truncated octahedral box of benzonitrile and THF molecules with an internal offset distance of 10 Å, using the LEAP module. This resulted in the addition of around 150 solvent molecules. All systems were neutral, and no explicit counterions were added. A two-stage geometry optimization approach was performed. First, a short minimization of the solvent molecules positions, with positional restraints on solute by a harmonic potential with a force constant of 500 kcal mol^{-1} Å^{-2} was done. The second stage was an unrestrained minimization of all the atoms in the simulation cell. Then, the systems were gently heated for 50 ps, incrementing the temperature from 0 to 300 K under constant-volume, periodic-boundary conditions and the particle-mesh Ewald approach to introduce long range electrostatic effects. For these steps, an 8 Å cutoff was applied to Lennard-Jones and electrostatic interactions. Bonds involving hydrogen were constrained with the SHAKE algorithm. Harmonic restraints of 10 kcal mol^{-1} were applied to the solute, and the Langevin equilibration scheme is used to control and equalize the temperature. The time step was kept at 1 fs during the heating stages, allowing potential inhomogeneities to self-adjust. Each system is then equilibrated for 50 ps with a 2 fs timestep at a constant pressure of 1 atm. Finally, a 100 ps unrestrained MD trajectory at constant pressure (1 atm) and temperature (300 K) was collected and analyzed using the PTRAJ module in AMBER.

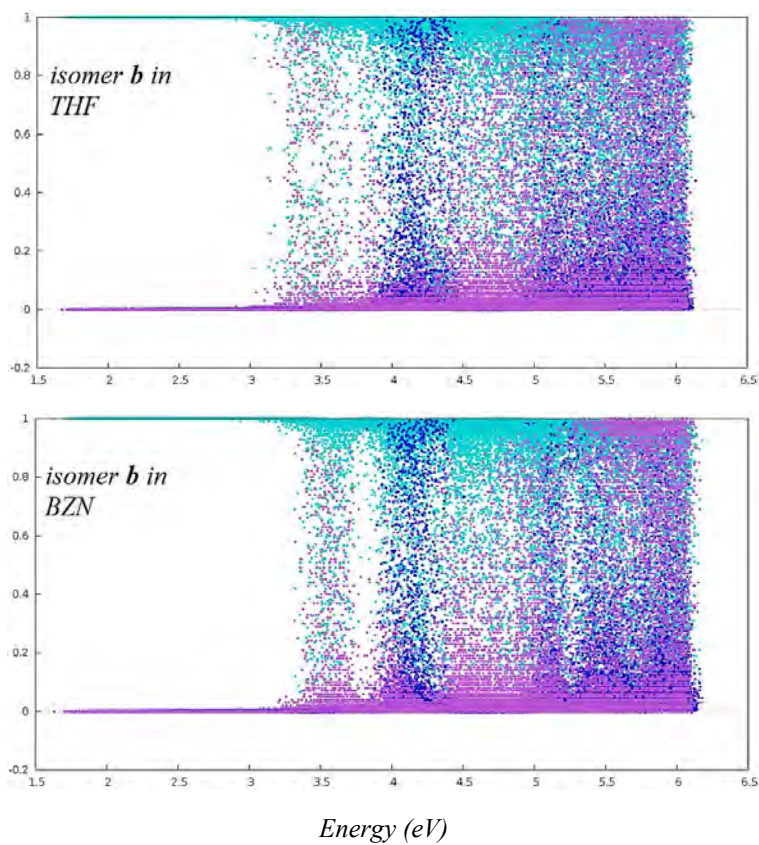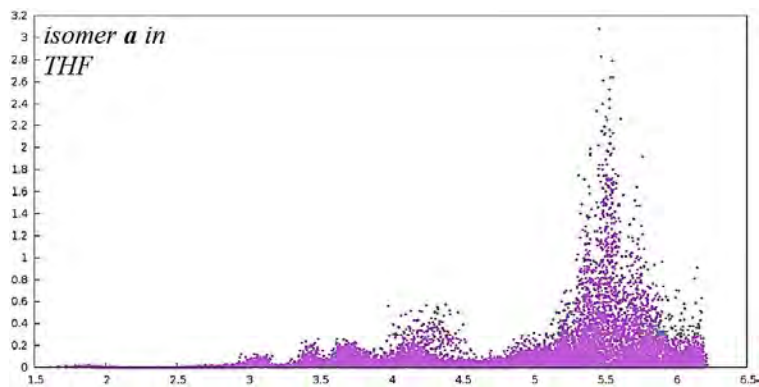### 2. Preliminary study at the ZINDO/CIS level of theory including solvent effects
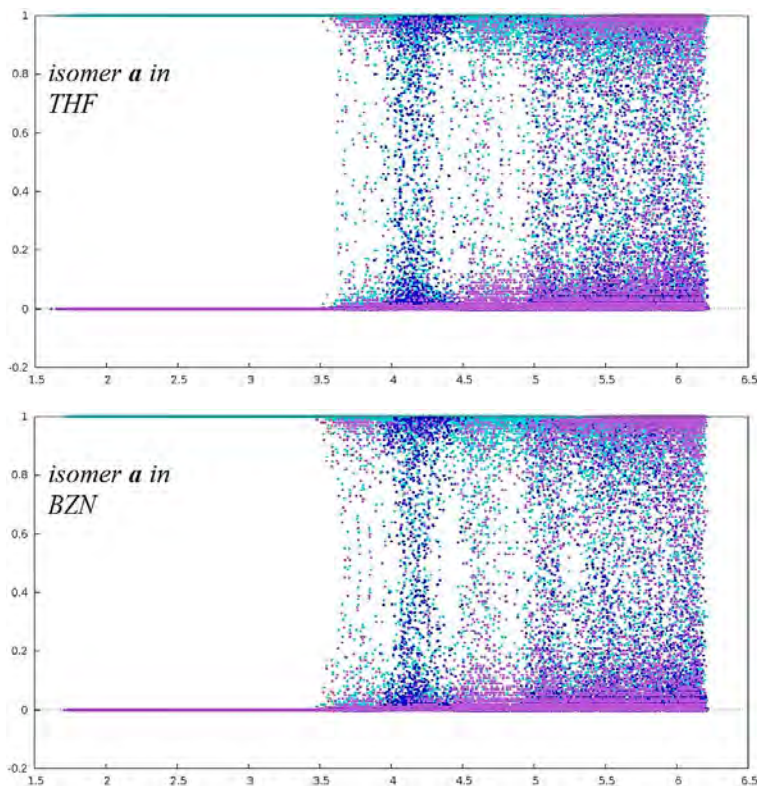
Energy (eV)

Figure S1 Distribution of $X_{ii}(F_{C60})$ (cyan), $X_{ii}(F_{TPA})$ (deep blue) and Δq (purple) as a function of the excitation energy. Top, results for isomer **a** in tetrahydrofuran (THF) and benzonitrile (BZN) as the solvent; bottom, results for isomer **b** also in THF and BZN.
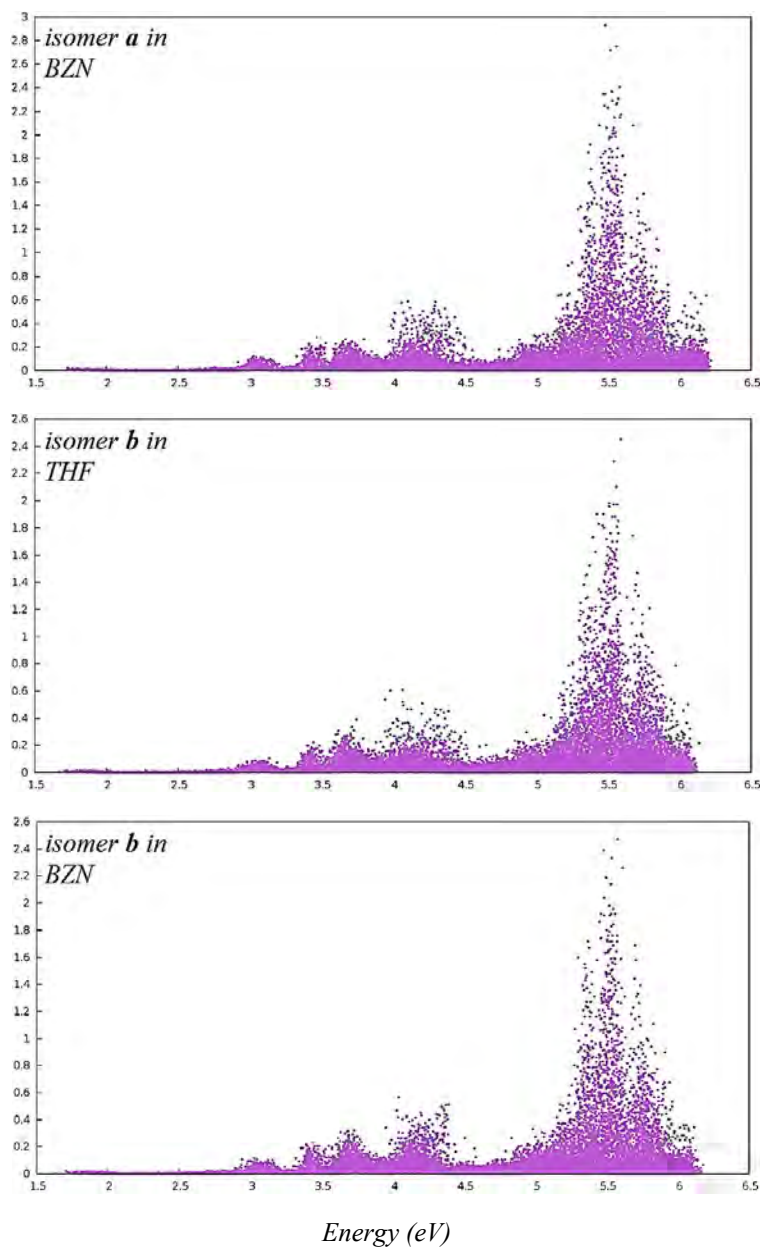
Figure S2 Oscillator strength as a function of the excitation energy.
Top, results for isomer **a** in tetrahydrofuran (THF) and benzonitrile (BZN)
as the solvent; bottom, results for isomer **b** also in THF and BZN.

Discussion. Figure S1 and S2 show results obtained at the ZINDO/CIS level of theory in a polarizable medium. Tetrahydrofuran (THF, ε = 7.43) and the relatively more polar benzonitrile (BZN, ε = 25.59) were the tested solvents. As shown in Figure S1 by visual inspection, when comparing the results calculated for isomer **a**, it is observed that the quantities X_{ii} and Δq calculated in THF and BZN are nearly the same. A similar conclusion can be reached for the results corresponding to isomer **b**. Not only that, the distribution of the oscillator strength for each calculated electronic transition remains practically unchanged when comparing the THF and BZN results, either for isomer **a** or **b**. In view of these observations we infer that, even though it is a very different approach, TD-DFT calculations in lack of a polarizable medium are still valid for a qualitative description of electronically excited states as presented in the present contribution.

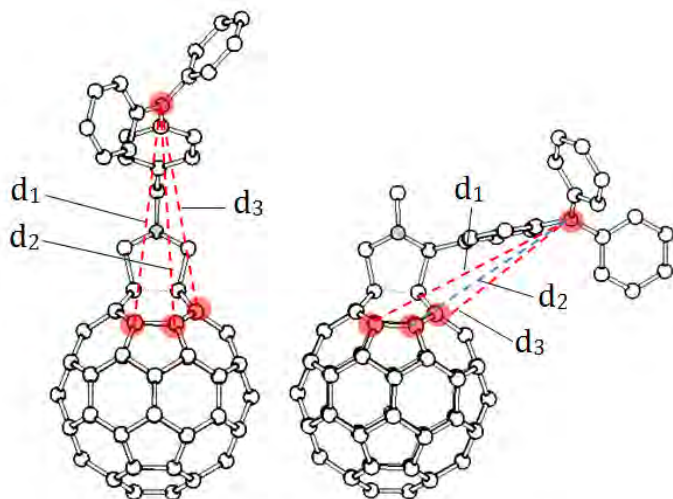### 3. Geometrical parameters of TPA-C$_{60}$

Figure S3 Three different lengths that report the distance between the TPA center and the fullerene surface. The longer d_i the farer the TPA fragment. (Hydrogen atoms are omitted).
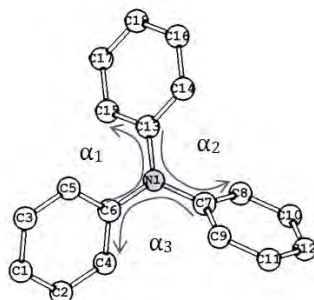

Figure S4 Three different dihedral angles that report planarity of TPA. A planar TPA is given by $\alpha_1=\alpha_2=\alpha_3=0°$. Curved arrows show how the dihedral angle is constructed; for instance, C6, N1, C13 and C15 forms α_1 in that order. (Hydrogen atoms are omitted).

Table S1 Geometrical parameters to account for the distance (in Å) between the TPA center and the fullerene surface and planarity of TPA (dihedral angles in degrees). Structure 0 refers to the geometry optimized with no constraints at the B3LYP/6-31G* level of theory.

			Isomer **a**			
Structure	d_1	d_2	d_3	α_1	α_2	α_3
0	8.07	8.04	8.04	44	42	40
1	7.91	7.80	7.84	46	42	25
2	7.39	7.44	7.66	54	59	26
3	7.86	7.81	7.76	61	48	31
4	8.34	8.61	8.50	36	51	76
5	8.53	8.15	7.93	45	48	48
6	7.69	7.65	7.84	32	57	41
7	7.69	7.96	8.07	43	26	33
8	7.56	7.63	7.86	53	43	37
9	8.09	8.31	8.32	67	52	18
10	7.84	7.85	7.94	68	43	50
			Isomer **b**			
Structure	d_1	d_2	d_3	α_1	α_2	α_3
0	8.10	6.86	6.14	42	43	39
1	7.54	6.33	5.70	48	35	43
2	7.97	6.79	5.97	47	69	14
3	8.33	7.13	6.29	55	35	40
4	8.17	7.06	6.21	48	62	42
5	7.78	6.60	5.89	33	56	46
6	7.92	6.74	5.98	36	49	52
7	7.84	6.59	5.62	40	24	67
8	8.06	6.89	5.97	48	60	62
9	7.82	6.62	5.87	68	15	91
10	7.39	6.12	5.42	34	35	64

Table S2 Variation of geometrical parameters as compared to Structure 0.
For example, Δd_2 for structure 6 in isomer **a** is equal to the difference between
d_2 in structure 6 of isomer **a** and d_2 in structure 0 of isomer **a**.

Isomer **a**						
Structure	Δd_1	Δd_2	Δd_3	$\Delta \alpha_1$	$\Delta \alpha_2$	$\Delta \alpha_3$
0	0.00	0.00	0.00	0	0	0
1	-0.16	-0.24	-0.20	2	0	-15
2	-0.68	-0.60	-0.38	10	17	-14
3	-0.21	-0.23	-0.28	17	6	-9
4	0.27	0.57	0.46	-8	9	36
5	0.46	0.11	-0.11	1	6	8
6	-0.38	-0.39	-0.20	-12	15	1
7	-0.38	-0.08	0.03	-1	-16	-7
8	-0.51	-0.41	-0.18	9	1	-3
9	0.02	0.27	0.28	23	10	-22
10	-0.23	-0.19	-0.10	24	1	10
Isomer **b**						
Structure	Δd_1	Δd_2	Δd_3	$\Delta \alpha_1$	$\Delta \alpha_2$	$\Delta \alpha_3$
0	0.00	0.00	0.00	0	0	0
1	-0.56	-0.53	-0.44	6	-8	4
2	-0.13	-0.07	-0.17	5	26	-25
3	0.23	0.27	0.15	13	-8	1
4	0.07	0.20	0.07	6	19	3
5	-0.32	-0.26	-0.25	-9	13	7
6	-0.18	-0.12	-0.16	-6	6	13
7	-0.26	-0.27	-0.52	-2	-19	28
8	-0.04	0.03	-0.17	6	17	23
9	-0.28	-0.24	-0.27	26	-28	52
10	-0.71	-0.74	-0.72	-8	-8	25

*isomer **a**, arithmetic mean = -0.12 ; standard deviation σ = 0.31*
*isomer **b**, arithmetic mean = -0.21 ; standard deviation σ = 0.28*
calculated taking into account all Δd_i

Table S3 Variation of geometrical parameters of isomer **b** as compared to Structure 0 of isomer **a**. Example given, dd_2 for structure 6 is equal to the difference between d_2 in structure 0 of isomer **a** and d_2 in structure 6 of isomer **b**.

Structure	dd_1	dd_2	dd_3
0	-0.03	1.18	1.90
1	0.53	1.71	2.34
2	0.10	1.25	2.07
3	-0.26	0.91	1.75
4	-0.10	0.98	1.83
5	0.29	1.44	2.15
6	0.15	1.30	2.06
7	0.23	1.45	2.42
8	0.01	1.15	2.07
9	0.25	1.42	2.17
10	0.68	1.92	2.62

arithmetic mean = 1.23 ; *standard deviation* σ = 0.86
calculated with all dd_i, except for structure 0

f. Chapter 6.2

Table S1 Franck-Condon excitation energies *Ex* in *eV*, oscillator strengths *f*, and dipole moments μ in debye for the twenty lowest-energy excited states as calculated through time-dependent CAM-B3LYP/6-31G* in the gas phase within the linear-response (TD) and Tamm-Dancoff (TDA) approximations. All the calculations were performed at the equilibrium geometry of the ground state.
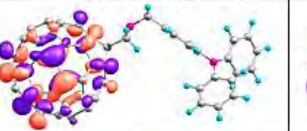
State	Ex		f		μ	
	TD	TDA	TD	TDA	TD	TDA
1	2.461	2.500	0.003	0.004	5.02	6.36
2	2.547	2.598	0.000	0.000	4.82	6.05
3	2.582	2.618	0.000	0.000	4.47	5.23
4	2.589	2.639	0.000	0.000	4.14	4.46
5	2.801	2.837	0.000	0.000	4.53	5.70
6	2.851	2.886	0.000	0.000	4.76	6.15
7	2.866	2.914	0.000	0.000	4.58	5.79
8	2.923	2.992	0.000	0.000	4.79	5.92
9	3.007	3.060	0.001	0.002	5.15	6.93
10	3.082	3.151	0.001	0.000	6.08	5.08
11	3.101	3.162	0.000	0.001	5.35	9.06
12	3.117	3.170	0.000	0.000	4.28	7.57
13	3.285	3.358	0.003	0.003	4.87	6.73
14	3.297	3.373	0.000	0.000	2.94	0.91
15	3.423	3.477	0.015	0.002	3.90	55.57
16	3.468	3.492	0.001	0.016	48.10	3.17
17	3.532	3.583	0.002	0.004	4.01	4.02
18	3.619	3.631	0.000	0.000	4.89	56.30
19	3.621	3.674	0.000	0.000	47.42	4.87
20	3.653	3.707	0.001	0.001	4.52	4.91

Table S2. Molecular properties of excited states as modeled by UCAM-B3LYP/6-31G* coupled to COSMO with benzonitrile in equilibrium solvation (top) and in the gas phase (bottom). Dipole moments μ in debyes, summations of all the atomic Mulliken charge distribution on a fragment Q_F in e^-, and the expected values of $<S^2>$. All the calculations were performed at the equilibrium geometry of the ground state.

State	μ	Mulliken Charges on Fragments			$<S^2>$
		Q_{C60}	Q_{bridge}	Q_{TPA}	
GS	4.83	-0.11	0.05	0.06	-
LES$_1$	6.72	-0.13	0.07	0.06	1.04
CTS$_1$	56.14	-1.05	0.05	1.00	1.06
CTS$_2$	57.74	-1.05	0.05	1.00	1.06
CTS$_3$	59.45	-1.05	0.05	1.00	1.06

State	μ	Mulliken Charges on Fragments			$<S^2>$
		Q_{C60}	Q_{bridge}	Q_{TPA}	
GS	4.11	-0.09	0.02	0.07	-
LES$_1$	5.12	-0.11	0.03	0.07	1.04
CTS$_1$	47.71	-0.90	-0.01	0.91	1.05
CTS$_2$	48.17	-0.90	-0.01	0.91	1.05
CTS$_3$	49.37	-0.90	-0.01	0.91	1.06

Table S3 Frontier molecular orbitals of excited states as modeled by UCAM-B3LYP/6-31G* coupled to COSMO with benzonitrile in equilibrium solvation. All the calculations were performed at the equilibrium geometry of the ground state.
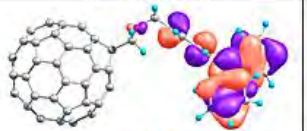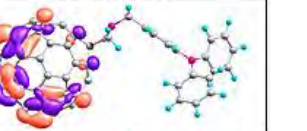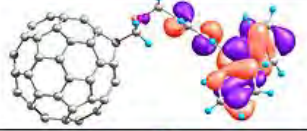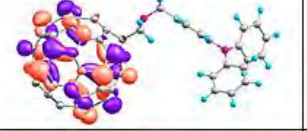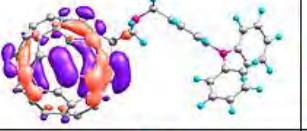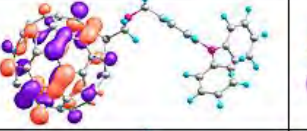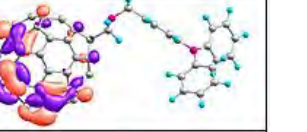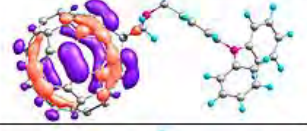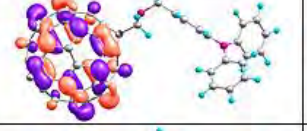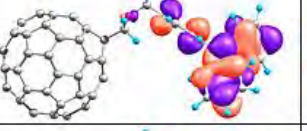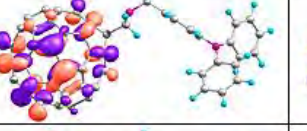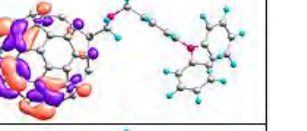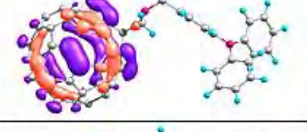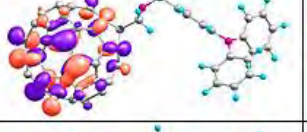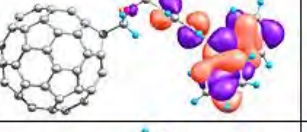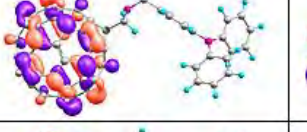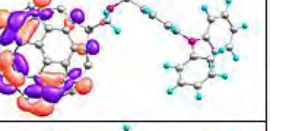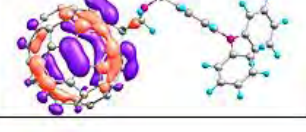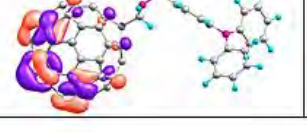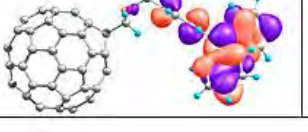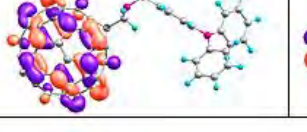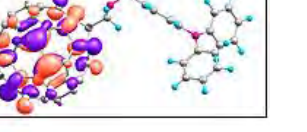
State	*in benzonitrile*				
	α HOMO-1	α HOMO	α LUMO	α LUMO+1	α LUMO+2
GS					
LES₁					
CTS₁					
CTS₂					
CTS₃					

Table S4 Franck-Condon excitation energies *Ex* in *eV*, oscillator strengths *f*, and dipole moments *μ* in debye for the twenty lowest-energy excited states as calculated through linear-response TD-B3LYP/6-31G* coupled to different solvation models in equilibrium solvation. All the calculations were performed at the equilibrium geometry of the ground state optimized through B3LYP/6-31G*.

State	*Ex*				*f*				*μ*			
	PCM	COSMO	SMD	GAS	PCM	COSMO	SMD	GAS	PCM	COSMO	SMD	GAS
1	1.783	1.806	1.795	1.808	0.001	0.001	0.001	0.001	56.12	56.20	56.99	48.83
2	1.894	1.894	1.885	1.907	0.000	0.007	0.009	0.002	56.64	6.43	7.04	5.15
3	1.895	1.917	1.909	1.917	0.007	0.000	0.000	0.000	6.56	56.87	57.79	49.14
4	2.009	2.008	2.001	2.016	0.000	0.000	0.000	0.000	6.95	6.96	7.66	5.39
5	2.023	2.023	2.016	2.030	0.000	0.000	0.000	0.000	5.37	5.36	5.86	4.49
6	2.069	2.069	2.064	2.072	0.000	0.000	0.000	0.000	5.11	5.10	5.55	4.32
7	2.143	2.166	2.158	2.172	0.000	0.000	0.000	0.000	58.34	58.45	59.57	50.11
8	2.191	2.190	2.186	2.192	0.000	0.000	0.000	0.000	5.73	5.73	5.98	4.64
9	2.203	2.202	2.196	2.216	0.000	0.000	0.000	0.000	5.40	5.39	6.16	4.46
10	2.216	2.215	2.213	2.221	0.000	0.000	0.000	0.000	6.36	6.36	7.05	4.95
11	2.248	2.247	2.236	2.264	0.001	0.001	0.001	0.000	6.15	6.15	6.77	4.91
12	2.341	2.340	2.328	2.365	0.002	0.002	0.002	0.001	8.49	8.51	9.40	6.34
13	2.416	2.415	2.407	2.431	0.005	0.005	0.006	0.001	7.46	7.48	8.29	5.69
14	2.423	2.422	2.419	2.433	0.000	0.000	0.000	0.000	7.34	7.35	8.13	5.57
15	2.492	2.491	2.488	2.500	0.002	0.002	0.003	0.000	6.67	6.68	7.48	5.06
16	2.573	2.572	2.536	2.586	0.001	0.001	0.009	0.000	3.86	3.36	25.66	3.21
17	2.604	2.603	2.571	2.614	0.010	0.010	0.003	0.003	4.28	4.23	8.09	3.86
18	2.633	2.648	2.596	2.714	0.008	0.009	0.014	0.004	28.48	29.07	5.71	23.32
19	2.723	2.738	2.640	2.802	0.021	0.021	0.021	0.012	29.58	29.75	29.59	23.44
20	2.843	2.843	2.834	2.856	0.030	0.032	0.043	0.008	4.95	4.88	6.36	4.16

Table S5 Franck-Condon excitation energies Ex in eV, oscillator strengths f, and dipole moments μ in debye for the lowest-energy localized and charge transfer excited states as calculated through linear-response TD-wB97XD/6-31G* in the gas phase. Excited state calculations were performed at the equilibrium geometry of the ground state optimized through wB97XD/6-31G*.

State	Ex	f	μ
GS	0.000	-	5.34
LES$_1$	2.501	0.017	6.87
CTS$_1$	3.936	0.017	50.51

Table S6 Molecular properties of the lowest-energy charge transfer state (**CTS$_1$**) in its equilibrium geometry as optimized by UCAM-B3LYP/6-31G* coupled to COSMO with benzonitrile in equilibrium solvation. Dipole moments μ in debyes, summations of all the atomic Mulliken charges on a fragment Q_F in e^-, and the expected values of $<S^2>$.

Spin	μ	Mulliken Charges on Fragments			$<S^2>$
		Q_{C60}	Q_{bridge}	Q_{TPA}	
Singlet	55.70	-1.05	0.05	0.99	1.06
Triplet	56.27	-1.05	0.05	1.00	2.06